Doctoral dissertation

Fabrication Processes and Photovoltaic Characterizations of Nanosilicon Membranes

ナノシリコン自立膜の作製と太陽電池特性評価

Department of Electronic and Information Engineering
Faculty of Technology
Tokyo University of Agriculture and Technology
Year of admission: 2007 - Registration number: 07834701

Romain Mentek

Academic supervisor: Yoshiyuki Suda
(Nobuyoshi Koshida)

論文要旨

　量子サイズナノシリコン自立膜の作製と太陽電池への応用に関する研究を行った。先ず陽極酸化と呼ばれるウエットプロセスの基礎技術を固めた後、その知見を nc-Si 自立膜作製技術に発展させ、ｐ型、ｎ型およびｐｎ接合の単結晶シリコン基板から大面積の nc-Si 自立膜を剥離する技術を確立した。また、深さ方向に対する粒径変化によるバンドギャッププロファイルの制御性を、吸収スペクトル、ＰＬ発光などの光学測定解析により確認した。これらをふまえ、ｐｎ接合基板から作製した nc-Si 自立膜太陽電池が 0.87V におよぶ非常に高い開放電圧を示すことを見いだした。さらに、光電変換効率と安定性の向上には、nc-Si の表面パッシベーションが有効であることを明らかにした。これらにより、nc-Si 自立膜がフルスペクトル太陽電池に必要な多接合素子のトップセル材料としての特性を備えていることが示された。

　以下、本論文を構成する全６章について、概要を記す。

第1章　序論

　本研究の背景と目的について述べる。始めに電気化学陽極酸化プロセスの特質を示し、ナノ結晶シリコンの形成、一般的特性と応用例を概説する。次にナノ構造シリコンの太陽電池への応用について、これまでの研究開発の状況をまとめる。さらに、太陽電池に関連する陽極酸化技術の例として、シリコンのスライス技術やナノシリコン層形成の概念と可能性をまとめる。

第2章　関連技術の現状

　本研究において最も重要な基本プロセスである陽極酸化法でのナノシリコン層の形成について、他のプロセス技術との比較しながら特徴を述べる。また陽極酸化法と密接に関係し太陽電池作製技術にも結び付くシリコン基板の非接触ウエットスライス技術について、開発の状況をまとめる。従来の機械的スライス法と比べて表面への損傷が抑えられ、低カーフロス化、マルチ処理化、高速化のニーズに応える技術に展開できる可能性を実証的に示した。

第3章　実験方法

　単結晶シリコンからナノシリコン自立膜の太陽電池素子の構造と作製プロセスフローを述べる。まず電気化学的手法による大面積ナノシリコン自立膜の分離方法を一貫プロセスとして確立した上で、光学的特性を測定する方法、薄膜電極の堆積法、太陽電池を作製し光起電力特性を測定評価するシステムを述べ、さらにナノシリコンの表面安定化する手法にもふれている。

第4章　ナノシリコン自立膜の光電変換特性

　本章ではナノシリコン自立膜の光学特性と光電変換能の検証を行う。先ず、上記方法に

より、ｐ型基板、ｎ型基板、およびｐｎ接合基板から任意の厚さのナノシリコン自立膜が作製できることを示す。また、それらの各ナノ自立膜の光学的性質を光吸収特性、フォトルミネセンススペクトルなどの測定によって詳細に解析し、適正な条件で作製した試料のバンドギャップは再現性よく 1.7ｅV 以上に拡大し、太陽光の全スペクトル成分を変換する多接合太陽電池のトップセルに要求される条件を満たしていることを明らかにする。それをふまえて、作製した各種自立膜構造セルの太陽電池特性を通常の光照射条件(AM1.5, 1sun、室温)において測定した。その結果、ｐｎ接合基板から分離したナノシリコン自立膜セルにおいて、0.875V という非常に高い開放電圧の光電変換特性を見いだした。Ｐ型またはＮ型の単独基板による試料の測定結果と合わせ、通常では得られないこの結果が、ナノシリコンの固有の効果に基づくことを明らかにしている。また、分光感度特性についてもpn 接合基板から作製したナノシリコン自立膜セルは約 450 nm の波長域にピークを持ち、基本的にトップセルに適うことを確認している。

第5章　　光電変換特性の安定化

　高い開放電圧を示す pn 接合型のナノシリコン自立膜セルの特性をさらに向上するため、ナノシリコン層の表面と内部の両面から、光電特性の検討を行っている。前者については種々の薄膜電極材料が与える影響、後者についてはナノシリコンドット表面の終端制御に重点をおいた。その結果、観測された高い開放電圧がナノシリコン自立膜に特有の物性によるものであることがさらに裏付けられた。また、化学エッチング、熱処理、有機分子表面処理、高圧水蒸気アニール、フォーミングガスアニールなどの効果を総合し、ナノシリコンドットの表面終端を修飾することによって太陽電池特性の安定性が向上することが判明し、高い開放電圧が良好なダイオード整流特性および短絡電流密度の向上を両立させるための基礎情報を得ている。

第6章　　結論

　本論文において得られた知見とその意義について総括する。ナノシリコン自立膜では、量子サイズのシリコンドットに由来して、短波長域の光電変換特性を示し、高い開放電圧を有することが明らかにされ、特性向上につながる情報も得ている。多接合太陽電池のトップセルとしての可能性が示された。

Abstract

To clarify the potential usefulness of quantum-sized silicon material as a wide-gap absorber in multi-junction solar cells, the photovoltaic properties of nanosilicon prepared through electrochemical process has been investigated. The material was fabricated in thin free-standing nanosilicon layers peeled out from pn-doped substrates as well as from single doped p- and n-type substrates for reference. Following the development of a sequential process flow for fabrication of nanosilicon membranes with designed nanostructures and thicknesses, the optical and photovoltaic characterizations were conducted.

It is shown from the analyses of optical absorption and photoluminescence spectra that nanosilicon membranes meet the band gap requirements for a top cell in multi-junction tandem cells. In addition, the fabricated nanosilicon membrane cells with a pn-junction structure exhibits a definite photovoltaic effect with a very large open circuit voltage of 0.875 V, never reported before in such devices. The observed spectral response with a peak in the short wavelength region supports the fact that the material might act as a wide gap absorber. Comparison with single doped material with different top contact configurations clearly indicates that the original junction inside the membrane plays an intrinsic role in the observed photovoltaic effect, while the contributions from the contacts are negligible.

Additional treatments of the samples including chemical etching in hydrofluoric acid as well as thermal annealing in an inert atmosphere suggest a strong contribution from the hydrogenated surface in the observed photoconduction characteristics. Replacement of interfacial hydrogen bonds by organic molecules appears to be a promising approach toward stabilization and functionalization of the material for practical application in solar cells.

These results on the photovoltaic behavior of nanosilicon membranes provide useful suggestions toward the development of the wide-gap component in efficient full spectrum solar cells.

Summary

Chapter II.   Related technology: electrochemical slicing

Chapter III.   Experimental methods

Chapter IV. Photovoltaic characterization of nanocrystalline porous silicon free standing membranes

Chapter V. Photovoltaic characteristics stabilization

Chapter VI. Conclusion

Preface

In the recent years global warming has become a preoccupying and complicated worldwide issue. A growing number of scientific evidences are indicating the warming of the climate since the year 1950, mainly due to human activity (industry, transport etc…) causing emission of carbon dioxide and others "greenhouse" gazes into the atmosphere. While the existence of global warming and its relation with human activity is still debated by some today, a number of political, economical and technological responses have emerged as soon as 1992 with the creation of an international treaty "the United Nations Framework Convention on Climate Change" (UNFCC), followed in 1997 by the Kyoto Protocol and more recently with the Copenhagen Summit in 2009.

Among the technological response to global warming is the obvious development of renewable energy in which energy is harvested from natural (and naturally replenished) resources such as wind, tides, geothermic heat and more particularly sunlight. The direct transformation of sunlight into electricity is realized by photovoltaic cells also called solar cells. From the discovery of photovoltaic effect by Henry Becquerel back in 1839, photovoltaics has, since the advance of the semiconductor technology, developed into an ever growing market where solar cells can now be found not only powering satellites in highly expensive aero-space project but also as panel mounted on roofs as well as in small electronics devices such as pocket calculators and cell-phone battery chargers. Recent years have seen an explosion in the PV electric generation capacity, jumping from under 5 GW in 2004 to largely over 20 GW in 2009. To support such a growth of capacity and to keep decreasing the cost per watt, researches are mainly taking two different orientations: increasing the efficiency of the cells and/or decreasing the production cost. The work presented in this thesis will follow these two orientations by presenting the results of our researches on a new electrochemical slicing method for solar cells silicon wafers followed by our investigations on porous silicon made by electrochemical etching as a new solar cells material for future advanced photovoltaic devices.

Chapter I.   Introduction

I.1 Electrochemical processing of silicon: Introduction

Early silicon electrochemistry mostly dealt with problem of anodic oxidation, chemical etching and electropolishing of the material. Investigation on anodic oxide growth started in the late 30s and further progress was achieved in the subsequent years with the development of various etching techniques for defect delineation and chemical polishing (CP) applications. Uhlir [1] was the first to report the presence of porous silicon (PSi) in 1956 when he discovers the formation of a brownish film at the surface of Silicon electrodes under particular conditions. Further investigation lead by Turner shows the presence of two distinct electrochemical reactions, the electropolishing and the porous silicon formation regimes [2]. But the real nature of the material remained unknown until 1971 when Watanabe and Sakai [3] first reported the porous nature of the observed films formed at the surface of Si anodes. A further step forward was achieved after the observation of visible photoluminescence at low temperature in 1984 [4] but the origin of the luminescent emission remained mostly unanswered until 1990-1991 when Canham proposed a quantum size effect to explain the observed phenomenon [5]. Such discoveries have since started a sparkling interest in the material for its potential applications in a wide variety of fields.

I.2 Electrochemical etching in Acidic solution

I.2.1 General overview

A wide variety of techniques, including both wet and dry processes such as reactive ion etching (RIE), are available for etching of silicon and their use mainly depends on the type of desired etching, isotropic or anisotropic for example. Despite the recent advance of RIE technology, wet etching still plays an important role in silicon processing and can be classified according to the constituent and pH of the electrolytes. The most common type of electrolytes are based on an acidic mixture of hydrofluoric acid (HF) with water or an organic solvent, due to the ability of HF to readily dissolved silicon dioxide. Since the formation of pores appears only in this type of electrolytes, this study will focus only on this variety of solution. The possibility of easily growing a high quality Silicon dioxide films, both by thermal process or wet electrochemical process, and subsequent easiness to remove that oxide film by chemical etching with HF has

largely participated in the dominance of Silicon over the semiconductor industry and plays an important role in processes investigated in the present study.

I.2.2 The electrochemical cell

The most typical and simplest electrochemical cell is shown in **Fig. 1.1**. The silicon material is immerged into an acidic solution containing HF mixed with a solvent (usually pure ethanol for increase wettability). In this setup, Silicon acts as the anode while the cathode is made of an HF resistant and conductive material such as Platinum or Tungsten. Since the silicon anode is in direct contact with the electrolyte, the back of the silicon anode must be isolated from the solution by an HF resistant material. In the case of a full immersion cell (as seen in **Fig. 1.1**), the back of the Si anode can be covered by an adhesive PTFE film or coated with an acid resistant wax. Another common method is the use of an "o-ring cell", where the surface of the Si electrode is separated from the acid solution through the o-ring, the surface of the electrode being only partially contacted in this case. The body of the cell itself should also be made of highly acid resistant material such as PTFE polymer. Several more advanced cells are also used in experiments where temperature control, solution flow as well as back lighting are required. While in most experiments a planar configuration for the two electrodes is used, various types of geometry and arrangement can be implemented.
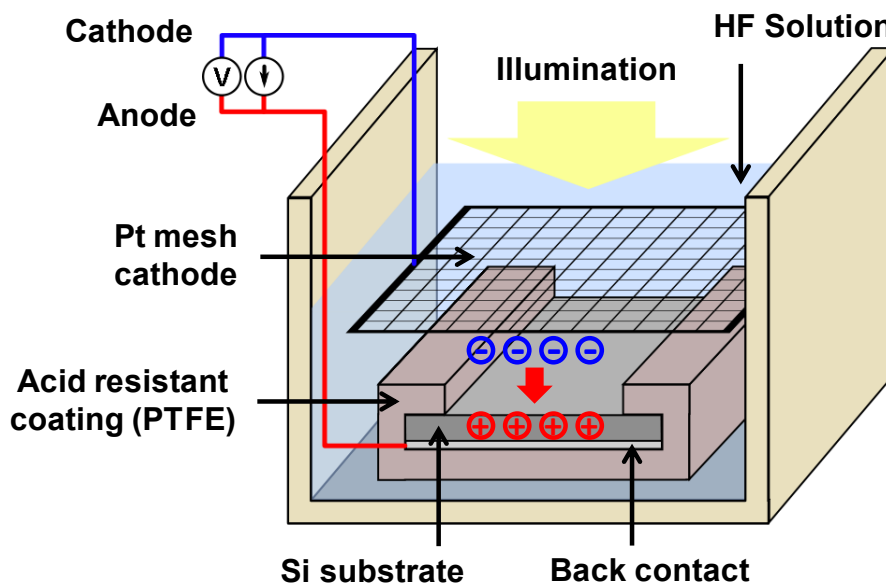
Fig. 1.1: *Isometric view of a typical, single tank full immersion anodization cell with front side illumination. In such structure, the silicon anode and the back contact are isolated by PTFE coating and fully immersed in the acidic solution.*

When silicon is in anodic polarization, the material starts to dissolve either partially (porous silicon) or completely (electropolishing) depending on the experimental conditions. The most important parameters during anodization are:

1. The electrolyte composition (content of HF, type of solvent used etc…)
2. The current density
3. The type and doping level of silicon substrate.

Other factors such as the temperature, illumination condition and crystal alignment of the material also have an importance in controlling the formation and morphology of the resulting material.

I.2.3 Current-Voltage characteristics

The typical current-voltage characteristics of p and n type Silicon in a HF based solution is showed in **Fig. 1.2**. The resulting characteristic of the Si/Electrolyte interface shares some similitude to that of a schottky diode. Under cathodic polarization, in the left part of the graph, silicon is stable and no dissolution occurs. When anodically polarized as shown in the right part of the graph, holes are supplied through the silicon material which starts to dissolve. In the case of N type silicon where electrons are the majority carriers, illumination of the sample is usually required for injecting holes near the dissolution interface and improving the porous layer formation.
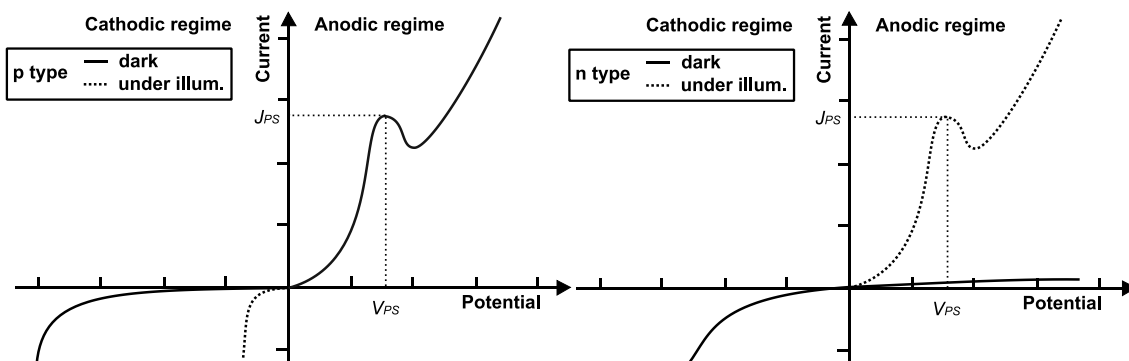
Fig. 1.2: *Typical current-voltage characteristics of silicon anode in HF base solution for p type silicon at the left and n type at the right. N type silicon requires illumination to efficiently generate holes in the material as seen in the strong difference between dark and illuminated condition compare to p type material.*

The electrochemical dissolution occurring under anodic polarization can be divided into two different zones corresponding to two distinctive reactions depending on the range of current density. The two zones are separated by a small current peak called the electropolishing peak at a corresponding current density J_{sp}. For low anodic density below the critical value J_{sp}, only a partial dissolution of silicon occurs leading to the formation of a porous material. When the current density exceeds J_{sp}, the reaction enters into an electro-polishing mode where silicon is completely dissolved, leading to clean and flat surface. Such an interesting behavior has actually been advantageously used (especially in this work) to detach the fabricated PSi layer after formation by application of an electropolishing current peak. The current density range at which PSi formation and electropolishing occur is heavily dependent on the electrolyte nature and content as well as the wafer doping. It is important to note that dissolution of silicon occurs both in galvanostatic or potentiostatic regime but the first method is preferred for a better control of PSi formation, since the reaction depends on the number of supplied charges as explained in the following section.

I.2.4 Dissolution chemistry

Silicon is relatively stable in fluoride based acidic solution under cathodic regime and at open circuit polarization, dissolution occurring only in anodic polarization. The electrochemical dissolution follows a complex reaction which differs depending on the anodic current density J_{ps} (or potential V_{ps}) regime.

The proposed dissolution reaction model at low current density ($J<J_{ps}$) is a divalent reaction shown in **Fig. 1.3** and written as **Eq. 1.1**. The model shows the importance of holes supply through silicon, the presence of a hole near the chemical interface starting the overall reaction.

$$Si + 4HF_2^- + h^+ \rightarrow SiF_6^{2-} + 2HF + H_2 + e^- \qquad \textbf{(Eq. 1.1)}$$
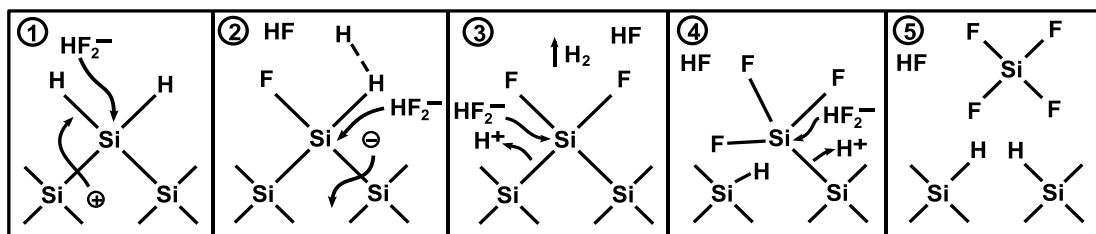
Fig. 1.3: *Proposed divalent dissolution model at the atomic scale for Silicon electrode in HF base electrolyte. Redraw from [6].*

For current density superior to the critical value J_{ps} the reaction can be divided into two concurrent phenomena shown in **Fig. 1.4**. First, silicon is electrochemically oxidized following a tetravalent reaction:

$$Si + 2H_2O + 4h^+ \rightarrow SiO_2 + 4h^+$$ **(Eq. 1.2)**
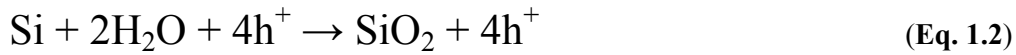
The next step is the chemical dissolution of the newly formed silicon oxide layer by the solution active species HF, $(HF)_2$ or HF_2^-:

$$SiO_2 + 2HF_2^- + 2HF \rightarrow SiF_6^{2-} + 2H_2O$$ **(Eq. 1.3)**
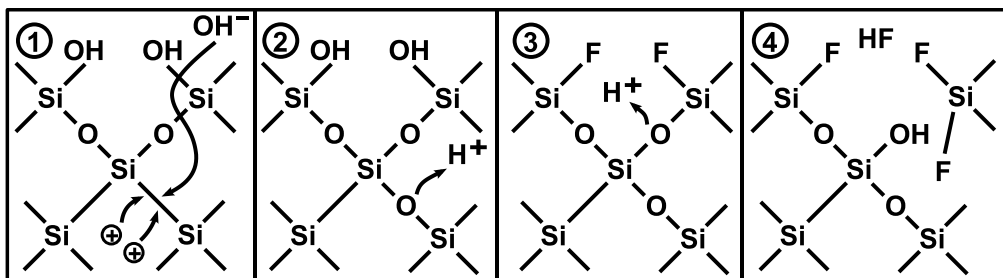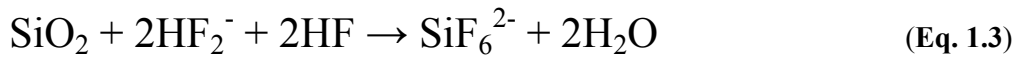
Fig. 1.4: *Proposed tetravalent dissolution model of Silicon electrode in HF base electrolyte. Silicon is first anodically oxidized (Step 1 and 2) and the corresponding oxide is then dissolved by active species of the HF solution (step 3 and 4). Redraw from [6].*

These two steps usually occur simultaneously or in a periodic manner (oscillating system).

The overall valence of the reaction in the PSi formation region is expected to be equal to 2, but contrarily to the theoretical reaction equation, it is found to be between 2 and 3 in practice, both divalent and tetravalent reactions occurring at the same time. The phenomenon is due to inhomogeneous spatial distribution of the current density leading to divalent or tetravalent reaction depending on the geometry and size of the pores at the dissolution interface. More details about the complete chemical dissolution of silicon are given by Lehmann [6].

I.3 Practical applications of electrochemical etching

I.3.1 Application of Silicon electropolishing

Investigation on electrochemical polishing started as early as 1956 by Uhlir [1] and 1958 by Turner [2] in order to produce flat, clean, defect free silicon surface, making electropolishing historically one of the oldest electrochemical process for silicon. Investigations on the technique also lead to the first observation of porous silicon formation which potential will be understood only several decades later. While an early promising candidate for planar polishing of silicon surface, the electrochemical process has later been superseded by far superior CMP technology which is still currently the most widely used polishing technology in the semiconductor industry. We will see in the next chapter that the inherent qualities of the electropolishing process can be used in a controlled manner for micromachining of Silicon, and especially the fabrication of deep and thin trenches in the material with potential application in wafer slicing as further expanded in section I.4 of this chapter. Another important application of the electropolishing effect is the simple "in situ" separation process for easy PSi layer lift-off from the silicon substrate right after the layer formation.

I.3.2 Application of Porous Silicon

Since the discovery of its visible luminescence, the main promising application for nanocrystalline PSi (nc-PSi) has remained related to this peculiar characteristic with strong hope in the possibility of fabricating efficient visible silicon based light source which would be inherently compatible with the current and standard silicon and VLSI processing technologies. Nevertheless, due to the large change in its physical properties compare to bulk silicon, the potential applications of porous silicon are far than just limited to luminescent devices. The overall physical properties of interest and their corresponding applications are shown in the non-exhaustive **Table 1.1**. A more detailed overview of current and potential applications of PSi is available in reference [7]

It is clear from the list that applications of PSi can be separated in two groups of active and passive applications, depending on whether one focus on the nanocrystalline nature of the PSi skeleton itself and its corresponding electronic properties or simply on its porous nature and its large internal volume available. Applications involving PSi as an active material includes luminescent devices, electron emitter, photosensing and photovoltaics. On the other hand, PSi is used as a passive element in most bio related applications such as drug delivery, acting as an

15

host matrix for foreign compounds and molecules etc…Applications related to solar cells will be discussed in more details at the end of this chapter in the section introducing porous silicon..

Physical characteristic	Potential applications	Reference
Luminescence (PL - EL)	LED, Display, Optoelectronics (Active devices)	[8][9]
Porosity dependent refractive index	Photonics: Waveguides Mirrors, Reflectors Cavities etc…	[10][11] [12][13] [14][15]
Large internal volume, host material for foreign compounds	Explosive, optical switch Sensors	[16][17] [18][19]
Low thermal conductivity	Sound / ultrasound emitter, position sensing	[20][21] [22]
Bio-compatibility	Drug delivery, in-vivo application, tracking material	[23][24]
Sacrificial layers	MEMS, transfer layer, growth template	[25][26]
Electron emission	Cold cathode emitter Ballistic lighting Flat panel display Hydrogen generation Lithography	[27] [28] [29] [30][31][32] [33] [34]
Band gap widening Photoconductivity	Photodetector Solar cells	See the end of chapter I for more details

Table 1.1: *Non-exhaustive list of PSi particular physical characteristics and their related potential applications. The number of proposed and investigated applications of PSi are far too numerous to be listed and discussed in details in this thesis.*

I.4 Introduction to Silicon wafering

I.4.1 Introduction

As of 2008, poly- and mono-crystalline silicon (poly-Si and c-Si) solar cells are still the dominant PV cells technology with more than 85% of the Photovoltaic market as seen in **Fig. 1.5** [35]. The fabrication of such cells requires the slicing of large silicon blocks (ingots) into several thin wafers. The main slicing method used until today is based on a mechanical multi-wire sawing technique to provide wafers for both the photovoltaic and microelectronic industry. Due to a strong focus on cost reduction, industrials and academics are currently working jointly to enhance the current mechanical technology as well as develop completely new approaches to wafering.
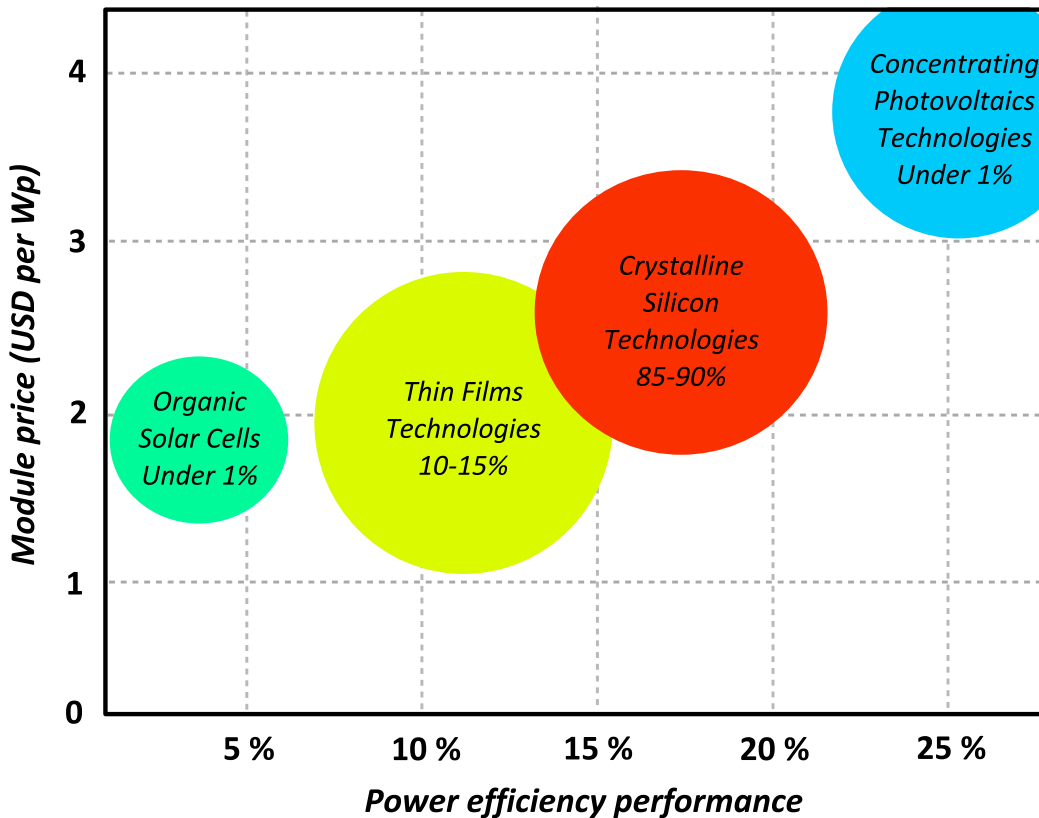
Fig. 1.5: *Power efficiency range and correponding module price for the four main commercial solar cells technologies and their respective market share. Redrawn from [35]*

I.4.2 Economical aspect and future roadmap

The economical aspects are prominent in all the PV manufacturing steps, each fabrication processes contributing to the total cost of the final solar panels and thus the cost per watt of photovoltaic generated electricity, an important factor in the race to competitiveness with other energy sources. As previously discussed in the previous section, the cost reduction for Silicon based solar cells can be achieved following two different approaches: focusing on the increase of power efficiency of the solar cell itself, and/or reducing the total processing cost of a cell with a strong focus on saving the raw silicon material. The total manufacturing cost of a typical c-Si solar module is shown in **Fig. 1.6** (summarized from [36] and [37]). The first few processing steps from the silicon feedstock to the finished silicon wafer represent 33% of the total cost of a solar panel. If we consider the cost from the point of view of one solar cell itself and not the total module, the silicon processing to its final wafer shape actually represent more than half of the total cost of the cell. One way of reducing the wafering cost relies on reducing the thickness of the Si wafers, increasing the number of fabricated wafers per Silicon ingot.

Raw material	Ingot growth	Wafer	Cell processing	Module assembly

14%	8%	11%	27%	40%

55%

Solar cell processing 100%
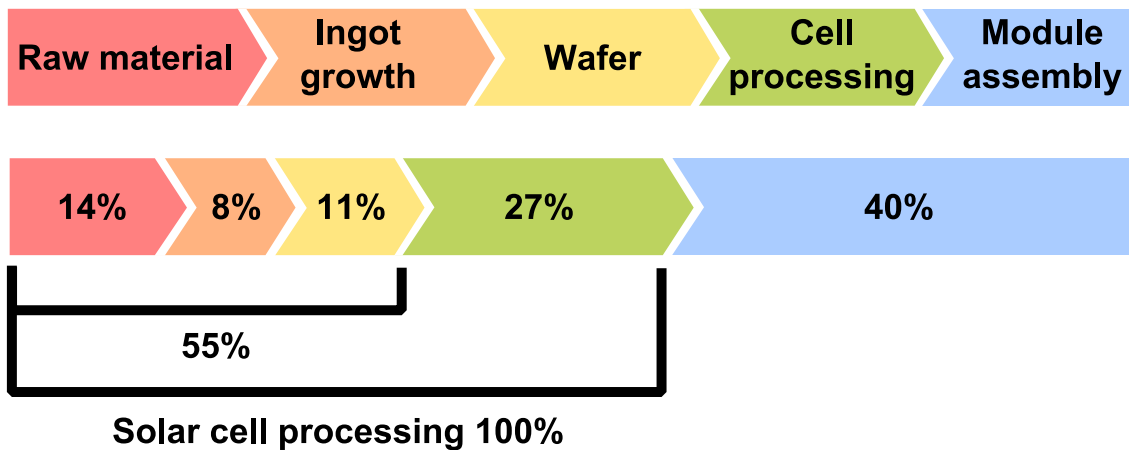
Fig. 1.6: *Repartition of the total cost of silicon solar cells between their multiple fabrication steps. Excluding the module assembly, the processing steps from raw silicon material to its solar grade wafer form represents more than half of the processing cost.*

The road to such "ultra-thin solar cell" wafers has been supported worldwide by different public and private groups and organizations including commercial companies, organizations such as NEDO in Japan, the Fraunhofer Institute in Europe and the NREL in USA. The general trend for PV wafer thickness decrease is shown in **Fig. 1.7** adapted from [38] and [39]. The reduction in the thickness of solar cell wafers in the future forecasts a thickness as low as 100 µm by 2020. Such a drastic

reduction in wafer thickness requires strong process improvements in the current historical wire sawing technology and has opened the door to a variety of new experimental slicing concepts toward ultra-thin PV wafers. Such new approaches include plasma cutting, electric discharge machining (EDM), numerous types of exfoliation methods and of course our own developed approach to wafer slicing by using a local electrochemical etching of silicon in acidic solution. A more complete description and comparison of the different new slicing technologies are presented at the end of this chapter.
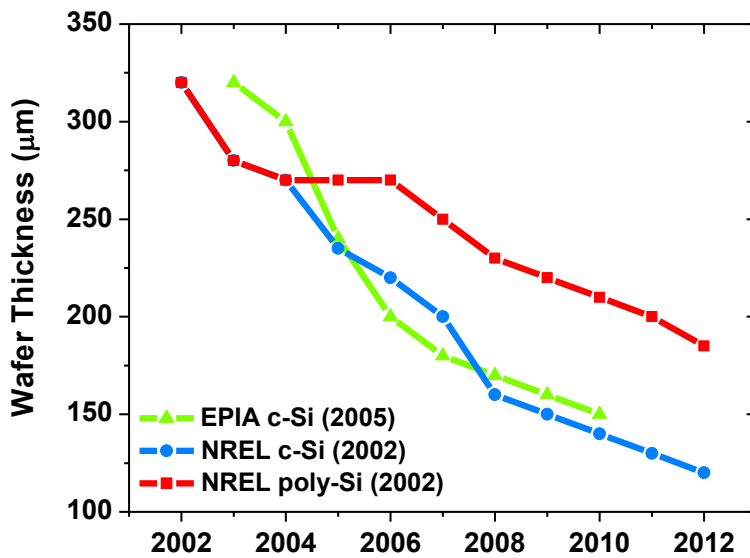
Fig. 1.7: *Wafer thickness decrease roadmap from an European (EPIA) and North American (NREL) organisations showing a strong decrease in solar wafer thickness for the years to come.*

I.4.3 Slicing technologies

Wafer slicing is an important step in the PV wafer manufacturing chain shown in **Fig. 1.8**. Fabrication of high quality silicon wafers starts by the melting of high-purity silicon raw material (in the form of nuggets or chips) which is either cast into square ingots for poly-crystal material or grown by pulling such as in the Czochralski method. The resulting roughly shaped ingots are then shaped to more practical size by cropping of the ingot extremity in the case of monocrystalline round ingot, followed by a squaring/bricking step in which the ingot take the shape and size of the final wafer (sometimes requiring a further step of edge grinding). The ingots are then prepared for the next step of wafer cutting in which the ingot is sliced into multiple wafers by a multi-wire saw system. Finally, the wafers are separated, cleaned and may be subject to quality control inspection including thickness variation measurement, bowing and warping deformations , defects density and

resistivity. A detailed overview of the multiple aspects of solar grade silicon manufacturing, including the wafering process, is given by Koch et al [40].
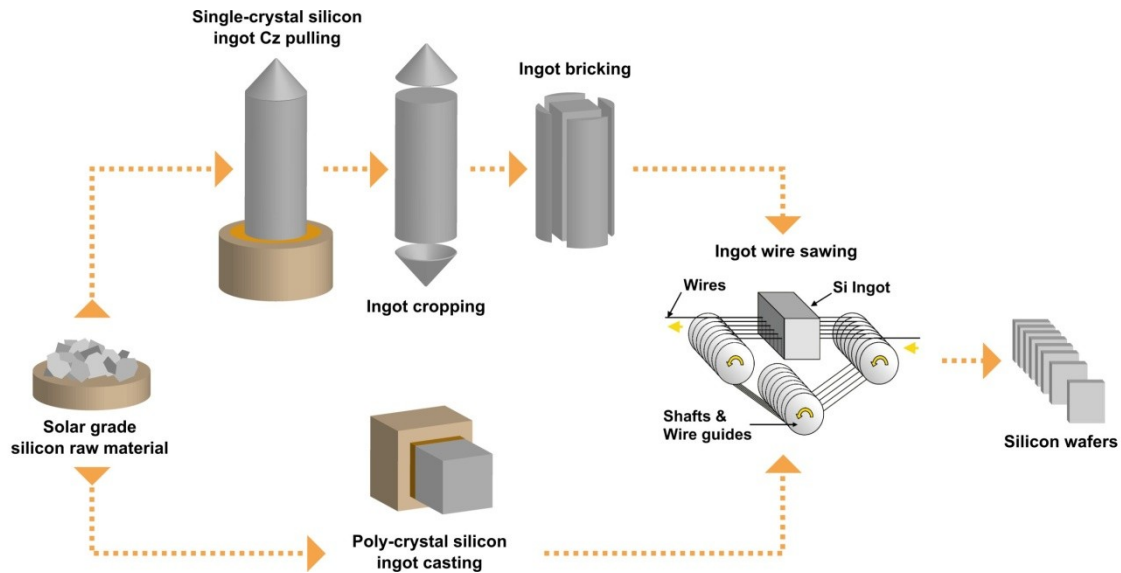
Fig. 1.8: *Typical manufacturing flow for the fabrication of single and poly crystal silicon from its raw unrefined form to its final form of wafer ready to be processed into a solar cell.*

I.4.3.1 Concept of Silicon slicing

Fig. 1.9 shows the basic concept of Si slicing. For simplicity, the slicing element is represented here by a wire mechanically grinding away the material. In practice, a wide variety of slicing tools relying on different physical processes are available (see the end of chapter III for further information). The most important parameter for efficient and economical slicing is the ratio between the sliced wafer thickness and the material loss induced by the slicing method, called the kerfloss. The historical wafer thickness for the microelectronics and PV industry is in the order of 500 μm and the kerfloss even lower. If one takes a wafer of 500 μm sliced with a kerfloss of 250 μm, we obtained a ratio of 2 to 1 which is economically acceptable. If for economical reason the wafer thickness is reduced to 250 μm while keeping the same 250 μm kerfloss constant, we obtain a ratio of 1 to 1, 50% of the raw material has been lost during the slicing process. The reduction of the kerfloss is therefore one of the most important aspect to maintain the slicing process economically viable while reducing the Si wafer thickness.
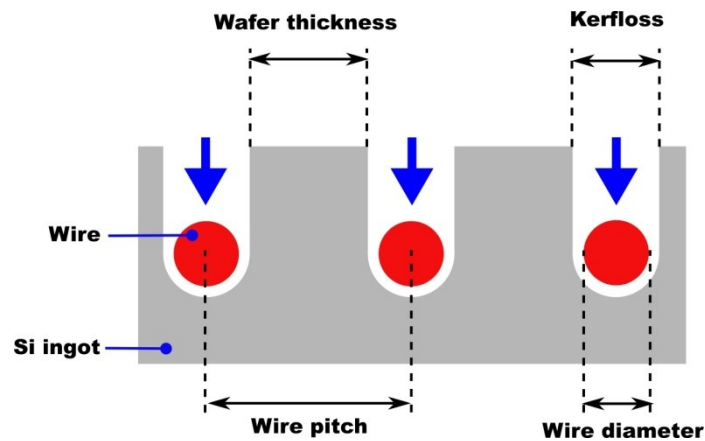
Fig. 1.9: *Schematic cross sectional view of silicon slicing showing the two main parameters of the slice: the resulting wafer thickness and the kerfloss representing the amount of lost silicon material.*

I.4.3.2 Standard Silicon slicing technology

Cropping: ID saw process

The cropping process consists of removing the conical extremity of the monocrystalline silicon ingot by using and inner diameter saw (ID saw). ID sawing is widely used to slice silicon and germanium material for microelectronic applications as well as numerous other materials (sapphire, quartz, gallium-arsenide etc…) but is limited to cropping in the photovoltaic industry due to its inability at multiple parallel slicing.

Bricking: Band saw process

Bricking is usually done on round monocrystalline silicon ingots to give them their final square shape necessary for the finished solar cells (square providing the best geometrical fill factor) and is also used in removing casting defects on polycrystalline silicon. Once more, the band saw is adapted for deep section slicing (along the ingots full length) but does not fulfill the requirements for parallel multi-slicing of wafers.

Wafering: Wire saw process

Wire saw is currently the only industrial process available for parallel multi-wafering. Prepared silicon ingots are sliced into multiple wafers in one run by several parallel metallic wires. The wires, of several hundred of kilometers in length, are fed from large spool rotating at a constant speed. The wires are kept evenly spaced and tensed by a system of wire tensioning and guide rollers. When the moving wires enter in contact with the surface of silicon ingots, they are sliced into thousands of

21

wafers. The cut grinding process is enhanced by the addition of abrasive slurry, consisting of Silicon carbide particles suspended in a slurry base (oil or glycol). Recent development has lead to the apparition of new methods using diamond coated wires, leading to higher performances and removing the need of slicing slurry and all the related supplying and recycling equipments [41].

I.4.3.3   Electrochemical silicon slicing

The method proposed here to produce deep trench through electrochemical etching in Silicon is very similar to the classical wire saw slicing in terms of implementation and geometry. As seen in **Fig. 1.10**, in the electrochemical process the slicing element should be an HF resistant conductor such as a metallic wire or ribbon but instead of purely mechanical grinding of the underlying silicon material, slicing is obtained by progressive local dissolution of silicon in the vicinity of the wire. Contrarily to mechanical wire saw, in the electrochemical process the wire does not need to rotate at high speed and can remain perfectly static and mechanical contact with the silicon material is not required. As already introduced earlier, the electrochemical slicing method use the electropolishing effect of HF based electrolyte at high current injection between the metallic cathode and the silicon anode. An ohmic contact should be formed at the back of the Silicon ingot by a metal layer evaporation eventually followed by a low temperature annealing step. Similarly to the formation of porous silicon, from a purely electrochemical point of view, the electropolishing effect is dependent on the type of electrolyte used, the content of HF and the range of current density applies to the electrochemical system. Further important parameters include the mechanical and geometrical configuration of the system. The influence of such parameters on the electrochemical slicing performance is discussed in more details in chapter II section II.1.2.
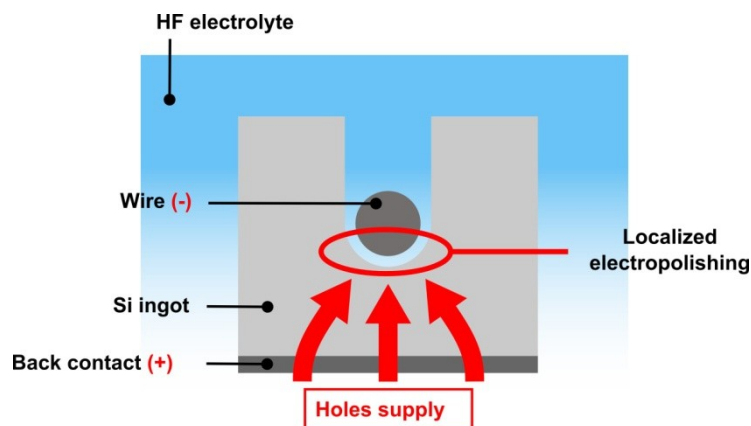
Fig. 1.10: *Schematic of the electrochemical slicing method with one metallic wire representing the cathode of the system.*

I.4.4 Practical wafering key requirements

In order to be economically competitive, silicon slicing methods should meet, if not exceed, a few key requirements related to their global impact on the fabrication cost of cells as well as their practicability in an industrial environment. Especially in the case of developing new methods, they are bound to compete with current technologies such as wire-sawing while also matching the requirement of the future ultra-thin wafer roadmap concerning the reduction of both wafer thicknesses and kerflosses.

The 2 basic requirements for the "ultrathin wafer roadmap" are:

● Ability to slice thin wafers (following the previously shown roadmap for example)
● Slice with a reduce kerfloss ≤ Wafer thickness

In terms of more economical requirements, a new slicing process will also have to compete with the current standard wire saw processing in terms of:

- Wield: the time required to slice a silicon ingot completely. Includes the intrinsic slicing speed of the process (grinding, lapping, etching etc…) and the ability to slice one ingot in multiple wafers in one sequence. Also includes keeping the probability of wafer wreckage during slice the lowest possible.
- Scalability: easily scalable to industrially available Si ingot size.
- Quality: Produce wafer with an overall good quality (surface roughness, level of contamination etc…) so as to limit the post-slicing processing such as cleaning, etching and polishing.
- Low manufacturing cost for low $/W: Keeping the slicing process simple and limiting the use of energy and additional expensive consumables such as chemicals.

The chapter II will introduce the electrochemical etching process and its possible application as a new silicon slicing method, including a summary of the overall achievement and performance of the process in relation to the previously discussed requirements. Finally, the electrochemical slicing method will be compared with both commercially available process and concurrent approaches currently under development as well.

I.5 Introduction to porous silicon

I.5.1 Formation of porous silicon

I.5.1.1 Fabrication and mechanism of formation

Porous silicon is usually fabricated by anodic electrochemical etching (hence sometimes referred as "anodization") of bulk Si substrate in a hydrofluoric solution (HF) [42]. Other techniques leading to the formation of PSi are galvanic etching [43] (no external power source, metal electrode required) or stain etching [44] (no external power source, no metal electrode) but are not popular due to difficulties to control the formation of the material compare to the electrochemical method.

Pores initialization at the silicon surface and their propagation is a challenging problem especially in view of the multiple and various natures of resulting porous structures obtained from different type and doping level. It is now widely accepted that the initialization of pores occurs at the location of defects or irregularities at the Si surface, but while such defects and in-homogeneities always exist in every semiconductor, only Si give rise to clear pores formation. Several processes have been proposed, including the deposition of insoluble species or the re-deposition of a highly resistive amorphous like Si material at the chemical interface, favoring an inhomogeneous local dissolution of the surface. Other explanations include defects induce by the presence of the substrate dopants as well as the role of hydrogen induced defects. More detailed discussions are available in several reviews [45][46].

Due to the formation of a depletion layer at the chemical interface between the electrolyte and the Si material, the formation dynamics and resulting morphologies of the porous layers are therefore dependant on the depletion width and the charge transport mechanism. The depletion layer width can reach the range of micrometers for lowly doped n-type material while it is far thinner for heavily doped n and p type and non-existent for lowly or moderately doped p type Si. The depletion layer effectively "passivates" the pore walls, leading to preferential etching at the tip of the pore. Highly doped substrates give rise to pore with a diameter of the order of 10 nm, lowly doped n type material under dark condition usually exhibits pores in the range 10 to 100 nm while under illumination their size varies from 0.1 to 20 μm. In the case of very small wall thicknesses, the quantum confinement can also be invoke to explain the depletion of holes and the stopping of local dissolution at such nanometric sites, the phenomenon is perfectly demonstrated by the micro-pores (below 2 nm) found in moderately doped p type samples. The standardized classification for pores size is given in **Table 1.2** [47].

Pore width	Denomination
≤ 2 nm	*Micro-porous*
2 – 50 nm	*Meso-porous*
> 50 nm	*Macro-porous*

Table 1.2: *Standard IUPAC classification for porous materials according to the size of the pores.*

In any case, such a complex formation process leading to a wide variety of material structure and quality cannot be described by a simple model and probably involved multiple inter-dependent effects including electrochemical, charge transport and diffusion, presence of defects as well as mechanical phenomena.

The formation of PSi and its characteristics are highly dependent on the anodization conditions, leading to the possibility of fabricating a wide variety of porous material with different structures, pore size, porosity and thickness. Anodization conditions include the HF concentration, the anodization current density (or potential), duration of anodization, wafer type and doping level (resistivity), crystal alignment, the temperature and illumination condition.

P-type silicon can be anodized readily in the dark with good control over the formation process while n-type may require illumination in order to photo-generate and keep the supply of holes constant. Anodizations realize under illumination or during a long time usually result in a gradient of porosity along the porous layer thickness due to longer exposition as well as difference of absorption of the incident light by the top and bottom of the formed layer. It is also important to note the particular case of doped junction structure: anodization of np type (n at the top, p at the bottom) does not present any particular problem while the opposite pn type structure is actually in reverse polarity during anodization, preventing the good injection of carriers. The structure can still be anodized with the assistance of external illumination as shown in a few reports concerning PSi EL diodes [48] [49], despite early report of the contrary [42].

	Porosity	**Formation rate**	**Critical current**
HF concentration ↗	↘	↘	↗
Current density ↗	↗	↗	NA
Anodization time ↗	↗	Constant	NA
Temperature ↗	NA	NA	↗
Wafer doping (p type) ↗	↘	↗	↗
Wafer doping (n type) ↗	↗	↗	NA

Table 1.3: *General summary of the effects of formation parameters on the anodization process.*

The general effect of formation parameters are summarized in **Table 1.3**. It is important to note the similar trend among most type and doping of Si, increase in porosity is seen for increase in current density and decrease in HF content. Only n type wafers shows a small irregularity at lower anodization current where the porosity of the material increase drastically when current decreases to low density as seen in **Fig. 1.11** [42]. The dependency of porosity on current density for a given type and doping of Si allows for the fabrication of complex structures by modifying the current during anodization. Multilayered systems are usually fabricated by alternating high and low currents resulting in high and low porosity, allowing the fabrication of periodic structures such as DBR (Distributed Bragg Reflectors) as well as optical cavities among other applications. The difference of formation conditions for p and n-type and doping levels is also used for selective etching in layers containing different doping regions [42][6].
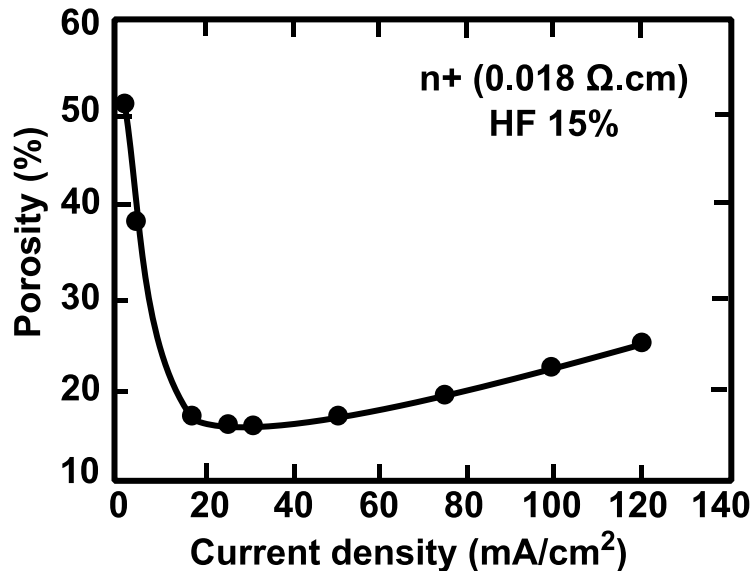
Fig. 1.11: *Variation of porosity in function of the anodization current for n type material in the dark. Anodization at low current density with photo-assistance allow for the fabrication of highly photoluminescent n type PSi.*

I.5.1.2 Post-fabrication treatment of PSi

The porous nature of the material renders it mechanically fragile compare to bulk Si substrate and care should be taken about the drying process employed, especially at higher porosity range. Furthermore, its highly packed three-dimensional structure features a large internal surface in the order of several hundred of m^2/cm^3 (in the range $100 - 800$ m^2/cm^3) [50] making the sample extremely sensitive to its surrounding environment and easily subject to external contamination but as the same time making a very interesting host material. Extensive studies on passivation of the

material surface have been conducted employing a variety of thermal and photo-electrochemical process toward the improvement of PSi stability and modification of its physical properties.

Once the formation of the porous layer is achieved, PSi is commonly rinsed in solvent like pure ethanol or de-ionized ultra-pure water. The PSi layers are then dried under a controlled nitrogen flow or simply by natural evaporation of the cleaning solvents. In the case of highly porous material, such as porosity exceeding 80% as well as in free-standing porous layers, mechanical stresses due to surface tension at the solid/liquid interface during evaporation can lead to cracks or even destruction of the layer. In this particular case, special drying techniques can be used to reduce or eliminate cracking, such as simply replacing ethanol or water by a solvent with lower surface tension such as pentane [51]. More efficient techniques can be found in Super Critical Drying and Rinsing (SCRD)[52][53]. SCRD has been used in this study to allow safe drying of large area free-standing film of porous material without damage. In such drying method, the samples are kept in ethanol and are washed away by high pressure liquid carbon dioxide (standard gas for SCRD) which is kept in this study at a pressure of 14 MPa and 40°C, well beyond its gas-liquid critical point, allowing for perfectly non destructive drying of the samples. Freeze drying was also reported with less success than SCRD [53].

 A wide variety of oxidation techniques are applicable to PSi in order to passivate its surface and enhance its physical properties. Freshly formed PSi, referred to as as-formed or as-anodized silicon, has its surface terminated by silicon-hydrogen bonds and due to its porous nature and large internal surface, is susceptible to external contamination, oxygen incorporation and finally growth of a native layer of oxide. The uncontrolled growth of native oxide can lead to drastic changes in the properties of the material and deterioration of performance and stability.

Intentional oxidation of PSi can be realized by thermal annealing as well as chemical and electrochemical oxidation. In the case of rapid thermal oxidation (RTO), PSi is oxidized at high temperature, preferably over 800°C, under a constant oxygen flow in order to grow good quality oxide. Another recently investigated oxidation method is high-pressure water vapor annealing (HWA). During HWA treatment, PSi is placed with a measured amount of de-ionized water in a hermetic chamber and is then heated, vaporizing the water and inducing a high pressure in the closed chamber. Typical annealing temperature is in the range of 150-300°C during 2 to 6 hours leading to pressure in the range of 1-4 MPa. HWA has proven to be a high quality oxidation process, leading to high quality oxidation and achieving high photoluminescence and electroluminescence efficiencies [54]. Recently, PSi treated with a combination of RTO and HWA has also shown stable and efficient blue photoluminescence as well as phosphorescence [55]. Beside anhydrous oxidation processes, wet chemical or electrochemical oxidation (ECO) [56][57] are also available.

Oxidation treatment generally leads to heavy modifications of the structural and physical properties

of PSi. When it is preferable to keep the original properties while still stabilizing the material, several techniques have been employed to prevent to some extent the aging of PSi. The techniques consist of either capping of the PSi surface, for example with the deposition of a conductive layer on the top surface either by sputtering (metals, transparent conductive oxides) or thermal evaporation (metals), filling of the pores as well as modifying the chemistry of the PSi surface. Surface modification using organic molecules as a substitution for surface hydrogen has already been widely investigated [58] and was found to be useful to stabilize the luminescent properties of PSi [59]. Possible passivation routes for PSi are too numerous to be discussed here and further developments will be given in the corresponding sections when deemed necessary.

I.5.2 Physical properties of porous silicon

I.5.2.1 Structural properties

Porosity is the primary parameter to define the structural properties of porous silicon and simply represents the ratio of void in the volume of porous material. The simplest measurement method is based on a series of three gravimetric measurements from which porosity is extracted. The sample is measured before anodization (weight m1, total Si weight), right after anodization (weight m2) and finally after removal of the PSi layer (weight m3, remaining Si substrate). The removal of the upper porous layer can be achieved by simple chemical etching into a KOH base solution. The total porosity is then obtained by the following formula:

Eq. 1.4:
$$\mathbf{P(\%)} = \frac{\mathbf{(m1-m2)}}{\mathbf{(m1-m3)}}$$

In the case of free-standing layer of PSi, where comparative measurement of the substrate with and without PSi layer is not possible anymore, the porosity can still be obtained from weight measurement of the free-standing PSi layer only. Knowing the weight, surface and thickness of the layer, it becomes possible to compare them to the equivalent (calculated) weight of a bulk Si layer of the same volume and therefore obtained the equivalent porosity. The technique while still useful is less precise than the previous method due to a degree of incertitude on several parameters such the surface (difficulty of accurately measuring poorly defined surface) and thickness (usually assumed to be constant over the films area). An alternative but more complex method such as gas adsorption measurement is also available to estimate porosity of the material.

While porosity is an easily estimated and understandable parameter for a first characterization of PSi

material, it does not give any details about the microscopic and nanoscopic structure of the material. PSi is better defined by the size of the pores, their shapes and their three-dimensional spatial distribution but such characteristics are extremely difficult to measure or estimate. It is also important to note that PSi can be presented according to two complementary points of view: Focusing on the porous aspect of the material and therefore presenting the characteristics of the pores and the void created in the material, or focusing on the morphology of the remaining Si skeleton, especially for structures in the nanometer size range where quantum confinement can occur. A complete understanding of the formation mechanisms of the various PSi morphologies is complicated by the large number of parameters involved in such process but trends exist depending on the doping of the original substrate.

P type substrate:

PSi made from moderately p doped substrate shows extremely small pores with small inter-pore spacing (a few nanometers) which are interconnected resulting in a highly packed and homogenous structure. As the substrate doping increases, the pore size and spacing also increase and leads to larger voids running perpendicularly to the surface. Such pores also features ramification with several smaller pores running laterally, leading to a silicon skeleton featuring small Si crystallite (similar in size to lightly doped p) covering more massive columnar structure.

N type substrate:

The case of n type substrate is more complex. Since the formation process of PSi is strongly dependent on the injection of holes from the substrate, obtained by illumination during formation for n type material, the resulting material strongly depends on the presence of such photo-assistance during the anodization process. For lightly doped n type wafers anodized in the dark, the resulting porosity is very low and the remaining Si skeleton is massive (macroporous). When anodized under illumination, higher porosities are achievable, and the resulting material is similar to the moderately doped p type (nanoporous) if the layer thickness remains small, under around $1\mu m$. Morphology of the resulting layer depends strongly on current and illumination intensity. When the layer becomes thicker, the PSi structure starts to change to macroporous silicon, with pores in the micrometer range, probably due to a deficiency of holes at the dissolution interface (light penetration limited in depth by the upper PSi layer absorption). For highly doped n type material, a gradient of porosity is visible along the depth, due to the continuous formation of new pores at the surface of the substrate rendering the top of the layer more porous than the bottom.

Due to the large internal surface of the PSi material (≥ 200 m^2/cm^3), the contribution of the surface to physical phenomena cannot be neglected and its chemistry plays an important role in optical,

electronic and electrical characteristics. The most dominant impurity present in freshly fabricated PSi layers is hydrogen, present in the form of Si-H$_x$ groups with x=1, 2 and 3. Hydrogen covers all the internal surface of porous silicon and is present during the electrochemical anodization process as well. After drying of the layer, hydrogen impurities can still be detected in the material even after several months. A typical FTIR transmittance spectrum of a freshly prepared self-standing layer made from n+ substrate is shown in **Fig. 1.12**. The measurement was taken a few hours after fabrication, to ensure a complete drying of the layer. Corresponding peak position and their attribution are listed in appendix A, compiled from [60][61][62]. The ratio Si / H has been estimated at around 0.6 / 0.1 which is very high and further studies confirmed that hydrogen atoms completely cover the surface of PSi.
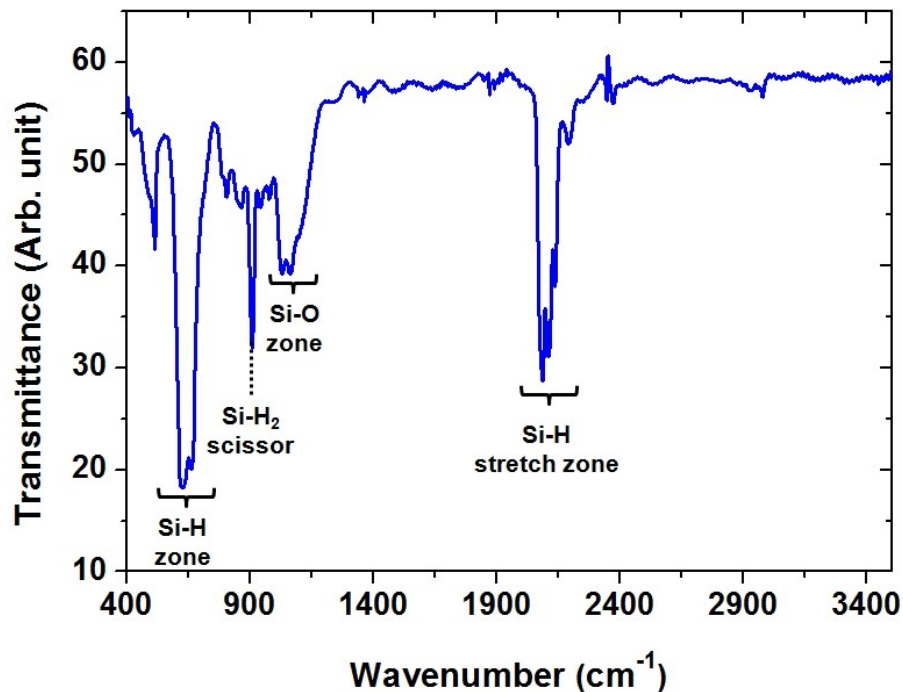
Fig. 1.12: *FTIR transmittance spectrum of an as-prepared n+ type free-standing layer of PSi. The typical hydrogen related vibrational groups are clearly visible together with an oxide related peak already present at the surface of the material even after short period of exposure to ambient air.*

A second impurity found in freshly formed PSi is fluorine, contaminant coming from the electrolyte itself. Similarly to hydrogen, fluorine has been detected in the form SiF$_x$ with x = 1, 2 and 3. The content of fluorine, not clearly estimated, seems to decrease strongly with time. The detection of HF and SiF$_6^{2-}$ species as well seems to indicate that the source of fluorine contaminant might be residual electrolyte trapped in the porous structure.

Beside the two previous "original" impurities originating from the formation process itself, the most important "external" contaminant is oxygen. Amount of oxygen can be traced in PSi material after

only a few minutes, and the amount increases drastically with time to reach very high levels. Si-O-X related groups are clearly visible in the FTIR spectra of our freshly fabricated sample (**Fig. 1.12**). The natural and inevitable oxidation of PSi mainly appears in the form of Si-O-Si and Ox-H-Si species which actually does not modify the original hydrogen passivation of the surface.

Finally the last common impurity can be found in the form of hydrocarbon, with a carbon contain of up to 10% in aged samples. It was found that the origin of carbon is hydrocarbon molecules from the atmosphere and that organic solvents used during rinsing of the samples (ethanol) are not responsible for the contamination.

It is also important to note that such modifications of the PSi surface chemistry can be induced during measurements whenever excitation source such as ions, photons or electrons are used. Precautions are therefore required during measurement in order to minimize the effect of degradation of the sample on the measured response. Data related to degradation and stability will be discussed in chapter IV and V.

I.5.2.2 Quantum confinement and related phenomena in porous silicon

I.5.2.2.1 Introduction to Si nanomaterials

Silicon based nanomaterials are a relatively new type of material which nanometer size features new physical properties compare to their bulk equivalent and have attracted a great deal of attention both for their new potential applications in devices as well as academic interest to understand the physics of these new nanometer scale materials. The term "nanomaterial" usually refers to material with a dimension of about 100 to 1 nm. These low dimensional materials are usually classified in function of their dimensionality, the direction in which the electronic carriers are free to move or not as seen in **Fig. 1.13**.
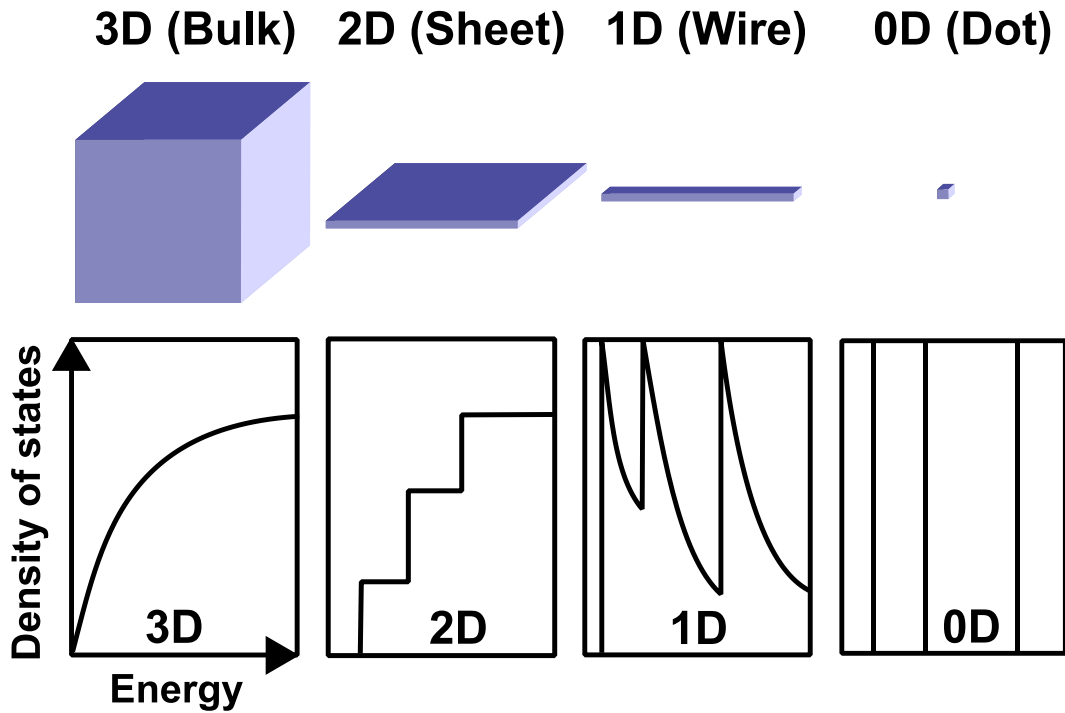
Fig. 1.13: *Schematic representation of spatial confinement from bulk 3D material down to 0-dimensional object ("dot") with their corresponding density of state plots.*

Bulk materials are considered 3D material as the electronic carriers are free to move in all three dimensions. If the material is then confined in 1 direction, we obtained a 2D thin film material called a quantum well also sometimes refers as nanosheet or nanoribbon. Further confinement in dimensionality leads to 1D (nano or quantum wire) and finally 0D structure, the quantum dot, where spatial confinement occurs in all three directions.

The spatial confinement of carriers in 3D has a direct effect on the allowed carrier energies. While carriers exist in bulk material in continuous energy band, carriers are restricted to discrete levels of energy when spatially confined in all three directions. In such confined system, the energy state, which can be described by the simplified relation in **Eq. 1.5** (quantum dot modelized as an infinite potential well), is inversely proportional to the square of the confinement dimension d. Simply said, the bang gap of the material can be shifted toward higher energy by reducing the confinement space of carriers as shown in the **Fig. 1.14**.

Eq. 1.5:
$$E_n = \frac{\hbar^2 \pi^2 N^2}{2md^2}$$

With $\hbar$ the reduced Planck constant, m the reduce mass, d the diameter of the dot.
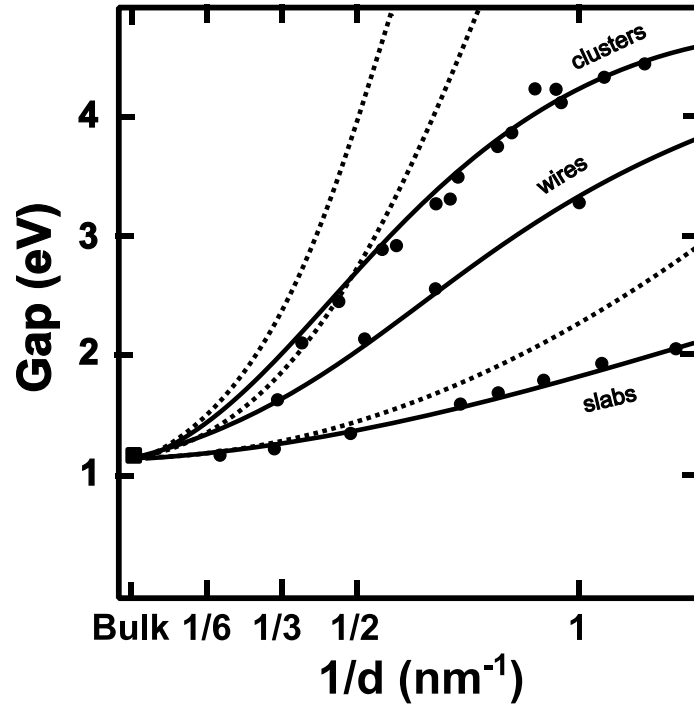
Fig. 1.14: *Theoretical calculation of the gap value in function of the confinement dimension for an hydrogen terminated Si slabs (sheet), wire and cluster (dot). Filled dots represent calculation using the density functional theory (DFT), dash lines using the effective mass model and the full line the finite barrier effective mass model. Redrawn from [63].*

The degree of confinement necessary to see the effects of such quantum confinement on the physical properties of the material is usually estimated from a parameter called the exciton Bohr radius. Exciton is a particular state of carrier excitation where the electron and hole formed by absorption of a photon remained bounded to each other by coulomb interaction. The remaining stable bound state, considered as a quasi-particle, has a structure similar to a single hydrogen atom with the single electron orbiting the hole. Similar to the definition of the Bohr radius, the orbiting distance between an electron and the proton in a hydrogen atom, there is an exciton Bohr radius representing the diameter or radius of the exciton. This parameter is an important criterion to assess the confinement dimension of a material. In Silicon, the exciton Bohr radius is estimated at around 4.9 nm. Considering a Si nanodot (0D), for a dot size superior to the the exciton bohr radius, there is either no confinement or weak confinement while for size smaller than the exciton bohr radius, there is strong confinement effect. Changes in physical properties start to be detectable when the strong confinement regime becomes dominant.

Observation of quantum dots and quantum confinement effect can be done with different analysis techniques among them the most popular are Transmission Electronic Microscopy (TEM, direct physical observation of the dots), absorption, Raman and photoluminescence spectroscopy.

33

Absorption and photoluminescence measurements related to PSi are discussed in two following sections.

The fabrication route to Si nanodots is usually divided in two main approaches, the bottom-up and top down approaches. Bottom up methods correspond to the formation of the material "atom by atom" [64], usually involving the direct formation of nano-clusters of Si by growth from a vapor phase such as in Chemical Vapor Deposition (CVD, dry process) or by synthesis in a liquid solution (wet process). On the other hand, top-down approaches are based on etching technique; where high quality crystalline silicon is indirectly nanostructured to form low dimensional Si structures. The most common methods are simple, purely chemical etching (such as stain etching) or the more popular electrochemical etching which is the method employed to form PSi in this study. Electrochemical etching gives a better control over the resulting material structure and show far more efficient visible photoluminescence than chemically etched Si nanomaterial.

Different others PSi formation method are available, involving the use of light stimulation in addition to the wet etching as well as mechanical dry erosion of Si substrate by electrical spark-erosion technique, plasma etching, reactive ion etching (RIE) etc… A good overview of all available techniques for the formation of PSi as well as other related Si nanomaterials is given in a review by Okamoto et al [65].

It is important to note that such a wide variety of fabrication processes inevitably leads to an even wider variety of resulting Si nanomaterials. For practical application, the selection of the process mostly depends on the ability to produce Si nanomaterials at a high yield while keeping cost low, especially true for photovoltaic applications. The possibility of accurately controlling the material characteristics besides the size itself, such as QD orientation and shape, inter-dots distance and surface states also play a key role. Bottom up approaches such as the various vapor phase deposition techniques tends to focus on the fabrication of highly ordered matrix of dots with highly controlled size density and dot separation, while top-down approach such as electrochemical etching or nanodots in colloidal form, including PSi, lead to more disordered material.

I.5.2.2.2 Bandgap of Porous Silicon

Due to the intrinsic nature of PSi, a network of interconnected more or less circular dots of varying sizes, a direct measurement of its bandgap is actually a very complex task. The material is actually the sum of different dots with different bangaps and experimental measurements give only an average but still meaningful value of the gap, sometimes referred as effective bangap. The two main methods employed in estimating the effective bandgap of PSi are photoluminescence measure (PL) and optical absorption. The two characteristics are explained in details in the two following sections.

-Photoluminescence

Photoluminescence measurement has been the tool of choice for characterizing PSi for years thanks to its efficient and visible luminescence. Bulk Si itself is an extremely poor light emitter at room temperature due to the indirect nature of its band gap. In such material radiative recombinations require the help of momentum conserving phonon and their probability is therefore extremely low. The long radiative lifetime of electron-hole pairs in the material (in the order of ms) means that the pairs, moving freely in the semiconducting material, have a high probability of encountering defects and luminescence killing centers, strongly increasing the nonradiative recombination rate. The discovery of visible light emission at room temperature from PSi in the early 90s has therefore generated a strong scientific and technologic interest in the material: Scientific due to the possible involvement of quantum confinement effect in the material and all its implication at a time where "nanoscience" was emerging; and technological due to the possibility of fabricating visible and efficient light source from the most commonly used material in the semiconductor industry.

PL from PSi has been reported in a wide range of energies, starting from near infrared (NIR), covering all the visible spectra up to near ultraviolet (UV). Such a wide range of emission has different luminescent band origins which are summarized in **Table 1.4** [66]. PL of PSi usually always refers to the visible red band (slow band) which is the most commonly investigated emission, partly due to the possibility of electric excitation of the band for potential application in electroluminescent devices. The second band located in the blue region (Fast band) is observed only in (strongly) oxidized PSi and its origin is attributed to defect in Silicon dioxide. Finally, the infrared band is mostly detectable only at low temperature and could be related to an amorphous Si phase in the material or resulting from the multiple dangling bonds at the PSi surface.

Spectral range	Peak wavelength	Band denomination	PL	CL	EL
UV	~ 350 nm	UV band	Yes	Yes	No
Blue-Green	~ 470 nm	F band	Yes	Yes	No
Blue-Red	400 – 800 nm	S band	Yes	Yes	Yes
Near IR	1100 – 1500 nm	IR band	Yes	No	No

Table 1.4: *Summary of the main luminescent emissions from PSi. F band and S band stands for fast and slow band, CL and EL for cathodo- and electro-luminescence respectively. The blue-red band is the most investigated emission range due the demonstration of possible electric excitation and consequently its potential application in electroluminescent devices.*

Mechanisms responsible for the PSi PL emission were classified in 6 groups by Bisi et al [61]. The most important and commonly accepted model is the quantum confinement model in the material,

where emission is intrinsically related to the Si nanostructures present in PSi films, while all others models proposed an extrinsic origin of the luminescence, mostly related to the surface of the material.

Model 1 & 2: Hydrogenated amorphous silicon phase and surface hydrides

Since the huge internal surface of PSi is almost completely covered by Hydrogen as well as containing a thin layer of amorphous Si like layer surrounding the PSi skeleton, Si-H_x species have been proposed as candidates for the luminescence of PSi films [67][68][69][70]. This model was proposed on the basis that PL exhibited by PSi has several common characteristics with emission form H-a-Si as well as Si-H_1, Si-H_2 and Si-H_3 species, including similar emission energy range and similar PL decay dynamics. Furthermore, PL intensity decreases with desorption of Hydrogen species from the surface and can be recovered after immersion in HF (re-hydrogenization of the surface). Against the model is the conservation of efficient PL after strong oxidation of the PSi layer (strong decrease in Hydrogen coverage). The decrease of PL intensity after desorption of hydrogen species is probably due to the formation of dangling bonds (non-radiative recombination centers) and not due to the absence of Si-H_x species. Measurements also show that the content of H-a-Si in PSi is relatively low and that its luminescence intensity temperature dependence is in opposition to that of PSi.

Model 3: Siloxene molecules

Now an abandonned explanation for the PSi luminescence, Siloxene type molecules (Si-O-H) were proposed as candidates for the origin of PSi luminescence due to, similarly to the previously discussed H-a-Si and surface hydride origins, similar emission characteristics (energy and decay)[71]. Against the model is the luminescence of freshly fabricated PSi containing no detectable Si-O-H groups or the luminescence of heavily oxidized PSi.

Model 4: Defects

Defects, both from Silicon itself and from its dioxide, have been proposed as possible luminescent centers as well. Since luminescent PSi can be fabricated in various way with different surface passivation (oxygen and hydrogen), there is a low probability that a single type of defect is at the origin of the luminescent emission. Moreover, emission from defect should be mostly independent on the porosity / structure size which is in contradiction with the tunability of the PL emission from PSi.

Model 5: Surface states

Once more, the huge internal surface of Si makes surface states a theoretically viable candidate for

PSi PL [72]. The model proposes that absorption takes place inside the Si nanostructure but the carriers radiative recombinations occur via surface states. Such a model easily explains the multiple PL bands observed from PSi. On the other hand, further investigations showed that PL in PSi originates from excitons coupling with momentum conserving phonon, indicating that PL arises from extended states and not localized ones, excluding surface states as potential origin of PL emissions.

Model 6: Confinement in crystalline Silicon nanodot & surface states contribution

The most desired explanation for PL emission from PSi and also the earliest proposed model [5]. While most other proposed explanations and models all have, to a certain extent, contradictory characteristics when compare to experimental results, only the quantum confinement model is consistent with experiments as a whole. Quantum confinement in Si nanodots is expected to lead to a widening of the bandgap, relaxation of momentum conserving rule and a size dependence of the PL energy. The last phenomenon can be clearly observed in samples that showed PL energy shift after successive chemical etching, linking the reduction in size of the nanocrystallites to the emission energy. A similar result is observed by absorption spectra where reduction in the crystallites size shoes a strong blue shift of absorption edge towards higher energies (discussed in the next section). A demonstration of the PL energy shift is shown in **Fig. 1.15** [5]. The large amount of studies of the visible band shows that while QC gives a good explanation for most observed phenomena, it cannot explain all experimental results accurately and it is almost certain that the large surface of the material plays a role and that the surface passivation can induce shift in PL energy as well. A better model has been proposed including the QC effect coupled with the presence of surface states, leading to the multiple emission processes as observed in **Fig. 1.16**.

Fig. 1.16: *Schematics of all the possible radiative recombination path from band to band (E₀), surface state to band (E₁ and E₂) or from state to state (E₃)*

Fig. 1.15: *Typical demonstration of the PL peak shift toward higher energy in function of the post-etching duration and hence decrease of PSi structure size, due to quantum confinement in smaller Si dots. Redrawn from [5].*

In addition to the previously discussed models, a number of other explanations were proposed which are now mostly obsolete. While the quantum confinement has been accepted by the majority of the scientific community, recent papers as late as 2008 [73] are still debating the relevance of such a model by proposing alternative explanations for the PL emission.

-Optical absorption

Optical absorption of porous silicon is another useful technique to obtain information on the bandgap nature and effect of QC in porous silicon. Usual characterization methods include measurement of optical transmission, photoluminescence excitation (PLE) as well as photothermal deflection spectroscopy (PDS). Optical transmission is the most widely used due to the relatively simplicity of the process. Still, the process requires the fabrication of thin, free standing layer of porous silicon with relatively homogeneous layer and high quality, flat surface in order to avoid any scattering. Optical absorption of PSi is also difficult to interpret directly due to the nature of the material. The total absorption of a layer actually represents the sum of multiple absorption processes taking places in crystallites of different sizes.
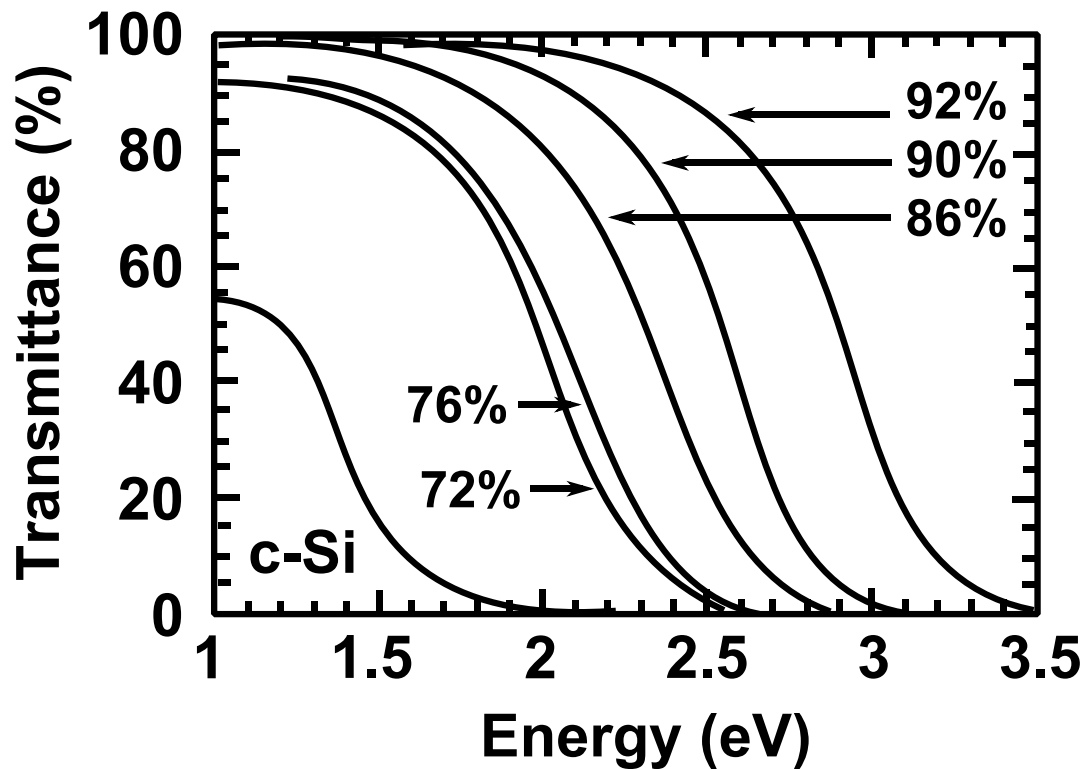
Fig. 1.17: *Optical transmission spectra of PSi free-standing layers of the same thickness but different porosities. The shift shows a strong supra-linear dependency on the porosity of the material. Redrawn from [74]*

A typical transmission spectrum taken on samples with similar thicknesses but different porosities is shown in **Fig. 1.17** [74]. From the measurement it is clear that PSi absorption edge is shifted toward high energy compare to bulk Si and that the shifting has a strong supralinear increase with the porosity. Shifting of the transmission is far larger between the samples of 90% and 92% compare to samples at porosity of 72% and 76% while the porosity variation is actually smaller. Such a strong supralinear behavior has been attributed to quantum confinement in nano-sized crystallites of PSi material. Further investigation also shows a strong dependence of absorption on the size distribution in the material. As seen in **Fig. 1.18** [75], when comparing two PSi layers made from p and p+ material in a similar porosity range, there is a clear gap in the absorption edge between the two, the main differences between the material being the size of the Si crystallites, p type material featuring far smaller size (~3 nm) than PSi made from heavily doped material (~10 nm).
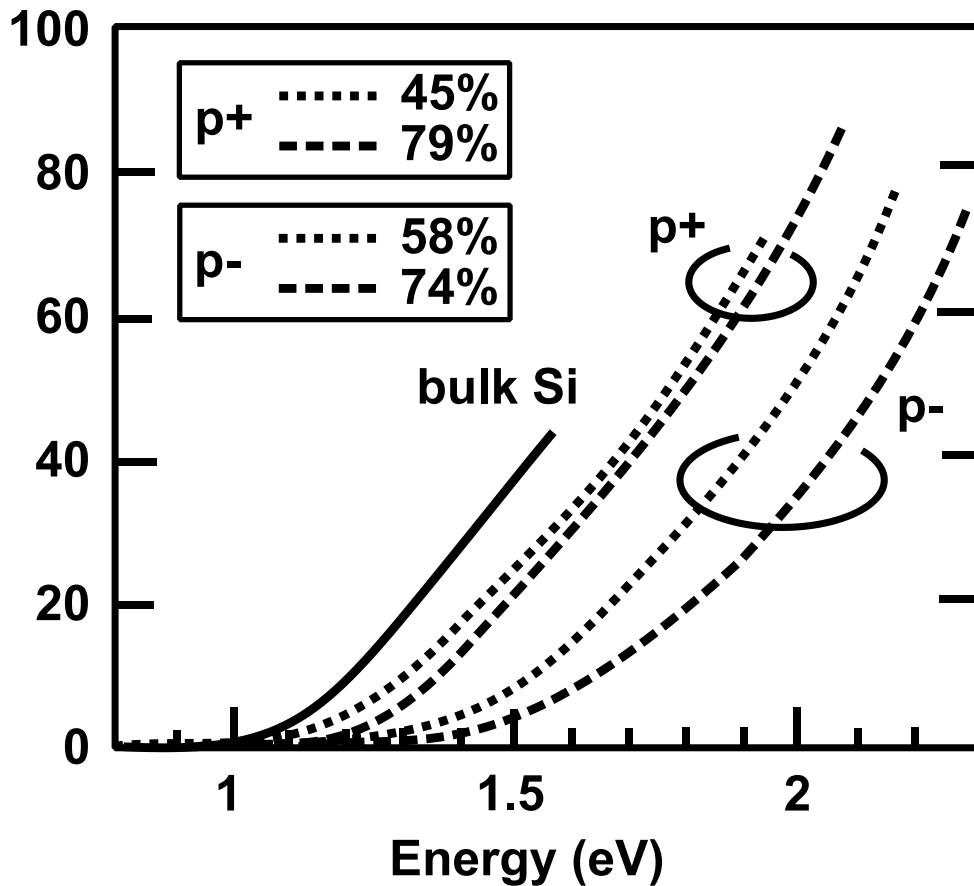
Fig. 1.18: *Absorption coefficient for free-standing layers made from moderately doped p- and heavily dopped p+ material. Despite a similar range of porosity, p- materials shows a stronger shift of the absorption edge due to its higher density of smaller Si dots compare to p+.*
Redrawn from [75]

Other important information obtained by measurement of the absorption coefficient of PSi is about the nature of the bandgap itself. As shown in **Fig. 1.18**, the tauc plot representation of the absorption spectra clearly shows that the PSi absorption increases smoothly with energy in parallel to the spectra of c-Si, indicating the indirect nature of its bandgap. No transition from an indirect to a direct bangap is observed optically, even in samples with ultra high porosity superior to 90%.

The high photoluminescence emission efficiency of PSi, similar to direct gap material, but the clear indirect gap nature of its optical absorption has lead to term the material has a quasi-direct semiconductor. While indeed the nature of its band gap is still indirect, the relaxation of the k conservation rule due to confinement actually allows for an overlap of electron and holes wavefunction tails as seen in **Fig. 1.19**, even in the case of strong separation as in indirect gap material. The overlap creates a new recombination path strongly increasing the probability of non-phonon assisted radiative recombinations of electron-hole pairs.

40
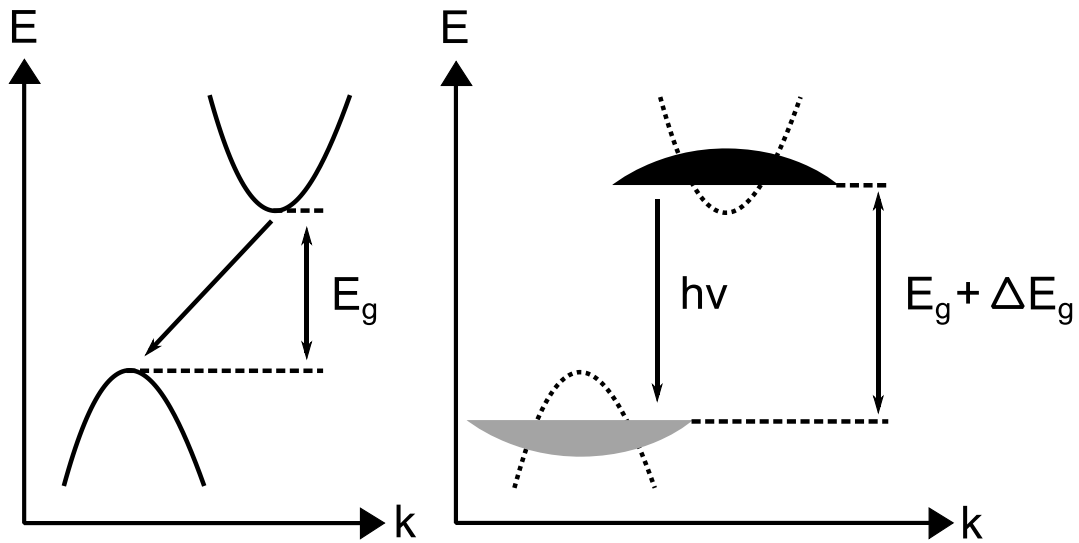
Fig. 1.19: *Typical band diagram for an indirect bulk semiconductor at the left, and a confined indirect semiconductor with relaxation of the momentum conservation rule allowing direct radiative transition at the right.*

I.5.2.3 Conduction phenomena in porous silicon

While the optical characteristics of PSi have been widely investigated, the electric characterization of the material is a far more difficult task and no clear consensus and definitively accepted explanations are available to explain the large amount of data and phenomena observed in the material. While quantum confinement effect in optical characteristics is now clearly identified, its effect on electrical characteristics and transport phenomena is still not clearly understood.

I.5.2.3.1 Conduction and carrier transport

I.5.2.3.1.1 Introduction

A first observation at the electrical characteristics of PSi shows that the material has a very high resistivity and is almost depleted of free carrier. The depletion could occur due to:

* The reduction of the thermally generated carriers by widening of the bandgap, and/or

* Trapping of free carrier by surface states

In highly porous and luminescent sample, the quantum confinement could be involved in the

41

conduction process but the strong increase in the resistivity is also visible in lowly porous material where the size of the remaining silicon structure is far too large to involve any contribution from the quantum confinement. Since the strong increase of resistivity is also visible in PSi made from highly doped substrate, a few investigations on the presence of the original substrate dopants have been conducted and reviewed [76]. They show that the dopants are present in the material in equal or even superior quantity than the original material doping level, but are in a neutral state. Simple estimations of the density of surface states in the material lead to density value up to 10^{19}cm^{-3}, which can lead to full compensation of the free carrier (full carrier freezing) even in highly doped material. Surface states trapping could explain the relatively high resistivity seen in low porosity samples while high porosity material could involve both trapping and quantum confinement effect.

Conductivity of PSi is also strongly dependent on the ambient condition. Measurement of conductivity in ambient air or under vacuum give strongly different results related to the adsorption by the large internal surface of different chemical species, especially water from the ambient humidity of air [77]. Residues of electrolytes and solvent from the fabrication process could also have an impact depending on the techniques and conditions employed to dry the PSi layers.

I.5.2.3.1.2 Effect of contact and structure

The fabrication of reliable and efficient contacts with PSi has been an early problem due to the peculiar surface nature of the material and the possibility that the deposited material might penetrate inside the material, creating conduction shortcuts. The most common materials used are metals including gold and aluminum as well as transparent oxide such as ITO for electroluminescent and photoconduction measurements. In most case (including this work), the au/PSi contact shows Schottky rectifying properties while Al/PSi or ITO/PSi tends to show an ohmic behavior. Further details about the impact of contact on the device characterization are presented in chapter IV.

The device structure used for electrical characterization of PSi usually involves a layer of PSi on top of the original Si substrate, leading to a contact/PSi/c-Si/contact structure as seen in **Fig. 1.20(a)**. Such a hetero-structure includes the effect of both the contact/PSi and the PSi/c-Si interface when measured in sandwich mode. In such structure where the PSi layer is relatively thin, the presence of a depletion area at the PSi/c-Si interface has been identified and most of the contribution to conduction and photoconduction come from the c-Si substrate and not from the PSi layer. The effect of metallic contact at the surface is minimal (but not non-existent) compare to the contribution of the rest of the structure.

A second method to investigate the electrical characteristics of PSi material only, at least without the

contribution of the underlying c-Si substrate, consists of separating the upper layer of PSi from the substrate resulting in a free-standing layer which structure is shown in **Fig. 1.20(b)**. The problem of double contacting the material at the top and bottom of the layer still remains.
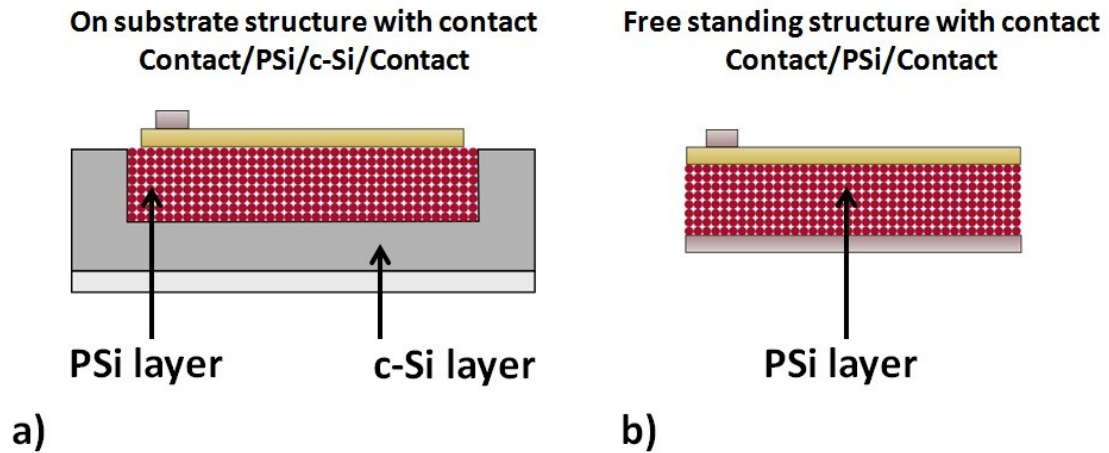
Fig. 1.20: *(a) Schematic of a typical "on substrate" Psi device, (b) structure of a free-standing PSi layer after separation from its host substrate.*

I.5.2.3.1.3 Proposed conduction and transport models

A myriad of conduction models has been proposed so far to explain the observed characteristics of the material and are rapidly summarize in the following two sections for low and high porosity material.

Low porosity material (P ≤ 50%)

As previously presented in the introduction of this section, low porosity material features a porous structure which size is too large to involve any quantum confinement. The bandgap of such material is similar or only marginally higher than bulk silicon and no PL in the visible range is detectable. However the material still shows a high resistivity compare to the original Silicon substrate from which it is made. Balagurov et al [78] investigated the conductivity of 30% porous layers made from highly doped p type substrate and found that the resistivity is strongly related to the presence of Hydrogen onto and into the material. Hydrogen can be detected in PSi at a density of 10^{19} cm^{-3} up to a depth of around 100 nm. The diffusion of hydrogen inside the material effectively passivate the boron impurity (by forming Si-H-B species) and strongly decrease the doping density of the material. Annealing of the same layers at different temperature shows strong changes in conductivity at the particular temperature of 150°C which might be associated with desorption of the same Si-H-B

species form the material. Dipping of the annealed layers in HF solution restores the original as prepared sample resistivity, confirming the proposed explanation for the high resistivity. Conduction in the material seems to be well explained by a space charge limited current (SCLC) model. Such explanation is relevant only to p type material and would not explain the similar high resistivity of n type material. In addition to impurity neutralization by hydrogen diffusion in the material, the large number of charged surface states was proposed to explain the large increase in resistivity even in low porosity material. In such model, the charged surface states constrict the conduction path by coulombic repulsion [79].

High porosity material (P ≥ 50%)

High porosity materials are more complex than their low porosity counterparts due to the presence of nanostructures which size are well in the quantum confinement region. A first explanation for the strong increase in resistivity would be the decreased thermal generation of free carriers due to the larger band-gap. This type of material also has the highest number of proposed model to explain its electronic transport including Poole-Frenkel, SCLC, tunneling, diffusion, various type of hopping models etc…

The resistivity of highly porous PSi is reported to be in the range $10^{10} - 10^{12}$ $\Omega.cm$. The material conductivity shows a strong dependence on temperature with an Arrhenius type behavior which activation energy E_a is in the range 0.3 -0.7 eV on average and prefactor σ_0 in the range 10^{-3}-$10^{-6}(\Omega.cm)^{-1}$ (see **Eq. 1.6**) [80][81]. A few studies instead better described the conduction temperature dependence by a Berthelot model instead of Arrhenius [82]. Among the transport model proposed, early investigation proposed a Poole-Frenkel [83] or a SCLC model for the conduction. In the early report by Ben-Chorin, the conduction can be explained using the Poole-Frenkel model with one activation energy for high injection regime and a second conduction path in low injection regime with a different activation energy. The observed conduction could also be described assuming a schottky type barrier at low voltage and a SCLC at higher voltage. It is interesting to note that even in such early reports it is already evident that several conduction paths could exist in one type of PSi material.

The large amount and disparity of models and parameters proposed to explain electronic transport in PSi is far too large to summarize as there was no apparent relation between all the reports, the difference in results being imputed to the difference of fabrication and sample treatment from one study to another. Until the team of Balberg [84] analyzed the large amount of data available together and found that all the results could be classified in two groups each following a different Meyer-Neldel Rule (MNR). The method employed here consists of first describing the temperature dependence of different PSi layers conductivity by using the simple Arrhenius model as shown in **Eq.**

1.6. The obtained conductivity pre-factor σ_0 and the corresponding activation energy E_a are then plot together as the logarithm of σ_0 versus the activation energy. The MNR implies that the plot is linear with the form shown in Eq. 1.7:

$$\text{Eq. 1.6}: \sigma = \sigma_0 \exp(-\frac{E_a}{kT}),$$

$$\text{Eq. 1.7}: \ln(\sigma_0) = B_{MNR} + \frac{E_a}{E_{MNR}},$$

With B_{MNR} and E_{MNR} two constants related to a specific transport mechanism. The plot of a large amount of different PSi layers is shown in **Fig. 1.21** where two MNR with different B_{MNR} and E_{MNR} are clearly visible. The two rules are related to two different conduction paths: One attributed to probable extended state conduction in a-Si like tissue covering the surface of nanocrystallites (MNR1), the second one related to inter-crystallites hopping between the nanocrystallites forming the PSi skeleton (MNR2). The model is sometimes referred as the pea-pod model, where the nanocrystallites correspond to peas covered by an a-Si like tissue resembling a pod. The two conduction path can co-exist at the same time in a single PSi material, the temperature determining which one is pre-dominant: conduction of the surface tissue appears dominant at high temperature ($\geq$ RT) while hopping dominates the lower temperature regime. Such model does not involve quantum confinement effect in the observed conduction. A review by Kocka et al [85] presents a similar conduction model made of three different possible conduction paths as seen in **Fig. 1.22**.
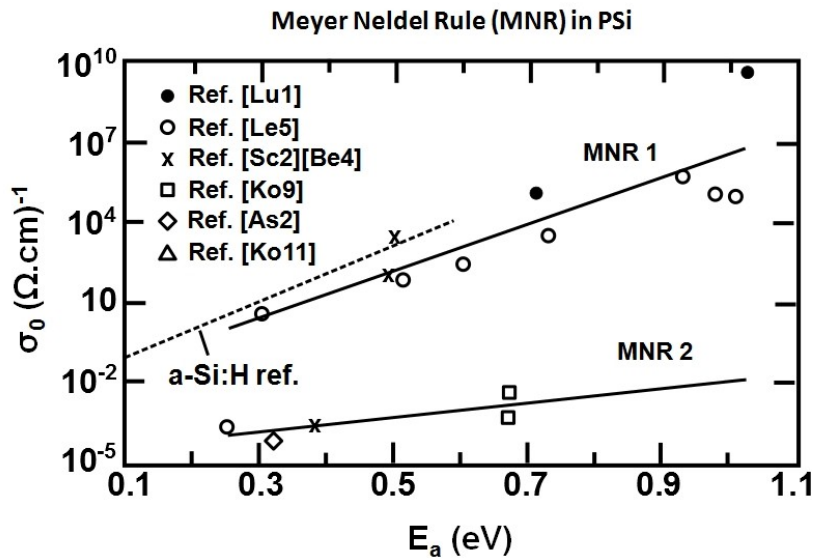
Fig. 1.21: *Demonstration of the existence of 2 different MNR from PSi conduction measurements compiled from different sources. The MNR1 is associated to surface contribution due to its strong similarity to MNR found in a-Si:H. MNR 2 has been associated to c-Si inter-crystallite conduction.*

45
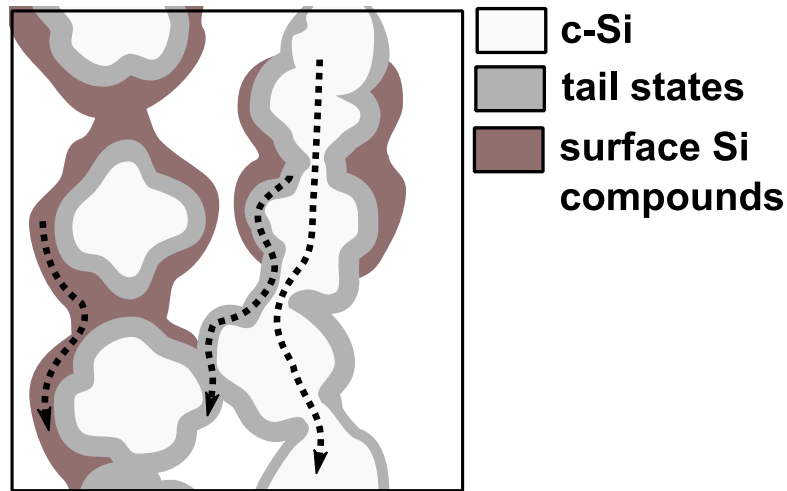
Fig. 1.22: *Schematic representation of the possible conduction paths at the nanometric scale. The conductions models proposed involved inter-crystallite conduction in c-Si, tail states conduction due to distorted Si bonds at the crystallite surface, and finally conduction through a tissue surrounding the material.*

To summarize, there is still no definitive model to explain all the conduction phenomena observed in the large variety of PSi materials investigated. However, in both low and high porosity material the surface appears to have a strong contribution through the presence of surface states and conduction channels.

I.5.2.3.1.4 Modelization as a diode

Various devices involving a PSi layer have been reported to show a rectifying behavior in different type of configurations including metal/PSi/c-Si as well as in free-standing PSi layers. Such rectifying diode structures have been modelized according to the two most common diode models: the pn diode and the schottky barrier. The two model can be described by exactly the same Shockley **Eq. 1.8**, with J_0 the saturation current, n the ideality factor, R_s the series resistance, T the temperature and k the Boltzmann constant. The difference lies in the expression of the saturation current J_0 which is assumed to represent the diffusion of minority carrier in pn junction while for Schottky-Richardson diode J_0 represent the thermionic emission of carrier across the barrier and is given as: (**Eq. 1.9**) with A^* the Richardson constant depending on the material and Φ_b the height of the barrier.

$$\textbf{Eq. 1.8:} \quad J = J_0[e^{[qV/nkT]} - 1],$$
$$\textbf{Eq. 1.9:} \quad J_0 = A^*T^2 e^{[-\phi_b/kT]},$$

Reports involving rectifying PSi devices show a very wide range of rectification ratio (RR) for the fabricated diode in the range RR=1 to RR=10^4 at a voltage of 1V [86]. Fitting of the diode characteristics with the previously presented models shows very high values for both R_s and n (2 < n < 125) confirming the inadequacy of such equation to correctly described the diode behavior of PSi devices. PSi made from pn substrate also shows rectifying behavior which could be originating from the pn junction inside the PSi layers. Experimental data of PSi made from pn junction are shown and discussed in chapter IV.

I.5.2.3.2 Photoconduction in porous silicon

Photoconduction is one of the less investigated and understood characteristics of the material. Early reports [87][88] shows the possibility of fabricating photodetector made of PSi with a strong response in the visible range. The work of Ozaki et al [89] showed a strong coincidence between the PC peak and the PLE peak in efficiently luminescent nc-PSi material, showing that the PL and PC excitation centers are probably the same. Most photosensitive devices were fabricated with the structure metal/PSi/c-Si and contribution from both the contact and the presence of an heterojunction between PSi and the underlying c-Si substrate were used to explain the photoresponse of such devices. Investigations conducted on free-standing layers gave a better insight in the intrinsic photoconduction phenomena of the material. It was found that the PC strongly depends on the structure of the material and its post-treatment. The product of mobility lifetime ($\mu_f\tau_f$) and the applied electric field was found to be in the order of 1 μm, far larger than the expected size of the silicon nano-structures (2-5 nm) [90] and was attributed to a possible surface conduction channel. In parallel to PC, a PV peak at around 440 nm was detected by Sedlacik et al [91] and attributed to surface contribution while the PC was linked to the bulk properties of nc-PSi material. Similarly to dark conductivity, the photoconduction of nc-PSi appears to be a combination of both "bulk" and surface properties intertwined. In all cases, the photocarriers collection efficiency is very low (< 1% even at high voltage ~100V) and PC is strongly affected by trapping in the material. Investigation on the effect of porosity increase on PL and PC shows that while PL peak shift is clearly detected, the PC response seems to be almost independent on the porosity [92]. A maximum was found at 400 nm and the PC was found to be "frozen" up by the large amount of trapping centers strongly decreasing the carrier lifetime and mean free path.

I.5.3 Application to solar cells

Silicon wafer based solar cells, the so-called "first generation" technology, has been the leading material of the photovoltaic industry for the last decades. After years of continuous structure and fabrication process improvements, the dramatically reduced production cost is now mostly dominated by the cost of the material itself, the silicon wafer. In order to further reduce the cost of such cells, a "second generation" of thin film solar cells has been developed, greatly reducing the amount of material used in the process and therefore the total production cost of the cells. In recent years, a third approach has been emerging [93] ("third generation") focusing on the dramatic need of reducing the cost of solar cells not only by reducing the fabrication process cost but by dramatically improving the cells power conversion efficiency by introducing completely new concepts of cells. These new concepts, some of them including the use of nano-materials, are presented in the following section.

I.5.3.1 Third generation solar cells concept

One of the earliest and most widely investigated concepts is the tandem cell. As seen in **Fig. 1.23**, in this configuration the cell is not constituted of only one single bang gap material but by a stack of multiple absorbers with different bandgaps. With the largest bangap material located at the top and the lowest at the bottom, light is sequentially absorbed from the highest energy in the top cell to the lowest energy in the bottom, each cell absorbing a narrow energy band close to its bandgap for better efficiency. For an infinite stack of absorber the theoretical limit of efficiency is 86.8% [94], but in practice the number of layers are generally limited to three, the top, middle and bottom cells. One limitation of such structure is that the cells are connected in series and the current is collected between the top and bottom layer (from a technical and practical point of view, electrically separated cells are not desirable). In this case, the total current of the tandem is limited by the lowest current produced in one of the layer while the total photovoltage is the sum of the individual photovoltage of each layer. To maximize the efficiency, each layer needs to be current matched to each other by carefully selecting the bandgap of the material .In practice however, matching is rather difficult to achieve. Several studies are currently focusing on the development and gap engineering of different new materials to use as new absorber in tandem structure.
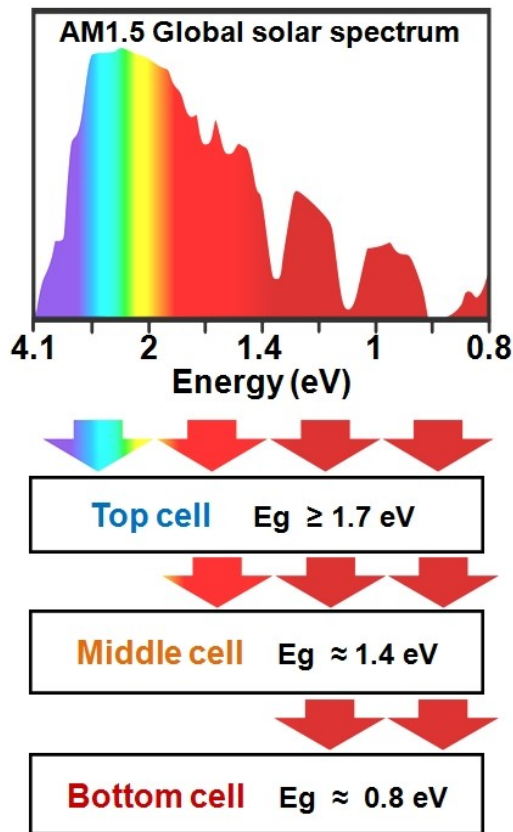
Fig. 1.23: *Example of the concept of multi-junction solar cells using a three stages structure with band gap distributed equally along the stacked layers. Absorption of each solar radiation energy range by a different absorber with a controlled gap allows for a higher theoretical efficiency than a single gap absorber structure.*

The second approach to higher efficiency cells focused on using the excess energy of photogenerated hot carriers before they lose their energy to the lattice by phonon emission. Total conversion efficiency can be improved either by increasing the photovoltage or the photocurrent. Increasing the photovoltage involves efficiently collecting the hot carrier before they have time to cool down, which means that the total process dynamic of collection in the cells should be fast compare to the carrier cooling dynamic. On the other hand, an increase in current can be achieved by using the hot carrier excess energy to generate additional electron-hole pair, the so-called "multiple exciton generation" (MEG) through impact ionization in the material. To be efficient the process requires that the impact ionization rate is larger than the carrier cooling rate as well as other relaxation processes. Such conditions are difficult to engineer but there is hope that the use of semiconductor nanostructures can help create such devices. Confinement in nanostructure strongly affects the carrier cooling dynamics, reducing the cooling rate and making impact ionization or carrier collection competitive with relaxation process. A good presentation and review of quantum dot based solar cells is given in a review by Nozik [95]. Numerous investigations on the fabrication and characterization of new nanomaterials are still going on, involving a wide range of different semiconducting materials. Among them, Silicon, with its strong, mature and cost effective industrial and application history has an important role to play in the form of silicon nanodots. Among the variety of fabrication process, porous silicon with its confirmed confinement effect and bang gap

widening is a potential candidate as a wide gap absorber for top cell in tandem structure. Despite the relative youth of the material, PSi has already seen a few applications in the photovoltaics field which are described in the following section.

I.5.3.2 Porous silicon in solar cell

PSi has been under investigation for applications in solar cells as early as 1982 [96], even earlier than the discovery of its visible luminescence in 1990. The possible applications and merits of PSi in Silicon based solar cells are [97]:

- Anti-reflection coating (ARC), low refractive index, good light diffuser
- Bandgap widening, PSi use as a wide gap material for use as a top window layer in multi-junction solar cells, surface passivation effect
- Down conversion of high-energy radiation to lower energy through re-emission (PL)
- Simple and cost effective overall process

To date, most of the published papers are related to the use of PSi as an anti reflection coating and few are dealing with the possibility of the material to act as a widegap absorber. In addition, a few other uses of PSi are also presented in the next sections

I.5.3.2.1 Porous silicon as a solar cell / process element

The main application of PSi in silicon based solar cells remains as an ARC to reduce the overall reflectivity of the devices due to the lower refractive index of the material compare to bulk Silicon as well as its good light diffusion properties.   In addition to top surface structuring, PSi has also been employed to form a back reflector (multilayer Bragg type reflector) onto low cost Si substrate where the thin film active layer is deposited onto the PSi layer [98].

Beside purely optical applications, PSi was widely used in layer transfer process (LTP) as an intermediate material in the fabrication of different Silicon based solar cells structure [99]. There are a large number of different processes being developed by different teams but they all share the same basic concept: the PSi acts as a surface conditioning step where the layer is formed on top of a low cost Si substrate, the active device being grown on top of the PSi layer which acts as a seed during growth. After bonding to a second foreign substrate, the deposited thin film device is separated at the PSi interface (hence the sacrificial layer name). The different processes slightly differs in their used of the PSi material whether the top active device is

deposited as is onto PSi or after a sintering step where PSi surface re-crystallize closing the gap at the surface of the film. Another variant developed at IMEC called "Epi-free" rely on the controlled sintering of the PSi layer to close the layer at the top surface while creating a void in between the Si substrate and the newly re-crystallized overlayer. The "floating" overlayer can then be separated for the rest of the substrate resulting in a usable thin layer for the formation of a cell, freeing the process of any epitaxial growth step [98].

PSi layer has also been used a doping template where impurity where diffused through a thin layer of PSi containing highly ordered vertical pores, reflecting the shape of the pore during the diffusion process at the interface between PSi and c-Si substrate [97].

I.5.3.2.2 Porous silicon as an active element

All the previously presented process involved PSi either as an intermediate material during the fabrication where it is removed from the final device, or as a purely optical component as in ARC applications. While PSi widegap nature has been widely investigated and discussed in relation to its visible strong photoluminescence, only a very small amount of information is available regarding the possibility of using the material as an active absorber in solar cell. This is probably due to the still ambiguous electrical nature of the material and the difficulty to investigate properly its electrical properties due to high resistivity of the material, large disparity of reported properties due to the wide range of fabricated PSi material and the difficulty to separate the response of PSi form crystalline Silicon in the case of on-substrate device structure (most widely studied structure due to its simple process fabrication).

Among the proposed applications for PSi as an active element is the possibility to convert high energy (UV and blue range) radiation to lower energy by absorption and re-emission through the material own photoluminescence. This down conversion of energy would enhance the response in the UV/Blue area but also requires that the photoluminescence process itself be rather efficient which is a strong limiting factor.

Surface passivation effect were also reported in detail by L. Stalmans [100] and while PSi shows promising passivation properties, the rapid degradation of its own electrical characteristics requires further improvement of its stability under ageing.

The most interesting application of PSi is simply as a wide gap absorber. While the concept seems perfectly realistic in view of the previously reported characteristics of the materials, there

is so far no satisfying experimental confirmation of the material acting as a wide gap absorber from the photoelectrical point of view. Furthermore, quantum confinement effects on conductivity are still not clearly understood. A vast amount of work is still required in this domain to get a better insight on the photoconduction phenomena in the material.

PV effect in PSi device was first reported in 1992 by G. Smestad et al [101]. In their study, the devices consisted of a PSi layer on top of a p type crystalline Si substrate. The PSi surface was contacted by a Pt probe in direct contact with the sample surface (no contact deposition). Under AM1.5 – 1 sun solar irradiance, a Voc in the range 0.3 – 0.4 V with a current in the order of 2 μA were recorded. The PV effect was attributed to the presence of a heterojunction between PSi and c-Si and the device was characterized by a large series resistance (~1 MΩ) and a large surface recombination in the PSi layer. After this initial report, only a small number of reports were published involving PV effect in PSi, most of them using the metal/PSi/c-Si/metal structure. In a 1997, L. Kore and G. Bosman [102] presented the PV results of a cell anodized in two steps, resulting in a double PSi layer of the top of the c-Si substrate. The two layers of PSi together with the bottom Si substrate were meant to act as three absorbers with three different band gaps, the famous "tandem cell" structure described earlier in this chapter. The device feature a very small PV effect with a Voc in the range 0.008 – 0.11 V, an Isc of around 0.021 – 0.027 mA with a corresponding fill factor of 0.23 – 0.24. The paper introduced the concept of band gap engineering in PSi, considering that the material indeed is a wide absorber which band gap is directly estimated from the photoluminescence spectra. Unfortunately, while encouraging, the results are not evidence at all of the activity of PSi itself as a wide gap absorber and no information is available about the spectral response of the expected tandem device.

The summary of reported PV effect in PSi and their corresponding characteristics are summarized in the **Table 1.5**. All samples listed in the table consist of a PSi layer atop c-Si substrate. The different light source used during characterization, the lack of clear photocurrent and photovoltage values as well as spectral response make the comparison between devices extremely difficult. In most reports, the overall PV response is explained by the presence of a double junction, a schotkky type barrier between the top metal contact and the PSi layer, and a second heterojunction between the PSi and the underlying c-Si substrate, both contributing to the photo-response of the devices. Several reports [103][104][105] showed that the contribution from the top metal contact was very weak, almost negligible and that most of the photo-response is due to the PSi/c-Si heterojunction with a strong contribution from the bulk Si substrate. To our knowledge, only one report [91] deals with the problem of c-Si strong contribution to photoresponse by investigating the spectral response of self-standing PSi layers. During their investigation, they found that for p type self-standing, two different photocurrent peaks exist, one located at 440nm which is almost independent of both the

polarity and amplitude of applied voltage and is detected even in the absence of externally applied electric field. This photovoltaic response has been attributed to the surface while the second peak located at 580 nm, inexistent without applied voltage, was attributed to the volume properties of PSi (nanosized c-Si islands).

Remarks	Structure	Illumination source	Voc	Isc - Jsc	FF	Reference
	Cu/nPSi/nSi/Al	59.4 mW/cm^2	0.330 V	0.2 mA/cm^2	NA	[106]
	Cu/pPSi/pSi/Al	59.4 mW/cm^2	0.235 V	0.13 mA/cm^2	0.3	[106]
	PSi/c-Si/Au	AM1.5-1 sun	0.36 V	0.002 mA	NA	[101]
	PSi/c-Si, np type wafer	Halogen 100W, 1mW/cm2 – 16 mW/cm2	0.183 – 0.327 V	1.41 – 26 μA	0.1 – 0.23	[107]
	Au/PSi/c-Si/Au	AM1.5-1 sun	0.37 V	240 μA	NA	[24]
Lateral illumination	Al/PSi/c-Si/Al	Am1–1 sun	0.08 – 0.11	0.021 – 0.027 mA	0.23 – 0.24	[102]
Photovoltage mostly ind. on contact material	Metal/PSi/C-Si	Monochro 633 nm 3mW	440 mV	NA	NA	[108]
Oxidized material	Al/PSi/c-Si/Al	Tungsten 22.4 mW/cm^2	0.52 V	4 mA	NA	[109]

Table 1.5: *Summary of the reported PV effects detected in PSi with their corresponding PV parameters and measurement conditions.*

Only devices involving PSi as the sole active material are listed here, several other papers are dealing with hybrid organic-inorganic PSi based cells used in conjunction with materials such as copper phthalocyanine [110], polypirolle [111], or eumelanin [112].

I.6 Presentation and objective of the study

The strong necessity to decrease the cost per watt of current photovoltaic technology has lead to numerous investigations on alternative processing to reduce the cost of fabrication, as well as the emergence of new PV devices and concept to increase the overall efficiency of PV cells. A first simple technical approach consist of reducing the cost of silicon wafer processing by reducing the thickness of the wafer and cutting down the loss of raw material generated by the current slicing processes. The second approach consist of increasing the efficiency of the PV cells themselves and has lead to the proposal of a wide variety of new devices structures and technologies, including the development of organic PV cells technology and the introduction of the multijunction device structure for inorganic cells for example.

Following these two different but parallel approaches, the main objective of this study is to use the simple electrochemical method of Silicon etching as a common process platform and investigate its potential ability to be used both as an alternative technology for silicon wafering and for the fabrication of nanocrystalline silicon for application as a widegap material for solar cells as described in the **Fig. 1.24**.

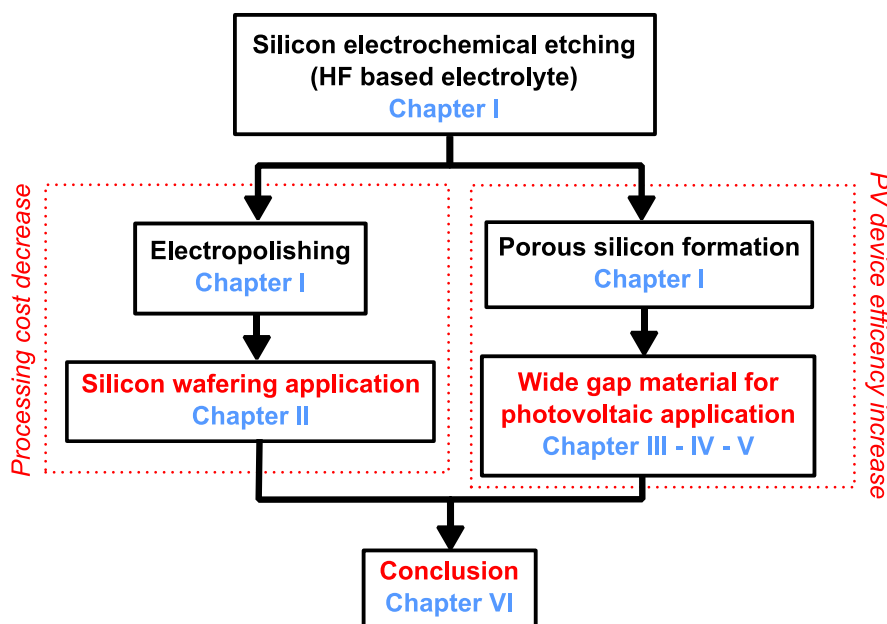**Fig. 1.24:** *Presentation of the objectives of the present study. Starting from a common electrochemical etching process, the study will focus on two different potential applications, the first one as a new wafer slicing method for ultra-thin solar cells silicon wafer, the second as a mean to produce nanocrystalline silicon material with potential application as a wide-gap absorber for the future generation of advanced solar cells.*

In a first time, the feasibility of the electrochemical slicing process based on local electropolishing of silicon will be investigated and further developed in terms of performance, scalability, and cost compare to current industrial process and concurrently developed new approach to wafering. In a second time, the possible use of nanocrystalline PSi as a wide gap active material in new generation solar cells will be investigated through the introduction of a new device structure consisting of free-standing PSi layers produced from pn type doped silicon substrate.

Chapter II will deal with the process of silicon wafer slicing or "wafering" and its different technical and economical aspects. The electropolishing process will be employed here as a local etching method to produce deep trench in silicon ingot and the results will be discussed and compare to current slicing requirement in performance and cost as well as others wafering alternative currently and concurrently developed by others research teams in the world.

The next section (Chapter III) will introduce the procedural method used for the fabrication and physical characterization as well as post-processing of the PSi free standing cells, including the layer separation process, contact deposition and the photoelectrical and photovoltaic characterizations will be presented in details.

The chapter IV will summarize and discuss the results obtained from the characterization of PSi free standing layers, including their overall characteristics for as prepared samples and their dependency on fabrication condition and device structure as well as further discussion about the stability of the material.

In chapter V, we will finally investigate the effect of several post-fabrication processes of the material, including chemical etching and annealing. Furthermore, chemical derivatization of the surface by organic molecules will be employed to investigate the possibility of increasing the stability and performance of the devices for practical application.

Finally, we will conclude in chapter VI by recapitulating the results obtained so far in this study and discussing possible future directions.

Bibliography of Chapter I

[1] A. UhIir, Bell Syst. Tech. J. **35**, p.333 (1956).

[2] D.R. Turner, J. Electrochem. Soc. **105**, p.402 (1958).

[3] Y. Watanabe, T. Sakai, Rev. Electron. Commun. Labs. **19**, p. 899 (1971).

[4] C. Pickering, M. I. J. Beale, D. J. Robbins, P. J. Pearson, R. Greef, J. Phys. C: Solid State Phys. **17**, p. 6535 (1984).

[5] L.T. Canham, Appl. Phys. Lett. **57**, p. 1046 (1990).

[6] V. Lehmann, Electrochemistry of Silicon: Instrumentation, Science, Materials and Applications, Wiley-VCH Verlag GmbH, Weinheim (2002).

[7] B. Gelloz, Silicon nanocrystals in Porous Silicon and Applications, in: Silicon Nanocrystals: Fundamentals, synthesis and Applications, Lorenzo Pavesi and Rasit Turan (Eds.) Wiley-VCH Verlag (2010).

[8] B. Gelloz, and N. Koshida, in: Handbook of Luminescence, Display Materials, and Devices, H.S. Nalwa and L.S. Rohwer (Eds.), American Scientific Publishers, Stevenson Ranch, CA (2003).

[9] B. Gelloz, and N. Koshida, in: The Handbook of Electroluminescent Materials, D.R. Vij (Ed.), Institute of Physics Publishing, Bristol and Philadelphia (2004).

[10] A. Loni, L.T. Canham, M.G. Berger, R. Arens-Fischer, H. Munder, H. Luth, H.F. Arrand, and T.M. Benson, Thin Solid Films **276**, p. 143 (1996).

[11] P. Ferrand, R. Romestain, and J.C. Vial, Phys. Rev. B **63**, 115106 (2001).

[12] J.O. Estevez, J. Arriaga, A.M. Blas, and V. Agarwal, Appl. Phys. Lett. **94**, 061914 (2009).

[13] E. Xifre-Perez, L.F. Marsal, J. Ferre-Borrull, and J. Pallares, Appl. Phys. B **95**, p. 169 (2009).

[14] P.J. Reece, G. Lerondel, W.H. Zheng, and M. Gal, Appl. Phys. Lett. 81, p. 4895 (2002).

[15] M. Ghulinyan, C.J. Oton, G. Bonetti, Z. Gaburro, and L. Pavesi, J. Appl. Phys. **93**, p. 9724 (2003).

[16] D. Clement, J. Diener, E. Gross, N. Kunzner, V. Yu. Timoshenko, D. Kovalev, phys. Stat. sol. (a) **202** (8), p. 1357 (2005) / **DOI 10.1002/pssa.200461102**

[17] M. du Plessis, Mat. Sci. and Eng. B **147,** p. 226 (2008).

[18] T. Dzhafarov, S.A. Yuksel, and C.O. Lus, Jpn. J.Appl. Phys. **47**, p. 8204 (2008).

[19] M.S. Salem, M.J. Sailor, K. Fukami, T. Sakka, and Y.H. Ogata, J. Appl. Phys. 103, 083516 (2008).

[20] H. Shinoda, T. Nakajima, K. Ueno, and N. Koshida, Nature **400**, p. 853 (1999).

[21] A. Uematsu, T. Kikusui, T. Kihara, T. Harada, M. Kato, K. Nakano, O. Murakami, N. Koshida, Y. Takeuchi, and Y. Mori, Brain Res. **1163**, p. 91 (2007).

[22] K. Tsubaki, H. Yamanaka, K. Kitada, T. Komoda, and N. Koshida, Jpn. J. Appl. Phys. **44**, p. 4436 (2005).

[23] E.J. Anglin, L.Y. Cheng, W.R. Freeman, and M.J. Sailor, Adv. Drug. Delivery Rev. **60**, p. 1266 (2008).

[24] J.H. Park, L. Gu, G. von Maltzahn, E. Ruoslahti, S.N. Bhatia, and M.J. Sailor, Nat. Mater. **8**, p. 331 (2009).

[25] G. Lammel, S. Schweitzer, P. Renaud, in Proceedings of the 14th IEEE International MEMS Conference, p. 578 (2001).

[26] C.S. Solanki, R.R. Bilyalov, J. Poortmans, J. Nijs, R. Mertens, Sol. Ener. Mat. & Sol. Cells **83** p. 101 (2004).

[27] N. Koshida, T. Ozaki, X. Sheng, and H. Koyama, Jpn. J. Appl. Phys. **34**, L705 (1995).

[28] Y. Nakajima, A. Kojima, and N. Koshida, Appl. Phys. Lett. **81**, p. 2472 (2002)

[29] Y. Nakajima, T. Uchida, H. Toyama, A. Kojima, B. Gelloz, and N. Koshida, Jpn. J. Appl. Phys. **43**, p. 2076 (2004).

[30] T. Komoda, Y. Honda, T. Hatai, Y. Watanabe, T. Ichihara, K. Aizawa, Y. Kondo, X. Sheng, A. Kojima, and N. Koshida, IDW.99, p. 939 (1999).

[31] T. Komoda, T. Ichihara, Y. Honda, K. Aizawa, and N. Koshida, Mater. Res. Soc. Symp. Proc. **638**, F4.1.1 (2001).

[32] T. Komoda, T. Ichihara, Y. Honda, T. Hatai, T. Baba, Y. Takegawa, Y. Watabe, K. Aizawa, V. Vezin, and N. Koshida, J. Soc. Inf. Display **12**, p.29 (2004).

[33] N. Koshida, T. Ohta, and B. Gelloz, Appl. Phys. Lett. **90**, 163505 (2007).

[34] N. Ikegami, T. Yoshida, A. Kojima, H. Ohyi, N. Koshida, M. Esashi, J. Micro/Nanolith. MEMS MOEMS **11** 031406 (2012).

[35] International Energy Agency, *Technology roadmap: Solar photovoltaic energy* (2010). Retrieved at: www.iea.org/publications/freepublications/publication/pv_roadmap.pdf

[36] D. Swanson, The Silicon Photovoltaic Roadmap, The Stanford Energy Seminar, (2011).

[37] W. Sinke, *PV revolution through accelerated evolution: EU PV TP contributions to the success of PV*, Solar Summit Freiburg (2008).

[38] A. Skumanich, SVC 2009 InterSolar NA Conference (2009).

[39] European Photovoltaic Industry Association (EPIA), Solar Generation Solar Electricity For Over One Billion People And Two Million Jobs By 2020 (2006).

[40] W. Koch, A. L. Endros, D. Franke, C. Habler, J. P. Kalejs and H. J. Moller, in: Handbook of Photovoltaic Science and Engineering, Antonio Luque and Steven Hegedus (Eds.), John Wiley & Sons Ltd, Chichester, West Sussex, England, (2003).

[41] Diamond Materials Tech, Inc, MeyerBerger group, Diamond Wire Photovoltaic Applications. Retrieved on 2013/10/11 at:

http://www.meyerburger.com/fileadmin/user_upload/diamondwiretech.com/factsheets/DW_PV_120 4LD_Fctsht_01.pdf

[42] A. Halimaoui, Porous silicon formation by anodisation, in: Properties of Porous Silicon, L.T. Canham (Ed.), INSPEC, The Institution of Electrical Engineers, London, 1997, p. 12.

[43] C.M.A. Ashruf, P.J. French, P.M.M.C. Bressers, and J.J. Kelly, Sens. Actuators A **74**, p. 118 (1999).

[44] R.W. Fathauer, T. George, A. Ksendzov, and R.P. Vasquez, Appl. Phys. Lett. **60**, p. 995 (1992).

[45] P. Allongue, Porous silicon formation mechanisms, in: Properties of Porous Silicon, L.T. Canham (Ed.), INSPEC, The Institution of Electrical Engineers, London, 1997, p. 3.

[46] G. X. Zhang, Porous Silicon: Morphology and Formation Mechanisms, in: Modern Aspects of Electrochemistry, Vol. 39, C.G. Vayenas, R.E. White, M.E. Gamboa-Aldeco (Eds.), Springer (2006).

[47] J. Rouquerol, D. Avnir, C.W. Fairbridge, D.H. Everett, J.H. Haynes, N. Pernicone, J.D.F. Ramsay, K.S.W. Sing, and K.K. Unger, Pure Appl. Chem. **66**, p. 1739 (1994).

[48] N. Lalic. J. Linnros, Thin Solid Films **276**, p. 155 (1996).

[49] P. Steiner, F. Kozlowski, W. Lang, Appl. Phys. Lett. **62**, p. 2700 (1993).

[50] R. Herino, Pore size distribution in porous silicon, in: Properties of Porous Silicon, L.T. Canham (Ed.), INSPEC, The Institution of Electrical Engineers, London, 1997, p. 89.

[51] O. Belmont, C. Faivre, D. Bellet, Y. Brechet, Thin Solid Films **276**, p. 219 (1996).

[52] LT. Canham, A.G. Cullis, C. Pickering, O.D. Dosser, T.I. Cox, T.P. Lynch, Nature **368**, p. 133 (1994).

[53] G. Amato, V. Bullara, N. Brunetto, L. Boarino, Thin Solid Films **276**, p. 204 (1996).

[54] B. Gelloz, A. Kojima, and N. Koshida, Appl. Phys. Lett. **87**, 031107 (2005).

[55] B. Gelloz, R. Mentek, and N. Koshida, Jpn. J. Appl. Phys. **48**, 04C119 (2009).

[56] B. Gelloz, T. Nakagawa, and N. Koshida, Appl. Phys. Lett. **73** (14), p. 2021 (1998).

[57] B. Gelloz and N. Koshida, J. Appl. Phys. **88** (7) p. 4319 (2000).

[58] J. M. Buriak, Chemical Reviews **102** (5), p. 1271 (2002).

[59] B. Gelloz, H. Sano, R. Boukherroub, D.D.M. Wayner, D.J. Lockwood, N. Koshida, Appl. Phys. Lett. **83** (12) p. 2342 (2003).

[60] I. Suemune, N. Noguchi, M. Yamanishi, Jpn. J. Appl. Phys. 31, L494-L4 (1992).

[61] O. Bisi, S. Ossicini, L. Pavesi, Surf. Sci. Reports **38**, p. 1 (2000).

[62] C. Tsai, K.H. Li, D. S. Kinosky, R.Z. Qian, T.C. Hsu, J. T. Irby, S. K. Banerjee, A. F. Tasch, Joe C. Campbell, B. K. Hance, and J. M. White, Appl. Phys. Let. **60** (14), p. 1700 (1992).

[63] B. Delley, E.F. Steigmeier, Appl. Phys. Lett. **67**, p. 2370 (1995).

[64] V. V. Kislyuk, O. P. Dimitriev, J. of Nanosci. and Nanotech. **8**, p. 131 (2008).

[65] H. Okamoto, Y. Sugiyama, H. Nakano, Chem. Eur. J. **17**, p. 9864 (2011).

[66] A.G. Cullis, L.T. Canham, P.D.J. Calcott, J. Appl. Phys. **82**, p. 909 (1997).

[67] L. R. Tessler, F. Alvarez and O. Teschke, Applied Physics Letters **62** (19), p. 2381 (1993).

[68] S. Shih, K. H. Jung, R. Z. Qian and D. L. Kwong, Applied Physics Letters **62** (5), p. 467 (1993).

[69] R. P. Vasquez, R. W. Fathauer, T. George, A. Ksendov and T. L. Lin, Applied Physics Letters **60** (8), p. 1004 (1992).

[70] S. M. Prokes, O. J. Glembocki, V. M. Bermudez, R. Kaplan, L. E. Friedersdorf and P. C. Searson, Physical Review B **45**, p. 13788 (1992).

[71] M. S. Brandt, H. D. Fuchs, M. Stutzmann, J. Weber and M. Cardona, Solid State Communications **81** (4), p. 307 (1992).

[72] F. Koch, V. Petrova-Koch and T. Muschik, J. of Luminescence **43**, p. 271 (1993).

[73] J. A. Pradeep and P. Agarwala, J. Appl. Phys. **104**, 123515 (2008).

[74] J. von Behren,, T. van Buuren, M. Zacharias, E.H. Chimowitzd, P.M. Fauchet, Solid State Commun. **105** p. 317 (1998).

[75] I. Sagnez, A. Halimaoui, G. Vincent, P.A. Badoz, Appl. Phys. Lett. **62**, p. 1155 (1993).

[76] A. Grosman and C. Ortega, Dopants in porous silicon, in: Properties of Porous Silicon, L.T. Canham (Ed.), INSPEC, The Institution of Electrical Engineers, London, 1997, p. 328.

[77] I. Schechter, M. Ben-Chorin, A. Kux, Anal. Chem. **67**, p. 3727 (1995).

[78] L.A. Balagurov, D.G. Yarkin, E.A. Petrova, Mater. Sci. and Eng. B **69–70** p. 127 (2000).

[79] V. Lehmann, F. Hofmann, F. Moller, U. Gruning, Thin Solid Films **255**, p. 20 (1995).

[80] A. Diligenti, A. Nannini, G. Pennelli, and F. Pieri, Appl. Phys. Lett. **68**, p. 687 (1996) - doi: 10.1063/1.116592

[81] J. Kocka, J. Oswald, A. Fejfar, R. Sedlacik, V. Zelezny, Ho The-Ha, K. Luterowa, I. Pelant, Thin Solid Films **276**, p. 187 (1996).

[82] J. J. Mares, J. Kristofik, J. Pangrac, and A. Hospodkova, Appl. Phys. Lett. **63** (2), p. 180 (1993).

[83] M. Ben-Chorin, F. Möller, and F. Koch, Physical Review B **49** (4) p. 2981 (1994).

[84] Y. Lubianiker and I. Balberg, Physical Review Letters **78** (12), p. 2433 (1997).

[85] J. Kocka, I. Pelant, A. Fejfar, J. of Non-Crystalline Solids **198-200**, p. 857 (1996).

[86] A.J. Simons, Porous silicon diodes, in: Properties of Porous Silicon, L.T. Canham (Ed.), INSPEC, The Institution of Electrical Engineers, London, 1997, p. 192.

[87] J. P. Zheng, K. L. Jiao, W. P. Shen, W. A. Anderson, and H. S. Kwok, Appl. Phys. Lett. **61** (4), (1992).

[88] C. Tsai, K.H. Li, J. C. Campbell, and A. Tasch, Appl. Phys. Lett. **62**, p. 2818 (1993) - doi: 10.1063/1.109220

[89] T. Ozaki, T. Oguro, H. Koyama, and N. Koshida, Jp. J. Appl. Phys. **34**, p. 946 (1995).

[90] P. Hlinomaz, 0. Klima, A. Hospodkova, E. Hulicius, J. Oswald, E. gipek, and J. Kocka, Appl. Phys. Lett. **64** (23), p. 3118 (1994).

[91] R. Sedlacik, F. Karel, J. Oswald, A. Fejfar, I. Pelant, J. Kocka, Thin Solid Films **255**, p. 269 (1995).

[92] J. Torres, H.M. Martinez, J.E. Alfonso, L.D. Lopez C, Microelectronics Journal **39**, p. 482

(2008).

[93] M. A. Green, Physica E **14,** p. 65 (2002).

[94] A. Marti, G.L. Araujo, Sol. Energy Mater. Sol. Cells **43**, p. 203 (1996).

[95] A.J. Nozik, Physica E **14**, p. 115 (2002).

[96] A. Prasad, S. Balakrishnan, S.K. Jain, G.C. Jain, J. Electrochem Soc. **129**, p. 596 (1982).

[97] V. Y. Yerokhov, I. I. Melnyk, Renewable Sustainable Energy **3**, p. 291 (1999).

[98] J. Van Hoeymissen, V. Depauw, I. Kuzma-Filipek, K. Van Nieuwenhuysen, M. R. Payo, Y. Qiu, I. Gordon, and J. Poortmans, Phys. Status Solidi A **208** (6), p. 1433 (2011) - DOI 10.1002/pssa.201000103

[99] R. Brendel, Jpn. J. Appl. Phys. **40**, p. 4431 (2001).

[100] L. Stalmans, J. Poortmans, H. Bender, M. Caymax, K. Said, E. Vazsonyi, J. Nijs, R. Mertens, Prog. Photovoltaics **6**, p. 233 (1998).

[101] G. Smestad, M. Kunst, C. Vial, Solar Energy Mater. and Solar Cells **26**, p. 277 (1992).

[102] L. Kore, G. Bosman, Solar Energy Mater. and Solar Cells **57**, p. 31 (1999).

[103] C. Palsule, S. Liu, S. Gangopadhyay, M. Holtz, D. Lamp, M. Kristiansen, Solar Energy Mater. and Solar Cells **46**, p. 261 (1997).

[104] A.S. Dafinei, A.A. Dafinei, Journal of Non-Crystalline Solids **245**, p. 92 (1999).

[105] H. Khalili, R. S. Dariani, A. MortezaAli, V. Daadmehr, K. Robbie, J Mater Sci **42**, p. 908 (2007) - DOI 10.1007/s10853-006-0010-2

[106] M.C. Arenas, Hailin Hua, J. Antonio del Rio, O.H. Salinas, Revista Mexicana de Fisica **54** (5) p. 391 (2008).

[107] M. Rajabi, R. S. Dariani, J. Porous Mater **16**, p. 513 (2009) - DOI 10.1007/s10934-008-9226-7

[108] Zhengfu Han, Junyan Shi, Hai Tao, Li Gong, Shaojun Fu, Chaoshu Shi, Xingyi Zhang, Physics Letters A **186**, p. 265 (1994).

[109] M.K. Lee, Y.H. Wang, C.H. Chu, Solar Energy Mater. & Solar Cells **59**, p. 59 (1999).

[110] I. A. Levitsky, W. B. Euler, N. Tokranova, B. Xu, and J. Castracane, Appl. Phys. Lett. **85** (25), p. 6245 (2004).

[111] M. Concepcion Arenas, Hailin Hu, J. Antonio del Rio, Aaron Sanchez, M.E. Nicho, Solar Energy Materials & Solar Cells **90**, p. 2413 (2006).

[112] G. Mula, L. Manca, S. Setzu and A. Pezzella, Nanoscale Research Letters **7**, p. 377 (2012) - doi:10.1186/1556-276X-7-377

Chapter II. Related technology: electrochemical slicing

II.1 Electrochemical slicing experimental methods
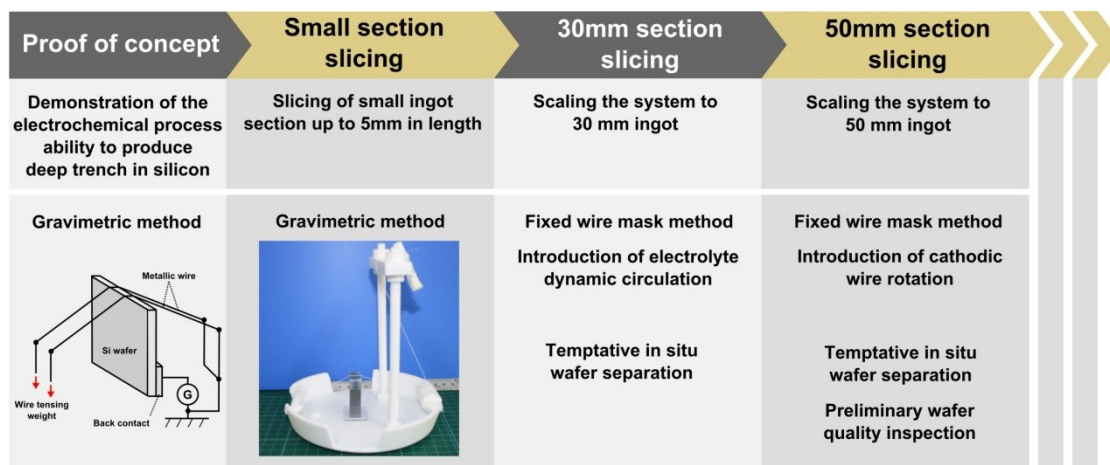
II.1.1 Presentation of the slicing systems

Fig. 2.1: *Workflow of the electrochemical slicing study from proof of concept to successful scaling of the system through different size of silicon ingot and the corresponding evolution of the slicing system and parameters involved.*

The general workflow of the electrochemical slicing process is presented in the diagram of **Fig. 2.1**. As a first step the electrochemical slicing method ability of producing trench by electrochemical etching was tested using a simple gravimetric wire tensing system on single crystalline silicon wafer as shown in **Fig. 2.2(a)**. In such configuration, the wires were fixed at one side of the system and the tension of the wires in contact in the Si wafer was kept constant by a weight attached to the opposite side of the slicing system (hence the denomination of "gravimetric" system). After confirming the applicability of the process, the system was scaled up to slice Si ingot surface from a width of 3 mm and gradually increased up to a width of 50 mm. Together with the scaling of the system, several process enhancement were introduced along the way: the gravimetric system was replaced by a fixed mask with adjustable wire tension and separation pitch. The mask itself was mechanically fixed on a micro-actuator and maintained at a fixed position over the Silicon ingot as seen in **Fig. 2.2(b)**. The descending speed of the wire mask toward the Si ingot was remotely controlled by a computer in the range of hundred of µm/min. The system was then modified to allow for a dynamic flow of the HF
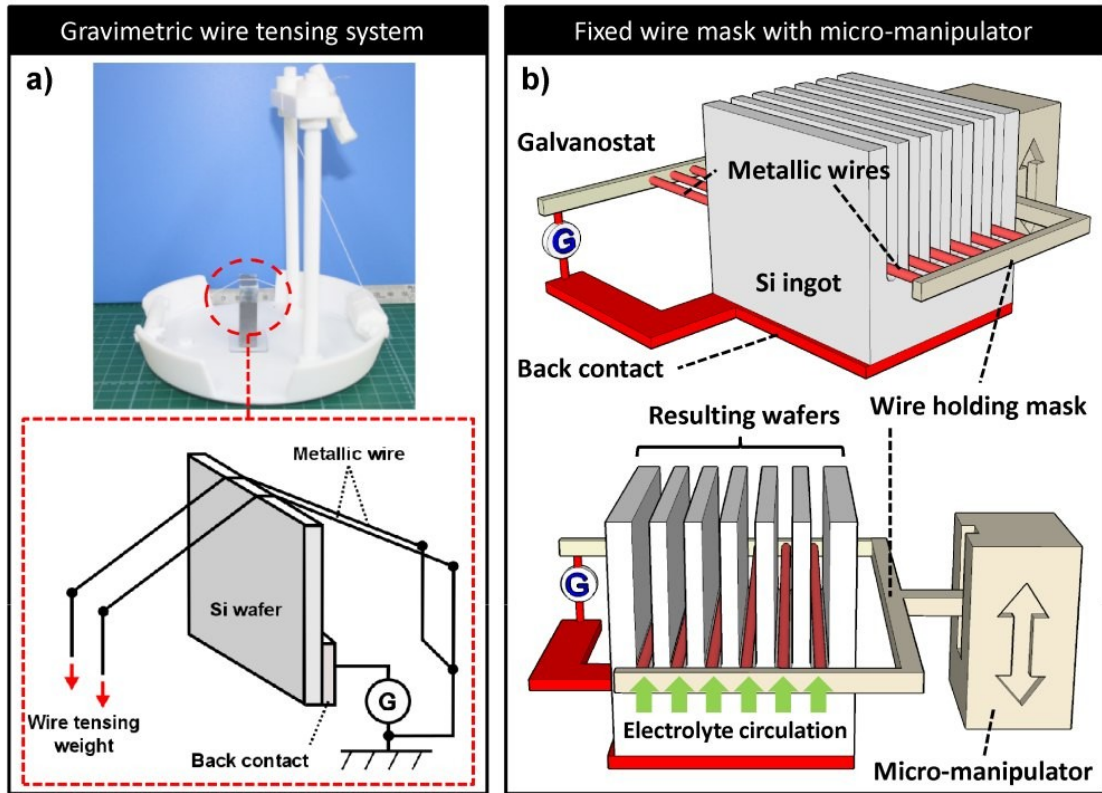
Fig. 2.2: *Schematics of the two slicing systems used in this study. The system on the left was used for basic investigation and prototyping while the more advanced system on the right was used for slicing larger section of silicon ingots.*

electrolyte in the vicinity of the wire, toward the interior of the kerf. The electrolyte was injected through the use of a PTFE diaphragm pump driven in pulse mode (non continuous flow) with an adjustable repetition rate. The effect of unidirectional injection of electrolyte from one side and bidirectional injection from both sides of the kerf was also investigated. Finally, mechanical low speed rotation of the wire cathode was introduced. Both electrolyte dynamic flow and cathode rotation were introduced in order to enhance the diffusion of the HF active species toward the etching interface, located inside the Silicon ingot volume. As the electropolishing rate is limited by the diffusion of chemical active species and not by the carrier injection since electropolishing is obtained at high injection regime, the control of the electrolyte content and flow are therefore important parameters in controlling the performance of the slicing process. The flow and cathodic rotation also helps evacuate the hydrogen gas bubbles generated by the electrochemical dissolution, bubbles that might otherwise remain trapped and condensate inside the silicon thin trench. The overall characteristics of the slicing system and the range of parameters used during experiments are summarized in **Table 2.1**. The parameters will be separately indicated for every results presented in the rest of this chapter.

Wire configuration	Wires number	1 to 6
	Wire diameter	$30 - 40 - 50$ µm
	Wire material	Tungsten (W) / Platinum Rhodium (Pt-Rh)
	Wire pitch	$1 - 0.8 - 0.4 - 0.3$ mm
	Wire lowering speed	20 to 120 µm/min
HF concentration		3 to 7%
Power supply	Current density	$25 - 110$ mA/cm
	Terminal voltage	$15 - 60$ V
Enhancement	Electrolyte flow	Yes
	Wire rotation	Yes
Silicon ingot type		Single and poly-crystal P-doped silicon

Table 2.1: *Summary of the basic slicing parameters range and capability of the slicing system.*

The generator used for the electrical driving of the slicing system was a galvanostat/potentiostat with a high power output. The electropolishing reaction requires high current density leading to high potential between the cathodic wires and the silicon material, far higher than typical current/voltage use in usual electrochemical process, usually not exceeding 1A/10V. In our case, a custom made galvanostat from Hokuto Denko (Japan) with an output capability of ±150V and ±13A was used to drive the slicing system.

II.1.2 Electrochemical slicing parameters

The two most important parameters controlling the electropolishing reaction are the HF content and the current density range. As already introduce in chapter I, electropolishing occurs for current density in excess of J_{ps}, the electropolishing density lower limit. J_{ps} is described by the following equation (from reference [1] page 61):

$$J_{ps} = C_{ps}c_{hf}^{n}e^{-E_a/kT}$$

with the constant $C_{ps} = 3300$, the activation energy $E_a = 0.345$eV and the exponent $n = 1.5$. J_{ps} is therefore dependent on both the temperature and the HF concentration of the electrolyte. Since the temperature control of a large quantity of hazardous liquid such as HF are rather difficult to easily

implement in our system, the concentration of HF will be the controlling parameters and will be chosen to allow suitable performance for the electrochemical slicing process while maintaining the current density / potential in acceptable range of values. The plot of J_{ps} at room temperature and 0^oC for different HF concentration is shown in the left part of **Fig. 2.3**. Lower HF content lead to a strong decrease of the current density requires to sustain the electropolishing reaction. Furthermore, the electrical conductivity of aqueous HF electrolytes also depends strongly on the HF concentration also seen in **Fig. 2.3** at the right (calculated from the equation in reference [1] page 9). Increase in the electrolyte resistivity would also enhance the locality of the electropolishing effect by carrier injection through the least resistant conduction path between the metallic wire and the ingot surface. HF concentration between 3 and 7% were used in this study. The HF was mixed with pure ethanol (99.5%) to enhance the wetability and increase the hydrogen gas evacuation from the electropolishing site.
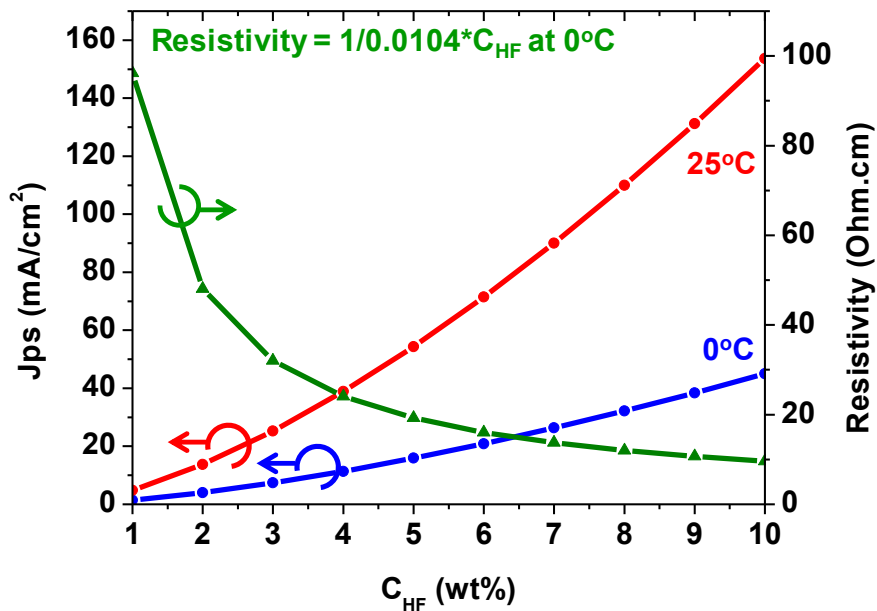
Fig. 2.3: *Evolution of the HF based electrolyte resistivity and critical electropolishing current density in function of the HF content (in weight %)*

Since the main motivation for the development of a new slicing technology is economical, the slicing process has to be kept the simplest and cheapest possible. The current density has to be kept in an acceptable range to limit the overall power consumption of the system if the process is to be scaled to a full industrial size. Similarly, the electrolyte was kept simple by avoiding the use of any chemical additive in the solution, decreasing the amount of waste and facilitating the recycling of the used solution.

II.2 Experimental results

II.2.1 Electrochemical slicing overview

The first demonstration of the ability of electrochemical etching of Silicon in HF was realized using the simple gravimetric system described previously in this chapter. The system was used in both a simple and double wires configuration for slicing wafers and in single wire configuration for slicing ingots of 25 mm in length. The slicing of a single crystalline (100) p doped wafer in a 5% HF solution with two wires parallel to the wafer surface under a current of 200 mA is shown in **Fig. 2.4**. The recorded potential during the slicing duration shows very low fluctuation until the complete separation of the sliced section for the substrate indicated by the potential strong increase at the end of the slice. Cross sectional views of the sliced wafer and of a kerf stopped during the middle of a slice are also shown in **Fig. 2.4(b)** and **2.4(c)**, the corresponding slice speed was 87.5 µm/min and the kerfloss measured at around 94 µm.
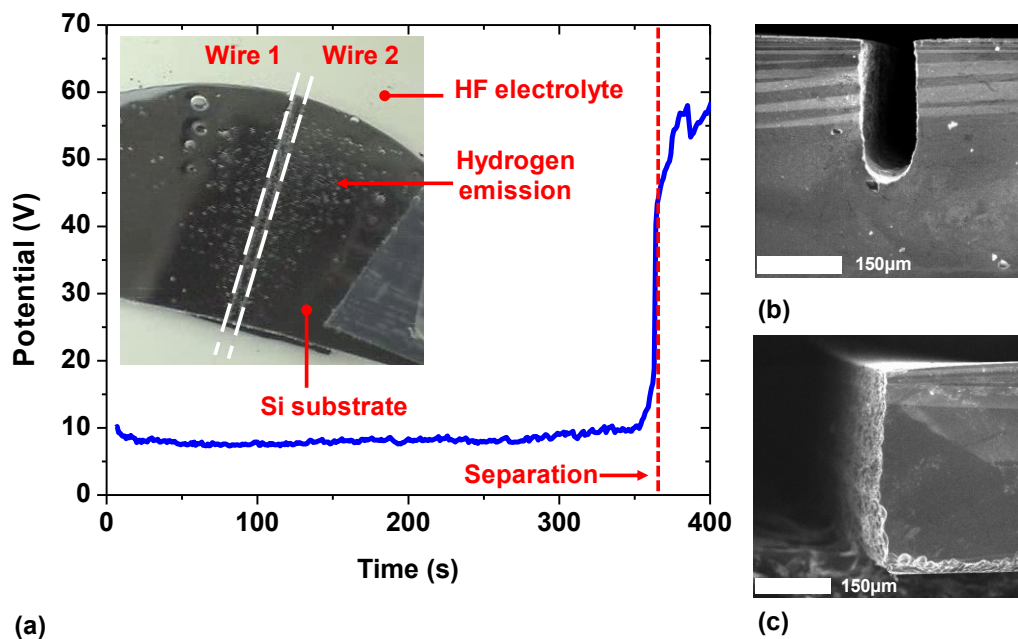
Fig. 2.4: *(a) Typical electrochemical slicing of a 525 µm thick wafer with the corresponding anodization cell potential showing a strong increase in the potential after separation of the wafer, (b) SEM micrograph showing the cross section of a typical kerf, (c) SEM micrograph of a cross section of a wafer after complete slicing.*

When the system is scale up to small poly-silicon ingot of a 25 mm in length and 20 mm in height, the corresponding result are shown in **Fig. 2.5**. The cross section of the slice clearly shows that starting at a depth of around 5mm, the kerf starts to show strong variation in the

kerfloss as well as the inability of the system to keep the slicing path straight to the bottom of the ingot. The use of a simple gravimetric system has clearly shown the ability of the electrochemical etching process to create kerf at a reasonable speed with low kerfloss for slicing of small section of silicon such as typical 525 μm wafer but show strong deviation for larger section of ingot. The next section will introduce the use of a more advance slicing system using a wire holder mask allowing for multi-wire slicing, wire position and speed control in order to scale the system for larger size of ingot.

Side view of the trench **Cross-section of the inside trench**
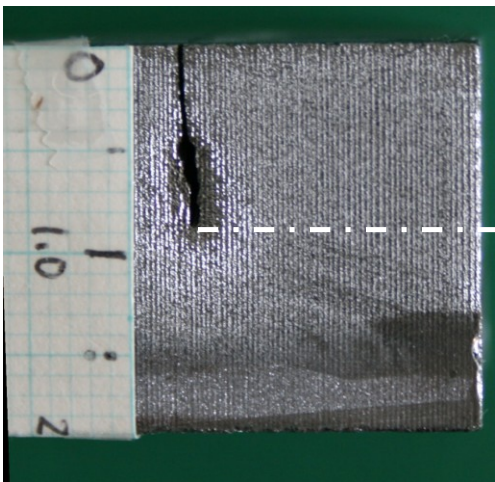
5 mm

Fig. 2.5: *Demonstration of a slice realized on a 25 mm wide ingot with the simple gravimetric slicing system. Mechanical removal of the right ingot chunk allows for the observation of the internal surface of the kerf.*

II.2.2 Multi-wire slicing

II.2.2.1 Small section ingot (3 and 5 mm)
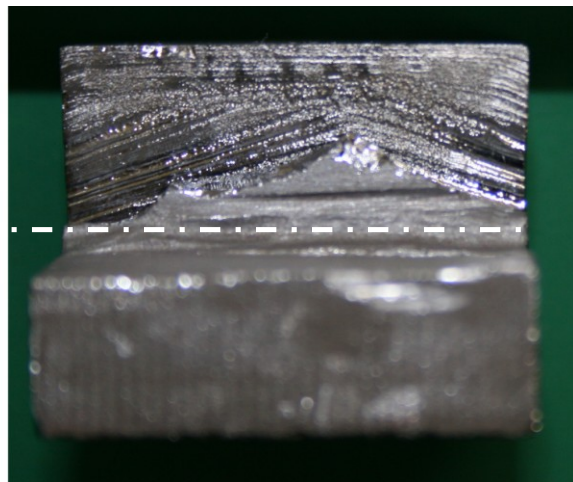
Following the preliminary results, a more advanced system was used which allows both the use of tightly fixed and tensed parallel multiwires in a configuration similar to systems used for classical wire saw slicing machines. In such configuration, the mask holding the wires is positioned at a fixed height over the silicon ingot and is lowered down at a constant speed during all the process. As a first step a low descending speed was chosen and gradually increased step by step until a maximum speed for a given set of slicing conditions without

breaking the wires was obtained. Wreckage of the metallic wires occurs when the lowering speed of the holding mask is superior to the dissolution speed of the electropolishing reaction at the interface between the wires and the silicon ingot. The ingots employed here were polycrystalline p type with a top width of 3 and 5 mm. Typical results of a multi-wire slice for 3 mm and 5 mm are shown in **Fig. 2.6** with the corresponding slicing parameters listed in the lower tables. The results show that the mechanical control of the tension and position of the wires provides clean and sharp trenches perfectly parallel to each others. The best overall experimental results are summarized separately in **Table 2.1**. The different results shown here such as the kerfloss and slicing speed are independent and does not necessarily belong to the same set of slicing experiment but were conducted with the same experimental condition. The effect of HF concentration has also been investigated using 3 mm ingots and the results are presented in the section II.2.3.1 The table shows that the difference in section of the ingot from 3 mm to 5 mm, while still limited, does not show strong differences in kerfloss and overall quality of the slice. In both case, trenches of depth in excess of 20 mm were achieved. Only the slicing speed of 5 mm ingot was slightly lower than the corresponding 3 mm one. Since the dissolved volume for 5 mm ingot is higher than in the case of 3 mm and both slicing experiments show the same kerfloss, the overall speed is logically lower in the case of a larger dissolved volume of silicon.

Best results	3 mm ingot	5 mm ingot
Speed setting / measured (µm/min)	90 / 89	70 / 67
Kerfloss (µm)	150	150
Cut depth (mm)	27	23.7

Table 2.1: *Summary of the best slicing performance obtained on 3 and 5 mm wide ingots*
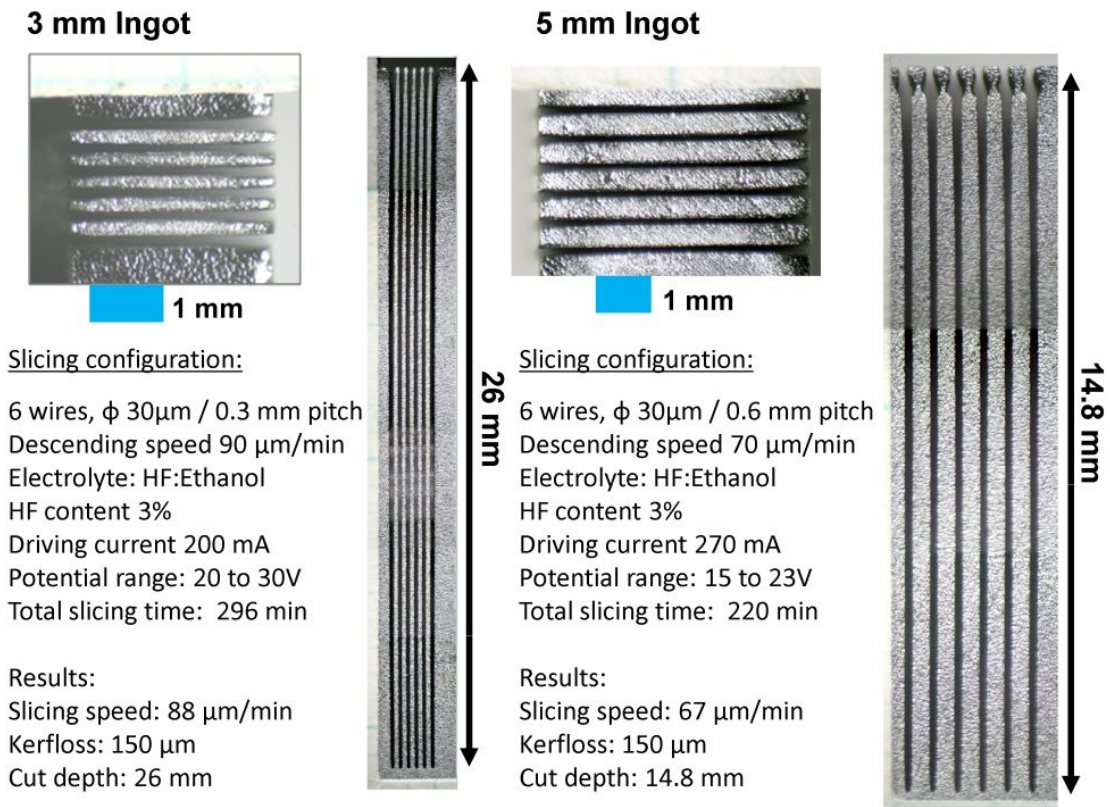
Fig. 2.6: *Typical slicing results obtained for silicon ingots of 3 and 5 mm in width.*

II.2.2.2 30 mm wide ingot

Scaling the system to bigger size of silicon ingot is one of the most important aspects of the slicing process and will consequently be the focal point of the next step of this study by scaling the electrochemical slicing system to ingot of 30 mm. While it might be tempting to focus on purely performance related aspects of the slice such as the speed and kerfloss while maintaining the sliced section to a non-practical and non-realistic size, the scaling to far larger slicing section might prove difficult and performance in such size range difficult to replicate.

With previous ingot size of 3 and 5mm, the width was small enough not to introduce noticeable problem of electrolyte circulation and flow inside the trench. With a width scale up to 30 mm, the problem of electrolyte and HF species diffusion inside the trench, already the limiting factor in electropolishing regime might become prevalent as the width of the trench increases. The consumption of the electrolyte active species near the electropolished surface is expected to lead to local gradients of concentration of HF species in the solution, gradients that cannot be

compensated if new "fresh" solution is prevented from efficiently circulating inside the kerf due to its very small volume. A new parameter was therefore added to the slicing process by implementing an electrolyte flow controller within the system. The electrolyte was directly pump out from the main electrolyte tank where the silicon ingot is immerged and release with a controlled rate at the wire location in the direction of the trench. The system was first use in a uni-directional configuration where electrolyte was injected from only one side of the ingot and then upgraded to an alternating bi-directional flow, electrolyte circulating from both side of the silicon ingot toward the center of the kerf as seen in **Fig. 2.7(a),** alternating the injection from left to right using a electrochemical valve to switch the flow from left to right at each repetition. The immediate effects of forced electrolyte circulation on slicing results are shown on **Fig. 2.7(b)** and **2.7(c)**. Without electrolyte circulation, the achievable slicing speed was very slow, 13 μm/min on average, with very large kerfloss of 430-460 μm for example 1 and 2 of **Fig. 2.7**. With added electrolyte circulation (unidirectional), the performances were returned to more typical result with a speed of 60 μm/min and kerfloss of 220 μm as seen in the right optical picture. These results were obtained using the same 3% concentration of HF and uni-directional electrolyte circulation. The injection of electrolyte from one side of the silicon ingot did introduce a variation of kerfloss from one side to the other and the differences are discussed in section II.2.3.3. The typical result for a successful 30 mm ingot slice is summarized and shown in **Fig. 2.8.**
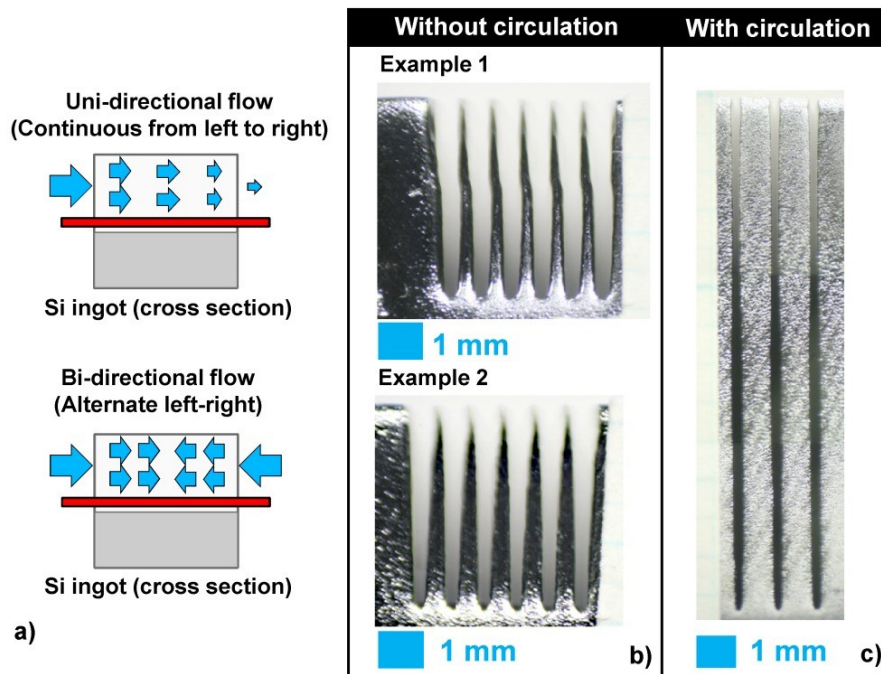

Fig. 2.7: *Schematic of the electrolyte uni and bi-directional injection mode and its corresponding effect on the slicing appearance and performance for a 30 mm wide ingot.*

69

Top view

1 mm ▪

Left side

Right side
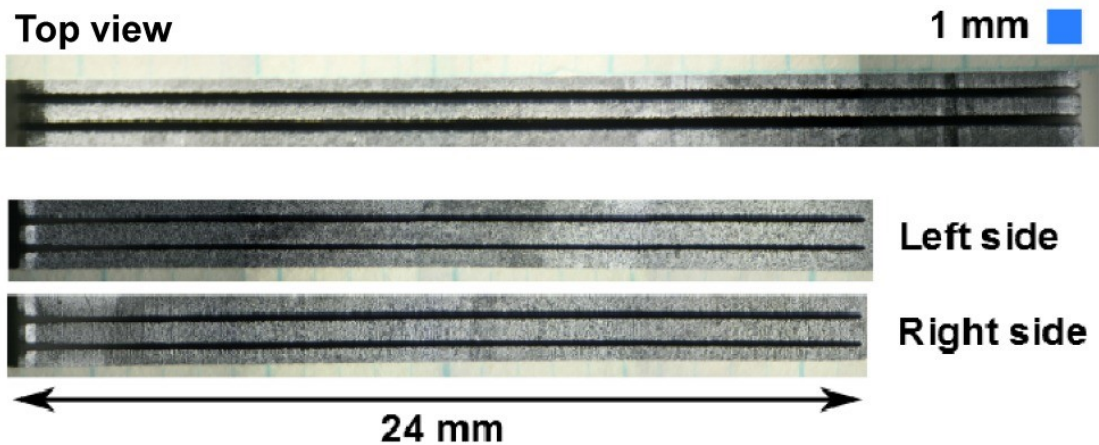
24 mm

Slicing configuration:

2 wires ϕ50μm / 0.8 mm pitch
Descending speed 60 to 84 μm/min
Electrolyte: HF:Ethanol   HF content 3%
Driving current: 600 mA
Total slicing time: 317 min

Results:
Slicing speed: 75 μm/min
Kerfloss: 150 μm
Cut depth: 24 mm

Fig. 2.8: *Typical slicing results obtained for a 30 mm wide ingot.*

With further improvement in the slicing parameters, including dynamically controlling the speed and current density in function of the potential fluctuation, strong improvement in the slicing performance were obtained as seen in **Table 2.2**. The system was finally able to slice through a depth in excess of 30 mm, leading to the possibility to produce so far 30 x 30 mm square wafers. The wafers were in-situ separated from the ingot by electropolishing the lower end of the wafer while the wires were kept stationary. The local increasing electropolishing around the wires finally allow for the separation of the wafer without damage. The resulting wafers were produced in two configurations, a single wafer of 30 x 30 mm^2 (2 wires slicing) and three wafers of 30 x 11 mm^2 (4 wires slicing) were produced safely as seen in the separation summary of **Fig. 2.9**.

Best results	30 mm ingot
Speed setting / measured (μm/min)	100 / 94.9
Kerfloss (μm)	130
Cut depth (mm)	31.8

Table 2.2: *Summary of the best performances obtained during 30 mm ingot slicing. With the introduction of electrolyte flow and better control of the experimental parameters, kerfloss and speed were enhanced compare to results obtained previously with 3 and 5 mm wide ingot.*
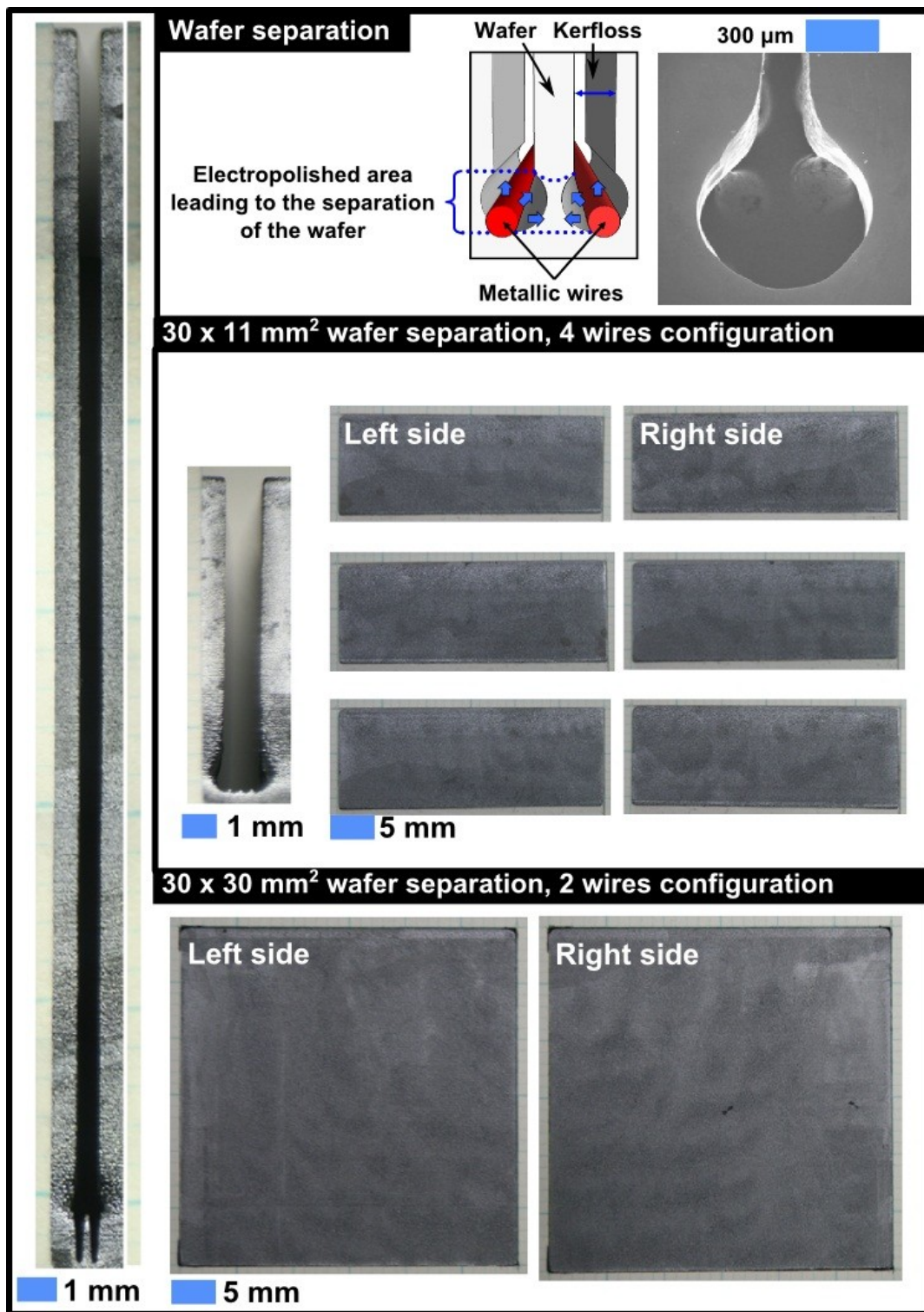
Fig. 2.9: *Demonstration of the in-situ wafers separation method realized in 4 and 2 wires mode resulting in the separation of 3 and 1 wafer respectively. The SEM micrograph at the top-right of the figure shows the strong radial etching occurring around a cathodic wire when kept stationary.*

71

II.2.2.3 50 mm wide ingot

The next step for the development of the electrochemical slicing system is the scaling to 50 mm ingots. The experiments were conducted in a similar configuration as for 30 mm ingot, with electrolyte circulation (alternate bi-directional flow) and monitoring of the current/potential and speed during the slicing. All the experiments were conducted in a 1 wire configuration. In parallel to forced electrolyte flow, a low speed balancing movement of the wire was later introduce in the system with a wire displacement speed in the range 20 to 50 mm/sec. Similarly to electrolyte forced circulation, the objective of the rotation is to help eliminate concentration gradient and evacuate hydrogen gas more efficiently. The results with and without wire rotation are shown in **Fig. 2.10**. The overall best performances with 50 mm ingot are summarized in **Table 2.3**. Overall, the results in 50 mm mode were promising with no visible decrease in slicing performance over 30 mm ingot. In fact, the highest slicing speed and therefore the lowest kerfloss were obtained using 50 mm, due to additional improvement and a better control of the slicing parameters over the previous slicing experiments.

Fig. 2.10: *Typical slicing results obtained on 50 mm ingot with and without cathodic wire rotation.*

Best results	50 mm ingot
Speed setting / measured (µm/min)	110 / 105
Kerfloss (µm)	140
Cut depth (mm)	26.1

Table 2.3: *Summary of the best performances obtained on 50 mm wide ingot.*

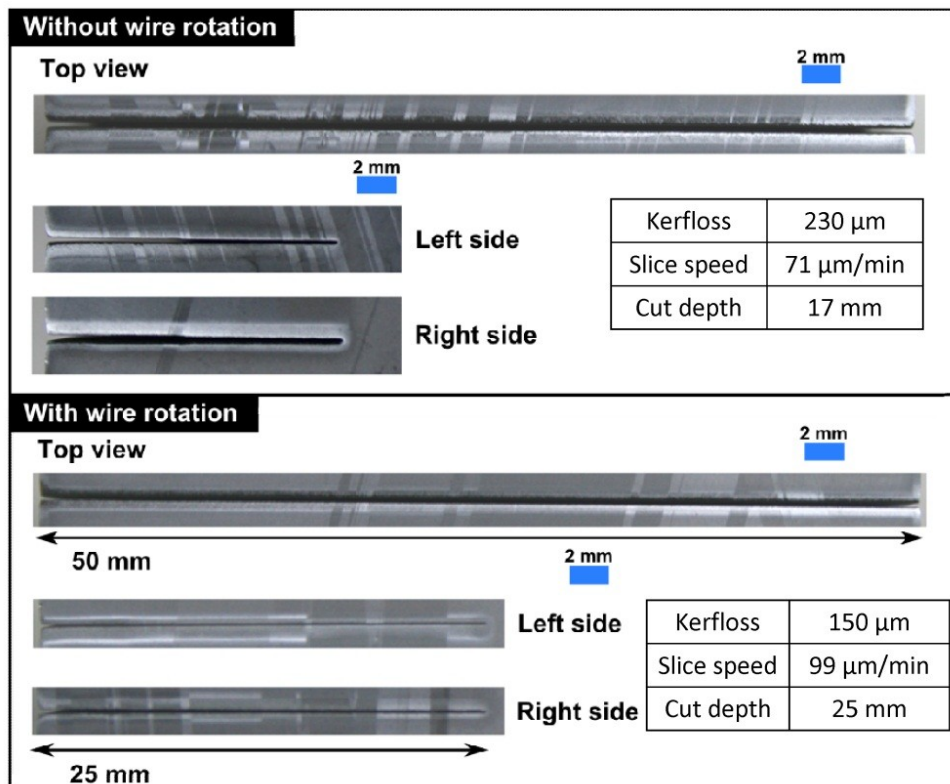The necessity of guaranteeing a constant supply of electrolyte at the dissolution front becomes primordial as the width of the slice increases. Larger section of ingot also means that the strength of the electrolyte flow will tend to decrease toward the center of the kerf. Indeed, slicing using 50 mm ingot actually shows a slicing depth gradient between the center of the kerf and its edge as illustrated in **Fig. 2.11**. The difference of depth between the center and the sides of a kerf were measured to be 2.5 mm for a 50 mm wide ingot. No detectable difference was measured between the left and right side depth. The **Fig. 2.11(c)** and **(d)** illustrates respectively the expected and the probable position of the metallic wire inside the kerf with a depth gradient. Since the wire is descending at a constant speed toward the dissolution front, the wire might actually enter in contact with the silicon ingot at the center of the kerf where the reaction speed is the lowest and the dissolution front the shallowest. The continuous lowering of the slicing tool induce a bending of the wire provoking an acceleration of the gradient due to dissolution occurring continuously at the edge where the electrolyte gradient is nonexistent. If the reduction in speed at the center of the kerf is too important, the strong bending of the wire may lead to its mechanical breakdown. The problem could be reduced by using a more powerful injection of the electrolyte toward the center of the kerf. The electrolyte circulation systems employed in this study was limited in term of performance and limited to only alternate flow from left to right using a chemical flow switch. For a practical application, industrial solutions exist with continuous flow at high rate which would eliminate the electrolyte gradient problem among others.

Position	Depth
Side (1)	20.7 mm
Center (2)	18.2 mm
Side (3)	20.7 mm
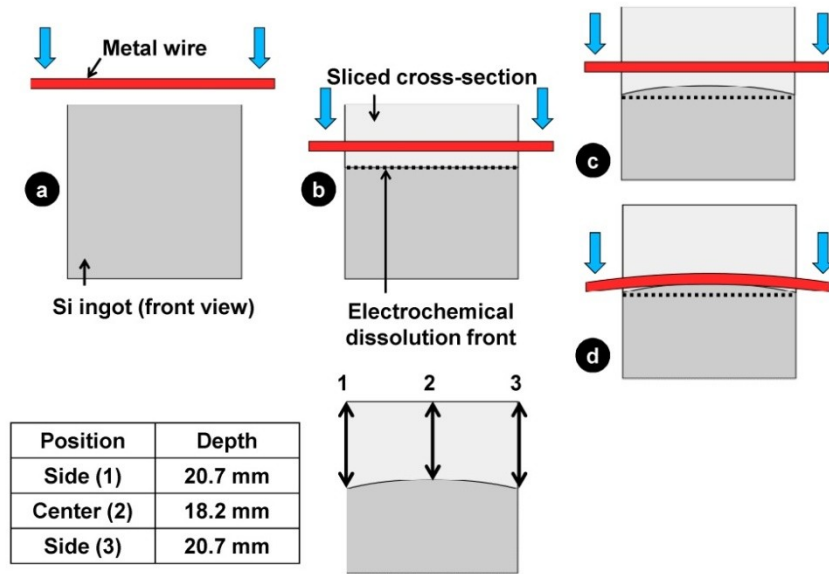
Fig. 2.11: *Illustration of the appearance of a depth gradient during long duration slicing. Step (d) shows the possibility of the wire entering in contact with the ingot and starting to bend under the tension produce by the continuous descent of the slicing tool. The bottom of the figure shows the experimentally measured depth gradient obtained on a 50 mm wide ingot measured from the center and the left and right edges.*

II.2.3 Effect of slicing parameters on performances

As previously seen in the experimental results, while the current density/potential and HF concentration controlled the electropolishing reaction, the lowering speed of the slicing wire also has a strong effect on the resulting kerfloss size. The resulting performance of the slice is an intricate relation between all these parameters and their effects on the overall results will be discussed in the following sections

II.2.3.1 Effect of HF concentration

We have seen previously that the HF concentration should be low enough to produce an electropolishing effect with a moderate current density. Keeping the concentration low also has an important economical as well as environmental aspect, reducing the amount of dangerous chemical waste after the slicing process. The concentrations used in this study were kept in the range 3 to 7%. The effect of increasing HF concentration is shown on 3 mm ingot slicing experiment summarize in **Fig. 2.12**. The others parameters were kept constant during the slice.

The resulting electropolishing effects are clearly visible on the overall appearance of the sliced ingot. As the concentration in HF is increased, the electropolishing effect becomes more apparent on the silicon surface around the cathodic wire as seen for a concentration of 6%. The whole surface of the ingot in contact with the HF electrolyte has a strong reflective and metallic appearance, typical of electropolished silicon. In contrast, with a concentration of 3%, the silicon surface kept the original rough non reflective appearance of the poly-crystalline ingot. The present results confirm our previous discussion about the effect of concentration, that a lower concentration of HF with a lower conductivity strongly enhances the locality of the electropolishing. Higher concentrations of HF also lead to larger kerfloss and over-etch of the trench around the side of the ingot clearly visible from the top view of the ingot. The over-etching effect is strongly decreased with a decrease of HF concentration which unfortunately cannot be decreased indefinitely as the concentration of HF is a strong limiting factor in the electropolishing process. Lower concentration would lead to the same problem introduce in the slicing or large section of silicon, the strong local decrease of HF active ions near the electropolished surface strongly limiting the efficiency of the overall electrochemical reaction.
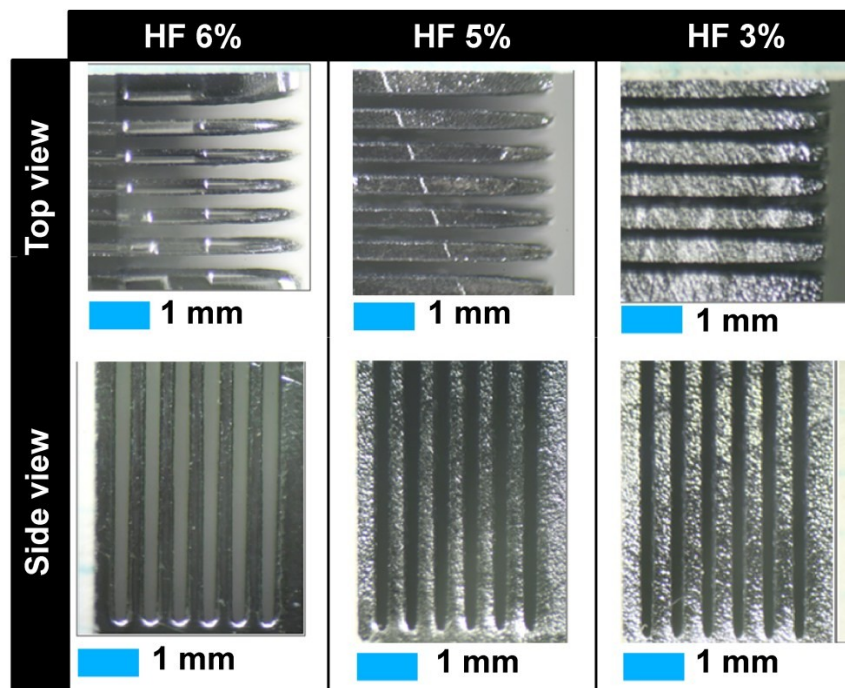

Fig. 2.12: *Effect of HF concentration on the size of the kerfloss and the visual appearance of the sliced ingot. Higher concentrations lead to an overly etched metallic appearance of the surface.*

II.2.3.2 Effect of speed variation on kerfloss

Our current slicing method relied on controlling the descending speed of the slicing tool (mask holding the wire and electrolyte circulation outlets) toward the silicon ingot. The controlling parameter is therefore the speed for a given set of conditions (HF content, current density, type of ingot), the methodology relying on increasing the speed to a maximum without breaking the wires. The effect of speed variation during a same slicing experiment is shown in **Fig. 2.13**. In this experiment, the solution and current density were kept constant and only the descending speed was increased during the slice. The effect of a speed increase is directly visible on the kerfloss value; as expected the kerfloss decreases with an increase in slicing speed. The results for different content of HF at a fixed current density are given in **Fig. 2.14** for ingot of 30 mm in width. A general non-linear decreasing trend with increase of the slicing speed is visible for all HF content. The differences between different concentrations are slightly less evident but a decrease in kerfloss with a decrease in HF concentration is still observable. The lower recorded kerfloss and speed were achieved with concentration of 3% (not shown in the graph, obtained with different conditions). The comparison between the experimental data of kerfloss versus slicing speed at a given current density and the theoretical calculation are discussed in section II.2.4.2.
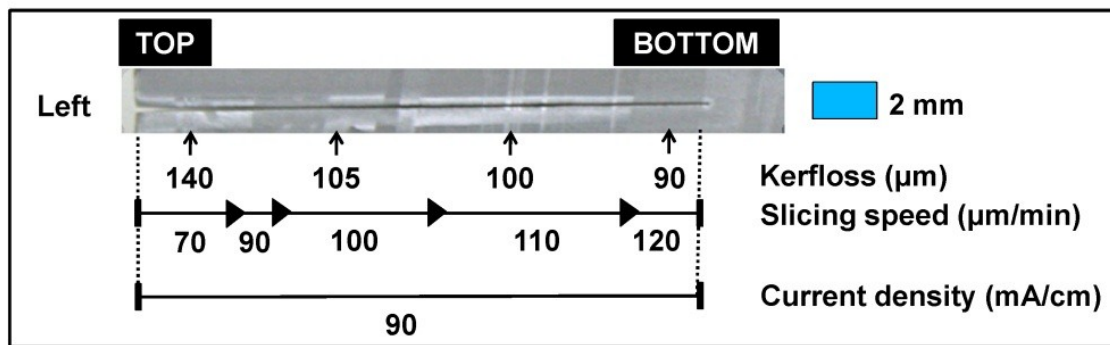
Fig. 2.13: *Variation of the kerfloss in function of the slicing speed. Higher speed produces lower kerfloss but the increase is limited by the overall chemical reaction efficiency. The inability of the electrochemical reaction to follow up with the tool descending speed results in wires breaking at higher speed.*
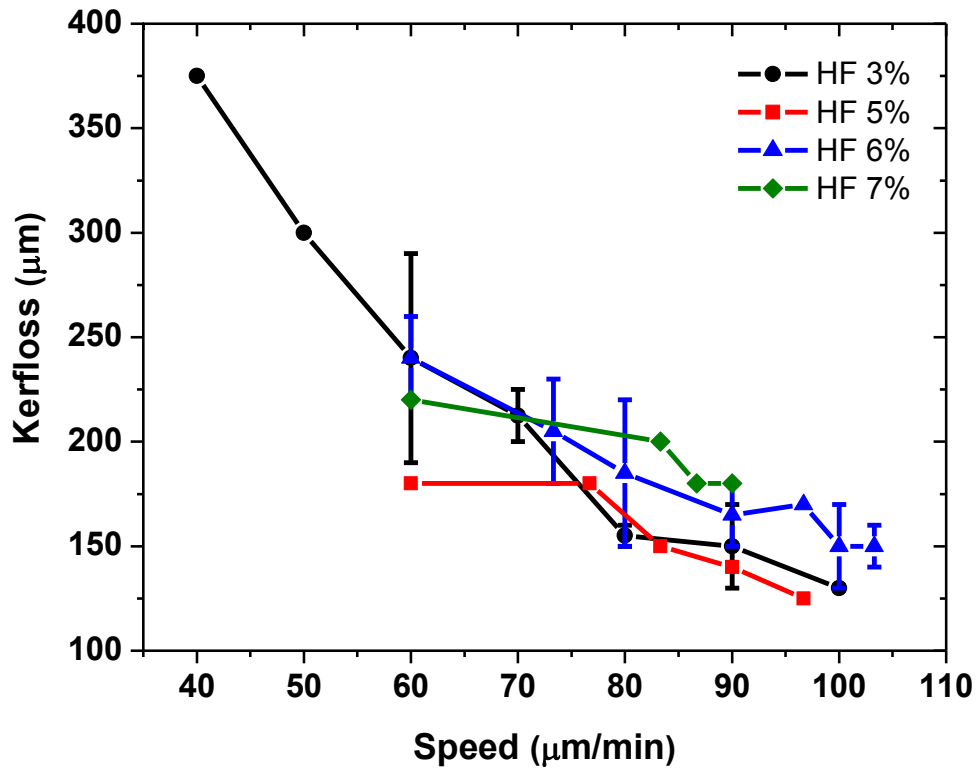
Fig. 2.14: *Experimental summary of the kerfloss variation in function of the slicing speed for HF concentration between 3 and 7%, obtained from 30 mm wide ingot. The vertical lines indicated the variation of kerfloss obtained for the same speed (when available).*

II.2.3.3 Uni and bi-directional flow

Electrolyte injection at the aperture between the wire and the ingot was introduced first with a uni-directional flow from one side of the ingot and then with injection from both sides as schematically represented in **Fig. 2.15**. The experiment was realized on 30 mm wide ingot. Optical pictures of the left and right side of the same kerf clearly show a variation of kerfloss from left to right. The electrolyte being injected from the left side in the uni-directional flow, the left kerfloss is smaller than the resulting kerfloss on the right side. With the introduction of an alternating bi-directional flow, the difference in kerfloss from left to right tends to disappear. Results for experiments realized in the same condition for uni and bi-directional flow and the corresponding effect on kerfloss are summarized in **Fig. 2.16**. On average, introduction of bi-directional flow strongly reduce the kerfloss variation, with an average variation ratio of 0.615 for uni-directional flow to a ratio of 0.853 for bi-directional flow (unity representing an identical kerfloss on both sides).
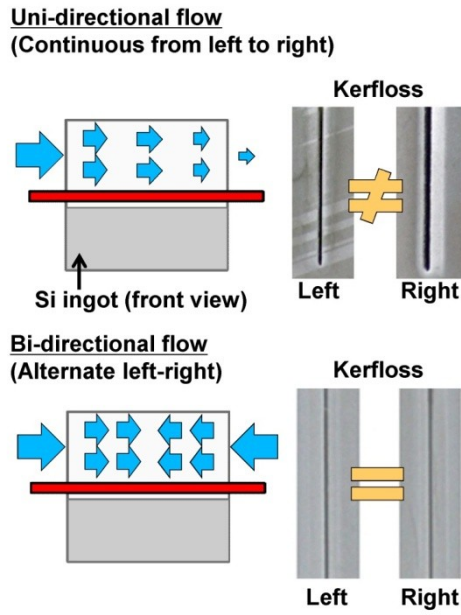
Fig. 2.15: *Schematic of the difference between uni and bi-directional electrolyte flow injection and its direct effect on the kerfloss variation from the two sides of the kerfloss.*

| Sample name | Solution flow | Slicing speed | Kerfloss | | Kerfloss variation Ratio |
			Left	Right	
Reference	Uni-directional (left injection)	100 µm/min	130	200	0.65
		110 µm/min	110	190	0.58
Sample A1	Bi-directional	100 µm/min	130	160	0.81
Sample A2		110 µm/min	130	150	0.87
Sample B1	Bi-directional	100 µm/min	135	160	0.84
Sample B2		110 µm/min	140	125	0.89

Fig. 2.16: *Summary of the kerfloss obtained in the two electrolyte flow modes. Bi-directional flow shows a strong increase in the kerfloss homogeneity between the two opposite face of the silicon ingot.*

78

II.2.3.4 Slicing in potentiostatic mode

Typically, electrochemical etching in silicon can be realized both in galvanostatic and potentiostatic regime. For practical reason, galvanostatic driving mode is usually preferred over the potentiostastic one since the overall electrochemical reaction strongly depends on the total of injected charges. Nevertheless, the possibility of slicing silicon ingot in potentiostatic mode has been demonstrated and a typical set of results is shown in **Fig. 2.17**. Overall, the results of the slice did not shown any drastic differences with the galvanostatic regime but further optimization of the slicing experiments were not conducted due to the lack of advantage over the galvanostatic mode.

Slicing configuration:

wires φ 30 μm / 0.8 mm pitch
Descending speed 60 μm/min
Electrolyte: HF:Ethanol
HF content 6%
Driving potential: 15V
Total slicing time: 300 min

Results:
Slicing speed: 59 μm/min
Kerfloss: 250 μm
Cut depth: 17.6 mm

Fig. 2.17: *Demonstration of a slicing experiment realized in potentiostatic mode.*

II.2.4 Electrochemical reaction efficiency study

II.2.4.1 Practical slicing efficiency estimation

During the slicing process, the entirety of the silicon ingot is immersed in the acidic electrolyte. While the content of HF was kept the lower possible to enhance the locality of the electropolishing phenomena, electrochemical etching actually occurs at various degree on the

entire silicon ingot surface in contact with the electrolyte. The total charge injected during slicing are therefore divided between charges consumed in the vicinity of the cathodic wire and participating directly in the slicing process, and the charges consume at remote location and producing a planar over-etched layer on the surface of the ingot as seen in **Fig. 2.18**. The over-etched edge was measured at the interface between a Teflon coated surface and an uncoated one. The total process efficiency, within the limitation imposed by the valence of the electrochemical reaction, is consequently defined by the ratio of the silicon volume removed through the slicing wire (kerfloss x ingot width x cut depth) and the volume of silicon removed on the whole surface of the ingot. An efficiency study on a practical slice is summarized in **Fig. 2.19**. First, the amount of dissolved silicon by the wires only is calculated and compare to the total amount of electric charge used during the process. Assuming a valence of 4, the efficiency obtained is 63.12%. The result means that around 37% of the injected electric charges do not directly participate in the slicing itself (located around the cathodic wire), but are lost due to the surface over-etching. In a second time, the total volume of dissolved silicon due to over-etching is estimated, using SEM pictures as reference to estimate the thickness of the removed surface. Since the silicon ingot was specially coated for the experiment, the total surface in contact with the electrolyte was well defined. If the total volume of removed silicon, including the effect of over-etching, is taken in account, the valence obtained is around 4.3. This value of valence is well within the reported range for electropolishing mode. The slight overestimation of the valence compare to the theoretical value of 4 could be due to a underestimation of the dissolved silicon volume in our calculation, where we assume that the over-etching produce a homogeneous etch depth of 100 μm on all the ingot surface.
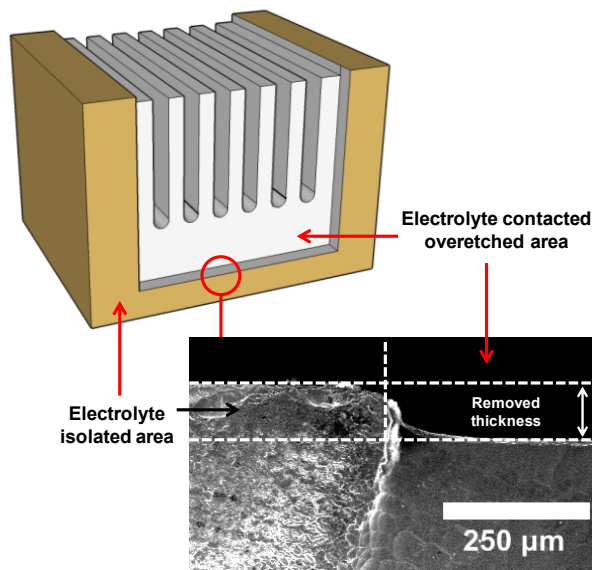

Fig. 2.18: *Illustration and SEM micrograph taken at the surface of a silicon ingot between a coated and uncoated region showing the effect of over-etching.*

Experimental efficiency estimation

- Total slicing current: 200 mA
- Slice duration: 329 min
- 6 wires configuration

- 3 mm wide ingot
- Cut depth: 27 mm
- Average Kerfloss: 160 μm

I.   Electric charge calculation

1C = 6.24E18 e

Current	Duration	Total charge	Number of elementary charges
0.2 A	19740 s	3948 C	2.4636×10^{22} e

II.   Dissolved Silicon volume estimation

Volume for 1 wire. Avogadro constant: 6.022E23

Width	Depth	Kerfloss	Volume		Number of atoms
0.3 cm	2.7 cm	0.016 cm	0.01296 cm^3	0.001076 mol	6.4777×10^{20}

Total volume (for 6 wires): $V = 6 \times 6.4777 \times 10^{20} = 3.8867 \times 10^{21}$ Atoms

III.   Efficiency estimation

Assuming a valence of 4

N = Number of Atoms dissolved / (Total of electric charge / Valence)

N = $6.4777 \times 10^{20}/(2.4636 \times 10^{22}/4) = 0.6312 =$ **63.12%**

IV.   Confirmation of the valence value

- Volume dissolved by wire slicing:
  $V_1 = 3.8867 \times 10^{21}$ Atoms
- Volume dissolved due to surfacial over-etching V_2:

Uncoated top surface $S_{top} = 0.3 \times 0.6$ cm^2

Uncoated side surface $S_{side} = 0.6 \times 3$ cm^2

Over-etching depth estimated from SEM pictures: 100 μm

Total volume dissolved by over-etching:

$V_2 = 0.3 \times 0.6 \times 0.01 + 2 \times (0.6 \times 3 \times 0.01) = 0.0378$ cm$^3 = 1.8893 \times 10^{21}$ Atoms

Total volume dissolved during the experiment:

$V_{total} = V_1 + V_2 = 5.776 \times 10^{21}$ Atoms

Valence estimation:

n = (Total of elect. charge)/(Total of dissolved mat.) = $2.4636 \times 10^{22} / 5.776 \times 10^{21} =$ **4.2652**

Fig. 2.19: *Calculation of the overall slicing efficiency based on the total dissolved silicon material measured on a Silicon ingot after slicing.*

It is of importance to note that the efficiency here is not related directly to the electrochemical reaction and its controlling parameters (HF concentration, density of injected charges etc...) but by the total surface of bare silicon in contact with the electrolyte and the geometry of the ingot. A decrease of the unprotected silicon surface would dramatically increase the overall efficiency of the process. In a practical slicing configuration, all the ingot length would be sliced at once, therefore eliminating the need to protect uncoated surface. However, over-etching would actually still occur on all surfaces in contact with the acidic electrolyte, including the surface of freshly sliced wafers.

II.2.4.2 Theoretical efficiency estimation

In the electropolishing mode, under galvanostatic regime the electrochemical dissolution rate is constant. As previously discussed, the valence of the reaction, the ratio of electric charge used and the number of dissolved atoms, has been estimated to be 4. Since the reaction rate is fixed and if we consider that the total charge used during the electrochemical slicing are all used for the material dissolution (no "leak" path, no extra chemical reaction, no evolution of the chemical process and chemical species overtime etc..), we can therefore easily estimate the volume of Silicon dissolved per second and by fixing a volume related parameters such as the kerfloss, it becomes possible to estimate the slicing speed versus kerfloss (and vice-versa) of the process for a given injection current.

In the following calculation, we consider the wire as a 1 dimensional object (the kerfloss is negligible compare to the slicing width) and the current is expressed in A/cm (A per length unit). For a given current I, we have $6.241 \times 10^{18} \times I$ elementary charge injected per second. Since the valence of the reaction is 4, we are therefore dissolving $1.5604 \times 10^{18} \times I$ Silicon atoms per second. The Silicon density of 28.086 g/mol and 2.33 g/cm^3 indicates that 1 cm^3 contains 5×10^{22} Si atoms or 1 atom of Silicon occupies a volume of 2×10^{-23} cm^3. We consequently obtain the dissolution of $3.121 \times 10^{-5} \times I$ cm^3 per second. Looking at the volume definition V= Depth x Kerfloss x Width in cm^3 and equating the volume equation with the volume of dissolved atom per second obtain previously, we can directly express the kerfloss in function of both the current and the slicing speed as follow (the A/cm of the current unit is solved with the volume width in cm):

$$\text{Kerfloss} = \frac{3.121 \times 10^{-5}.\,I}{\text{Speed}}$$

with I in ampere and the speed in cm/s.

The resulting simulation results for four different current densities are shown in **Fig. 2.20**. The values shown here represent the upper possible values for the slicing speed. In order to obtain higher performances, a modification of the intrinsic properties of the chemical reaction would be required to obtain a reaction valence higher than 4 which is the main limiting factor of the slicing process. Several experimental data are plotted together with the theoretical curves in **Fig. 2.21**. For this estimation, the kerfloss variation in function of the slicing speed at a fixed current density obtained from experiments on 50 mm ingots were used for comparison with theoretical values. The experimental conditions were a HF content of 4% at a current density of 100 mA/cm. The table indicates the theoretical and experimentally obtained kerflosses for three different slicing speeds. The experimental values of the kerfloss are actually quite lower than the calculated value, indicating that the totality of the current was not used directly to produce the kerf. Indeed, the intersection between the positions of the experimentally obtained kerflosses with the corresponding speed gives a current slightly higher than 60 mA/cm for the three different speeds. The difference in practical and theoretical current is approximately 35%, in concordance with the 37% value estimated in section II.2.4.1 for the over-etching. A decrease in the volume of silicon dissolved by over-etching would allow for higher slicing speed: assuming the same condition of 100 mA/cm and a kerfloss of 100 μm but with an efficiency of 100%, the theoretical speed would be in excess of 180 μm/min compare to the average 100 μm/min obtained currently with an efficiency of 63%.
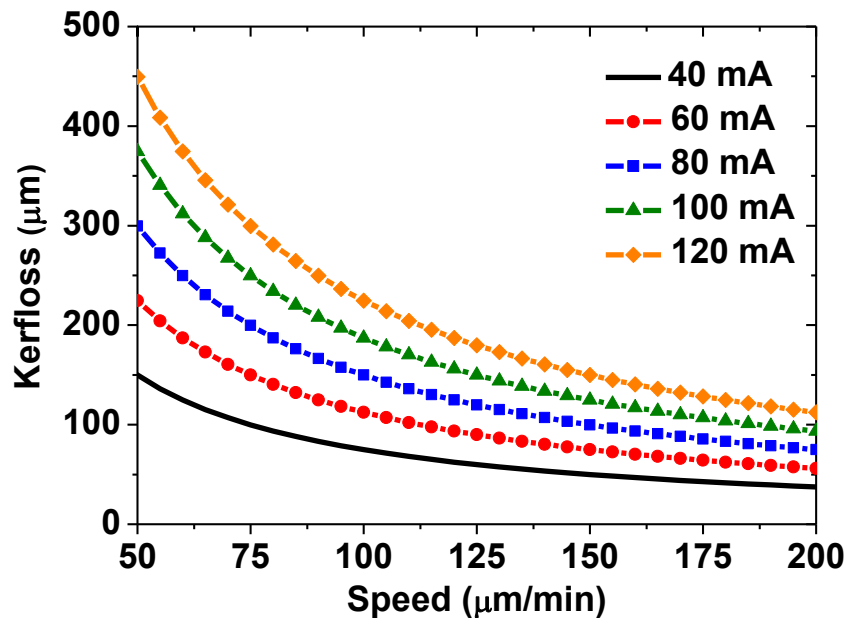
Fig. 2.20: *Theoretical estimation of the kerfloss in function of the slicing speed and the slicing current. The simulation basically assumes an electrochemical reaction with a valence of 4.*
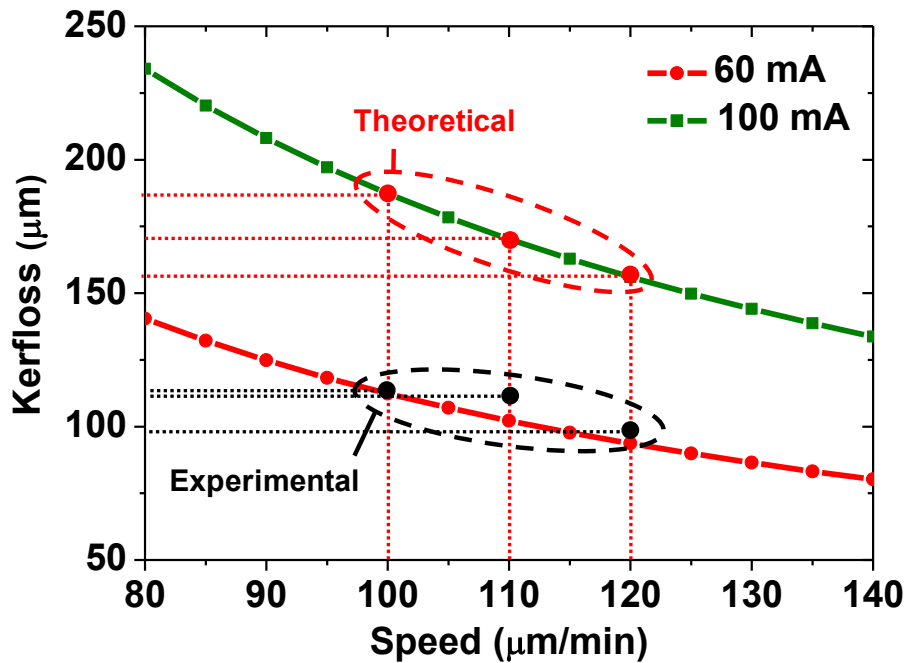
HF 4% - 100 mA		
Speed (µm/min)	Kerfloss (µm) Experimental	Kerfloss (µm) Theoretical
100	109	187
110	108	170
120	98	156

Fig. 2.21: *Comparison of experimental and simulated data for a slice realized at HF 4% under 100 mA. The experimental data at 100 mA point to a practical efficiency corresponding to theoretical value obtained at a current of around 60 – 65 mA, in accordance to our own calculation of an efficiency of ~65%.*

II.3 Concurrent approaches overview and conclusion

II.3.1 New approaches overview

To answer the increasing demand on thin wafers and to support the various project roadmaps to ultra-thin wafering, a wide variety of concurrent slicing solutions based on multiple approaches have been proposed and experimentally demonstrated by different groups in parallel to our own electrochemical slicing process. The simplest and easiest approach consists of enhancing the current wire saw based technology with a strong focus on wires material. The current trend in wire sawing is the slow but progressive move to diamond coated metallic wires which despite

higher cost, enhance the slicing capability of the wire saw technique while keeping all the previous advantage and knowledge of the technology accumulated over the past decades. In parallel to this classical approach, several new concepts were recently proposed and are currently under investigation. Such concepts include plasma etching, new methods of thin foils exfoliation using mechanical crack propagation or impurity implantation induced cleaving as well as Electric Discharge Machining (EDM). These new concepts and their advantages and limitations will be rapidly presented in the following sections.

II.3.2 Plasma based slicing

The plasma slicing system is based on the local dry etching of silicon. The ingot is placed in a closed chamber filled with a silicon etchant gas (nitrogen tri-fluoride or SF_6)[2][3] and a plasma is created between the silicon ingot surface and an blade shaped copper electrode. Etching of silicon proceeds at the surface of silicon and the position of the blade is controlled, descending toward the silicon ingot. The concept is basically similar to our electrochemical slicing system, the HF electrolyte being replaced by a gas and the metallic wire by copper blades. The available results of plasma etching confirms the possibility of producing trench in silicon but are limited to small section and low depth slicing. The capability of the process to slice efficiently in multi-blade mode still has to be demonstrated.

II.3.3 Electric discharge slicing

Electric discharge machining (EDM) is actually a rather old technology which has been recently investigated for silicon ingot slicing as well, in the form of Wire EDM (WEDM). In such process, the slicing tool is a metallic wire located at a small distance from the silicon ingot. The space between the two electrodes (metal wire and silicon ingot in the case of ingot slicing) is filled with a dielectric liquid, most commonly de-ionized water. When a high electric voltage is applied between the two electrodes, breakdown occurs and the electric discharge between the wire and the silicon surface removes the material locally. The process features good surface quality and high slicing speed (> 600 μm/min) but is limited to the slicing of single wafers at a time so far [4][5]. The efficiency of the process is also strongly dependent on the resistivity and purity level of the material.

II.3.4 Silicon exfoliation

The slicing processes presented so far are all rather similar in concept, they use a physical tool (as a wire or a blade) to remove silicon, the physical phenomena involved in the removal of the material being different (mechanical, electrochemical, electrical etc…). The silicon exfoliation concept uses a completely different approach. The group of IMEC [6] proposed a mechanical exfoliation system where a crack parallel to the silicon surface is created and mechanically propagated along the ingot surface, resulting in a thin foil of silicon peeled from the original ingot. The crack is created by the deposition of a metallic layer (with a screen printing technique) at the top of the silicon ingot and followed by annealing at high temperature. During cooling of the material, thermal expansion mismatch between the metal layer and the silicon material creates a crack near the silicon surface. The upper layer is then completely separated from the silicon ingot and the metal is etched away chemically resulting in a thin foil of silicon material with a thickness of 30-50 μm. Few information are available concerning the practical performance of the process, including the crack propagation speed and the fact that the system can be used only for sequential single wafer exfoliation. The process is also apparently kerfless.

A slightly different approach has been under development at SiGen [7][8], where cleaving of the ingot upper layer is induced by first implanting a hydrogen layer at a predetermined depth inside the silicon ingot creating a stressed cleave layer. The separation is induced at the implanted layer, resulting in thin layers of Si material cleaved out form the ingot surface. Wafers with a thickness of 50 μm are achievable without material loss but similarly to the process developed at IMEC, the system does not allow for the cleaving of several wafers at a time (as of May 2011, implantation of up to 64 cleaving layers at a time has been reported. The separation of the Si foil seems to still be a one by one process, see reference [9]).

II.4 Conclusion

The general characteristics of all previously presented slicing processes are summarized in **Table 2.4** and compare to our own proposed electrochemical slicing solution. While most of the presented slicing solutions are quite different in concept and approach to slicing, from the overall available performance summary and state of advancement of the technology, the proposed solutions can be roughly divided into two groups. The first group concerned the solutions which are still at the proof of concept level. Such technology includes the plasma etching and to a less extent the IMEC cleaving technology. While both have shown their capability to produce kerf in silicon ingot, the lack of experimental data on multi blade slice,

deep section trenching for the plasma etching and the lack of information about the overall processing speed performance of IMEC's cleaving solution clearly shows the low advancement of the technologies toward practical and industrial use. On the other hand, technologies such as WEDM and of course diamond wires sawing already benefit from their maturity as commercial process and years of experience from the industry. The single wafer limit of WEDM process is somehow compensated by is high slicing speed already on par with classical wire sawing. SiGen wafer cleaving technology also shows far more advanced results than its kerfless slicing counterpart and better ability to scale to parallel wafer slicing. The electrochemical slicing process, from a point of view of performances and ability to slice relatively deep trenches in multi-wire mode clearly shows that the process has clearly passed the stage of proof of concept and its superior slicing ability compare to competing plasma etching for example.

Further improvement are still obviously necessary to make the electrochemical etching process competitive in regard of its more advance wire saw competitors, especially in terms of slicing speed. The electrochemical process is inherently limited by the chemical reaction holding a valence of 4, fixing the upper limit for maximum efficiency. There is still a lot of space for improvement both in term of slicing system design and chemical reaction improvement. The scaling to a larger number of wires does not seem to be an obstacle for the electrochemical process. Scaling to industrial size of the system, including higher performance electrolyte circulator with higher flow rate as well as pumping in fresh electrolyte and pumping out the used HF species might actually improved the overall performance of the process. Further investigations are also required, in terms of temperature control effect on the electrochemical reactions, substituting the base chemical solution with different type of solvents as well as the possibility of mixing chemical additives. The number of solutions for the electrochemical slicing system improvements are numerous and easily implementable at an industrial and practical scale. The limiting factor for silicon slicing improvement will, independently of the physical process used, be the economical aspect of the process, as the simplest process with few control parameters will always be favored compare to most complex and demanding ones.

Name	Mitsubishi Electric [5]	National Taiwan University [4]	Toyo Advanced technologies / AIST [2]	Nagoya Univ. Meijo Univ. Nu-Eco Eng. AIST [3]	IMEC [6]	This study	SiGen Polymax [7]	Diamond Wire material (Meyer-Burger) [10]
Type	EDM	EDM	Plasma etching	Plasma etching	Exfoliation	Electrochemical etching	Exfoliation	Grinding
Wafer thickness (µm)	200	250	No wafer slicing reported	≥ 12 No wafer produced	$30 \sim 50$	≥ 200	150-50-20	180
Kerfloss (µm)	250	280-290	120–150	300	NA, potentially kerf free	130	Kerf free	150
Speed (µm/min)	266	635	60	31	NA, apparently slow process	110	NA (~10s/wafer)	~ 700
Parallel slicing	×	×	×	△	×	○	△	○
Status	Development	Development	Development	Development	Development	Development	Development	Commercial
Date of publication	02/15/2007	2003	11/01/2008	2008	07/15/2008	2010	March 2009	2011

Table 2.4: *Comparison of different approaches to silicon wavering*

Bibliography of Chapter II

[1] V. Lehmann, Electrochemistry of Silicon: Instrumentation, Science, Materials and Applications, Wiley-VCH Verlag GmbH, Weinheim (2002).

[2] M. Yamaguchi, Y. Abe, A. Masuda, M. Kondo, Solar Energy Mater. & Solar Cells **93**, p. 789 (2008) - dx.doi.org/10.1016/j.solmat.2008.09.052

[3] T. Ideno, H. Inui, S. Takashima, H. Kano, M. Kondo, M. Hiramatsu, and M. Hori, Jap. J. of App. Phys. **47** (7), p. 5648 (2008) / http://dx.doi.org/10.1143/JJAP.47.5648

[4] W.Y. Peng, Y.S. Liao, Journal of Materials Processing Technology **140,** p. 274 (2003).

[5] Mitsubishi Electric, Newsletter No.0704 (2007). Retrieved on 2013/10/11 at: http://www.mitsubishielectric.co.jp/news/2007/0215-c.html

[6] IMEC, IMEC news, SEMICON WEST 2008, San Francisco, California. Retrieved on 2013/10/11 at:

http://www2.imec.be/be_en/press/imec-news/archive-2008/imec-reports-new-promising-method-to-fabricate-ultra-thin-silicon-solar-cells.html

[7] Silicon Genesis Corporation, PolyMax™ Enhanced Thin PV Wafers Technology, product brochure (2008).

[8] F. Henley, Kerf-less wafer production, Photon's 4th PV Production Equipment Conference, Silicon Genesis Corporation (2009).

[9] A. Fujisaka, S. Kang, L. Tian, Y-L. Chow, A. Belyaev, Implant-Cleave Process Enables Ultra-thin Wafers without Kerf Loss, RenewableEnergyWorld.com (2011), retrieved on 2013/10/11 at:

http://www.renewableenergyworld.com/rea/news/article/2011/05/implant-cleave-process-enables-ultra-thin-wafers-without-kerf-loss

[10] Diamond Wire Photovoltaic Applications, Diamond Materials Tech, Inc, MeyerBerger group, retrieved on 2013/10/11 at:

http://www.meyerburger.com/fileadmin/user_upload/diamondwiretech.com/factsheets/DW_PV_1204LD_Fctsht_01.pdf

Chapter III.   Experimental methods

III.1 Fabrication of free-standing porous silicon layers

The typical process flow used for the fabrication of the nc-PSi devices is shown in **Fig. 3.1**. The process is basically divided in three sections, the pre-anodization preparation of the substrate common to all devices, the anodization itself, and finally the post-anodization processing. Each step of the process flow will be rapidly described in the following sub-sections. The core processes shown in **Fig. 3.1** are the key steps in controlling the resulting characteristics of the material, including the anodization parameters, the nature of the post-anodization treatments of the devices and the structures and materials used to contact the nc-PSi layers. Since the fabrication of nc-PSi from p and n substrate is already widely documented, the following sections will assume that the substrate used is of pn type.
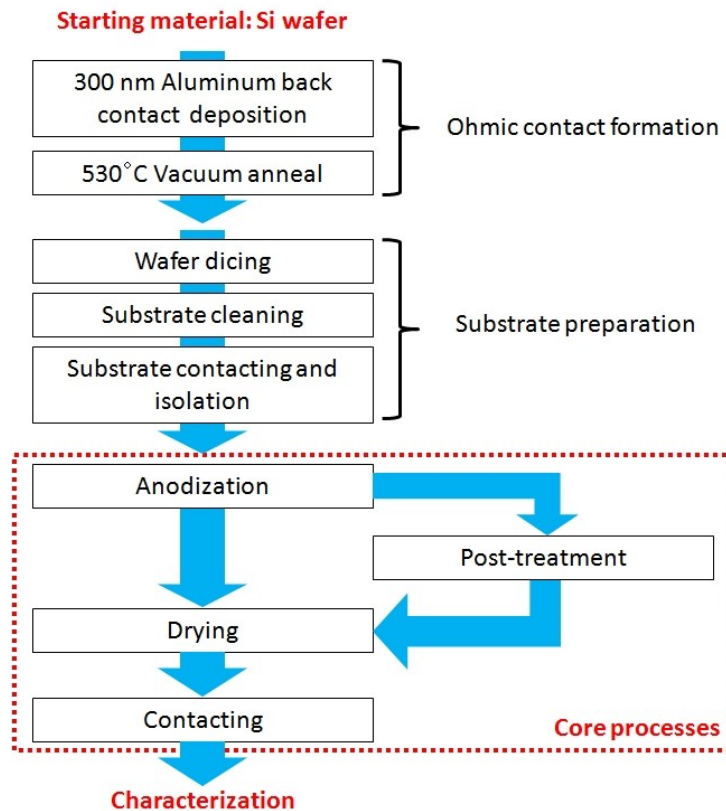

Fig. 3.1: *Process flow for the fabrication of free-standing nc-PSi layers.*

III.1.1 Experimental fabrication procedure

III.1.1.1 Substrate preparation

The devices presented here were made from high quality microelectronic grade silicon wafers with a (100) crystal orientation. The wafers were back-deposited with a 300 nm thick aluminum film by vacuum deposition before being vacuum annealed at 530°C during 1 hour to form an ohmic contact. The wafer were then sliced into small square pieces of 1.6 x 1.6 to 2 x 2 cm^2 and then cleaned in a pure acetone bath at room temperature under ultra-sonification during 20 min followed by a boiling pure ethanol bath during 20 min as well. The samples were then blown dried under a N$_2$ gas flow. Back contacting was realized by applying a thin ribbon of copper onto the Al deposited back surface of the samples. Isolation of the back contact from the electrolyte was realized by covering the whole surface of the sample by PTFE tape, except for a window cut on the top surface of the silicon sample, defining the anodization window area. Typical size for the anodization window was 1.4 x 1.4 cm^2. For the pn type substrate used in this study, the description of the material is given in Appendix B.

III.1.1.2 Electrochemical formation condition

All the devices presented here were fabricated using an electrochemical cell similar to the setup introduced in chapter I. The anodization was conduct as is at room temperature without electrolyte circulation. An external illumination source (front illumination) was used in the case of n and pn type substrate in order to obtain nanoporous material. The light source was fixed at an approximate height of 20 cm resulting in an illuminance of 8000 lx at the wafer surface. The light bulbs used were flood type Iwasaki Eye lamp with a color temperature of 5900K (equivalent to a black body radiation centered at 490 nm) and electrical power rating of 500W. The incident powers as well as the spectrum of the illumination have a noted effect on the resulting characteristics of the material.

The anodization was conducted under galvanostatic regime with current density in the range 5 to 50 mA/cm^2. Typical anodization duration for pn type substrate was 900 s, with the first 450 s under illumination. Illumination is necessary especially at the beginning of the process when the substrate is still in reverse polarization leading to high terminal potential without photo-assistance. At the end of the 900 s of formation, a particular current pattern is applied to the substrate to provoke the separation of the upper nc-PSi. The process of separation will be discussed in more detail in section III.1.2. A typical I-V anodization characteristic is shown in

Fig. 3.2. The overpotential due to the presence of the junction in reverse polarization is visible during the first 60 s of the anodization. The successful separation of the nc-PSi layer is indicated at the end of the graph by an abrupt decrease in potential. Typical values used to produce nano-crystalline PSi as well as the conditions for separating the PSi layers in function of the substrate type are listed in Appendices C and D.

After fabrication, the samples were rinsed in three successive bathes of pure ethanol and kept as in ethanol until the following drying step.
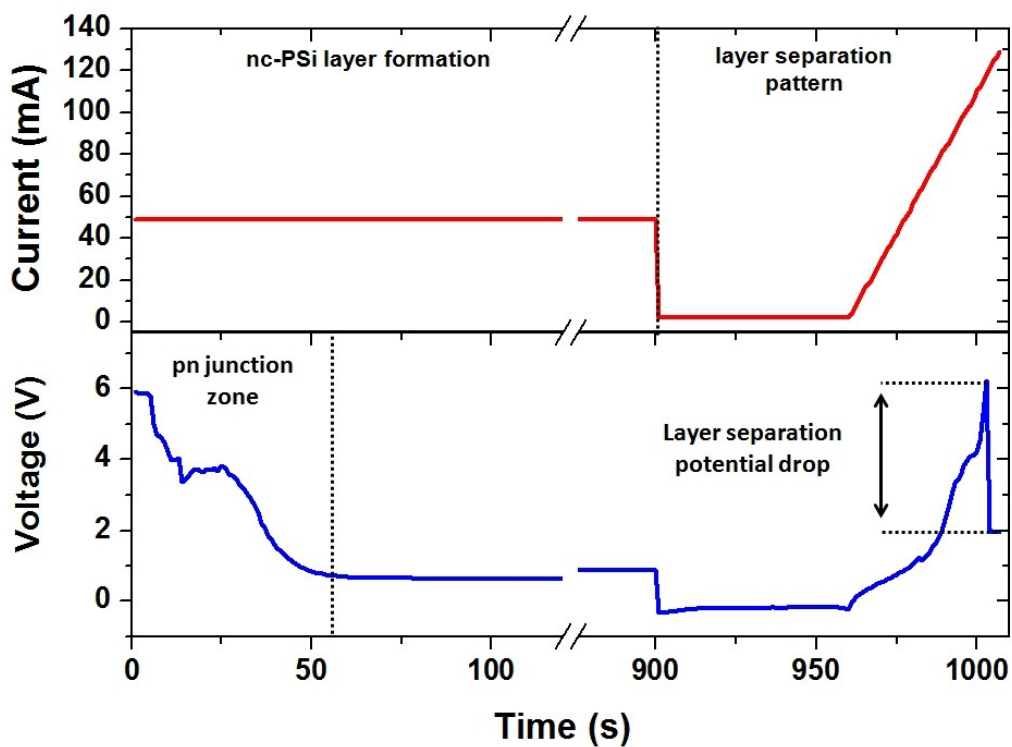

Fig. 3.2: *Typical I-V characteristics during formation of a nc-PSi layer from pn type material. The junction overpotential is visible at the beginning of the process while at the end of the formation the strong decrease of potential indicates the successful separation of the layer.*

III.1.1.3 Post-processing

III.1.1.3.1 Drying

After the rinsing stage, the samples were directly transferred from their rinsing bath into a supercritical dryer chamber filled with ethanol while avoiding drying in air. The supercritical liquid used here was an ethanol/CO_2 mixture at a temperature of 40°C under a pressure of 14 MPa to achieve super-criticality. The total drying process time, including the rise time to criticality and total purge of the gas in the chamber was 50 min. While not strictly necessary in the case of moderately porous material, the super-critical drying method strongly decrease the wreckage of nc-PSi free standing, especially in the case of p type material (porosity of around 65-70%) or large area layers, maintaining the integrity of the film in comparison to natural drying in air. The use of N_2 flow for controlled drying is not applicable to free-standing layers due to the fragility of the material. Alternatively, drying using pentane as the last rinsing solvent also helped preserve the structural integrity of the films.

III.1.1.3.2 Contact fabrication

Fabrication of the contact was realized by vacuum evaporation of a metal, Au or Al, onto the nc-PSi films through a metallic mask. The common masking sizes include square mask of 0.6 x 0.6 cm^2, 0.8 x0.8 cm^2, rectangular mask of 0.25 x 0.5 cm^2 or circular mask of 0.5 cm in diameter. For PV characterization, free-standing membranes were contacted in a sandwich configuration with a 300 nm Al layer as a back contact and a 10 nm semi-transparent Au film as a top contact. In parallel to Au, ITO was also employed as a top and back contact, deposited at 100W / 11 min under Ar/O_2 flow in a 200/1.5 sccm ratio, resulting in a ITO film of around 70 nm. The 10 nm thin Au and 70 nm ITO films transmittance spectra are shown in **Fig. 3.3**. Effects of the nature of the contacting material and structure on the photo-electrical characteristics of the devices are discussed in chapter IV section IV.2.2.4. On top of the contacting layer, a small 1.5 mm circular contacting pad of Al (300 nm) was deposited to provide higher mechanical support for the external contacting probes. The different contacting structures used in this study are summarized in **Fig. 3.4**.
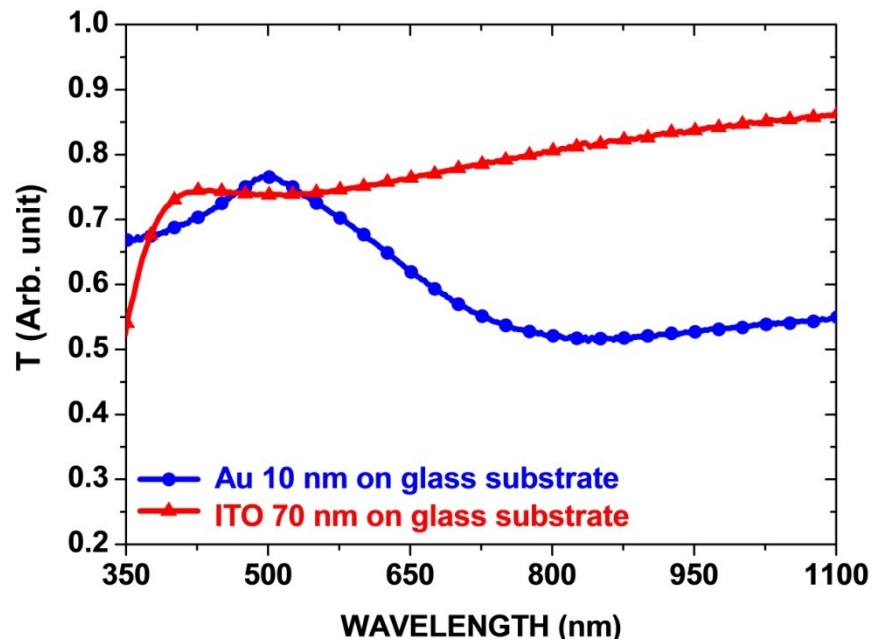
Fig. 3.3: *Transmittance spectra for a 10 nm thick Au and a 70 nm thick ITO film deposited on a glass substrate. The two material are used as a top contact in free-standing nc-PSi devices.*

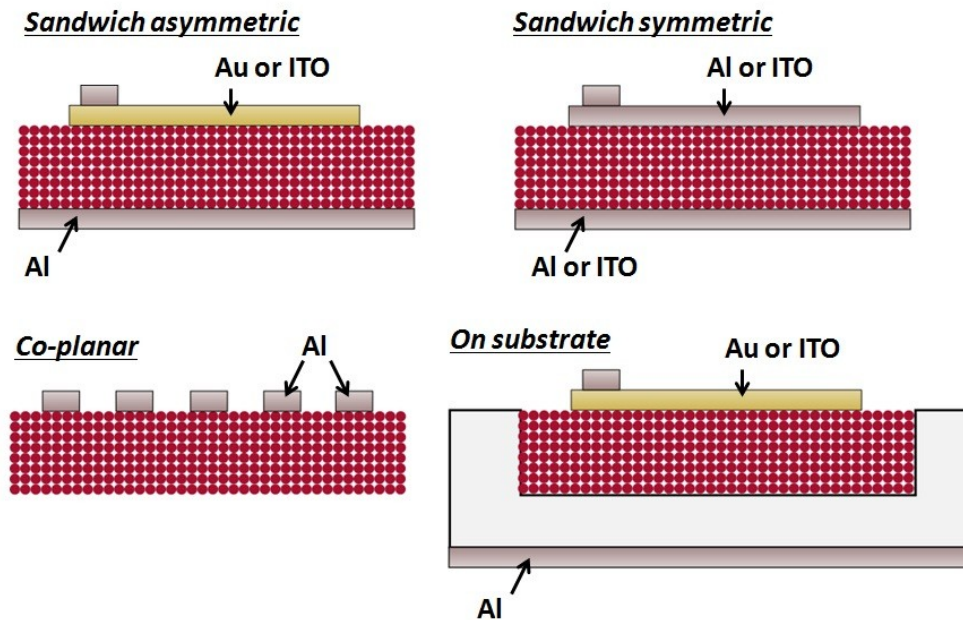**Fig. 3.4:** *The different structures used to investigate the conduction properties of nc-PSi layers in function of the different contacting materials. Co-planar configuration was used only to assess the surface homogeneity of the material.*

94

III.1.1.3.3 Surface chemical modification

Surface chemical modification of PSi (sometimes called surface derivatization) has been reported with a large range of passivating material and techniques [1][2][3][4][5]. The most common and easy to implement method is based on a low thermal budget hydrosilylation of the large material surface. The technique consists of replacing the highly hydrogenated PSi surface (hydrogen coverage > 99% for freshly fabricated material) with organic mono-layers covalently bonded through Si-C or Si-O-C bonds. The resulting surface after modification is largely covered with the long organic molecules attached to the surface as shown schematically in **Fig. 3.5(a)**. Covalent bonding can be obtained either through direct thermal route or by using a catalyst assisted chemical reaction. Derivatization can also be obtained though light irradiation, but in the case of PSi it requires that the host material is luminescent enough, the reaction being triggered at the surface of Si by its intrinsic luminescent emission and not the external excitation [6]. For practical reasons, the simple thermal route will be privileged in the case of PSi for its ease of implementation.
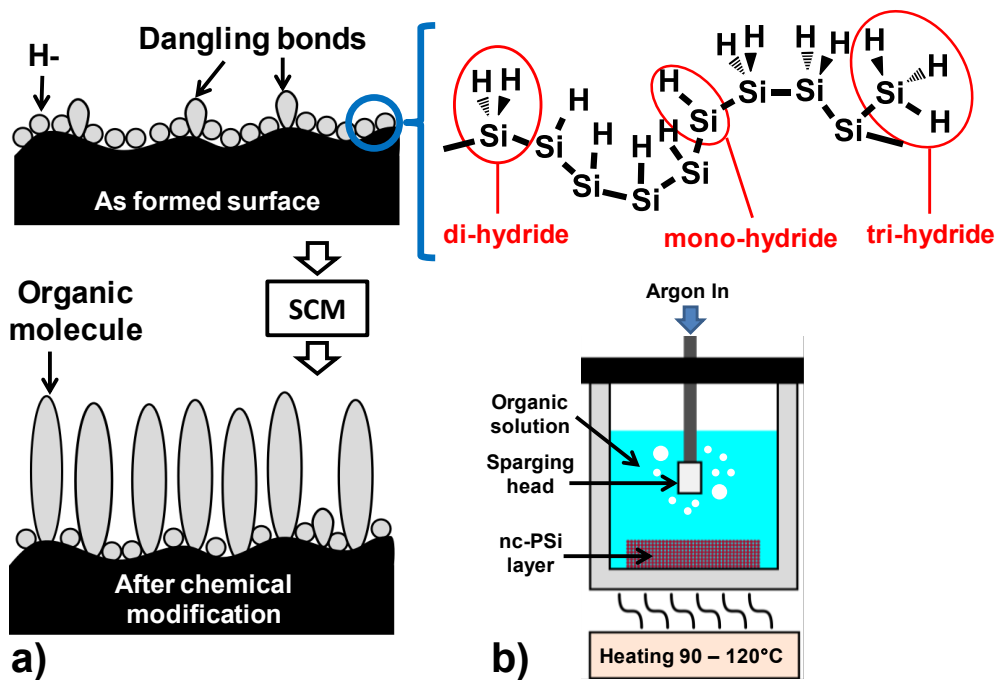

Fig. 3.5: *a) Schematic representation of an as fabricated PSi surface with both hydrogen and dangling bonds represented, at the right a zoom-in view at the surface showing the different possible Si-H$_x$ bonding configuration, (b) Schematic of the surface modification process including bubbling of an inert gas in the solution to remove diluted oxygen.*

Surface chemical modification (SCM) was employed on as-prepared nc-PSi membranes to replace the original hydrogen passivated surface by more stable organic molecules. The expected effects of SCM on nc-PSi are a stabilization of the material characteristics in time and might also involve a modification of its other physical characteristics (mostly undocumented for nc-PSi material so far). The nc-PSi samples are immersed into an organic solution at a temperature in excess of 90°C (reported range of SCM temperature in the literature are 90 to 120°C in general) and kept in the solution for a duration of several hours (from 3 to 12 hours, sometimes longer) as seen in **Fig. 3.5(b)**. The samples are then rinsed in solvent and allow to dry naturally in air.

In order to limit partial oxidation of the material during SCM, the organic solutions were first filtered in a chromatographic column with activated alumina pellets. The solutions were then further cleaned through sparging, where inert Ar gas was bubbled in the solution for at least 2 hours before introduction of the samples in the solution and allow to bubble for the rest of the SCM process. The sparging step eliminates dissolved gas (especially oxygen) from the organic solution, reducing the rate of oxidation on the resulting chemically modified samples. The solvent used for rinsing after SCM were 1-1-1 trichloro-ethane followed by rinsing in heptane. In the case of modification by acrylic acid [7], the samples were rinsed in two successive bathes of chloroform. Due to the strong induction of surface stress on the modified and fragile nc-PSi membranes, especially observed in decene solution, the samples were mechanically constrained between Al mesh holders, maintaining the sample in a flat position while allowing the wetting of the material surface through the mesh structure. The different solutions used in SCM are listed in **Table 2.2** and their corresponding molecular structures are shown in **Fig. 3.6.**

Chemical name	Molecule	Chemical group	Bond type
1-Decene	$C_{10}H_{20}$	Alkene	Si-C
Dodecene	$CH_3(CH_2)_9CH=CH_2$	Alkene	Si-C
Ethyl-undecylenate	$H_2C=CH(CH_2)_8CO_2C_2H_5$	Ester	Si-C / Si-O
Undecylenic Acid	$CH_2CH(CH_2)_8COOH$	Carboxylic acid	Si-C / Si-O
Decanal	$C_9H_{19}CHO$	Aldehyde	Si-O

Table 2.2: *List of organic molecules used for the surface modification of nc-PSi.*

Fig. 3.6: *Simplified schematic representation of the organic molecules used during surface modification of Silicon. The active unsaturated carbon bond used during substitution with surface hydrogen is indicated by a red asterisk for reference.*

The replacement of the surface hydrogen with organic molecules is possible through the substitution of the carbon double or triple bound with the Si-H terminated surface. The unsaturated double carbon – carbon bond present in alkenes lead to a Si-C single bond while aldehydes lead to a bonding through the substitution of the C=O double bond resulting in a surfacial Si-O bond. In the case of species containing both a C=C and C=O bond, it is assumed that both substitution occur in parallel. A schematic representation of the Si surface after substitution with the different possible organic species is shown in **Fig. 3.7**.

Fig. 3.7: *Schematic representation of the Si-H substitution with organic species containing carbon-carbon double or triple bond (Alkene, Alkyne) and oxygen-carbon (Aldehyde) leading to final Si-C or Si-O bonding respectively. Note that in the case of alkyne substitution, different bonding configurations are possible including possible bridge bond with the neighboring silicon atoms (the simple mono-hydrosilylation is shown here).*

97

The exact chemical reaction and process of the thermal hydrosilylation is not completely understood but two basic chemical paths have been proposed, one involving the presence of residual fluoride from the preliminary HF etch (used to produce the hydrogenated surface in flat Si surface and to form PSi), and the second based on the direct nucleophilic attack of the organic species on the hydrogenated Si surface [8].

III.1.2 Separation of the porous layer

The ability to separate the upper nc-PSi layer from the host bulk Si substrate is a key step in the device fabrication process. Separation of the nc-PSi layers is usually achieved by rapidly switching to a higher current density to promote electrochemical polishing at the dissolution front [9], separating the upper nc-Si layer from its substrate as seen in **Fig. 3.8**. Single doped or np doped materials are usually efficiently separated by this simple method, but pn material is more difficult to separate due to the reverse polarization of the material. The injection of a high current peak usually lead to high over-potential and to poor or no separation of the layer at all. Illumination cannot be used during separation of the layer due to the limited penetration depth of light in the material and the necessity to generate hole near the dissolution front at the deepest part of the layer. In such case different type of pattern can be used to help separate the layer in a controlled way and avoiding over-potential at the cell terminal. An example of three different patterns, including the typical current step, is shown in **Fig. 3.8(a), (b)** and **(c)**. Smoother transitions to higher current density using a slowly increasing current slope actually increased the successful separation rate. Further increase of the rate can be obtained by intercalating a low current step before the current slope. In that case, the low current density follow by an increase in current creates two different layers of Psi with different porosities. The strong difference in porosity creates a mechanical stress at the interface helping the layer separation from the substrate.
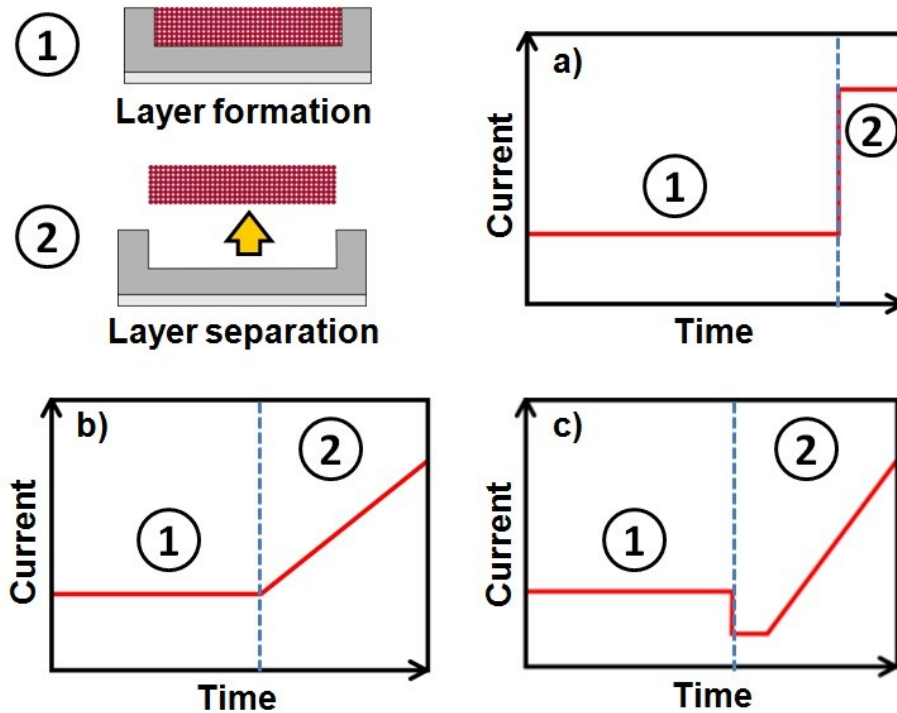
Fig. 3.8: *Process flow for separation of the upper nc-PSi layer from its bulk host. Three different current patterns a), b) and c) were used to increase the separation success rate without damaging the layer.*

As previously introduced, singly doped n and p type material in any doping range, can be separate relatively easily with simple tweaks of the current peak at the end of the fabrication process. As seen in **Fig. 3.9**, during the separation step of single doped p and n type layers, there is no visible potential drop indicating the separation of the layer, indicating that the injection of the current before or after separation of the PSi layers is mostly unchanged, etching proceeding on the underlying bulk substrate surface after separation. In the case of pn type material, after porosification of the pn junction, the cell potential drops to lower potential in a range similar to the expected values for n type material. Since the separation step occurs at the interface between porosified n type and the substrate, the separation should proceed similarly to single doped n type substrate. But the strong increase in the potential during high current injection as well as the strong decrease of the same potential after layer separation actually indicates that the porosified pn junction of the original substrate is still electrically active and appears to prevent the correct injection of current during the separation step, even after porosification of the material.
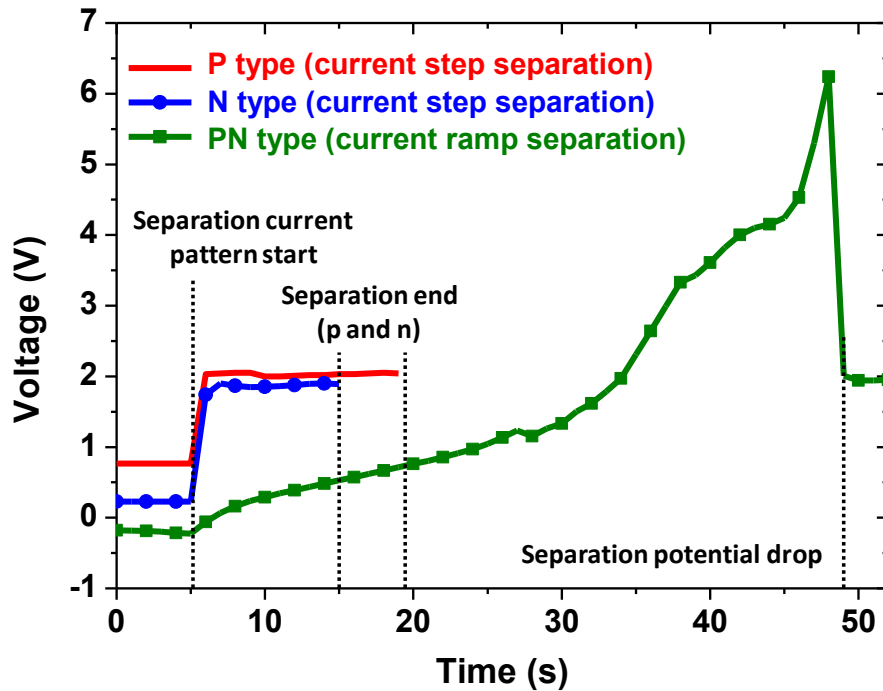
99

Fig. 3.9: *Comparison of the anodization cell potential during separation between p, n and pn type materials where all layers where successfully separated. Only in the case of pn type material a strong decrease in the potential indicates the success of the separation.*

The success of the layer separation appears to be strongly dependent on the layer thickness as well. For pn type substrate, the typical thickness used in this study was about 30 μm. Attempts at decreasing the thickness through decrease of the anodization duration lead to a strong increase in separation failure rate. Below around 25 μm, the layers start to peel in a strongly inhomogeneous manner with small 1 to 2 mm in diameter spots being separated while the rest of the layers remains attached to the substrate. Increase in the terminal current step used for separation lead to an etching of the surface of PSi instead of the separation of the layer. The same observation was made for n+ substrate, which were successfully separated under classic conditions until reaching a thickness of around 15 μm. The different observed steps of the separation of a PSi layers are shown in **Fig. 3.10** for pn type material. The schematic was deduced from observation of the separation state of the layer after both successful and failed separation at different degrees. First, notable circular pattern are visible on the remaining Si substrate after separation and the same pattern is visible as well at the back of the free standing nc-PSi layers. The pattern is also visible on the top of the layer to a lesser extent. The origin for the appearance of such pattern is currently unknown. After careful observation of three different anodization sites formed atop a unique circular wafer, it appears that the circular lines are

actually running parallel to the outer diameter of the wafer as shown in **Fig. 3.11**. After observation of nc-PSi layers after a failed separation attempt, it clearly appears that the separation starts randomly along these same circular lines, first as small spots of a few millimeters then expanding along the line to form a larger separated area, finally covering all the surface of the anodized substrate. The separation phenomena also appear to start from the center of the sample and progressing toward the edges of the layer. Even after a successful separation, the nc-PSi layer remains weakly connected to the substrate at the edges and requires to be further mechanically separated. The appearance of radial patterns was observed on n+ type as well but not on p type material.
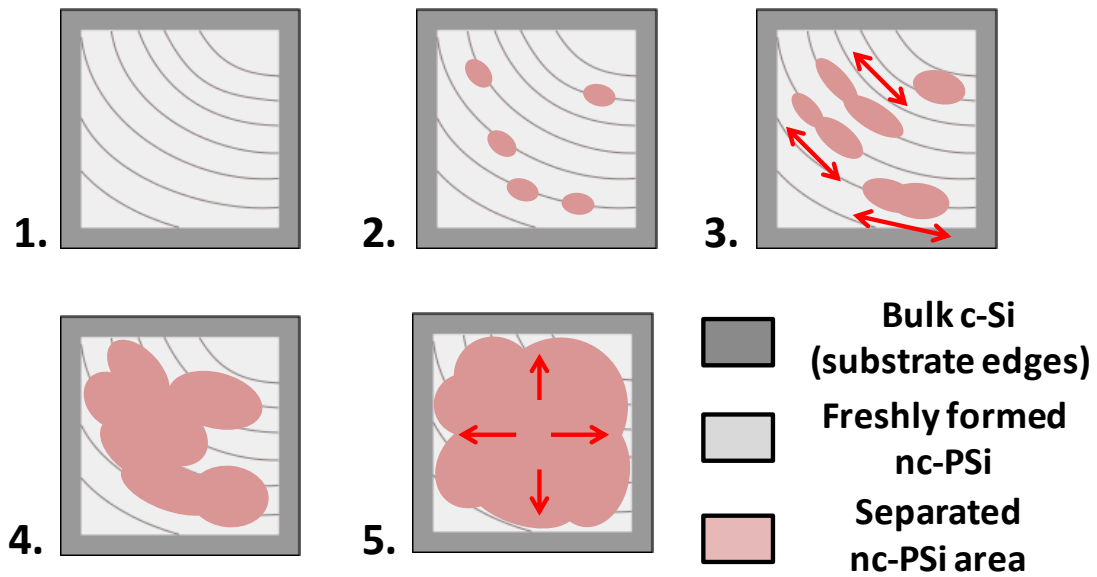

Fig. 3.10: *The different proposed steps occurring during the mechanical separation of the pn type nc-PSi layers.*
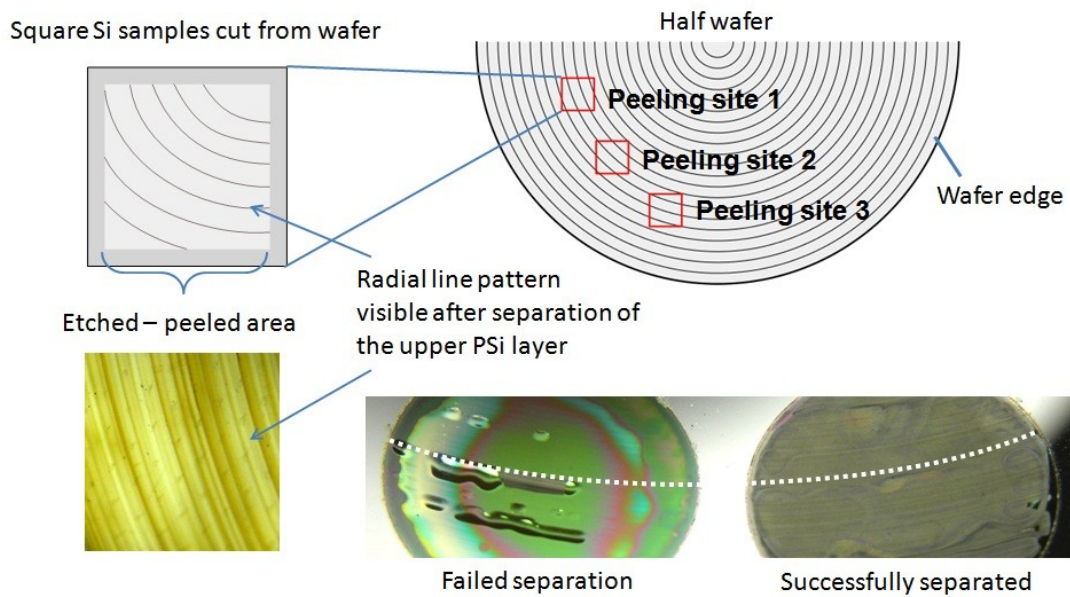
Fig. 3.11: *Example of the radial lines present at the surface of separated layers and wafers. The lines are running parallel to the radius of the wafer and appear to be the starting dislocation point for the separation of the layers.*

From the previous observations, it is clear that the separation of nc-PSi layers depends not only on the ability to induce electro-polishing at the dissolution front but may be strongly dependent on the structural properties of the nc-PSi layers as well (porosity and thickness). Since the control of the separation current intensity and the pattern duration and shape have a limited effect on the success rate, further control parameters are needed to fabricate and separate successfully thinner layers of the material. The possible parameters are schematically represented in **Fig. 3.12**. From early electrochemical investigation of the characteristics of Si in HF based solution [10], it was demonstrated that the electropolishing current threshold J_{ps} was strongly dependent on the HF content and the overall viscosity of the solution. The summary of the effect of the parameters variation on J_{ps} are summarized in **Table 2.3**. A reduction of the required current value can be achieved with decreasing the HF content or by increasing the viscosity of the solution, either by decreasing the temperature or by using a viscous additive such as glycerol. Glycerol will replace a percentage of the original solvent (ethanol) to increase the overall viscosity of the solution. A minimum volume of ethanol is still required for efficient wetting of the material and rapid elimination of hydrogen gas bubbles during anodization. In addition to lowering the current requirement for electropolishing, increase in viscosity also show a modification of the PSi/c-Si interface featuring smoother surface at higher viscosity level [11][12].
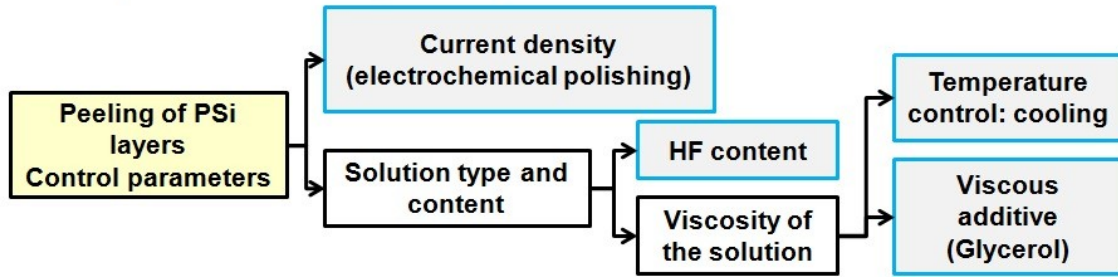
Control parameters during film separation:

Fig. 3.12: *Schematic of the possible routes to help separate thinner layers of nc-PSi material.*

Parameter	J_{ps}
HF content ↘	↘
Temperature ↘	↘
Viscosity ↗	↘

Table 2.3: *Variation of the J_{ps} parameter in function of the HF content, temperature and viscosity. The temperature and viscosity are basically the same parameter since an decrease in temperature provokes an increase in the viscosity of the solution.*

In our study the use of lower concentration of HF for the separation step did not help the separation of the layer due to a strong increase of the resistivity of the solution and consequently the terminal potential of the electrochemical cell. We have therefore focused our attention on controlling the viscosity of the solution through both control of the temperature and the addition of glycerol. For controlling the temperature, an o-ring type cell was fabricated where only a part of the surface of the substrate is in contact with the electrolyte. The back contact being separate from the solution tank, in contrast with the full immersion cells described in chapter I, it becomes possible to cool down the silicon substrate through the conducting back contact as seen in **Fig. 3.13,** using a cool plate / Pelletier module connected to the back of the substrate.
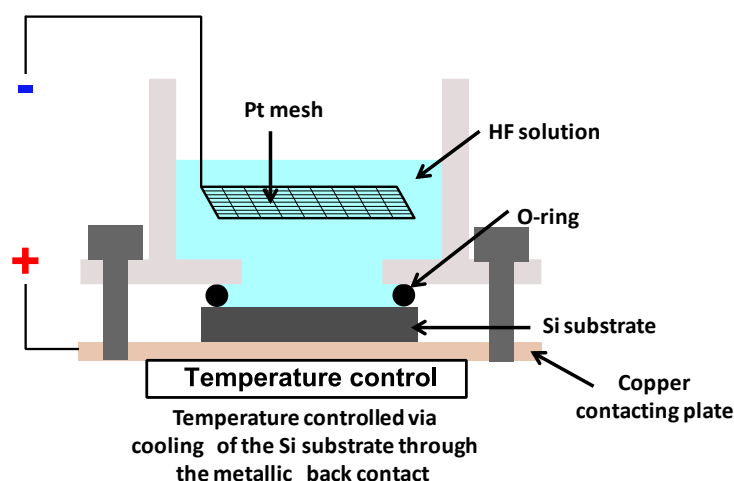
Fig. 3.13: *Schematic of a modified o-ring anodization cell allowing the cooling of the substrate through the back contact*

Cooling of the substrate directly is an easier and simpler method than cooling of the electrolyte itself through an external HF resistant apparatus. Since the solution vessel are made of acid resistant material like PTFE, PP or PE, cooling of the vessel itself is quite inefficient due to the poor thermal conductivity of the material. Temperature control can be achieved by conducting the separation step into a close refrigerating chamber but the presence of HF in the solution requires the venting of the evaporating gas and the chamber to be acid resistant.

The separation was conducted in three experimental sets with different conditions including the cooling of the substrate down to 5°C, as well as adding high purity glycerol to the solution while keeping the HF content constant. The two mixing ration used here were HF : Ethanol : glycerol in proportion 3:2:1 (glycerol 16.7%) and 2:1:1 (glycerol 25%). The same solution was used during formation and during separation (with glycerol or not) but substrate cooling was started after the end of the formation and the separation current pattern was not applied to the cell until the stabilization of the substrate temperature to 5°C for at least 1 min. The experiments were conducted mainly on pn type material but also on heavily doped n and p substrate. The results of the separation process are summarized in **Fig. 3.14**. The resulting layers were classified in three categories: no visible separation (cross mark), partially separated with local separation of layer fragments of 1 to 3 mm in size (triangle mark) and finally the separated layer (circular mark) for layer of 3 mm in size and over. The results clearly show an increase of the separation success with increase of the viscosity of the solution. Nc-PSi layers were successfully separated down to a thickness of around 13 μm for pn type material and around 8 and 6 μm for n+ and p+ material respectively, using only the substrate cooling as parameter for the two single doped materials (no glycerol additive). We have confirmed separately that layers with the same thickness could not be separated without cooling. The difference in thicknesses

104

achievable for the three different materials type clearly shows that the separation process is type dependent. The use of the layers separated with the o-ring cell configuration was restricted by the limited section of anodized surface possible with the cell and the limited range of cooling temperatures. Further decrease of the layers thickness could be achievable at lower temperature.

Control parameters / Thickness range	Temp. No control (RT)	Temp. control (5ºC)	Temp. control (5ºC) + Glycerol 16.7%	Temp. control (5ºC) + Glycerol 25%
40-30 µm	O	O	O	O
25-23 µm	X	O	O	O
18-16 µm	X	Δ	O	O
15-13 µm	X	X	Δ	O

(O) Complete separation **(Δ) Partial separation / Broken layer** **(X) No separation**

Separation results for n+ and p+ type layers	Type	n+	p+
	Min. thickness achieved	8 µm	6 µm

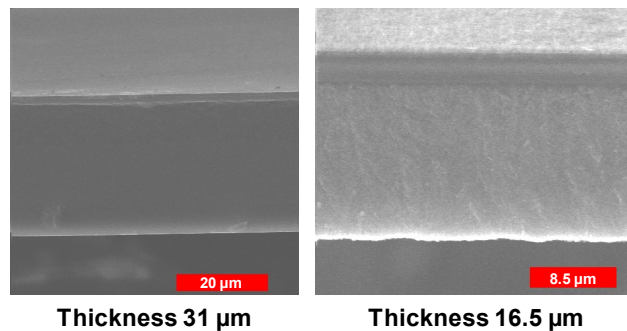**Thickness 31 µm**   **Thickness 16.5 µm**

Fig. 3.14: *Demonstration of the effect of the solution viscosity on the separation of nc-PSi layers. The upper table concerns the pn type material only. An example of thinner separated pn type layer is shown at the bottom right.*

III.2 Optical characterization

III.2.1 Photoluminescence

Photoluminescence spectra were recorded under constant excitation from a He-Cd laser in 325 nm mode. The laser was focused at the surface of the sample using a set of lens resulting in a spot of less than 1 mm. Since we were interested in measuring only the spectral distribution of the PL, the exact size of the spot as well as the laser intensity were irrelevant. Detection was realized through a monochromator equipped with a CCD camera. A filter was placed at the exit of the laser to avoid undesired emission beside the 325 nm mode. Similarly, to avoid the

detection of the laser and its harmonic through the monochromator, low-pass filter were used to prevent the laser radiation to enter the monochromator slit. All spectra were corrected with the response of the whole system (Filter + monochromator + CCD camera).

III.2.2 Absorption spectra

The absorption spectra of free-standing layers of nc-PSi were estimated from the transmittance and reflectance spectra measure with a spectrophotometer Hitachi U-4100 with a 5° specular reflectance mount unit. Measures were conducted in the range 300 to 2000 nm and were auto-corrected by the system through a preliminary background measurement. Transmittance measurements on free-standing layers were realized from both side of the layer to confirm the good homogeneity of the layer. Absorption coefficient α was obtained through the classical Beer-Lambert law considering an identical reflectance R on both side of the sample as seen in **Fig. 3.15**. The estimation works relatively well for homogeneous material such as nc-PSi made from single doped p or n material but cannot be applied to np or pn material due to the presence of multiple structure of different size and thickness in the material.
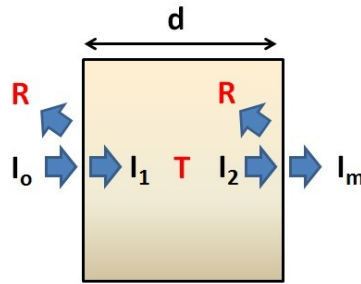
$$T = e^{-\alpha d} \text{ , } I_1 = (1-R)I_o \text{ and } I_m = (1-R)I_2$$

$$\alpha = \frac{1}{d}\ln\left[\frac{(1-R)^2}{T}\right]$$

with α the absorption coefficient in cm^{-1}
d thickness of the material section in centimeter
R and T the reflectance and transmittance of the material

Fig. 3.15: *Expression of the absorption coefficient from the measured transmittance and reflectance using the Beer-Lambert law.*

III.3 Photovoltaic characterization

III.3.1 General photovoltaic characterization

III.3.1.1 Solar irradiance

The recent strong development and advance in the PV industry and scientific community has lead to the need to standardize the photovoltaic characterization especially in view of performance comparison and result reproducibility. Today, most PV characterization are done using a "Solar simulator" which basically is a high power light source reproducing the solar irradiance spectrum with more or less accuracy. The sun basically acts as a black body irradiating at a temperature of approximately 5800K. The light emitted travel through space and the terrestrial atmosphere of earth until reaching the ground level. From earth, the observable solar spectrum is strongly affected by the chemical composition of the multilayered structure of the atmosphere containing absorbing species such as ozone, carbon and water. The power density from earth is also dependent on the observation position from the incident solar radiation (distance and angle). Solar irradiance has therefore been standardized using the concept of Air Mass (AM) which defines the optical path of solar irradiance through the terrestrial atmosphere. AM1 hence refers to 1 atmosphere thickness while AM0 refers to no atmosphere and is used exclusively to characterize PV cells for application in space. In practice, the AM1.5 standard is most commonly used representing an average of 1.5 atmosphere thickness to match the optical path of solar irradiance at the most common latitude of solar applications (mid-latitude such as America, Europe, Japan etc…). AM1.5 is sometimes follow by the letter D or G meaning Direct or the universally used Global irradiance, taking in account both direct and diffuse irradiance. A typical AM1.5G spectrum is shown in **Fig. 3.16** [13]. The total power density of the solar irradiance shows strong variability in function of the atmospheric conditions but for practical purpose has been fixed at a level of 1000 W/m^2 or 100 mW/cm^2, commonly referred at 1 sun. Power densities in excess of 1 sun or under "solar concentration" are used only in specific solar concentrator application or to investigate accelerated aging effect on the cell performance.
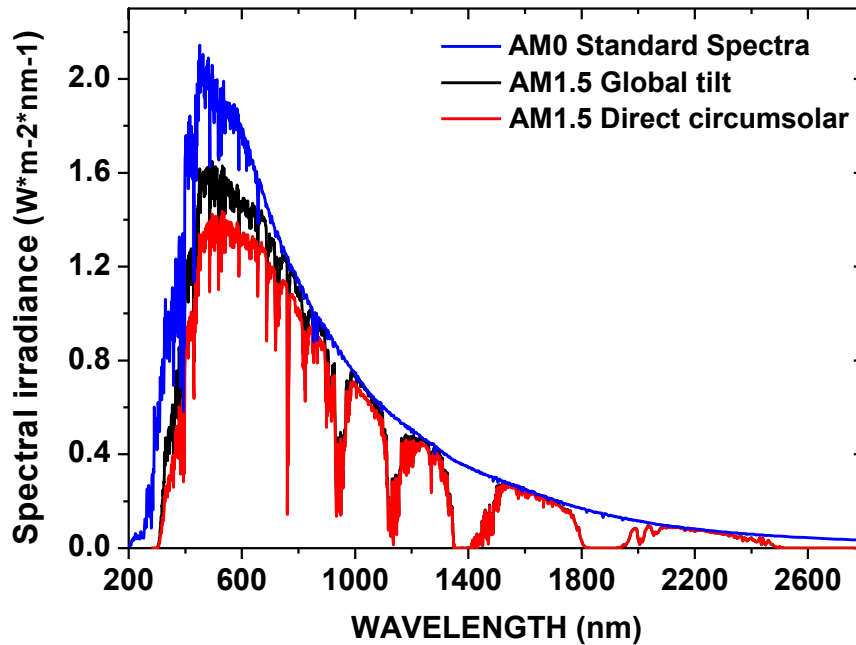
Fig. 3.16: *Spectral distribution of the solar irradiance from the AM0 (ASTM E-490), AM1.5D and AM1.5G standard (ASTM G-173-03)*

PV measurements in this study were realized under AM1.5G irradiance at 1 sun. The samples were maintained at a temperature of 25°C by cooling through the metallic back contact. Top contact was realized by using spring probes with round tip to provide good electric contact with the fragile nc-PSi layers without damaging them. The illuminated area of the cell was defined by using a mask with a square aperture corresponding to the size of the deposited top contact resulting in aperture area of 2.5 x 5, 5 x 5, 6 x 6, 8 x 8 or 10 x 10 mm^2 depending on the size of the cell.

III.3.1.2 Electrical characterization of photovoltaic cells

A basic solar cell acts as a light absorber; each photon with an energy superior to the bandgap of the material is absorbed, creating a pair of electron-hole which then needs to be collected. The separation of the photo-generated carrier requires an internal electric field generally realized through a pn junction by doping or by using hetero-junction structure of different materials or even metallic contact in the case of schottky type cells. Under illumination, the total current at a given voltage is given by:

$$I = I_L + I_{dark},$$

with I_L the current due to carrier photogeneration and I_{dark} the dark current due to the polarization of the diode. In the case of an ideal cell, the dark current can be represented by the ideal Shockley diode equation leading to:

$$I = I_L - I_0[e^{\left(\frac{qV}{kT}\right)} - 1]$$

with I_0 the reverse saturation current of the diode. The total current in the dark and under illumination is shown in **Fig. 3.17**.
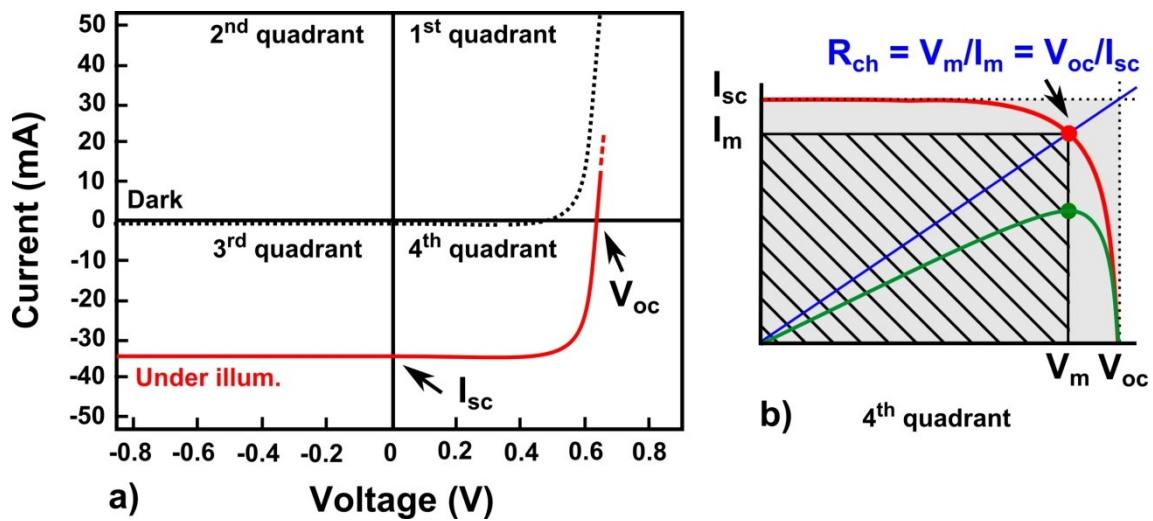

Fig. 3.17, *(a): Typical I-V characteristics of a solar cell under dark and illuminated conditions, (b): the 4th quadrant showing the main parameters defining the power efficiency of a solar cell.*

Important parameters related to the PV cell are located in what is usually referred as the 4th quadrant:

- At 0 bias, in the absence of any external electric field the photo-generated current is referred as the short-circuit current I_{sc}.
- Similarly, the electric field present in the device when no net current flows is referred as the open-circuit voltage V_{oc}.

The two parameters V_m and I_m, the voltage and current at the maximum power output of the cell $P_m = V_m \times I_m$, are used to define the Fill Factor (FF) representing the ideality of the cell. As seen

in figure 3.17(b), the fill factor geometrically represents the largest rectangle that can be fitted within the IV curve. The FF is determined through the following formula:

$$FF = \frac{V_m I_m}{V_{oc} I_{sc}}$$

With all the previous parameters known from the IV characteristics, the power efficiency of the cell can be calculated through the following equation:

$$\eta = \frac{P_m}{P_{in}} = \frac{V_{oc} I_{sc} FF}{P_{in}}$$

with P_{in} representing the input power of the cell which is usually fixed at 1 sun – 100 mW/cm^2.

Real solar cells are far from being ideal and several limitations and parasitic effects are present, the two most common effects being the series and shunt resistance R_s and R_{sh} as seen in the typical equivalent solar cell model shown in **Fig. 3.18**.
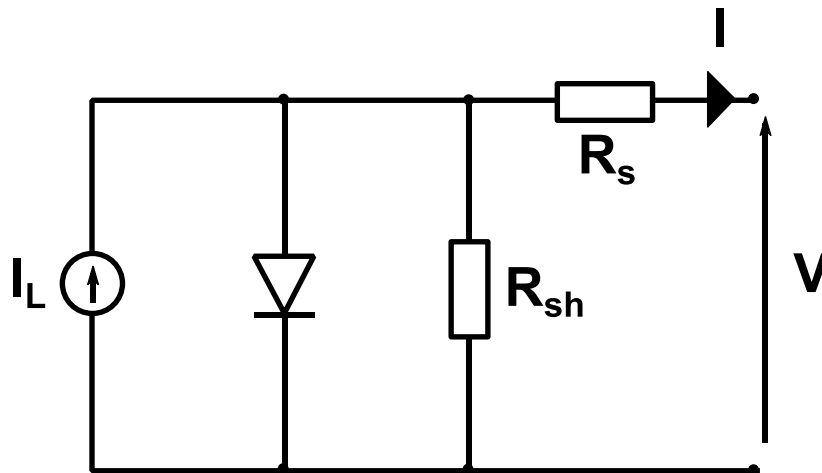

Fig. 3.18: *Typical equivalent circuit used to model a solar cell, including the two parasitic resistances R_s (series resistance) and R_{sh} (shunt resistance)*

The series resistance is due to cumulative resistive effects along the current path in the PV devices, from the material itself as well as the top and bottom contact. High series resistance strongly reduces the fill factor of a cell. On the other hand, the shunt resistance represents possible alternate current paths in the device and strongly affects the open circuit voltage. In the presence of both a series and shunt resistance effect, the diode equation can be rewritten as:

110

$$I = I_L - I_0[e^{\left[\frac{q(V+IR_S)}{nkT}\right]} - 1] - (V + IR_S)/R_{SH}$$

Alternatively, the effect of parasitic effects can also be estimated by a simpler parameter called the characteristic resistance of the cell defined by $R_{ch} = V_m / I_m$ or $R_{ch} = V_{oc}/I_{sc}$, graphically shown in **Fig. 3.17(b)** as well.

III.3.2 Spectral response

The spectral response corresponds basically to the conversion efficiency of the PV device for a given wavelength. For each wavelength, the ratio of collected carriers is compared to the number of received photons. The corresponding ratio is often termed Incident Photon Conversion Efficiency (IPCE) or quantum efficiency (QE) and can be written as:

$$IPCE = \frac{Ne}{Np}$$

with Ne the number of electrons collected from the cell and Np the number of photons incident to the cell surface.

Since the light is monochromatic, the number of photons can be easily calculated from the measured irradiance power of the light source using the formula:

$$Np = \frac{P_\lambda \lambda}{hc},$$

with P_λ the power in watt, λ the wavelength in meter, h the Planck constant (6.626×10^{-34} J.s) and c the celerity of light (2.998×10^8 m/s) rewritten as:

$$Np = 5.0307 \times 10^{15}. \lambda. P_\lambda,$$

With P_λ in watt and λ in nanometer.

The IPCE formula as it is corresponds to the efficiency view from the exterior of the cell, the External Quantum Efficiency (EQE), without taking in account the reflectivity of the device surface and therefore the amount of reflected photons at each wavelength. By taking in account the reflectivity, one can calculate the Internal Quantum Efficiency through the modified formula:

$$IQE = \frac{Ne}{Np(1-R)} = \frac{EQE}{(1-R)}$$

The formula can even be more refined by taking into account the non-ideal transparency of the top contact material in account. The spectral response is one of the most important characterization tool in PV and gives information about the volume properties of the cells, each wavelength being absorbed at a different thickness in the material and therefore can give insight in the loss mechanisms present in the device from surface defects for the short wavelength to problem of photocarriers diffusion in the material at visible wavelength etc…

In this study two types of measurement systems were used to characterize the devices. In the range 350 to 1100 nm, an IPCE measurement system from Newport was used. The system consists of a xenon lamp coupled with a double grating monochromator. A filter wheel was placed in the optical path between the light source and the monochromator to cut the undesired light energy range. The measurements were realized with a Keithley semiconductor analyzer in a four probes configuration. The samples were mounted on a specially designed holder and contacted in sandwich mode between to copper plates. The reference Si detector and the samples holder were placed on an optical rail parallel to the monochromator output slit, the surface of both the detector and the samples under measurement being positioned at the same distance from the light source. The detector used for measuring the lamp power spectrum was a UV enhanced silicon detector.

III.3.3 Under solar concentration

Linearity of the nc-PSi PV devices was tested under concentrated illumination from the same solar simulator used for classical PV characterization. Concentration was obtained through the use of a set of two Fresnel lenses [14] mounted on a metallic slide allowing for the adjustment of the lens height. The system configuration allowed for a concentration up to 10 sun maximum. The measurement were done by opening and closing the simulator shutter right before and after the measurement to avoid any undesired long time exposition of the devices and the cooling system to the intense concentrated light. Monitoring of the concentration level was done through a pyranometer with the surface of the thermopile adjusted to match the height of the device under characterization. Care was taken to monitor the illumination intensity at the exact same location of the PV devices and to adjust the lens plane parallel to the device plane by using a 2 dimensional level tool. At high concentration, a shift as low as 1 mm in inclination of the lens produces strong variation of the total illumination power and induces strong in-homogeneity of illumination on the device surface.

Bibliography of chapter III

[1] S. Pace, L. Gazagnes, P. Gonzalez, C. Guimon, M. Granier, D. Cot, J-M Devoisselle, and F. Cunin, hys. Status Solidi A **206** (6) p. 1326 (2009) - DOI 10.1002/pssa.200881080

[2] J. E. Bateman, R. D. Eagling, D. R. Worrall, B. R. Horrocks, and A. Houlton, Angew. Chem. Int. Ed. **37**, No. 19 (1998).

[3] R. Boukherroub, S. Morin, D.D.M. Wayner, D.J. Lockwood, Physica Status Solidi A **182** (1) p. 117 (2000).

[4] B. Gelloz, H. Sano, R. Boukherroub, D.D.M. Wayner, D.J. Lockwood, N. Koshida, Appl. Phys. Lett. **83** (12) p. 2342 (2003).

[5] J. M. Buriak, Chemical Reviews **102** (5) p. 1271 (2002).

[6] M. P. Stewart, E. G. Robins, T. W. Geders, M. J. Allen, H. Cheul Choi, J. M. Buriak, phys. stat. sol. (a) **182**, p. 109 (2000).

[7] R. Bywalez, H. Karacuban, H. Nienhaus, C. Schulz, H. Wiggers, Nanoscale Res. Lett. **7**, p. 76 (2012).

[8] R. Boukherroub, S. Morin, D.D,M. Wayner, F. Bensebaa, G.I. Sproule, J.-M Baribeau, D.J. Lockwood, Chem. Mater. **13** (6), p. 2002 (2001).

[9] J. von Behren, L. Tsybeskov, and P. M. Fauchet, Appl. Phys. Lett. **66**, p. 1662 (1995) - doi: 10.1063/1.113885

[10] D. R. Turner, J. Electrochem. Soc. **105** (7), p. 402   (1958) - doi: 10.1149/1.2428873

[11] S. Setzu, S. Letant, P. Solsona, R. Romestain, J.C. Vial, Journal of Luminescence **80**, 129D132 (1999).

[12] M. Servidori, C. Ferrero, S. Lequien, S. Milita, A. Parisini, R. Romestain, S. Sama, S. Setzud, D. Thiaudiere, Solid State Communications **118,** p. 85 (2001).

[13] C. Honsberg, S. Bowden, http://pveducation.org retrieved on 2013/11/07

[14] Richard M. Swanson, Photovoltaic Concentrators, in: Handbook of Photovoltaic Science and Engineering, Antonio Luque and Steven Hegedus (Eds), John Wiley & Sons Ltd, The Atrium, Southern Gate, Chichester, West Sussex, England (2002).

Chapter IV. Photovoltaic characterization of nanocrystalline porous silicon free standing membranes

IV.1 Photovoltaic effect in on-substrate nc-PSi

As a first step of assessing the effect of nc-PSi on photovoltaic characteristics of bulk silicon substrate, thin to moderately thick layers of nc-PSi grown onto two different types of c-Si substrates were investigated.

IV.1.1 Photovoltaic and spectral characterization

IV.1.1.1 PN-type substrate

The starting material used here was a Sb doped n type (100) substrate with a resistivity of 0.01 – 0.02 Ω.cm (corresponding impurity level of $1x10^{18} – 4x10^{18}$ cm^{-3}). A p type layer was ion implanted at the top with a dose of $3x10^{15}$ cm^{-2} of boron resulting in a junction depth in-between 800 and 1000 nm after high temperature annealing. It is important to note here that the junction formation conditions (depth and doping level difference between the p and n zone) were chosen here not for optimal PV performance but to allow the fabrication of free-standing layer on nc-PSi which success strongly depend on the rectifying quality of the junction. Higher doping difference for the p and n region prevents the correct separation of the layer due to very high reverse potential. Furthermore, several level of different doping for the pn junction did not show any drastic difference on the PV characteristics. Variation of the PV performances in function of the formation parameters will be discussed in section IV.2.2.3.

The pn substrate were anodized in HF:Ethanol 1:1 (HF 27.5 wt%) under different current and duration resulting in layers of nc-PSi of less than 1 μm. The samples were contacted in an Au/nc-PSi/c-Si/Al sandwich structure and measured under AM1.5-1 sun illumination. The results of the characterization are shown in **Fig. 4.1** and PV performances summarized in **Table 4.1**. The non-optimal junction formation parameters introduced previously clearly produce poor performance as seen in the characteristics of the non-anodized reference bulk substrate. In contrast all samples with a PSi layer at the top shows drastically increased PV performances.
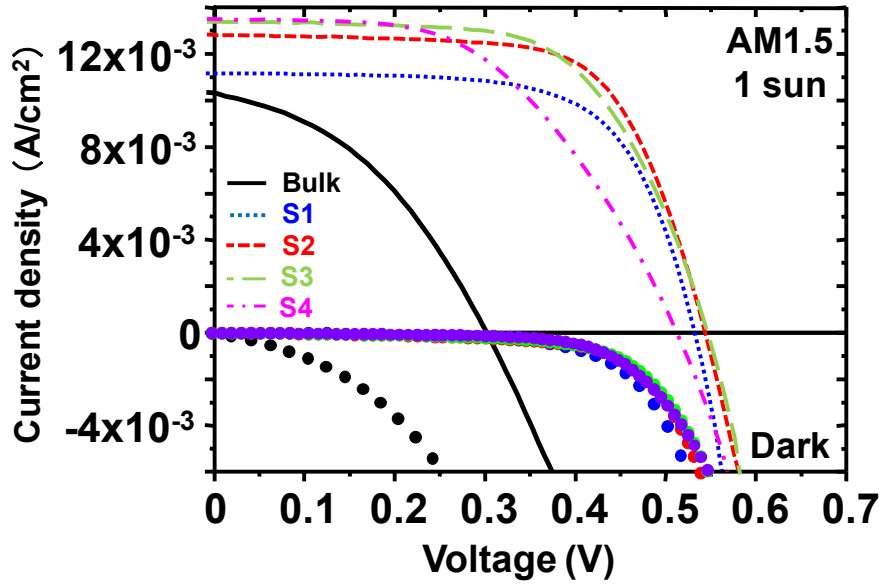
Fig. 4.1: *I-V characteristics of pn type substrate under AM1.5G – 1 sun illumination (full lines) and the corresponding dark current (dot lines).*

Name	Anodization charge	FF (%)	J_{sc} (mA/cm^2)	V_{oc} (V)	η (%)
Bulk reference	NA	39.8	10.28	0.301	1.23
S1	1.47	66.6	11.06	0.532	3.92
S2	5.88	67.1	12.71	0.544	4.64
S3	14.7	62.3	13.29	0.546	4.52
S4	29.4	51.6	13.41	0.512	3.54

Table 4.1: *Summary of the photovoltaic characteristics for 4 different anodized pn type substrates in function of the anodization charge and compare to an unmodified bulk pn substrate as a reference.*

Several trends are clearly visible:

- A strong increase in the short-circuit current in function of the quantity of charge used during anodization
- Similarly an increase in the V_{oc} with the amount of charge is visible
- A decrease of the power efficiency and fill-factor at higher quantity of charges

The corresponding spectral responses of the sample are shown in **Fig. 4.2(a)** and **(b)**. The external quantum efficiency shows a strong increase of the efficiency compare to bulk silicon, especially in the visible from 800 nm to the 500 nm blue-green range. If the corresponding spectra are corrected for the surface reflectance of each sample as shown in **Fig. 4.2(b)**, the difference in efficiency with the bulk reference is drastically reduced. The response of all the anodized samples is still slightly enhanced at longer wavelength and some of the samples still have a higher efficiency in the visible range than the bulk reference.
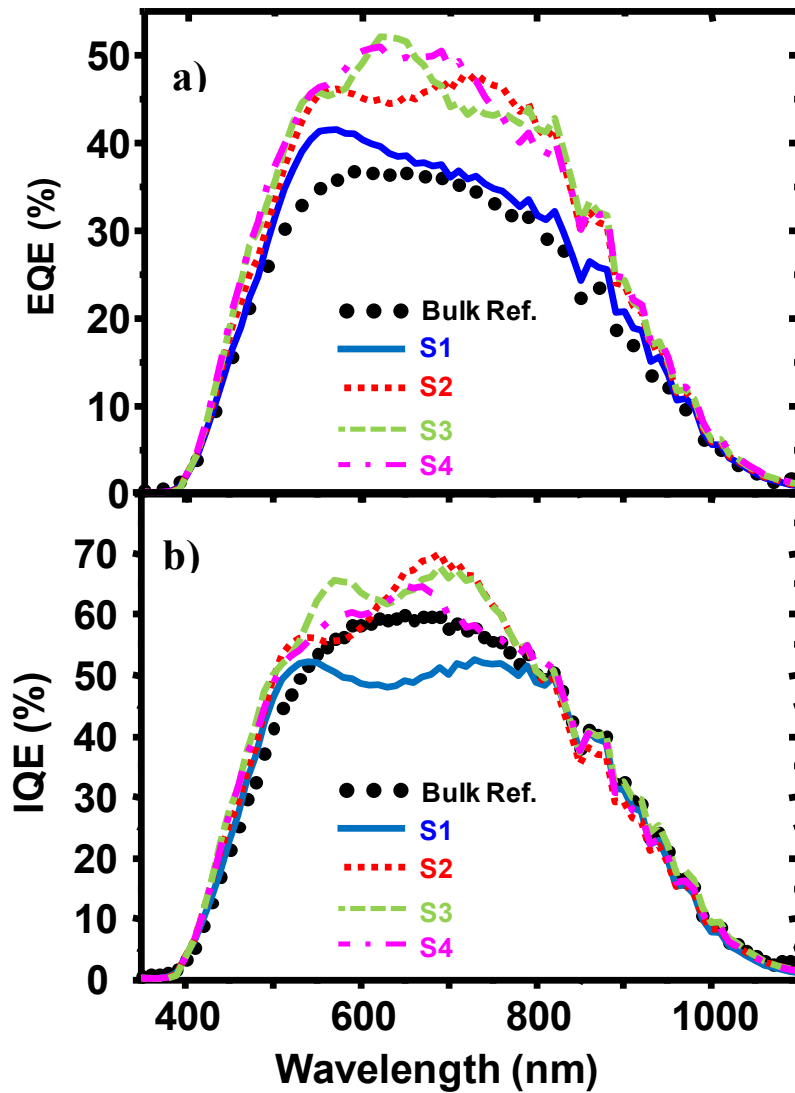

Figure 4.2: *Quantum efficiency of pn type substrates before and after correction for the surface reflectance.*

IV.1.1.2 NP-type substrate

In the case of np type substrate, since the junction is in forward during anodization, there is no restriction in the doping range that can be used to make the junction. The substrate were made from lowly doped p type wafer of resistivity $1 - 3$ $\Omega.cm$ (corresponding impurity level of $5x10^{15} - 2x10^{16}$ cm^{-3}) with a phosphorus layer implanted at the top, resulting in a n type layer with an impurity concentration of $5x10^{19}$ cm^{-3} and a junction depth of approximately 1.3 µm. A back surface field was also created through over-doping of the back side of the wafer with an impurity level of $4x10^{19}$ cm^{-3}. The samples were prepared in a similar fashion than pn type substrates. Their corresponding PV characteristics and performances are summarized in **Fig. 4.3** and **Table 4.2** respectively.
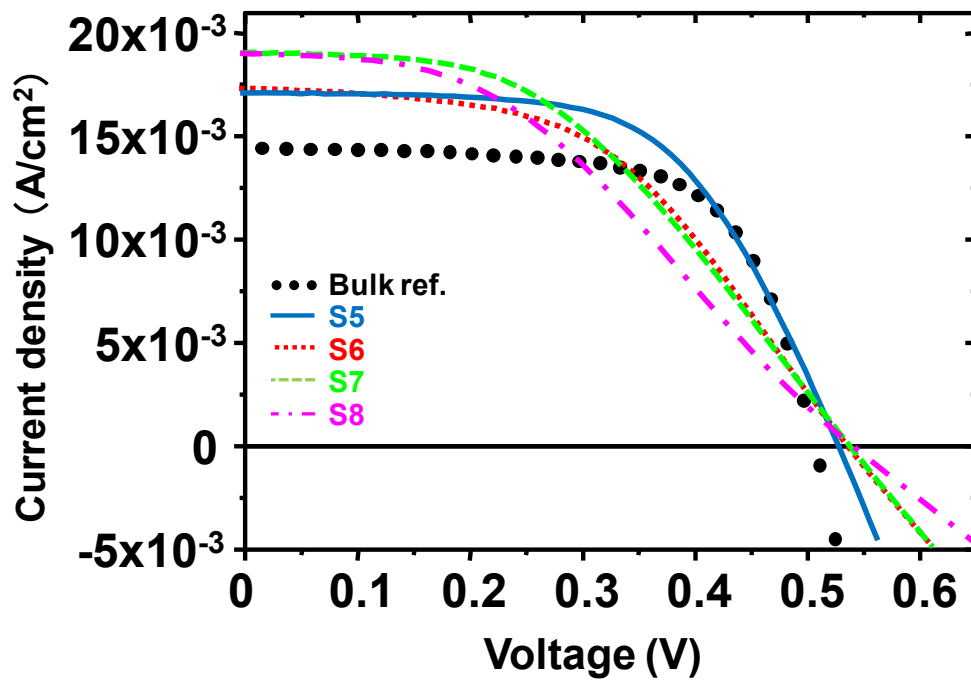

Fig. 4.3: *I-V characteristics of np type substrate under AM1.5G – 1 sun illumination (full lines) and the corresponding dark current (dot lines).*

117

Name	Anod. charge	FF (%)	J_{sc} (mA/cm^2)	V_{oc} (V)	η (%)
Bulk ref.	NA	67	14.46	0.506	4.91
S5	0.41	59.5	17.14	0.527	5.38
S6	0.77	49.4	17.35	0.536	4.6
S7	1.15	44.9	19.09	0.537	4.6
S8	1.53	40	19.04	0.541	4.11

Table 4.2: *Summary of the photovoltaic characteristics for 4 different anodized np type substrates in function of the anodization charge and compare to an unmodified bulk pn substrate as a reference.*

Due to the higher quality of the original np junction, the differences in performance between the bulk reference and the anodized sample are greatly reduced. Similarly to pn samples, typical trends are clearly visible with increase of the charge amount during anodization. The short-circuit current and V_{oc} are continuously increasing while the fill factor and power efficiency are decreasing at higher charge formation. Such results are in accordance with the expected increase in thickness and resistivity of the PSi layers. After an initial increase in efficiency for low charge formation sample S5, the following trend is in a decrease of the PV performance for the following samples S6, S7 and S8. After correction for the surface reflectance, the internal quantum efficiency spectra shown in **Fig. 4.4(b)** clearly demonstrates the decrease of internal performance of the PSi devices even for samples anodized at low charge density and therefore having very thin PSi layers. The results clearly demonstrate that the effect of on-substrate PSi is purely optical, acting as a anti-reflection layer, and that the electrical activity of the PSi layer cannot be clearly estimated in such devices.
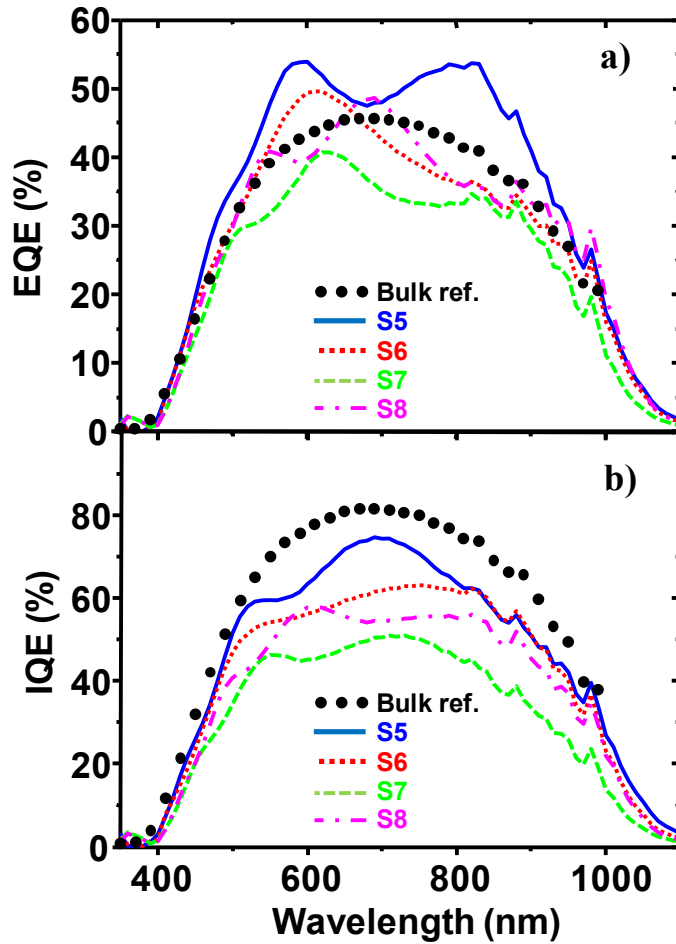
Fig. 4.4: *Quantum efficiency of np type substrate before and after correction for the surface reflectance.*

IV.2 As prepared free-standing nc-PSi

Since the effect and contribution of PSi to the photo-conversion is difficult to estimate in PSi/c-Si structure devices and that the contribution of PSi appears to be mostly of optical nature, the material will be investigated in the form of thin free-standing layers in the rest of the chapter. The free-standing layers were prepared following the separation process described in chapter III. Starting material employed here were both single doped p and n material in moderate and highly doped quality as well as pn and np substrate presented in the previous section. The following section, especially the photovoltaic characterization, will focus mostly on pn type samples which are the type of material presenting the most interesting characteristics in this study despite being the most difficult to separate from the substrate. Np-type material will be presented rapidly for comparison but its PV characteristics investigation was limited due to the high resistivity of the underlying p type layer and very low photo-generated current. Single

doped n+, p- and p+ material characteristics will be shown as well for comparison with the pn type material.

IV.2.1 Structural and optical characterization

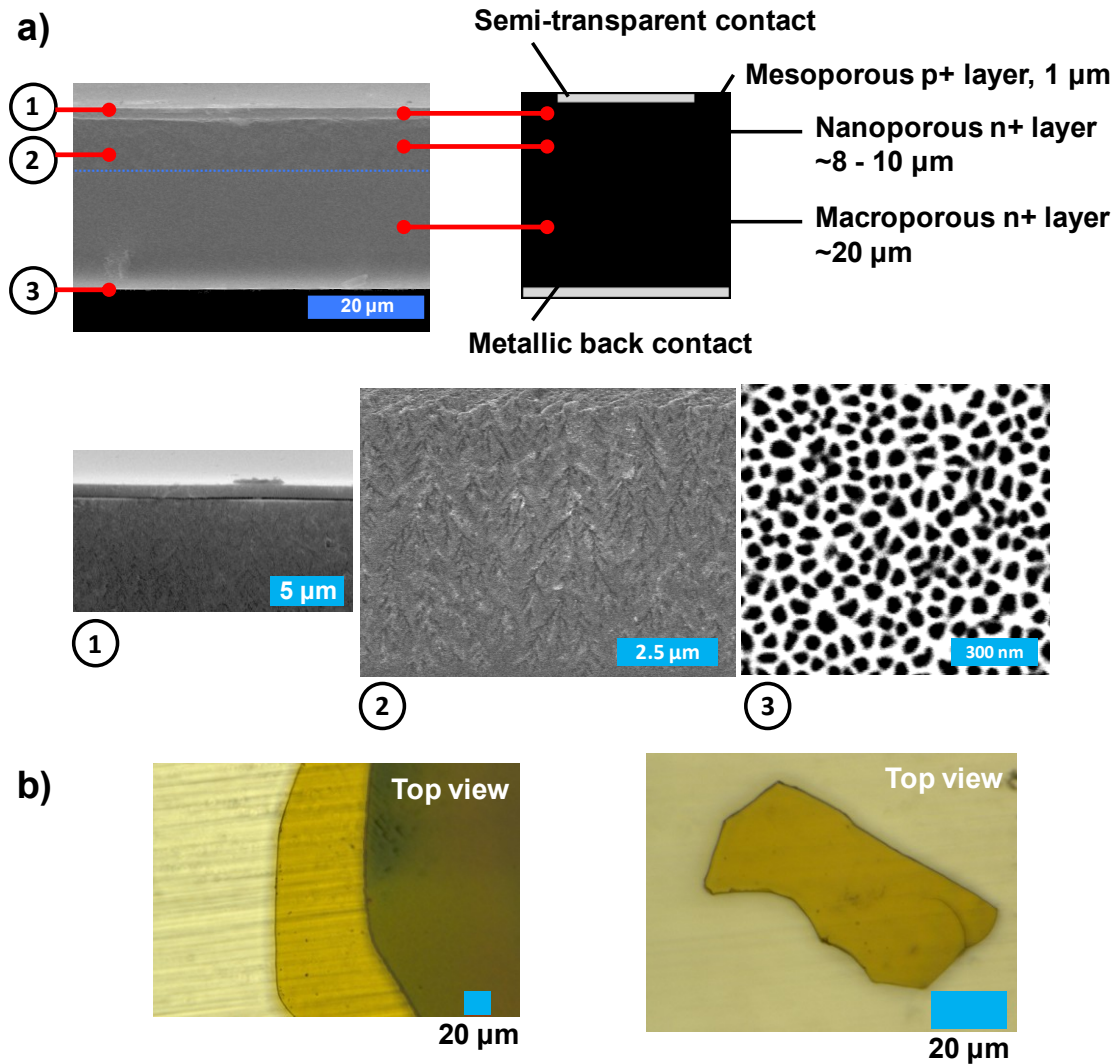### IV.2.1.1 Structural characterization

Fig. 4.5: *a) Cross sectional SEM micrograph of a pn type nc-PSi layers showing three different regions labeled 1, 2 and 3 with their corresponding micrographs. The corresponding estimated structure of the device is also indicated at the top right of the graph, b) optical picture of the upper p type layer observable in sample with high porosity due to the natural separation of the upper layer*

A typical scanning electron microscope (SEM) micrograph of a pn type layer is shown in **Fig. 4.5(a)** with the corresponding schematic off the device. At the top of the free-standing membrane, the upper p-type layer is clearly visible all along the cross section of the samples with a thickness of approximately 1 μm as seen in micrograph 1. Below the p type layer, in micrograph 2, a structural pattern is distinguishable with a fine sub-nanometric fractal branching structure. This layer corresponds to the n type part of the layer under illumination during formation. The illumination is kept during 450s from the beginning of the anodization and is then switched off resulting in a second layer of porous n type material with no visible features. Finally, as seen in the micrograph number 3, the bottom layer features relatively large holes in the size range 50 – 100 nm (macroporous), with remaining Si walls too large to present any confinement effect. Since the layer was separated from the Si substrate through injection of a large current, the visible structure at the bottom surface of the membranes could be the result of the separation itself and might not represent the structure of the whole bottom macro-porous layer. The illumination was not kept during all the anodization process due to an effect of over-etching of the top layer surface under constant illumination and the subsequent separation and cracking of the PSi film surface. The top p type layer is clearly visible in samples anodized in low concentration of HF resulting in strong porosity and the peeling of the upper layer from the rest of the free-standing membrane as seen in the optical picture of **Fig. 4.5(b)**.

IV.2.1.2 Photoluminescence

Photoluminescence spectra were measured from the top of the free-standing layers at room temperature. Typical spectra of as-prepared p-, n+ anodized under illumination and np type samples are shown in **Fig. 4.6**.
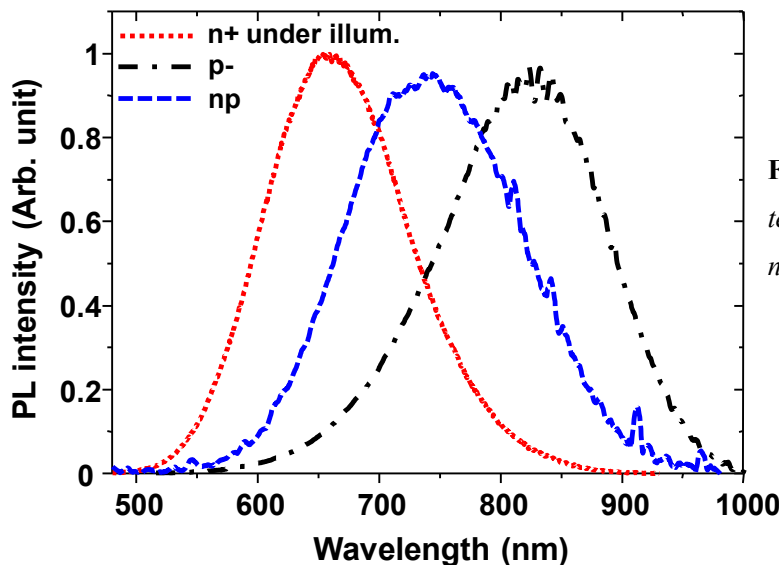

Fig. 4.6: *Example of room temperature PL specra for p-, np and n+ fabricated under illumination.*

The intensity of each PL spectrum was normalized for comparison. Layers made from n- and n+ anodized under dark condition as well as pn type sample did not show detectable PL from the top surface. If anodized under illumination, n type material transforms from a non luminescent to a strongly photoluminescent material, putting in evidence the strong effect of photo-assistance during the anodization process. A deeper investigation on the pn type layer shows that while the top p+ type layer is almost non luminescent; the underlying n+ type layer clearly shows a luminescent spectrum as seen in **Fig. 4.7**. The spectra were taken at first from the top layer (no PL) and after subsequent mechanical removal of the p type layer. The PL intensity increases while progressing toward the n+ type material. The low intensity of the emission also indicates that the active luminescent layer is probably very thin, less than 1 μm. The wavelength of the emission peak at around 650 – 670 nm (1.9 – 1.85 eV) also match the PL spectrum of n+ material fabricated under the same condition.
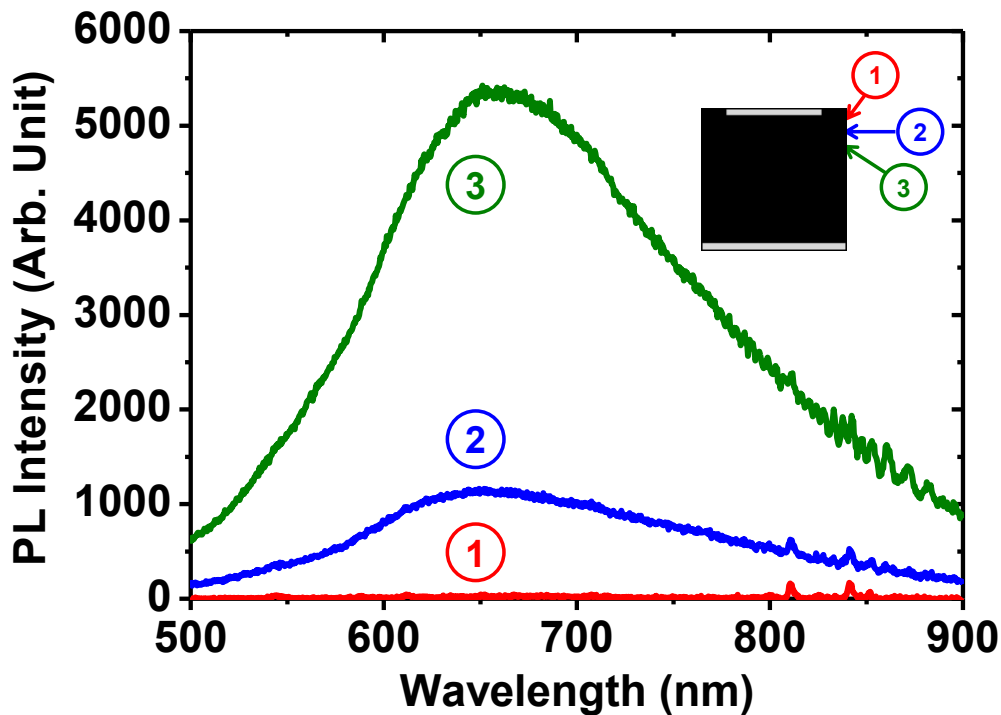

Fig. 4.7: *Room temperature photoluminescence spectra of pn type material. The three layers indicated in the inset were successively removed. The increase of photoluminescence intensity along the thickness indicates that the luminescence originates from Si nanodots produced in the n-type layer located under the non-luminescent compact p type layer.*

The combination of both the structures seen in SEM micrographs as well as the PL detected in the n type area allow us to propose a basic band diagram based on the three observed region as shown in **Fig. 4.8**.
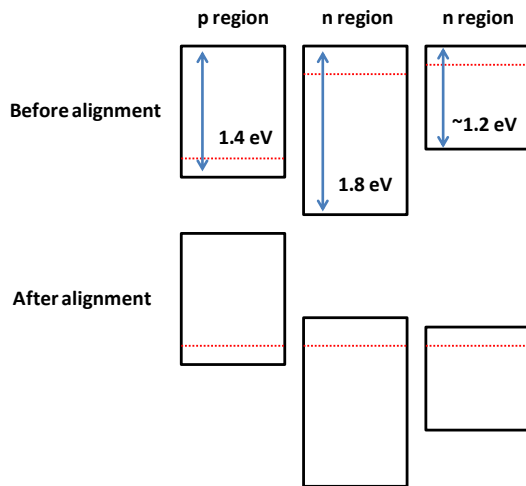

Fig. 4.8: *Schematic of the possible band alignment between the three different observed PSi regions in the material. Band gap values were estimated from PL, absorption spectra in combination with various data review.*

Due to the strong increase in the resistivity of the material, PSi is usually assumed to be intrinsic. Since in our devices, the effect of contact being ruling out, a rectification and a corresponding PV effect is observed, the p and n region are therefore assumed to retain their type and doping leading to the alignment seen in the bottom graph. The possible band discontinuities between the three materials are not shown here. The junction between the two n type regions is strongly graded, the transition between the nano-porous region to the macro-porous lower one is not abrupt and strong variations of the structure along the depth are expected, with possible mix of nano and macro phase at the same depth in the material.

IV.2.1.3 Absorption spectrum

Absorption coefficient was obtained through the measure of the optical transmittance and reflectance of the free standing layers. The obtention of a correct estimation of the absorption requires that the material be homogeneous all along the thickness of the material section which limits the use of the technique to the highly homogeneous p-type PSi and to a lesser extent n-type anodized in the dark. N-type anodized under illumination as well as pn and np samples are actually composed of different types of material with different structures and porosity, due to the presence of p and n material in the junction and due to a gradient of porosity present in n type fabricated through photo-assistance as well as the difficulty to produce good free-standing membranes of that type of material, making these materials difficult to analyze optically. Furthermore, the optical transmission method is not sensitive enough to give correct information

on the absorption near and below the band gap of the material and in such case more advanced technique such as photothermal deflection spectroscopy (PDS) are usually employed. The optical measurement method is classically used in the tauc absorption range using a tauc plot representation allowing for a visual estimation of the optical band gap of the material.

Typical absorption spectra of p and n type material are shown in **Fig. 4.9** as a Tauc plot (square root of the absorption coefficient times the photon energy versus the photon energy). The estimated porosity for the p type material was 68% and the n type material 40% (anodized in the dark). The free-standing layers were further oxidized by HWA (260°C, 1.3 MPa, 3 hours) and RTO (900°C – 30 min under O_2). An example of color shift obtained on free-standing layers made from p type material is shown in the inset of **Fig. 4.9**. Due to the fragility of the layers, heavy oxidation step are difficult to implement and the layers need to be mechanically constrained in specially designed holder made of high temperature resistant material such as alumina. Furthermore, even if constricted mechanically, the surface of oxidized layers show strong distortions and bending of the surface making optical characterization difficult.
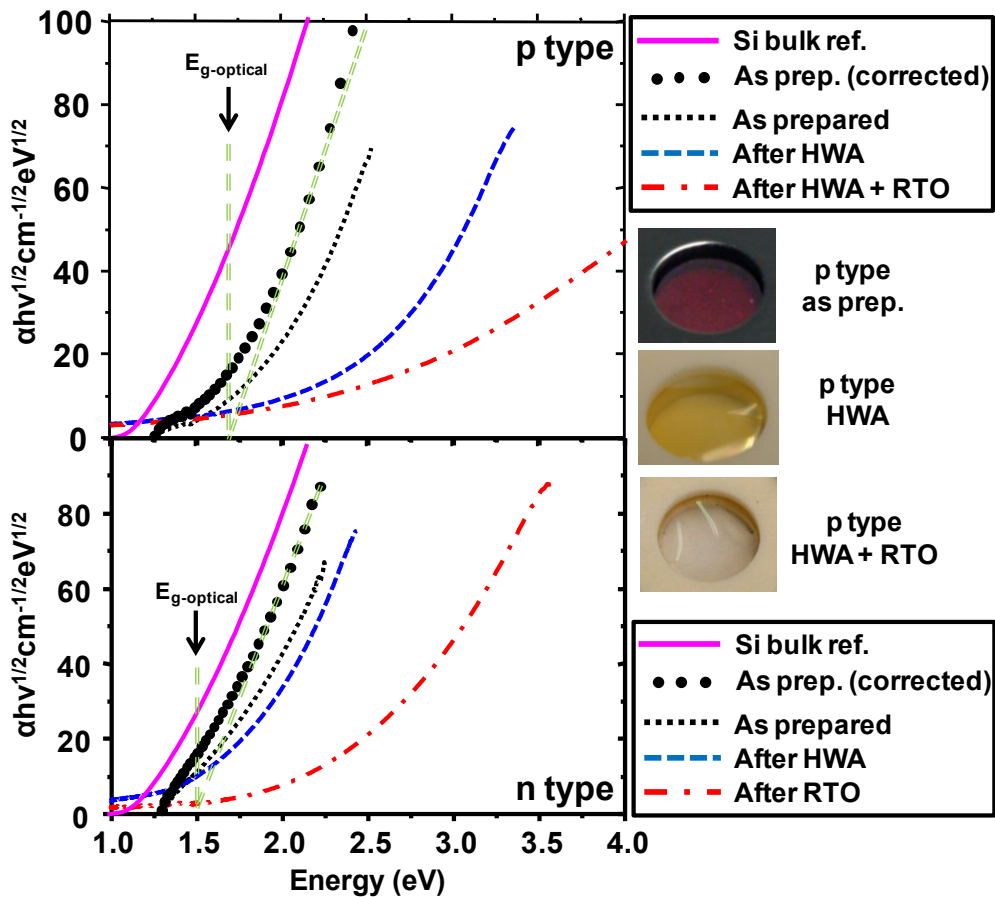

Fig. 4.9: Tauc plot of the *absorption of p type (top graph) and n type (bottom) as prepared and after different oxidation steps. Dot lines indicate the absorption of as prepared material after porosity correction.*

The dashed lines represent the absorption coefficient as measured while the dot lines represent the absorption coefficient of as-prepared material after porosity correction. Spectra of oxidized samples were not corrected. The absorption edge of both p and n type material are clearly shifted toward higher energy compare to the bulk Si reference even after porosity correction. The shift is more pronounced for p type material containing a higher density of small dots compare to the more bulky, almost non luminescent n type material. The effect of oxidation is also higher in the case of p type material; a low temperature process such as HWA induced a strong shift in the absorption spectra while for n type material the effect of the HWA oxidation step was very limited. Higher shift was obtained on n-type after oxidation through RTO, probably inducing a higher oxidation level and decreasing significantly the size of the remaining Si structures, a decrease not achievable through HWA only. As previously discussed in chapter I, the tauc plot shows a slow increase in the absorption in parallel to bulk Si showing that nc-PSi remains an indirect band gap material with no direct and strong transition in the absorption edge. The extrapolation of the as-prepared material curve to zero absorption gives an estimation of the optical gap $E_{g-optical}$, estimated at 1.68 eV and 1.5 eV for p and n type respectively, while their corresponding luminescent emissions peaked at 1.5 eV and 1.46 eV. In the case of p type material, the difference in energy between the PL peak center and optical edge correspond well with the usually reported PL shift of 0.2 eV toward lower energy compare to other characterization methods, in our case the estimated optical bang gap [1]. An important aspect to note is the strong difference in luminescence intensity between the p and n type material, with an emission visible with naked eye for p time while emissions from n type anodized in the dark had an extremely low efficiency and required acquisition through large aperture and long time exposure to obtain a detectable spectrum. The p type material is made of a high density of small Si nano-structures small enough to strongly emit in the visible range while n type (processed in the dark) might be formed of a mix of both large and small particles with a strong density of the former. Finally, while optical transmission and PL characterization are good enough to obtain an rough estimation of the average band gap of the porous material, it should be noted that the strong differences between the two methods, optical transmission is more sensitive to large, strongly absorbing Si dots while luminescence probes only the smallest luminescent structures in the material, make the correlation between optical gap and photoluminescence energy difficult to make.
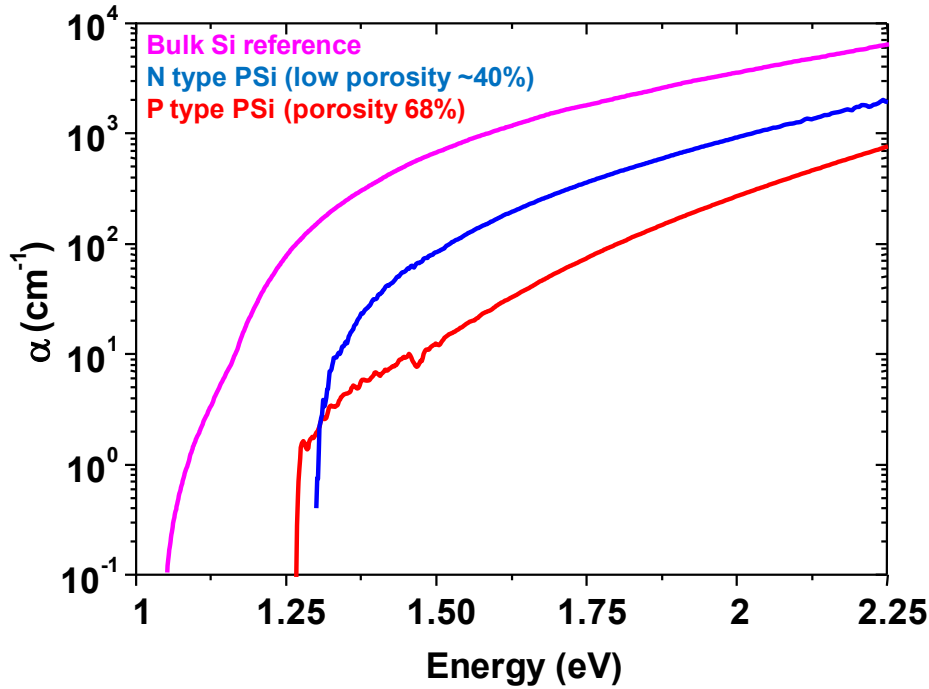
Fig. 4.10: Semi-log plot of the *absorption spectra of p type and n type as prepared layers with bulk Si as reference. The sharp drop especially visible on the p type curve is a measurement artifact due to the limited sensitivity of the measurement setup.*

The measured absorption coefficient is re-plotted in semi-log scale in **Fig. 4.10**, for the same p and n layer as previously shown in **Fig 4.9**. While data obtained through optical transmission measurement are not the most suitable for analysis of absorption near and below the band gap of the material, a difference of variation in the absorption coefficient for n and p type compare to bulk Si is still noticeable in the lower energy range, between 2 and 1.25 eV. The absorption of n type PSi appears to be following the curve of bulk Si relatively well over all the observed energy range while p type material shows a far higher deviation, increasing at lower energy. Similar experimental data obtained through PDS for p and n type in the same range of porosity of our samples is shown in **Fig. 4.11**, redrawn from a review by Kovalev et al [2]. Experimental data for p and n meso and microporous material are accompanied by the corresponding absorption estimation for porosity of 45 and 72% using the Bruggeman effective medium approximation method. Similarly to our own results, the low porosity n type material follow the bulk Si reference well and the theoretical model agree well with the experimental measures. In contrast, for p type material, the absorption of the porosified material matches the bulk reference only for energies higher than 3 eV. For lower energy, there is a strong increasing deviation from the theoretical model, with an exponential variation of the absorption with energy and a corresponding slope of 180 meV, comparable to 150 meV extracted from our own experimental

126

data. Such a deviation of the absorption has been early linked to the possible presence of an Urbach tail similar to the one observed in a-Si [3][4]. Sub-bandgap absorption bands were detected through PDS measurement and were attributed to the contribution of Si-H and Si-F in the material. In reference [4], a similar band tail was observed with a width in the range 150 to 300 meV. While the observed tail was strongly similar to the defect model used to describe amorphous silicon based material, the author clearly indicate that the observed exponential dependence should not be explained only by the presence of an averaged density of states in the material and noted that the dependence could be the results of confinement in the nanometric Si structures. Finally, in reference [5] the team of Kovalev investigated the effect of temperature on the absorption in p type material showing a tail like behavior in the energy range 1.7 to 2.6 eV. They show that the normalized absorption coefficient of p type microporous PSi in function of the temperature was identical to c-Si (in which no band tail is observable). Furthermore, the absorption spectra of PSi at different temperature remain perfectly parallel to each others, in contradiction with the Urbach model where all curves should extrapolate to a common point. The effect of desorption of hydrogen form the surface, and therefore the increase in surface defect states, was also investigated on samples annealed in an inert atmosphere up to 600 °C. A desorption of 50% of the surface hydrogen lead to an increase of only 30% of the absorption coefficient, with the same spectral behavior (same Urbach energy) observed before and after hydrogen desorption. The strong increase in surface states did not strongly alter the absorption behavior of the material (compare to strong quenching of both PL and photoconduction, as shown later in chapter V). The detected small increase of absorption after anneal was also observed in mesoporous material where absorption is dominated by large Si crystallites with the same electronic structure as c-Si. The authors carefully indicate that such results do not contradict the existence of a tail states in PSi but remarks that the effect of such tail are minor and that the observed absorption characteristics are mainly due to the crystalline core of the material, including the effect of confinement in the smallest structures.
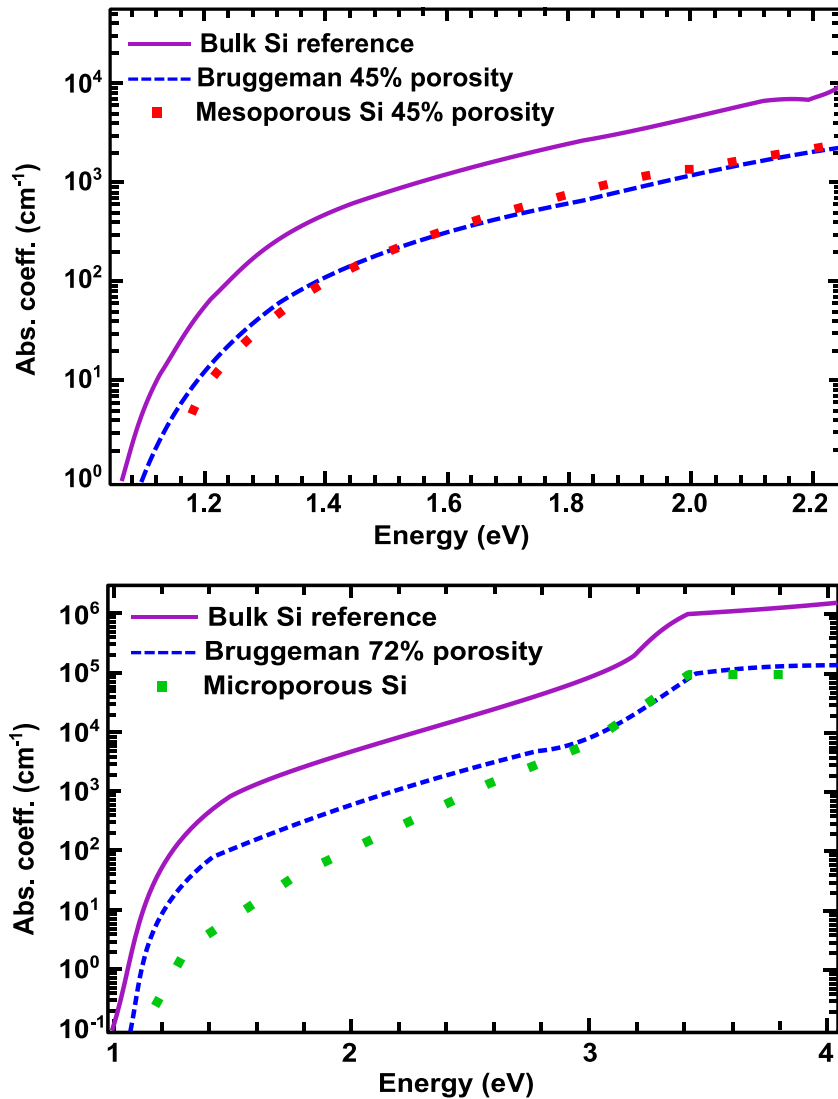
Fig. 4.11: *Semi-log plot of the absorption spectra of p type and n type as prepared layers redrawn from reference [5], plotted together with the corresponding Bruggeman EMA for comparison.*

In the case of p-type material oxidized at high temperature, the photoluminescence also show an interesting phenomenon with the apparition of a blue emission in addition to the typical red-orange emission as shown in **Fig. 4.12**. Activation of the blue luminescence required several step of time limited oxidation steps to avoid breaking the layer. The blue luminescence located at around 430 nm appears only after the final stage of HWA. Blue luminescence has already been investigated separately on on-substrate samples and the origin of the emission has been attributed to either localized states in silicon dioxide or at the interface Si/SiO_2 [6][7].
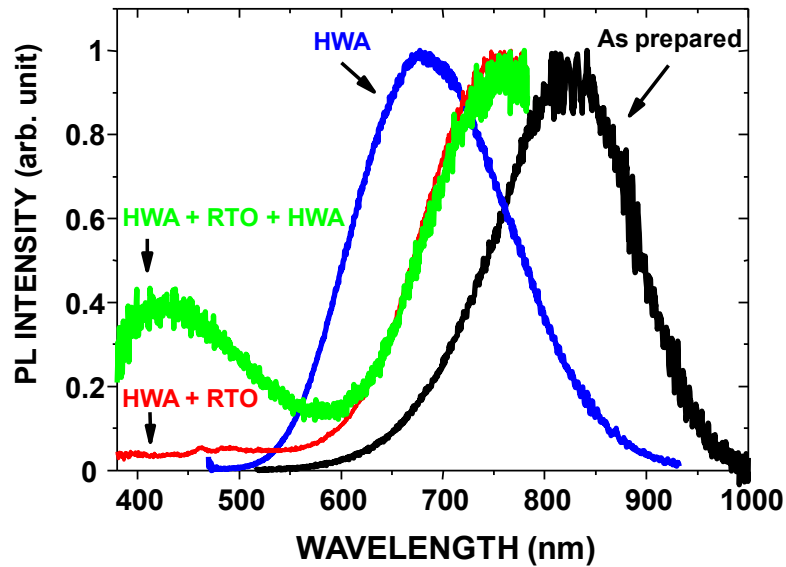
Fig. 4.12: *PL spectra of self-standing as-anodized p type nc-Si layers of 68% porosity, after a set of successive oxidation treatments in chronological order: HWA, RTO and finally HWA.*

While the oxidation treatment is extremely useful to enhance, stabilize and investigate the optical properties of nc-PSi, the structural changes induced by oxidation are too important in the case of active devices such as solar cells where generated photocarriers need to be efficiently extracted. In the following sections, PV characterization will be conducted on as-prepared samples and alternate passivation techniques will be investigated later in the following sections and the next chapter.

IV.2.2 PV characterization

IV.2.2.1 Single doped p and n type material

As a first step the photoconduction of single doped material made from n+, p and p+ material were investigated for comparison with the following pn and np type layers. Material from p+ and n+ were of low porosity (between 40 to 50% on average, mostly non luminescent material) while p-type material had a porosity of 68% with visible luminescence. The measurements were carried out in a sandwich configuration with Au as a top contact and Al at the back. Typical PV characteristics of the three types of devices are shown in **Fig. 4.13** with the corresponding normalized spectral response as **Fig. 4.14**.
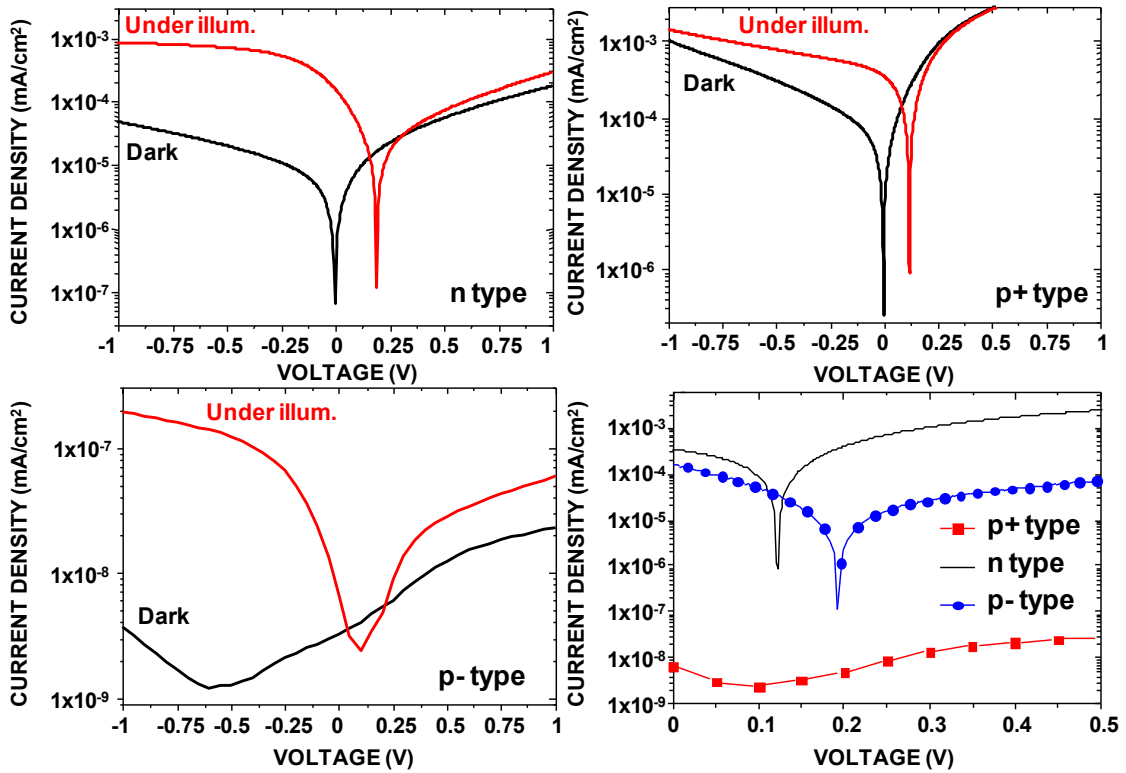
Fig. 4.13: *I-V characteristics under dark and illumination condition for single doped n, p+ and p- devices. The semi-log plot at the bottom right summarized the detected PV characteristics.*
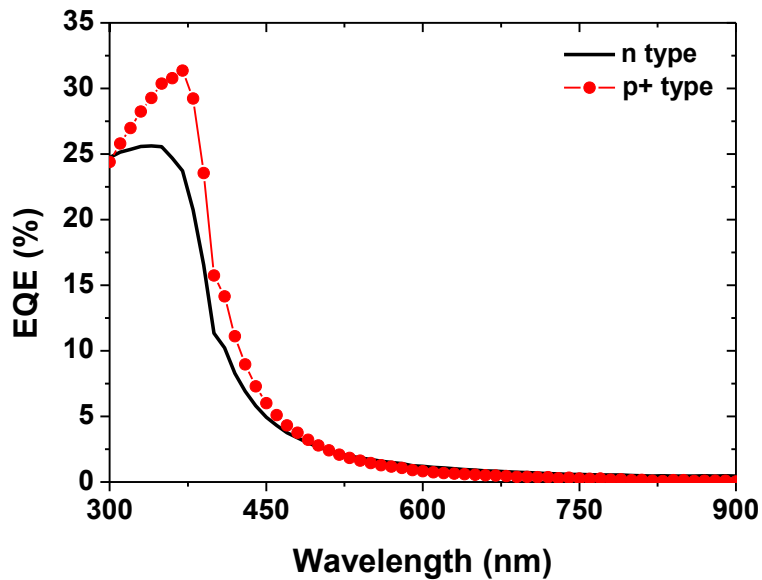

Fig. 4.14: *Corresponding spectral response for n and p+ type devices. p- material photocurrent under monochromatic illumination was too low to be accurately measured.*

130

The respective layer thickness for p-, p+ and n+ were 37, 7 and 35 μm respectively. The p+ and n+ material shows similar characteristics with low rectification ratio (RR at ±0.5V of 2.7 and 8.9 for p+ and n+ respectively) with strong leaking in reverse polarization. Both materials show a photovoltaic effect with relatively low V_{oc} in the range 0.1 to 0.3 V. Their spectral response, recorded in short-circuit, is also almost identical, with a strong response in the UV range and no contribution past 500 nm. The fact that both materials have no internal field (no junction) and a response in the UV strongly suggests the presence of a Schottky barrier at the Au/nc-PSi interface that could explain both the low quality of the resulting diode and the response in the high energy involving separation near the surface of the material. Indeed the contribution of the Au layer to the diode characteristics and therefore the observed PV effect was later confirmed and discussed in section **IV.2.2.4**. For the p-type material however, strong charging effect is visible due to the high resistivity and high density nano-structure of the material. Due to the extremely low photo-carrier extraction efficiency at low bias voltage, the spectral response could not be detected. Furthermore, while all devices fabricated from p+ and n+ material show rectifying property, p-type material IV characteristics were almost symmetric.

IV.2.2.2 pn-type material

Nc-PSi layers made from pn-type material shows drastically different characteristics that their single doped counterparts. A typical set of pn-type nc-PSi layers PV characteristics are shown in **Fig. 4.15(a) and (b)**. First of all, the pn-type material shows far higher rectification ratio with an average of RR = 25 - 50 at 1V due to a reduced current leak in reverse polarization. The most interesting phenomenon in such layers is the PV effect detected with a large open circuit voltage up to 0.875V as shown in **Fig. 4.15(b)**.
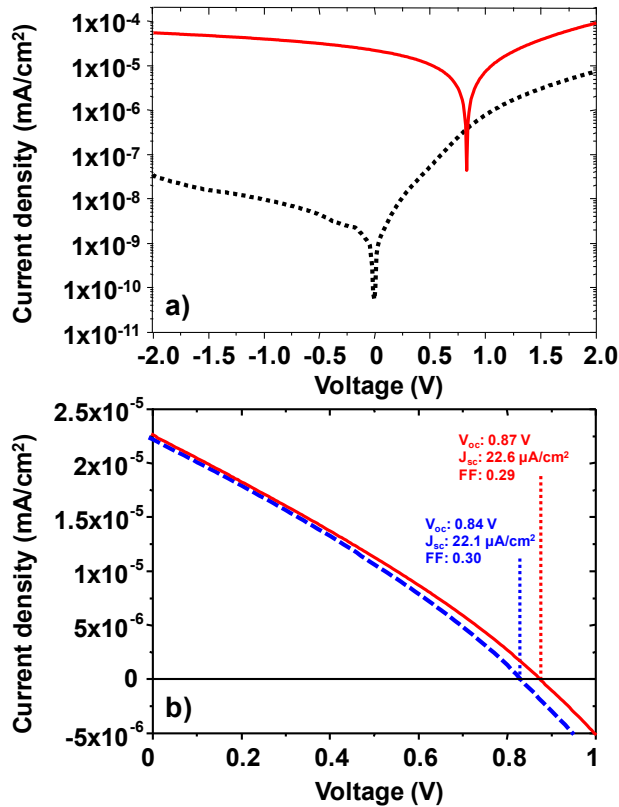
Fig. 4.15: *(a) Typical semi-log plot of the photovoltaic characteristics of a pn type membrane cell, (b) 4th quadrant plot of two pn layers fabricated in the same condition. The blue and red characteristics (V_{oc} of 0.84V and 0.875V respectively) were measured from two different devices made from the same free-standing layer, showing a good homogeneity between devices made from the same substrate.*

In such layers, the V_{oc} was detected in the range 0.35 to 0.875 V with strong inter-sample variations. The highest value of 0.875V is a very high value for silicon based cell, far exceeding both the original value obtained from the bulk substrate ($V_{oc} \sim 0.5 - 0.55$ V) and the typical V_{oc} measured in high quality c-Si solar cells (V_{oc} between 0.6 to 0.7 V) [8][9]. To our knowledge, such a high value has never been reported elsewhere. The typical value in structure involving nc-PSi were presented and summarized at the end of chapter I, with V_{oc} in the range 0.08 to 0.52 V. These values were measured with on substrate structures only and no report of PV effect in free-standing layers with clear indication of both short circuit current of open circuit voltage has been published so far. High values of V_{oc} were also only recorded in pn type material in stark contrast with the previously discussed single doped material. The semi-logarithmic plot of PV characteristics for both pn type and single doped material is shown in **Fig. 4.16**.
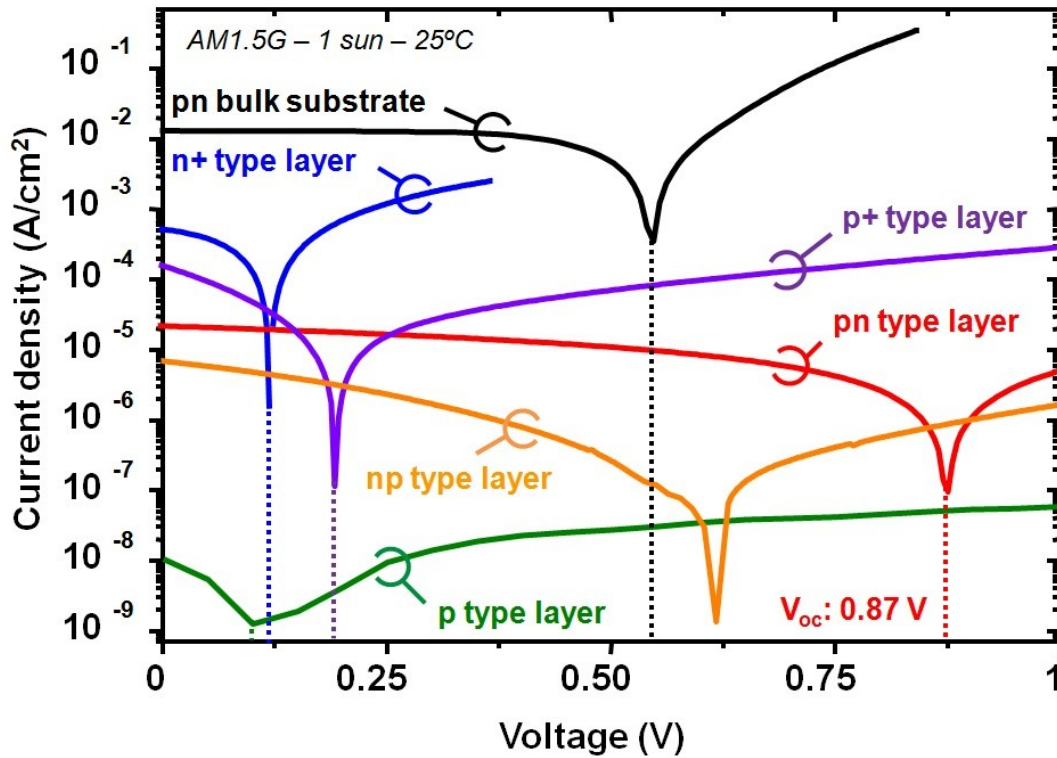
Fig. 4.16: *Comparison of the photovoltaic characteristics of pn and np type layer featuring relatively high V_{oc} with Schottky type devices made from single doped p, p⁺ and n⁺ type material. The result of a non-anodized bulk pn type cell is given as a reference. All the samples were contacted in the Au/Si material/Al configuration for the measurement.*

On the other hand, the short circuit current I_{sc} of such devices is limited by the high resistivity of the nc-PSi film, especially for sample with a substantial thickness of around 25 to 30 μm as the ones presented here. The typical characteristic resistances R_{ch} of pn-type layers are in the range 100 to 200 kΩ. The dark junction resistance defines as $R_j = dV / dI$ for a pn-type device is shown in **Fig. 4.17.** The graph shows a limited saturation in both forward and reverse polarization with a corresponding estimated series resistance Rs of around 300 kΩ (36 to 300 kΩ over several samples) from the forward part of the characteristics, a very high value for a PV device. A shunt resistance of approximately 70 MΩ (4.3 to 70 MΩ) was estimated at 2V in reverse polarization, in line with value expected for a shunt resistance. Such high resistive value clearly shows the necessity to both reduce the overall thickness of the layer and to enhance the surface passivation of the material.
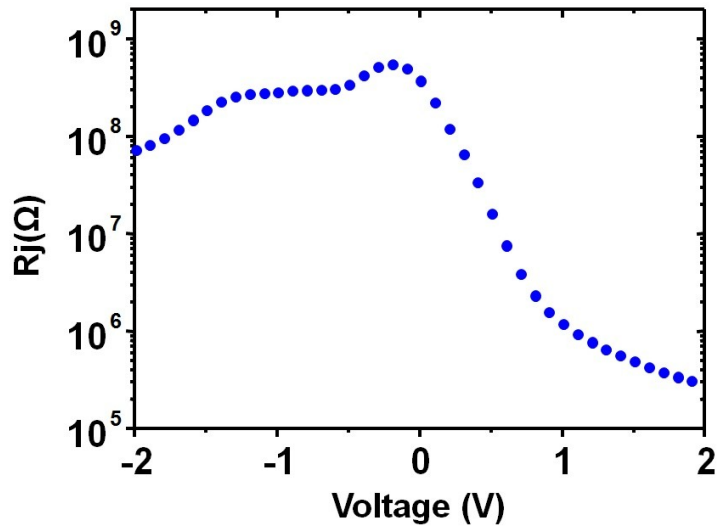
Fig. 4.17: *Junction resistance of a pn type device estimated from the dark I-V measurement. The resistance at high injection voltage in forward and reverse polarization corresponds to an approximation of the series and shunt resistance respectively.*

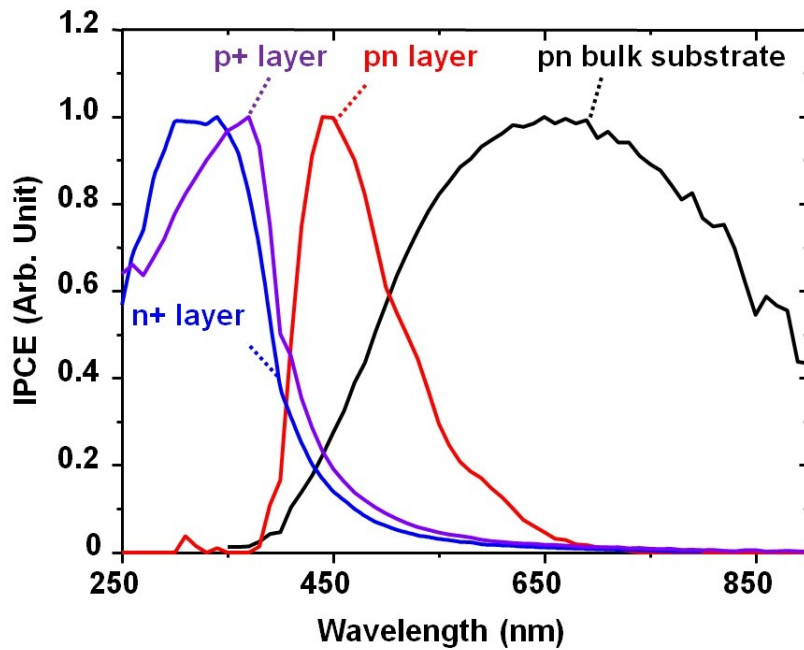**Fig. 4.18:** *Normalized incident photon conversion efficiency for three types of nc-PSi membrane cells in comparison to the original bulk pn type cell. The strong short wavelength responses of single doped layers suggest a Schottky type behavior. The response for pn type layers located at around 450 nm is independent of the nature of the contacting material and originates from the intrinsic properties of the nc-PSi material.*

134

The corresponding spectral response of pn type layers plotted together with p+, n+ and the original Si substrate are presented in **Fig. 4.18**. The pn-type layer shows a distinctive response located at around 450 nm with long response tail down to around 800 to 850 nm. No response was detected past 900 nm. The response appears shifted compare to the bulk reference and no response could be observed in the UV range, excluding the same mechanism as in single doped material. While there is strong variation in the measured J_{sc} and V_{oc} fron one sample to another, all devices show extremely similar spectral response with very low variation of the peak position in the range 430 to 450 nm. The response was independent on both the nc-PSi formation conditions and also independent on the applied voltage as seen in **Fig. 4.19**. While the apparent shift in response of the material can be interpreted in terms of bandgap widening, it is important to note that at the same wavelength of 450 nm, the original Si substrate still has a very low response tail and due to the great difference in absolute efficiency between the two materials, the response of the nc-PSi is lower than the corresponding efficiency of the bulk substrate at 450 nm and therefore still lies within the response spectral distribution of the bulk Si material. A clear confirmation of the shift could be obtained if the efficiency of the nc-PSi material was largely increased at the same energy compare to the Si substrate.
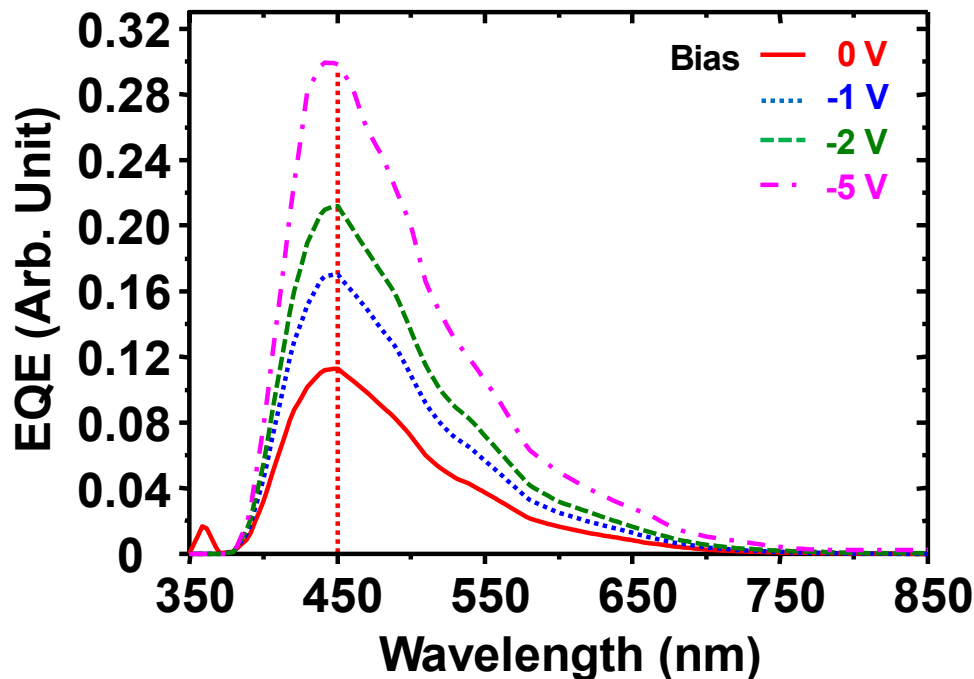

Fig. 4.19: *IPCE of a pn type membrane at different voltage bias showing almost no dependence on the applied voltage.*

The dependency of the spectral response of photodetectors made with nc-PSi material shows contradictory results. A shift toward higher energy of the photo-response in function of the

135

porosity has been reported by Kalhili et al [10] with a shift from 600 to 520 nm. The shift was attributed to bandgap widening but the results are not completely convincing. On the other hand, Torres et al [11] reported that while a clear shift in the PL emission energy was detected with increase in porosity, no modification of the PC peak was detected. The efficiency of the photo-conversion also strongly decreased at higher porosity, similarly to the difference seen between n+ and p type material previously presented in this section. They attributed the freezing of the PC to the large density of surface states, strongly affecting the lifetime of the photo-generated carriers. Carrier trapping is one the most probable effect detected in our sample as well considering that the material is as prepared, un-modified with a large quantity of dangling bonds, impurities and defects located at the surface. Since the PL emission intensity of our pn type devices is extremely low due to a very thin luminescent layer, the radiative recombination path cannot be accounted to explain the low photo-carrier collection of the devices.

IV.2.2.3 Effect of formation parameters

The effects of formation parameters on the PV characteristics of pn type layers have been investigated. During formation, the solution type and content was kept constant and the formation current was varied in the range 5 to 50 mA/cm^2. The effects of anodization current variation on the PV parameters I_{sc}, V_{oc} and the fill factor are plotted in **Fig. 4.20**.
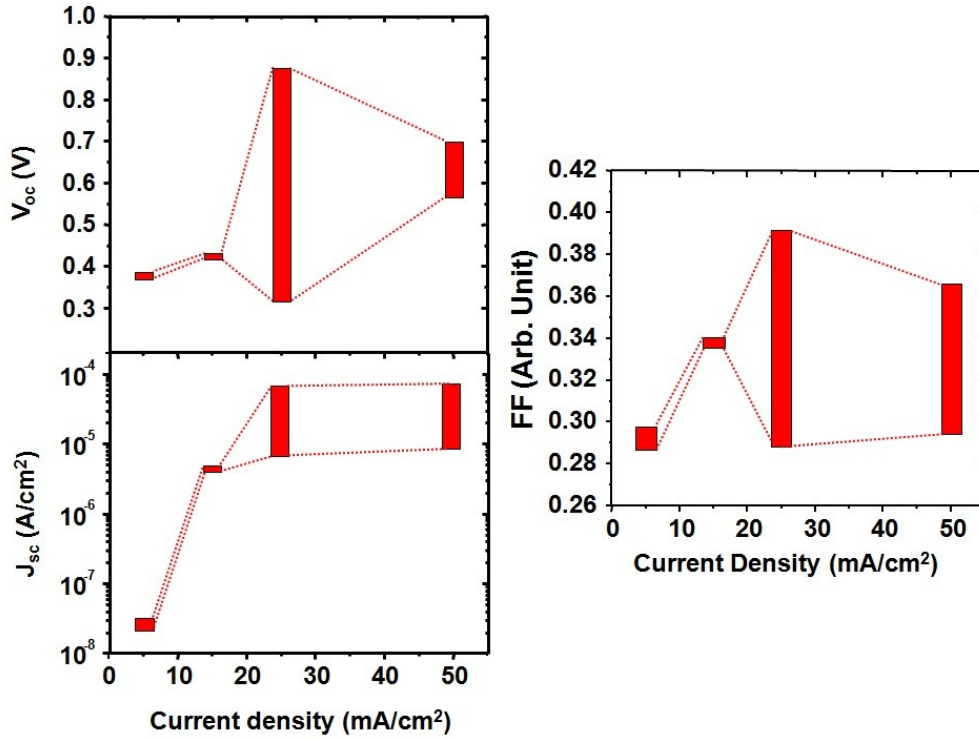

Fig. 4.20: *The V_{oc}, J_{sc} and FF values as a function of the anodization current at a fixed HF electrolyte content (HF : Ethanol 1:1). The strong inter-sample variation clearly visible for the V_{oc} at 25 mA/cm^2 is thought to be due to differences in the surface state of the material after fabrication. Post-fabrication dipping in HF electrolyte strongly reduces the parameters variation.*

Both the I_{sc} and the V_{oc} shows a decrease starting at current density of 15 mA/cm^2 and strongly collapsing at 5 mA/cm^2. Such a decrease is assumed to originate from the underlying n+ type material which porosity strongly increases for low current density anodization as previously introduced in chapter I. In PSi, the porosity typically increase with the anodization current except in the particular case of n type material which strong increase in porosity degrades the photo-conduction of the device. Samples anodized under a current density of 5 mA/cm^2 also features a measurable PL directly from the top surface as seen in **Fig. 4.21**, in comparison with samples prepared at 25 mA/cm^2 which PL was barely detectable. The results clearly indicate that if the luminescent and highly porous layer present at the junction between the p and n

material is responsible for the observed high V_{oc} PV effect, a strong increase in its porosity or thickness would irremediably compromise the conversion efficiency of the device. Another interesting phenomenon observed in **Fig. 4.20** is the strong inter-sample variation concerning the open-circuit voltage. In pn layers made in the same conditions, a variation of V_{oc} from 0.3 to 0.87 V was recorded. Despite strong variations between samples made from different substrate sets, different devices made from a unique layer show the same characteristics. The variation might arise from uncontrolled parameters during the fabrication and does not seem to be related to the device fabrication itself. We will see further in detail the relation of the V_{oc} characteristic variation and the effect of post-anodization treatment in chapter V.
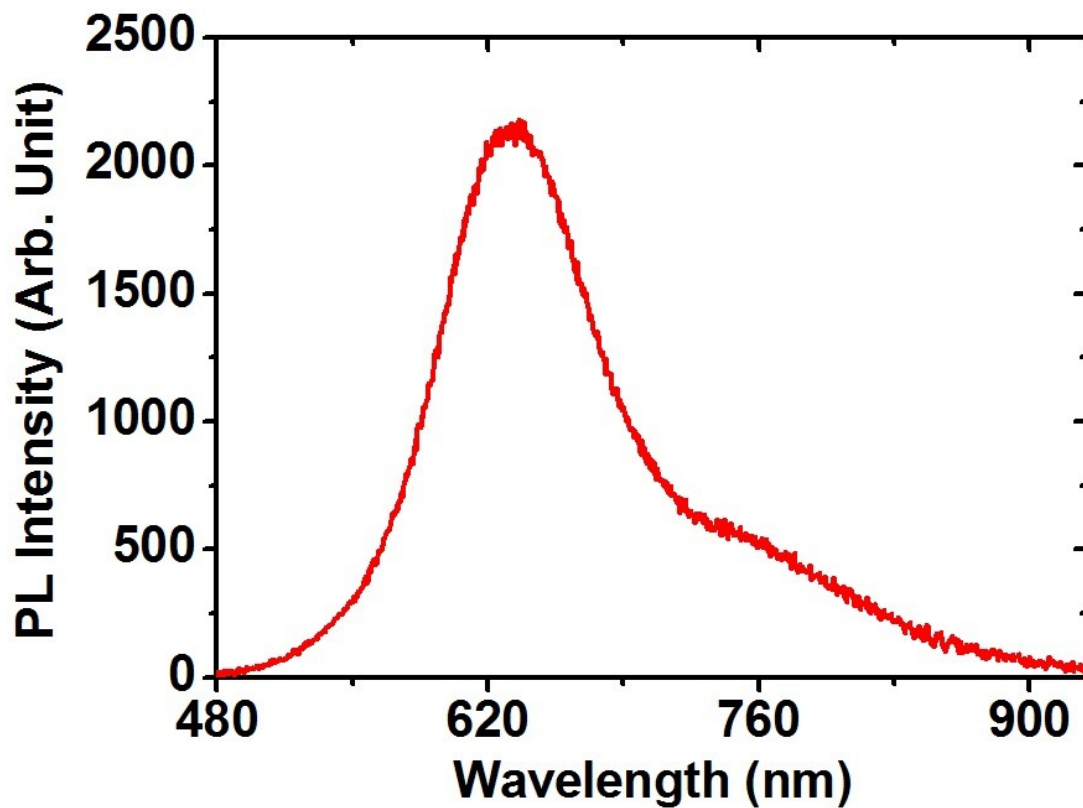

Fig. 4.21: *PL spectrum of a pn type sample anodized at 5 mA/cm^2 featuring a strong visible luminescence due to the strong decrease of the nanostructure size at lower formation current.*
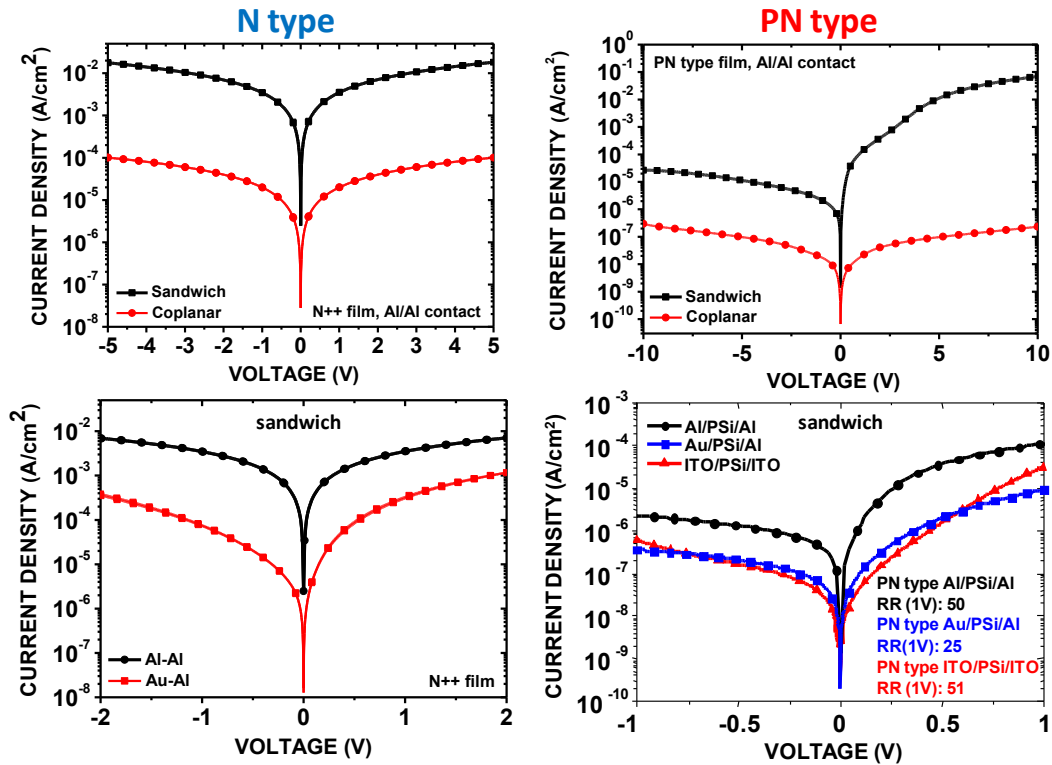
IV.2.2.4 Effect of contacting material

Fig. 4.22: *Effect of the top contacting materials on the rectification properties of the nc-PSi devices. N type layers show a dependence on the nature of the contacting metal with low rectification detected only with Au as a top material. In comparison, the pn type material shows higher rectification ratio independently of the nature of the contact material.*

In order to clarify the origin of the observed PV effect and the contribution of the top contacting material, layers made from pn and n+ type silicon were fabricated and contacted both in co-planar, symmetric and non symmetric sandwich structures using both Au and Al as contacting materials. The pn type layers were further contacted in sandwich with ITO layers as well. Previously presented PV characteristics for pn and n type material all employed an asymmetric Au/PSi/Al structure featuring lowly rectifying behavior for n type and moderately rectifying one for pn material. When contacted symmetrically with Al contact, the n type material features a perfectly symmetric IV characteristic even at high injection regime in both co-planar and sandwich modes as seen in **Fig. 4.22**.

On the other hand, the pn type material features a strong rectifying characteristic even with Al as a top contact. As expected, the co-planar characteristic was perfectly symmetric. The same rectification was observed when contacted with ITO on both sides as well. The n type material

139

shows a rectifying behavior only when contacted with Au, showing the Schottky nature of such contact. The depletion layer between n type material and the top contacting Au metal could explain the observed PV effect with a low V_{oc}, a strong short wavelength response showing that carrier separation occurs near the surface of the device. On the other hand, the strong rectifying characteristic of pn type independently of the contacting material indicates the presence of the pn junction in the material even after porosification. A similar effect was reported early on EL devices using a similar pn structure. Such luminescent devices show enhanced efficiency compare to equivalent single doped devices [12][13]. The origin of the enhancement was imputed to the presence of the original junction in the material. We are expecting the same contribution of the junction in the observed PV effect as well. If the effect of the doping remains active in the porosified material, it could at least partially solved the difficult problem of doping efficiently Si nanostructures. For samples contacted with ITO on both sides, a PV effect similar to the one obtained with Au contact has been measured as seen in **Fig. 4.23**. The devices show a similar spectral response than with Au, showing the negligible impact of top contacting material on the photoconductive characteristics of the material.
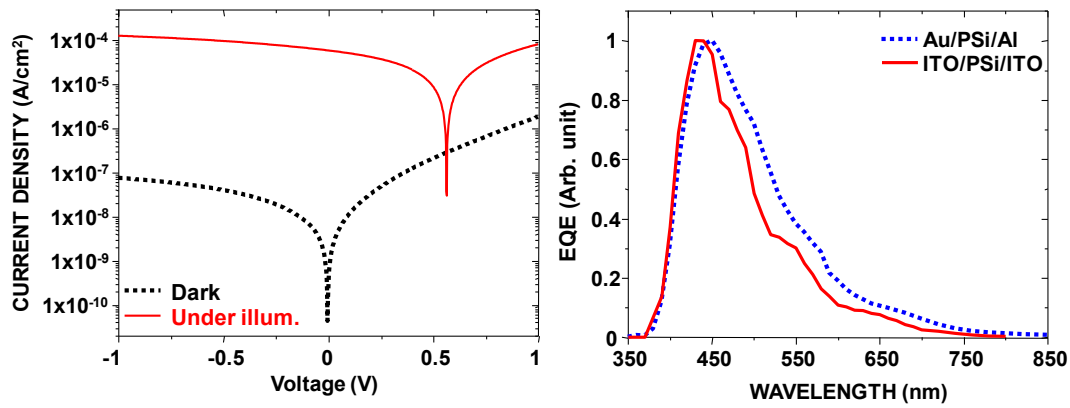
Fig. 4.23: *Photovoltaic characteristics of a pn type layer contacted by ITO on both side in sandwich configuration (ITO/nc-PSi/ITO structure). The device show relatively high V_{oc} with a spectral response similar to devices contacted in the Au/nc-PSi/Al configuration. The result confirms the negligible contribution of the contact on the observed photovoltaic response of the device.*

A second aspect confirming the schottky behavior of Au/PSi interface can be observed through dark conduction fitting of both n and pn type materials using the thermionic-emission-diffusion equation:

$$J = A^{**}T^2 e^{-\frac{q\phi_b}{kT}}[e^{-\frac{qV}{kT}} - 1]$$

140

With ϕ_b the barrier height in volt and A^{**} the effective Richardson constant which value used here was 120 A/cm²-K² (assuming bulk n type Si material). The effect of a series resistance R_s was included as introduced in chapter III. The results of the fit for n and pn type material are given in **Fig. 4.24**. The thermionic-emission-diffusion model fitted relatively well with the IV characteristics of n type material in the forward polarization up to 2V. The barrier height and ideality factor both show moderate and realistic values. On the other hand, fitting of the pn type material IV characteristic were not successful. The best fit did not match satisfactorily the experimental data and the corresponding parameters, especially the high value of n, pointed to the inadequacy of the model. When replace by a simple power law:

$$J = AV^n$$

with both A and n constant, the fitting shows a far better matching to the curve at least for higher injection regime between 1 and 2V. A factor of 3 also seems to be relatively realistic, showing that the conduction in nc-PSi might be space charge limited as previously discussed in chapter I. The SCLC model also fits well with the physical nature of nc-PSi, being a disordered material almost completely depleted of free carriers.
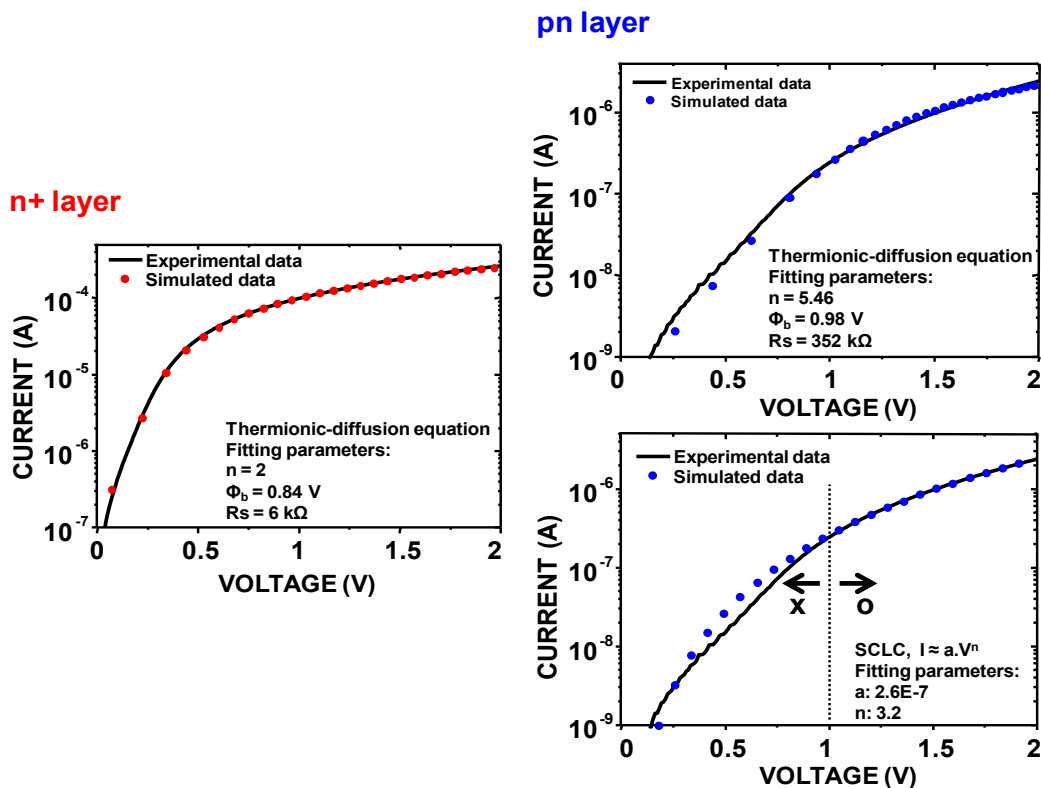

Fig. 4.24: *Fitting of dark I-V characteristics using a thermionic-diffusion model and a SCLC model for n and pn type layers.*

The large internal surface of the nc-PSi material makes it extremely sensible to external condition and contamination. The original hydrogen layer covering most of the material surface right after fabrication is slowly changed to oxide or hydroxyl group even if care is taken in the material handling and storage. The effect of surface is accentuated during measurement when modifications of the material are induced by light excitation, electron beam or more simply electrical characterization.

IV.2.3.1 Degradation under illumination

In the case of PV application, the extremely wide energy range and high power spectra of a solar simulator generates visible variation in the characteristics of the material over time. **Fig. 4.25(a)** and **(b)** shows the time-variation of the I_{sc} of pn and n+ type layers under solar illumination for 90 min and 60 min under a constant voltage bias. The current shows a slow exponential decrease before slowly starting to saturate. In most cases, the current did not completely stabilize even after exposition of more than three hours to AM1.5G light. A similar trend for the V_{oc} is seen in **Fig. 4.25(c)**. The current variation could not be fitted with a simple exponential but rather by a double exponential with two different time constants as shown in the inset of **Fig. 4.25(d)** for both n+ and pn type, indicating the possibility of multiple parallel degradation phenomena in the material. The temperature of the devices under illumination was maintained at the standard temperature of $25^{\circ}C$ to eliminate any possible effect of temperature variation. The time variation of the characteristics were also far slower than typical measurements time scale and previous PV characteristics and spectral response measurement were not affected by the aging phenomena of the material. The variations were also strongly samples dependent with some peculiar case where the I_{sc} and V_{oc} increased exponentially instead of decreasing.
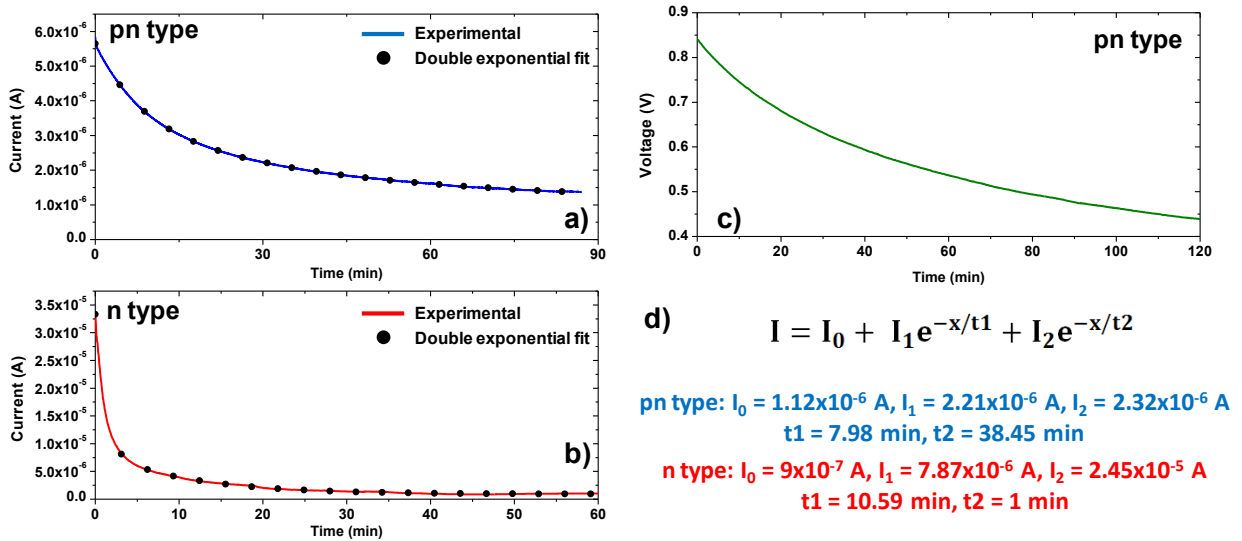
Fig. 4.25: *Time variation of the photocurrent and photovoltage under AM1.5 – 1 sun illumination for pn and n type material. The corresponding double exponential fit function is shown in inset d).*

Among the possible explanation for the observed degradation of the conduction over time is the slow reaction of the material large surface with air and its slow oxidation or the rapid formation of siloxene / hydroxyl species at the surface [10]. The weak Si-H passivation layer present at the surface of as prepared material could be easily broken by thermal and photoexcitation from an external light excitation source. Indeed, photo-induced desorption of hydrogen from PSi surface has been detected by Collins et al [14], and a accelerated degradation of the PL of the material was especially notable for energy in excess of 3 eV (~ 413 nm). Due to the similitude between the conduction and PL degradation under light illumination, desorption of hydrogen is a strong candidate to explain the degradation phenomena. FTIR measurements done on a p type free-standing layer before and after exposure to solar irradiance for 2 hours did not show marked difference in the hydrogen vibrational group intensity. Longer exposure to light excitation might be necessary to detect any significant change of the surface chemistry. A more complete investigation of the photoconduction time variation is available [15][16] and shows a dependence of the variation in function of the wavelength. Desorption of hydrogen from the surface was also cited as one possible explanation. The previous results all show the necessity to enhance the surface passivation of the material for any further practical applications. The effect of such modifications of the material and their impact on stability will be discussed in chapter V.

IV.2.3.2 Geometrical homogeneity of free-standing layers

Another factor accounting for the large variability of the nc-PSi characteristics is the possible in-homogeneity of both the thickness of the layer as well as its volumic nano-structural properties. The surface of nc-PSi layers, especially for the pn type, shows strong color variation between the center and edge of the sample surface due to etching in-homogeneity during fabrication. To assess the variation of the layer characteristics along the surface, free-standing layers of pn and n type material were contacted with a large Al layer as the back contact and a matrix of smaller Al pad at the top resulting in a device structure shown in the inset of **Fig. 4.26**.
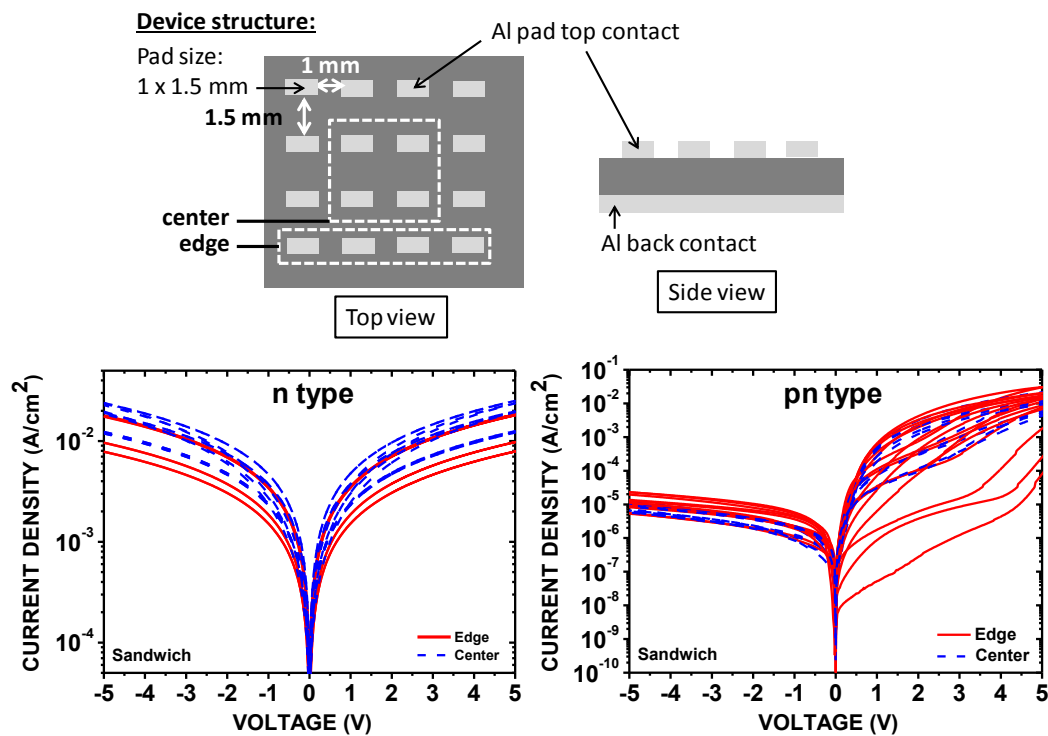
Fig. 4.26: *Surface homogeneity test on n and pn type material showing a notable difference in conductivity between the center and edge of the layer especially fot pn type fabricated under photo-assistance.*

The center and edge of the pad matrix was aligned to the center and edge zone of the nc-PSi layers. Each device was measured in sandwich configuration using a double voltage sweep. The results for both n and pn type material are shown in **Fig. 4.26**. Pads located in the center and edge zone are plotted in blue and red respectively. N type material shows moderate variation from one device to another with all recorded devices current minimum and maximum being contained within 1 decade at a given voltage. Devices located at the edge of the layer tend to

144

have slightly higher resistivity than in the center but the difference is relatively small. All devices did not show any notable hysteresis both in forward and reverse polarization. Such results are in accordance with the low porosity of the material and the absence of in-homogeneity due to illumination effect since the material was prepared under dark condition. The case of pn material is notably different. The difference between devices located at the center and edge of the layers is noticeable by the presence of a strong hysteresis in the forward region for devices located at the edge of the layer showing a strong trapping effect. Such devices also tend to have slightly higher reverse current probably due to a degradation of the junction quality on the edge. During anodization, the silicon area located at the edge of the etching mask tends to be over-etch, especially for long etching duration, resulting in a material with a higher porosity and probably a different nanostructure than the center of the top of the layer. The effect is clearly visible through PL measurement where the edge usually shows strong visible luminescent while the center is mostly non luminescent. The higher porosity of the material can explain both the degradation of the diode characteristics and the presence of strong trapping inside the highly photoluminescent material located at the edge. In order to avoid the effect of such edge over-etching on the electrical characteristics of the device, care has been taken to align the top contact at the center of each device.

Bibliography of Chapter IV

[1] O. Bisi, S. Ossicini, L. Pavesi, Surf. Sci. Reports **38**, p. 1 (2000).

[2] D. Kovalev, H. Heckler, G. Polisski, and F. Koch, phys. stat. sol. B **215**, p. 871 (1999).

[3] M. H. Chan, S. K. So, and K. W. Cheah, J. Appl. Phys. **79** (6), p. 3273 (1996).

[4] E. Bustarret, M. Ligeon, I. Mihalcescu, J. Oswald, Thin Solid Films **255**, p.234 (1995).

[5] D. Kovalev, G. Polisski, M. Ben-Chorin, J. Diener, and F. Koch, J. Appl. Phys. **80** (10), p. 5978 (1996).

[6] B. Gelloz, R. Mentek, and N. Koshida, Jp. J. of App. Phys. **48** 04C1191 (2009).

[7] B. Gelloz, B, N. Koshida, ECS J. of Solid State Sci. and Tech. **1** (6) p. 158 (2012).

[8]L. Barraud, Z.C. Holmann, N. Badel, P. Reiss, A. Descoeudres, C. Battaglia, S. De Wolf, C. Ballif, Solar Ener. Mater. & Solar Cells **115**, p. 151 (2013).

[9] C. Honsberg, S. Bowden, http://pveducation.org retrieved on 2013/11/07

[10] H. Khalili, R. S. Dariani, A. MortezaAli, V. Daadmehr, K. Robbie, J Mater Sci **42**, p. 908–913 (2007) - DOI 10.1007/s10853-006-0010-2

[11] J. Torres, H.M. Martinez, J.E. Alfonso, L.D. Lopez C, Microelectronics Journal **39**, p. 482 (2008).

[12] P. Steiner, F. Kozlowski, W. Lang, Appl. Phys. Lett. **62**, p. 700 (1993).

[13] J. Linnros, N. Lalic, Appl. Phys. Lett. **66**, p. 3048 (1995).

[14] R. T. Collins, M. A. Tischler, and J. H. Stathis, Appl. Phys. Lett. **61**, p. 1649 (1992) - doi: 10.1063/1.108440

[15] T. Frello, E. Veje, O. Leistiko, J. Appl. Phys. **79** (2), p. 1027 (1996).

[16] Md.N. Islam, P.S. Dobal, H.D. Bist and Satyendra Kumar, Solid State Communications. **107** (1), p. 43 (1998).

Chapter V. Photovoltaic characteristics stabilization

V.1 Post-formation Treatments

V.1.1 Chemical etching

In order to get a better understanding of the large PV characteristic variation observed in pn type nc-PSi layers, a set of samples fabricated in the exact same conditions (HF 27.5 wt% - 25 mA/cm^2) were exposed to further chemical etching through dipping in a HF in the same proportion as the electrolyte used during the layer formation. Right after fabrication, the layers were dried under super critical condition and their weights were measured. The layers were then re-introduced into an HF solution for duration between 30 min to 6 hours. After etching the layers were dried again under super critical condition and their weight were measured a second time to assess the volume of silicon lost during the chemical etching. The PV characteristics parameters V_{oc} and I_{sc} for layers etched at different duration are shown in **Fig. 5.1**.
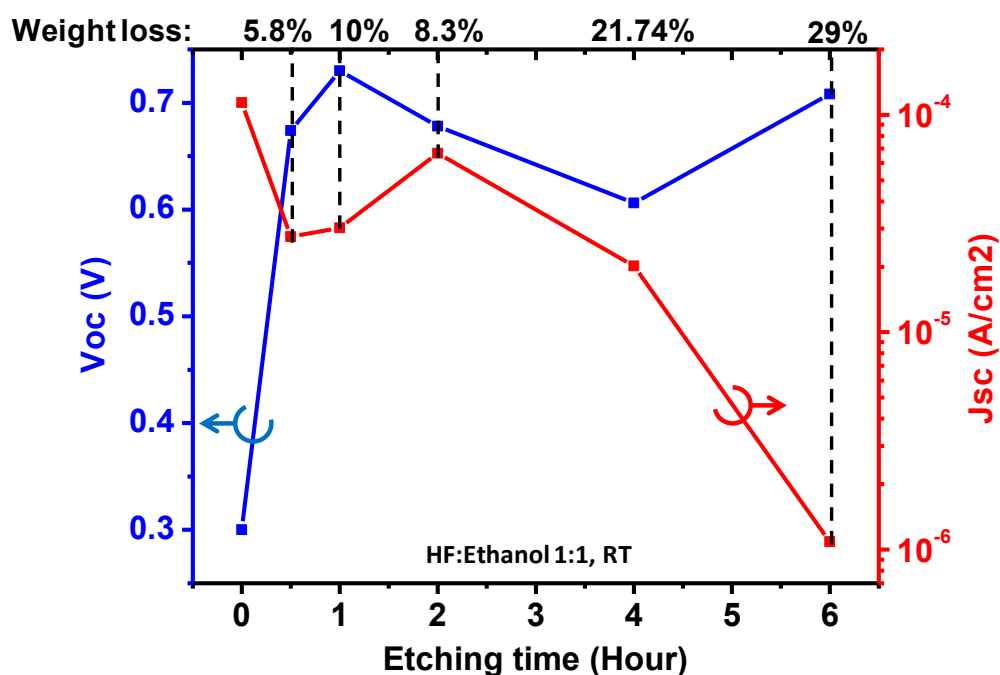

Fig. 5.1: *Variation of the V_{oc} and J_{sc} values with the post-fabrication chemical etching duration. The decrease in weight of the free-standing layer, estimated from the weight measure before and after etching, is indicated in percent at the top of the graph. Samples at time 0 h correspond to as-prepared ones.*

The weight loss of the samples estimated from the measurement before and after etching is indicated at the top of the graph for each measured sample. As expected, a linear decrease of the J_{sc} is clearly visible with the increase in etching duration due to the linear increase in the porosity and therefore the resistivity of the material. However, the most remarkable phenomenon is the strong increase and stability of V_{oc} after exposure to HF solution even for duration as short as 30 min. In the set of samples presented here, the sample at duration 0 min was not subject to post etching and measured directly after fabrication. That sample features characteristics in the lower range of value with a small V_{oc} of 0.3 V. Right after post chemical etching, all samples features a V_{oc} in the higher range of value, even for longer duration. The variation of V_{oc} seems to be almost independent on the etching duration and therefore the porosity of the material. Nc-PSi material when exposed to HF solution has its surface rapidly stripped out of any native oxide layer and is subsequently recovered by hydrogen atoms and the material is then relatively stable with extremely low etching rate; at room temperature Silicon in a 27.5% HF solution without additive or gas bubbling has an etch rate far below 1 nm/h [1]. A short exposure of 30 min cannot realistically lead to drastic increase in porosity or decrease in the nanostructures size in the material. The phenomenon observed here indicates a strong involvement of the surface passivation / chemistry in the measured PV characteristics. A plot of the inter-sample characteristics variation with and without chemical post-etching is shown in **Fig. 5.2**. While variation still remains after post-etching, the range of value detected has been considerably decreased and the average value of the observed V_{oc} greatly increased. The involvement of surface passivation on photo-electrical characteristics has been further confirmed by investigation of the effect of thermal annealing on the nc-PSi material presented in the following section.
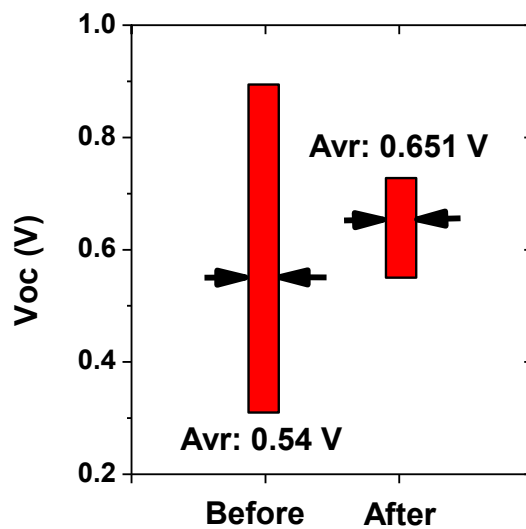

Fig. 5.2: *Variation and average value of the V_{oc} before and after post-chemical etching in HF (measured on 10 devices or more).*

V.1.2 Thermal annealing

In the previous section, the results after post-fabrication etching show a possible relation between the surface passivation by hydrogen atoms and the observed high V_{oc} and its large variability from one sample to another. Since the as-prepared material both before and after post-fabrication etching is largely covered by hydrogen, representative differences between the hydrogen coverage before and after the chemical etching could not be detected. Oppositely, the desorption of surface hydrogen by thermal annealing could provide further indication on the involvement of the surface on the observed photo-conductive phenomena. Both as-prepared pn and n type samples were annealed under an inert Ar atmosphere at two different temperatures of 200 and 600°C for 30 min right after fabrication of the layers. The corresponding FTIR spectra measured in transmittance mode are shown in **Fig. 5.3**.
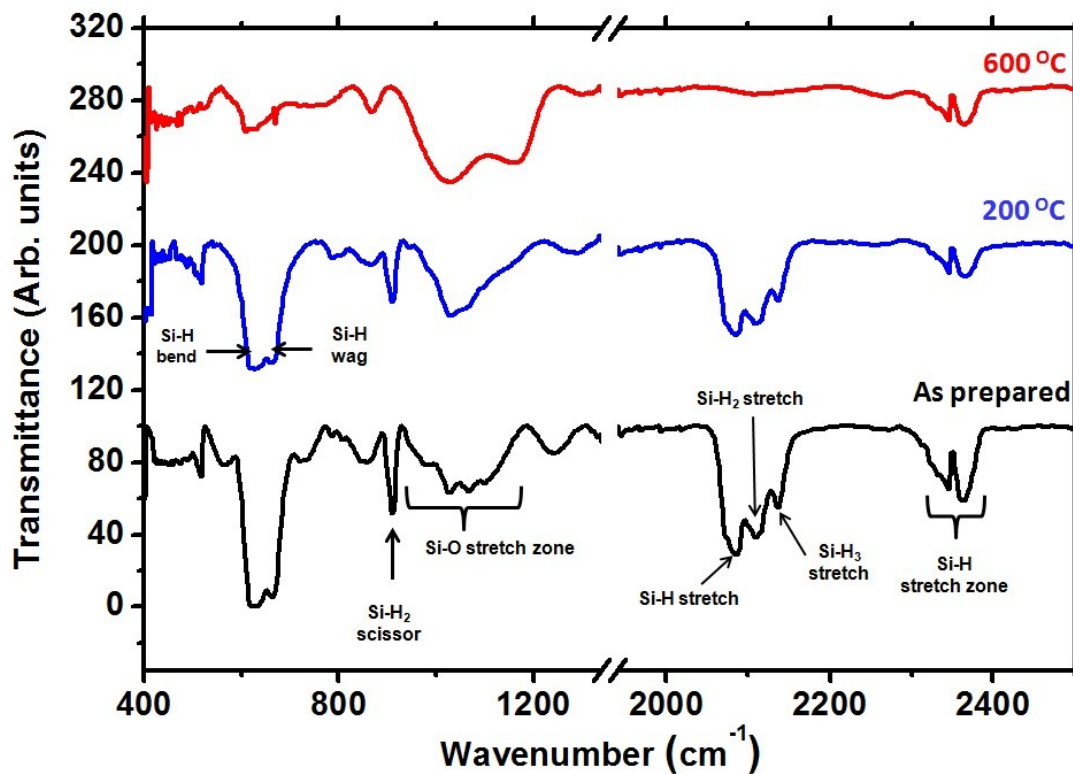

Fig. 5.3: *FTIR spectra in transmittance mode for three layers of nc-PSi as prepared and after annealing in Ar gas at 200 °C and 600 °C during 30 min. The typical peak positions and their respective attributions to Si-H$_x$ and Si-O$_x$ are indicated as a reference. The energy zone around 1200 to 2000 cm^{-1} does not contain relevant information.*

The as-prepared material features the expected Si-H$_x$ vibrational groups at locations 625-630 cm^{-1} for Si-H bend or wag, 660-662cm^{-1} for SiH wag or SiH2 roll, 905-910 cm^{-1} for SiH$_2$ scissors and finally 2083, 2110 and 2135 cm^{-1} for SiH, SiH$_2$ and SiH$_3$ stretching respectively. Annealling at 200°C did not induce any drastic change in the FTIR spectra and only a small decrease in Si-H group is visible. A partial oxidation of the material is also to be expected and visible for wavenumber in the range 1050-1160 cm^{-1}. The Si-O related group peaks are actually already visible in the as prepared sample as well. The low 200°C anneal step did not introduce strong modification of the sample electrical characteristics as seen in **Fig. 5.4(a)**.
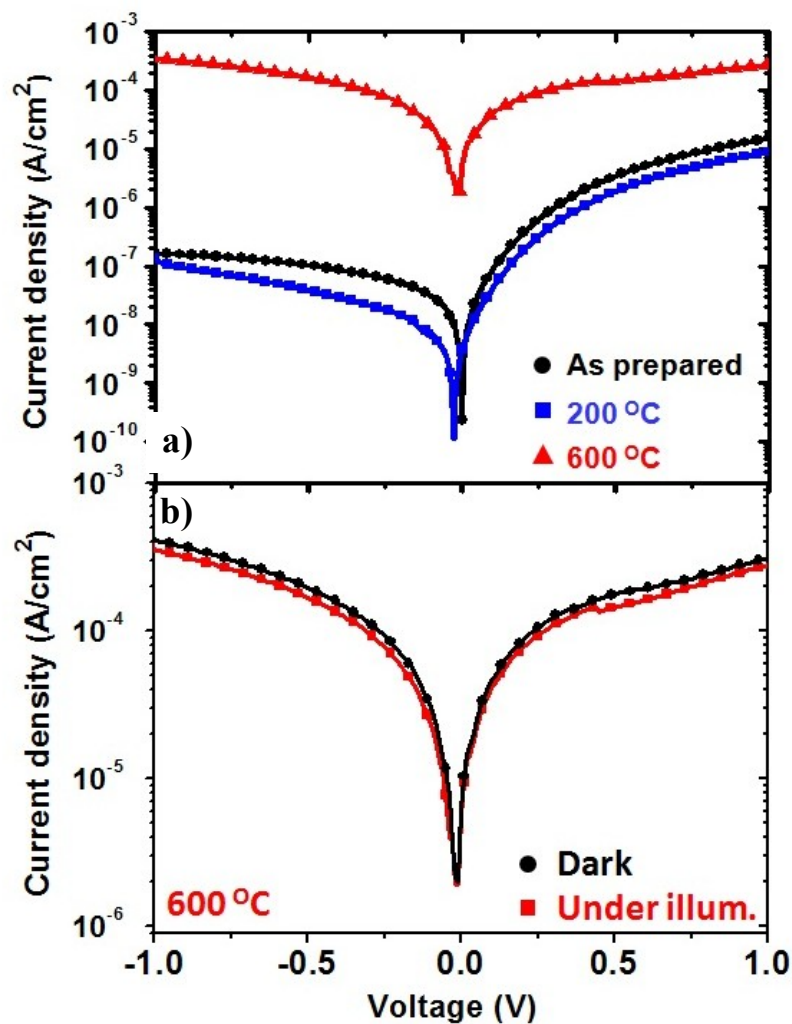

Fig. 5.4: *J-V characteristics of free-standing pn type nc-PSi layers before and after argon annealing at 200°C and 600°C. The top graph shows the modification of the dark current before and after anneal. The bottom graph shows the conduction under dark and illumination condition for the sample annealed at 600 °C.*

In contrast, after annealing at 600°C, the Si-H$_x$ groups almost completely disappeared from the FTIR spectrum, accompanied with a slight increase of the oxide related peak. The complete desorption of hydrogen form the surface is followed by a strong increase of the dark current. The reverse current at a bias of -1V is more than three orders higher after annealing. Similar results were obtained previously by Balagurov et al [2] on low porosity p type material showing strong increase in the dark conductivity for annealing temperature of 150 and 550°C. They attributed such a strong increase to the desorption of hydrogen not only from the surface but more specifically from dissociation of Si-H-B complexes possibly present in the material. The passivation of boron dopants inside the nc-PSi materials by hydrogen atoms was proposed as a possible explanation for the high resistivity of their p type material despite its low porosity (rapid diffusion and passivation of boron imputiry by hydrogen is a well known phenomena [3][4]). In comparison, during our investigation a strong increase in resistivity was detected only for temperature of 600°C and not 200°C. The same trend as pn type was also observed in n type material as well, showing no clear relation with the type of dopant presents in the material. While passivation of phosphorus dopants by hydrogen in n type material cannot completely be excluded, the passivation effect should be clearly far less important than for boron impurities. Furthermore, the two temperatures used for annealing here are also in concordance with previously reported hydrogen desorption temperature from silicon [5]. In addition, measurement under AM1.5G-1 sun illumination as seen in **Fig. 5.4(b)** shows a complete disappearance of the PV effect and photoconduction altogether, for both pn and n type material. We are strongly expecting that the quenching of the photoconduction could be reverse by re-hydrogenation of the surface by a dipping procedure in HF for example. The dipping step could not be realized on the samples presented here due to the presence of metallic contacts necessary for the electrical characterization. The previous results might be explained following two different reasoning: the desorption of hydrogen from the surface actually activate a low resistivity conduction path through surface channels shunting the contribution from the silicon nanostructures were photo-carrier generation is expected to occur; or that the presence of hydrogen species at the surface of nc-PSi are directly involved in the observed photoconductive effect and that their disappearance form the surface are also accompanied with the disappearance of photoconductive effect.

V.2 Surface chemical Modification (SCM)

As previously shown in section **IV.2.4.1**, as prepared nc-PSi is a relatively instable material due to the nature of its surface termination and the immense internal volume available strongly increasing the risk of various external contamination. Stabilization techniques for the optical properties of the material (PL and EL) have been widely investigated using various oxidative techniques. Due to the limited thickness of nc-PSi layers employed in such devices, the oxidation proved to be the most efficient passivation technique while having a moderate degradation effect on the electrical characteristics of the devices. In the case of free-standing layers with a thickness of around 30 μm as in our current investigation, oxidation seems to be an inadequate technique, especially in view of the fragility of the material and the extreme process condition required to obtain a good quality oxidation of the material. For such devices as free-standing layers, the best solution would involve techniques which do not induce drastic change to the material structure and do not require electrical contact, eliminating electrochemical processes. The chemical modification described in detail in chapter III was employed here on as-prepared pn type free-standing layers.
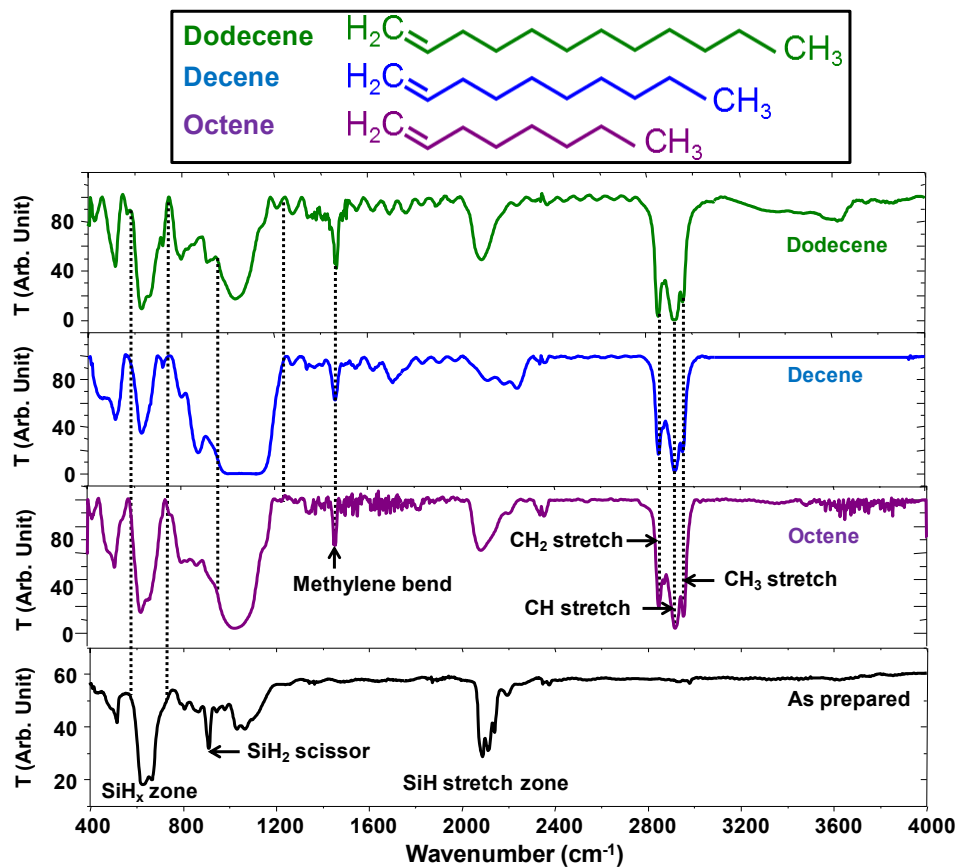

Fig. 5.5: *FTIR transmittance spectra for pn type layers modified with alkene 1-octene, 1-decene and 1-dodecene. Typical energy peaks are indicated as reference.*
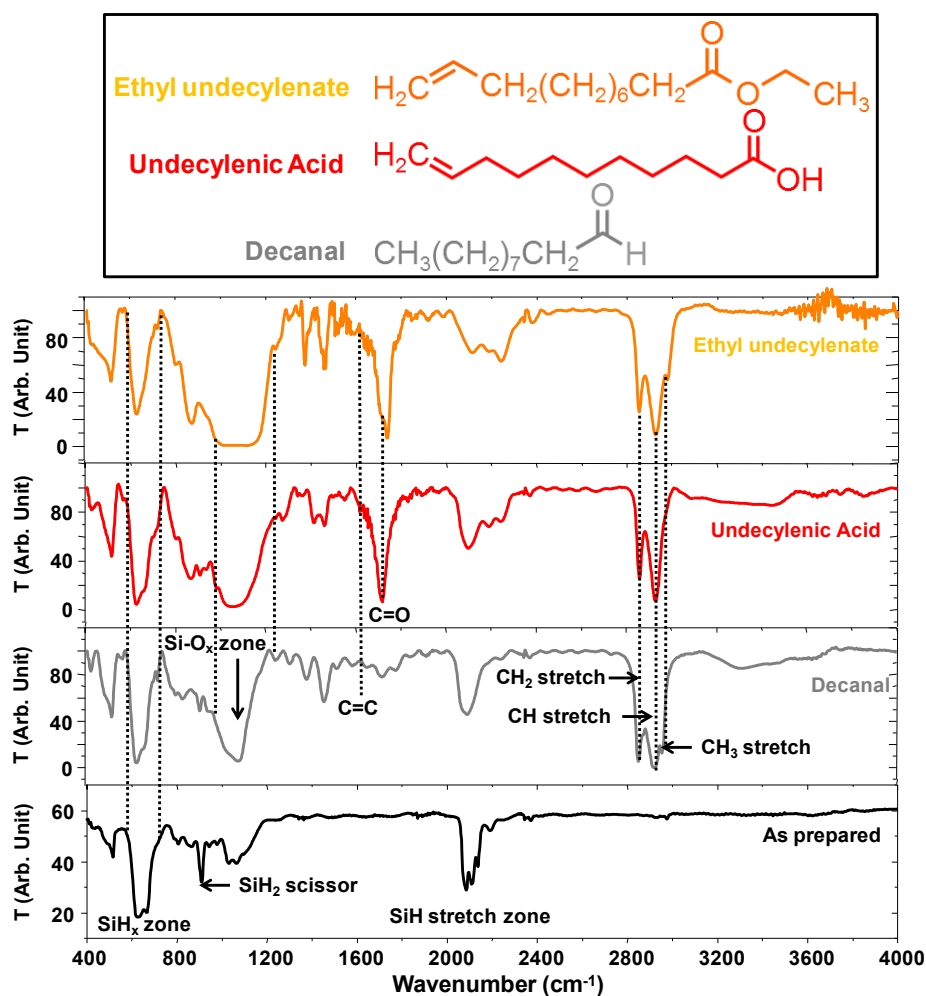
152

Fig. 5.6: *FTIR transmittance spectra for pn type layers modified with decanal (aldehyde), undecylenic acid and ethyl undecylenate. Typical energy peaks are indicated as reference.*

The samples were tentatively modified using alkene molecule such as 1-decene, 1-octene and 1-dodecene, as well as aldehyde group decanal and finally with molecule containing carboxyl group such as undecylenic acid and ethyl undecylenate. The FTIR transmittance spectra for as prepared and modified layers are shown in **Fig. 5.5** for alkenes and **Fig 5.6** for the rest of the organic molecules. After modification, the presence of organic molecules at the Si surface is visible mainly through the appearance of CH_x vibrational group at energies 2860, 2925 and 2960 cm^{-1} for CH_2, CH and CH_3 respectively, visible for all the organic molecules. Specifically related to alkene, a methylene bending (H_2C double bonded with the rest of the chain) peak is also visible between 1463 and 1470 cm^{-1} for octene, decene and dodecene. Following the discussion in chapter III section III.1.1.3.3 concerning the possible reaction pattern for undecylenic acid and ethyl undecylenate containing both a carbon-carbon and a carbon-oxygen double bond, the observation of an additional peak visible at 1720 cm^{-1} attributed to C=O vibration clearly shows that the chemical substitution actually occurred with the C=C and not C=O bond, resulting in a

153

surfacial Si-C configuration. Similarly, the absence of peak at 1640 cm^{-1} corresponding to the double bonded C atoms in all samples clearly shows that the site was used for bonding with the silicon surface and demonstrates the absence of trapped organic solution at the nc-PSi, confirming the covalent bonding at the Si surface instead of simple physical adsorption. A slight decrease and modification of the Si-H, Si-H$_2$ and Si-H$_3$ can be seen after modification, indicating the consumption of hydrogen species replaced by the organic ones. The presence of hydrogen vibration peaks after chemical modification clearly indicates that the passivation of the surface by carbon groups is only partial and that a large number of hydride species remained
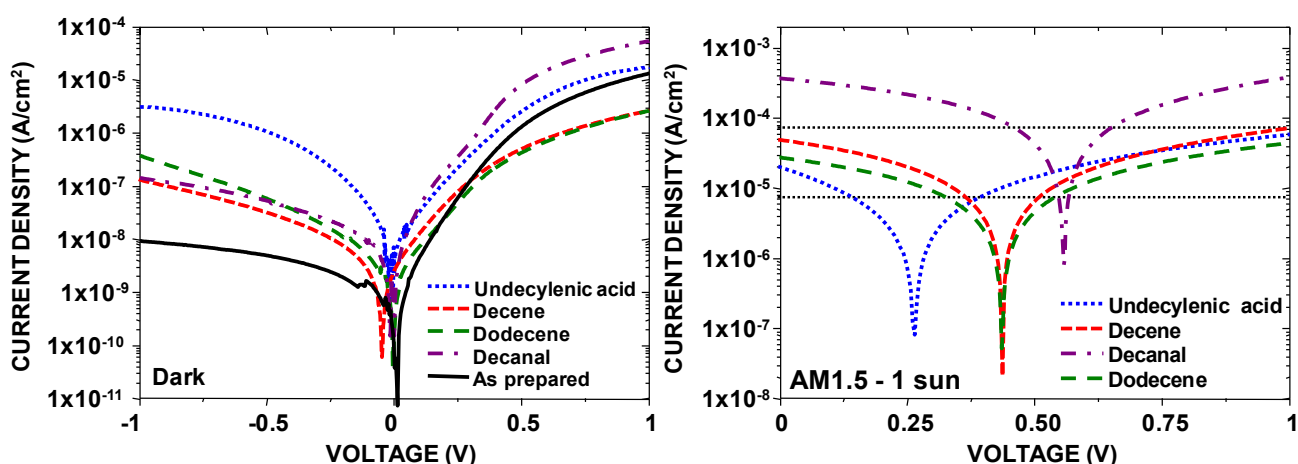
Fig. 5.7: Dark and under illumination I-V characteristics after chemical modification of the surface by organic molecules.

on the surface of the material. The surface coverage is intrinsically limited due to the size of the molecules, the surface crystal alignment and steric effects. The corresponding dark I-V and PV characteristics for layers modified with the 4 organic species are shown in **Fig. 5.7**.

The dark characteristics of nc-PSi after modification shows a slight loss of the device rectifying properties compare to as prepared material. The effect is especially apparent in the sample modified by undecylenic acid which features the highest reverse current and therefore the lowest PV performance. Decene and dodecene presents similar characteristics both in dark and under illumination with the same value of V$_{oc}$ and similar dark conduction, as expected for 2 molecules which only differ by the length of their carbon chain (10 for decene and 12 for dodecene). Modification by decanal is a particular case where a significant increase in J$_{sc}$ was recorded with the highest value of V$_{oc}$ among the modified samples. The corresponding measured spectral responses of the modified devices are shown in **Fig. 5.8**.

Fig. 5.8: *IPCE of pn type devices after various organic surface modifications compare to the original as prepared material response.*

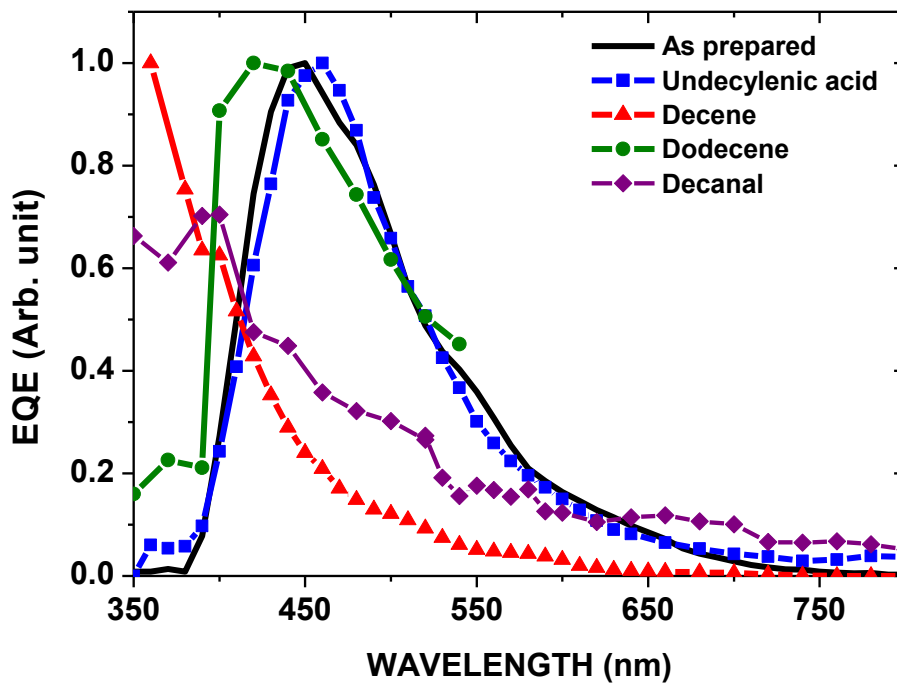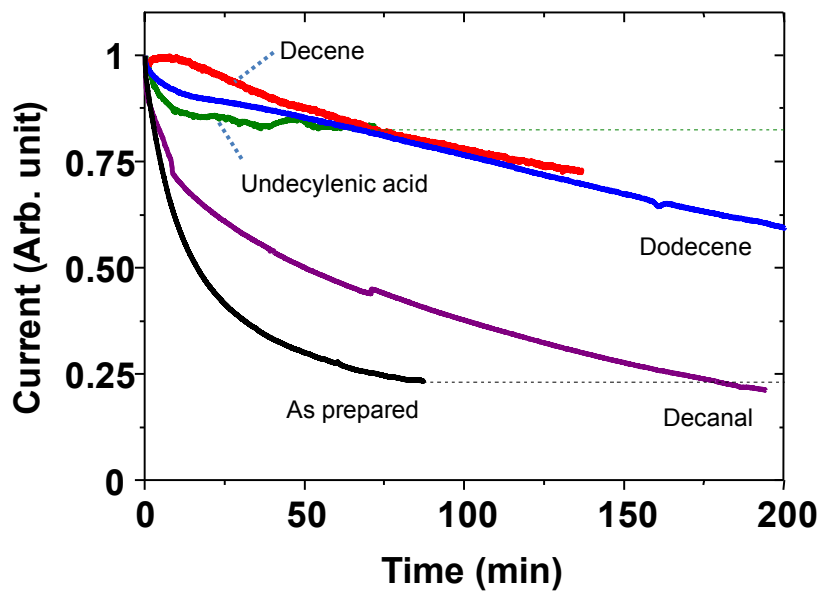
Fig. 5.9: *Time variation of the photocurrent of pn type devices before and after various modifications.*

155

Undecylenic acid and dodecene both feature a response similar to the as-prepared material. On the other hand, both the decene and decanal show a strong shift of the response toward the UV range. The shift can be interpreted as either a de-trapping of the original response due to a better passivation of the surface of the material or by the contribution of the organic species themselves. From the previously presented PV and spectral response data and their relative spread in characteristics, it becomes clear that the modification of the silicon surface is strongly dependent on the type of molecule, the type of bonding and the physical coverage and packing conditions of the molecule at the Si surface. Similar spread in the PSi photo and electro-luminescent characteristics after organic derivatization has been previously observed as well [6]. All molecules bonded with the Si material through a Si-C link all features PV performances in the same range as the unmodified material. Only devices modified with the aldehyde decanal did show a strong increase in the observed photo-generated current, a phenomena that could be explained by the difference in surface bonding, decanal being the only molecule linked through a Si-O bond in this study. Aldehide decanal as well as alkenes are known to have a low conductivity, around 0.067 µS/cm for decanal, suggesting that the passivated surface should be non-conductive as well. Furthermore, as indicated in the review of Shirahata et al [7], molecules bonded through Si-O feature a higher surface coverage than the corresponding Si-C bond, a difference that could explain the difference of characteristics observed when compare with alkene modified devices. Concerning the alkene groups, the results obtained from passivation through decene and dodecene are homogeneous excepted for the difference in spectral response. A closer look at the dodecene response actually shows a small but visible shift compare to as-prepared material. The amplitude of the spectral shift might actually depend on the physical and structural difference between the modified devices due to inter-sample variation but are not expected to originate from the difference in molecules since decene and dodecene have similar structures, differing only in the length of their carbon chain (10 and 12 respectively). The poor electrical performances of devices treated with undecylenic acid might arise from a specifically poor coverage ratio of the surface and the presence of strong disorders in the organic layer [8].

From the point of view of the stabilization, the current-time variation for each device is plotted in **Fig. 5.9**. After modification, each device shows an increase in stability compare to as prepared material, with decanal featuring only marginal increase while undecylenic acid show strong stabilization properties. Such a strong stabilization is in stark contrast with the poor electrical properties of the device, as seen previously in **Fig. 5.7**. If we consider a poor reaction ratio with undecylenic acid, various different modifications of the surface occurring in parallel to the hydrosilylation could have the same aging effect as long time exposure to light (poor and

uncontrolled oxidation of the surface) resulting in an accelerated aging of the device. The resulting material would therefore shows no further variation in time, the surface being already in the same condition as sample aged under long time illumination. In the case of alkene group, once more decene and dodecene show extremely similar time-variation properties due to the similarity of the bonded organic molecule. The preliminary results show a promising passivating effect which need to be further controlled to obtain higher stability of the material. The FTIR spectra of **Fig. 5.5** and **5.6** shows that non-negligible oxidation occurs during the derivatization process and further improvement in the modification procedure, such as better degassing of the organic solutions as well as modification under inert atmosphere might be necessary to obtain a better results in terms of stability and performance. The strong intensity of the oxide peak can be explained by the large thickness of our samples as well. The presence of a strong saturating oxide peak in the decene modified sample can explain for example the capacitive effect seen in the dark I-V characteristics of **Fig. 5.7** with a slight shift of the curve with a non null current at 0 bias. In the same manner, the presence of strong hydrogen peak even after modification indicates that the organic coverage is limited. The replacement percentage limitation was already demonstrated in reference [6] and in the case of our devices, the derivatization time was limited to 3 hours. Longer modification duration could enhance the passivation of the material even further. Lastly, it is possible to mix different solution to obtain the combine effect of different type of molecules. From our own results, it is clear that the strong increase in photocurrent induce by decanal is extremely interesting in terms of performance enhancement but limited by poor stability while oppositely undecylenic acid provided a strong stability with poor PV performances. The combine effect of decanal and undecylenic acid could greatly benefit the photo-conversion performance of nc-PSi material. Several other types of molecules are also available, including the use of shorter molecule from acrylic acid for example, shorter molecules providing higher coverage of the surface. Reports on such modification on silicon nanodots are very recent [9] and their possible application to nc-PSi are still widely unknown.

Bibliography of Chapter V

[1] V. Lehmann, Electrochemistry of Silicon: Instrumentation, Science, Materials and Applications, Wiley-VCH Verlag GmbH, Weinheim (2002).

[2] L.A. Balagurov, D.G. Yarkin, E.A. Petrova, Mater. Sci. and Eng. B **69–70** p. 127 (2000).

[3] S. M. Pietruszko, M. Pachocki, J. Jang, Journal of Non-Crystalline Solids **198-200,** p. 73-76 (1996).

[4] K. J. Chang and D. J. Chadi, Phys. Rev. Lett. **60** (14), p. 1422 (1988).

[5] H. Neergaard Waltenburg, J. T. Yates, Surface Chemistry of Silicon, Chemical Reviews **95** (5), p. 1589 (1995).

[6] J. M. Buriak, Chemical Reviews **102** (5), p. 1271 (2002).

[7] N. Shirahata, A. Hozumi, T. Yonezawa, The Chem. Record **5**, p. 145 (2005).

[8] S. Pace, L. Gazagnes, P. Gonzalez, C. Guimon, M. Granier, D. Cot, J.-M. Devoisselle, and F. Cunin, P hys. Status Solidi A 206 (6), p. 1326 (2009). DOI 10.1002/pssa.200881080

[9]R. Bywalez, H. Karacuban, H. Nienhaus, C. Schulz, H. Wiggers, Nanoscale Res. Lett. **7**, p. 76 (2012).

Chapter VI.   Conclusion

This study had for main objective to demonstrate the possibility to use nanocrsystalline porous silicon has an active element for solar cell, based on the assumption that the material behave as a wide-gap material. For that purpose, the fabrication of free-standing layer of nc-PSi was investigated and the photovoltaic properties of the material investigated. The most important achievements obtained are listed in the following section VI.1. In parallel to the achievements, an overview of the limitations and problems posed by the material in relation to the wide gap nature of the material are presented in section VI.2. Finally, further suggestions and discussion for future investigations will be discussed in the last section.

VI.1 Achievements summary

- Introduction to a new free-standing device structure made from already doped junction type material for photo-electrical characterization of the nc-PSi only, without contribution from the bulk Si substrate.

- Investigation on the nc-PSi membranes separation process shows the possibility to reduce the thickness of the layers and to increase the separated surface up to wafer size without damage. A better understanding of the separation parameters, including patterning of the peeling current and control of the solution viscosity through chemical additive and/or temperature controlled has been obtained.

- For the first time, a distinct PV effect was observed in free-standing pn type devices without the presence of c-Si substrate. The detected PV effect features a relatively high V_{oc} up to 0.875V under Am1.5G – 1 sun, suggesting the possibility that the material might be acting as a wide-gap absorber.

- The observed PV was attributed to the intrinsic properties of the nc-PSi material itself:
  - Effect of contact negligible on the observed rectifying and PV characteristics for pn type devices.
  - Clarification about the presence of a junction inside the porosified material: both sandwich contacting with different materials as well as the observation of a particular IV characteristics during material formation and separation of the pn layers (overpotential during high current injection, strong potential drop after layer

separation) clearly indicate that the junction remains active in the material even after porosification.

● The observed PV characteristics and its large performance variation were shown to be related to the apparent surface passivation of the material. Strong effect of post-treatment of the surface on electrical properties, including HF chemical etching and annealing, similar to that observed on luminescence (quenching of both PL, EL and PV/PC after complete desorption of hydrogen) were obtained. Since the effect of the surface chemistry appeared to be pre-dominant over the structure of the device itself (changes in thickness of the three layers present in the material as well as changes in the original pn type junction structure did not show conclusive change in the devices characteristics), the study therefore strongly focused on possible surface passivation over investigation of the device structure and optimization.

● Demonstration of the possibility to moderately stabilize the material using surface chemical modification with organic molecules, without important degradation of the material properties. Modifications of the PV characteristics, such as spectral response shift and increase in photo-generated current, were observed.

● A comparison table with concurrent approaches to Si nanodots based solar cells is shown in **Table 6.1**. The results listed here are based on full Si nanodots cells, without contribution from an underlying substrate, similarly to our own free-standing membrane devices.

Reference	Material	J_{sc} (mA/cm^2)	V_{oc} (V)
[1] Kurokawa et al (2009) *Tokyo Institute of Technology*	Si QD layer in carbide matrix Inclusion of nitrogen	0.42	0.289
[2] P. Löper et al (2012) *Fraunhofer Institute*	Si QD in carbide matrix	0.34	0.37
[3] I. Perez-Wurfl et al (2010) *University of New South Wales*	Si QD in oxide matrix (Co-sputtering & annealing)	0.02	0.492
[4] C.Y. Liu et al (2010) *Univ. of Minnesota*	Colloidal Si nanodots (spin casting)	0.148	0.51
[5] S. Yamada et al (2010) *Tokyo Institute of Technology*	Si QD layer in carbide matrix Inclusion of oxygen	0.34	0.518
This work	Electrochemically prepared nc-Si	0.383	**0.875**

Table. 6.1: *Comparison of different Si nanodots based PV devices using different approaches to the problem. The table includes reported characteristics of devices containing only Si nano-structures as absorber.*

VI.2 Limitations of the technology and discussion

• The energy conversion performance of the material is currently very low. A summary of the best results obtained for V_{oc}, J_{sc}, FF, η and the IQE at the SR peak 450 nm under 0V bias (summarized from different devices) are shown in **Table 6.2**. The current thickness of the devices, in excess of 25 μm, is thought to strongly limit the efficient extraction of the photogenerated carriers, especially considering that the lower part of the device made of low porosity n type material cannot theoretically behave as a widegap material. The current thickness of the devices also strongly expands the absorption of the membranes towards the infrared region, limiting the possible application of the material as a top cell material where transparency is required to transmit without loss the corresponding spectral region to the underlying middle and bottom cells. Secondly, while the presence of an "Urbach tail" behavior in PSi might not be related directly to the presence of a high density of state at the surface of the material, a general observation of characteristics of the material (both structural and electronic) strongly suggest the involvement of such states in the observed

characteristics. It is currently not completely clear if the most common type of impurity present in PSi, hydrogen, is responsible for such states and if the element is indeed present inside the material at depth up to 100 nm, that would make most PSi structures, even the largest one, almost completely passivated by hydrogen.

Parameters	V_{oc}	J_{sc}	FF	η	IQE at 450 nm Bias 0V
Value	0.875 V	68.79 µA	0.39	0.0174 % (as-prep.) 0.055 % (after SCM)	11%

Table. 6.2: *Summary of the highest performance achieved on full nc-PSi free-standing membrane cells.*

- Among the wide range of approach to Si nanodots fabrication, the processing of PSi is a simple and cost effective method resulting in a highly disordered material made of dots with a large variation in size and shape for the resulting Si "dots". In comparison, concurrent approaches focus on fabricating the material at the dot level, with highly expensive processing method, but with a strong control of the size, shape and spacing of the dots. Variations in size, shape and spacing of the dots have been shown both theoretically and experimentally to have a strong impact on the resulting characteristics of the material. Due to the simplicity of the PSi formation and the disordered nature of the process, accurate control over the size, shape and spacing of the material is a difficult task. The presence of both small highly luminescent and large non photo-luminescent crystallites in the material at the same time are a an important issue in terms of electronic conduction path as the largest Si structure, with similar electronic structure as c-Si, will prevail over the smallest one, strongly reducing the probability to observe a wide-gap behavior in the material. Beside the purely electronic phenomena such as the presence of states within or at the surface of the material, the fractal like geometrical aspect of the material is expected to play an equally strong role.

- As already discussed before, the high value of V_{oc} and the shift in the spectral response are not yet conclusive evidences of the material acting as a wide gap absorber. The actual apparent shift of the response of the membrane devices compare to bulk c-Si can be interpreted as a widening of the bandgap in the material. The problem here is that the peak located at 450 nm in this study is still within the response of the original bulk Si substrate. Since the quantum efficiency of the nc-PSi devices at that wavelength are well below the

reference substrate, even for the best devices, the apparent shift of the spectral response cannot be definitively related to a widening of the bandgap. A drastic increase of the response over the original material would be a better indicator of such band gap widening effect.
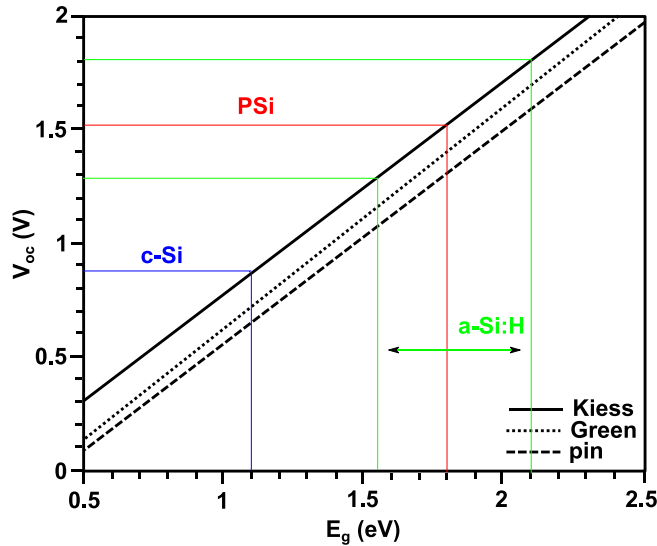

Fig. 6.1: *Theoretical calculation of the maximum achievable open circuit voltage V_{oc} in function of the material band gap according to three different models. The corresponding value for c-Si, PSi and a-Si:H are indicated as references.*

Secondly, if we take a look at the theoretical value of the open circuit voltage dependence on the material band-gap, as shown in **Fig 6.1** (redrawn from [6]), we obtain a theoretical maximum value of 1.5 V for a corresponding band gap of 1.8 eV. The actual highest measured V_{oc} on nc-PSi devices of 0,875 V is actually near the maximum range of voltage calculated for c-Si material with an estimated maximum voltage around 0.9 V but currently well below the maximum for a 1.8 eV gap material. The presence of the lower band gap p type layer at the top of the nano-porous layer might actually limit the value of the open circuit voltage. The V_{oc} value is also in the same range as those reported in pin type a-Si:H with Voc in the range 0.85 V. The similitude with a-Si does not stop here. The presence of a-Si like material in PSi has been early detected [7] through Raman spectroscopy with conflicting reports about the actual presence of an amorphous phase. A broad peak located around 480 cm^{-1} related to amorphous silicon was reported and the presence of such peaks was seen in a wide variety of luminescent p type material with the amorphous phase apparently present all along the surface and thickness of the PSi layer [8], but not in n type material (structural information of n type PSi are actually very scarce). An early explanation for the possible presence of an amorphous phase was proposed by Kunz [9], with a detected lattice dilation up to 1% compare to c-Si occurring in nanometric Si dots, leading to an apparent amorphization of the material near the surface. Another explanation

involved the re-deposition of atomic like Si species on the PSi surface during formation, forming Si nanoclusters as well as amorphous like tissue surrounding the crystalline cores of PSi [10]. An estimation of the amorphous phase in high porosity p type material gives an amount as high as 25%. The surface is also mixed with Si-oxide subspecies SiO_x in a non negligible quantity. PSi therefore appears to be an extremely complex multiphase material where competitive processes, especially the quantum confinement in the c-Si core and contribution from the multiphase surface, both contributing to the observed large variation of properties. In our devices, the similar range of band gap value between PSi and a-Si make the comparison of PV and SR characteristics difficult to analyze. As previously introduced in Chapter I, the surface conduction channel was proposed to be the dominant contribution at room temperature over conduction in confined crystallites, strongly suggesting the probability of a surface related effect in the observed PV. The chemistry of the surface of PSi material is also clearly involved in the observed PV effect as seen after treatment of the material though HF exposure and thermal annealing, whether the contribution is due to surface passivation by hydrogen or the presence of an amorphous coating at the surface. In opposition to the surface channel is the fact that the large V_{oc} PV effect is seen only in pn type material, and the fact that the presence of a junction in the porosified material indicates an involvement of the remaining c-Si nano-structure contained in the material.

- Due to the multilayer nature of the devices, strong inter-sample variation and strong effect of the surface chemistry, no distinct relation between the observed photovoltaic parameters J_{sc}/V_{oc} and the estimated band gap of the material have been found.

VI.3 Future prospects

Due to the extremely complex nature of the material and the inherent instability of its surface chemistry, a large amount of work is still required to get a better understanding of the real nature of nc-PSi material in view of its photoconductive and photovoltaic properties. The following sections will list the possible ways to pursue and improve the current characteristics of the material for future experimental work:

Thickness of the devices:

The current thickness of the devices presented here were in the range 25 – 30 μm. In such thick layer, most of the low porosity n type region at the bottom of the device is not expected to play an important role in the observed PV characteristics. A reduction of the thickness of the layer would therefore decrease the conduction path necessary to collect the photo-generated carriers, in addition to decrease the total absorption of the layer for a better matching of the absorption spectra of the PSi films with application as a top solar cell (current layers of ~25 μm are absorbing down to the NIR). Through a controlled separation process, we have shown the possibility to decrease the thickness of the pn type layers from around 30 μm down to 13-14 μm. The current separation technique was limited by the temperature control ability of our current experimental system, limited to cooling down to 5°C. The technique can be employed down to sub-zero temperature, in conjunction with a slight decrease of the HF volume ratio, to further reduce the thickness of nc-PSi layers below 10 μm. Thinning of the top p+ layer through modification of the junction formation conditions (decreasing the junction depth) is also expected to improve the efficiency of the devices.

Type and structure of the device:

The material was mostly investigated using an highly doped p+n+ structure with a relatively low doping difference between the p and n region and relatively deep junction (within 1 μm). Small increase in the p type region doping level as well as a small decrease of the junction depth did not show any visible modification or relation with the measured material characteristics. The impact of the junction properties were probably well within the relatively large inter-sample characteristics variation. The p+n- configuration was unfavorable to the layer separation and so far no layer of that type could be separated (due to strong reverse over-potential during the separation step). The reverse n+p+ and n+p- were investigated as well; in that case the nano-porous material is the lower p region. A PV effect was detected in this type of device as well, with limited photo-conversion efficiency due to the presence of the thick nano-porous p type layer at the bottom of the material. Polarity inversion compare to the expected original doping of the material was also detected in several samples. A rapid summary of the results obtained on n+p- material are shown in **Appendix E**.

Post-processing of the material:

The possibility to obtain high stabilization through chemical derivatization is still an actively investigated technique. The number of possible candidates is very large and the structure of each organic species might have a strong effect both during the surface modification process, such as coverage and bonding structure with the host material, as well as in the observed modification of the

material properties due to in-homogeneity in the coverage and alignment of the molecules with the surface (possibility of bending, twisting etc…). From a theoretical point of view, the use of smaller molecules would produce a better coverage of the surface and reduction of the in-homogeneity through reduced steric hindrance. Small molecules would also chemically diffuse more easily inside a complex nanometric material such as PSi. Preliminary experiment involving modification through acrylic acid was attempted on PSi without indication of any modification of the surface though covalent bonding. Similarly, while most report on PSi modification involves species such as decene and decanal, shorter molecule of alkene such as octene, heptene and their aldehyde counterparts octanal, heptanal etc…could be used to modify the surface of the material as well. A lot more work is required in this domain.

Concerning the current SCM involving Alkenes or aldehydes, the range of parameters available is large and the current experiments were conducted on a very limited range. Organic solution dipping was limited to 3 hours on average, but reports on longer dipping time up to 24 hours were reported with high stability achieved on electroluminescence. In addition to longer dipping time, change in the composition of the organic solution also appears to be an interesting route to improvement. The possibility to change from neat, concentrated solution to lower dissolution without decreasing the efficiency of the method was already demonstrated [11] and we are seeing even further possibilities in the mixing of different organic species. Since the stability and the performance of the passivated material appears to be strongly dependent on the organic species, a combined of both highly stable passivating molecules (such as undecylenic-acid) as well as species showing increase in photo-generated current (decanal) would greatly benefit the material toward practical applications. Further possibility of modifications of PSi toward stabilization and functionalization of the material are numerous and the number of possibilities in that particular field appears to be almost infinite.

Bibliography of Chapter VI.

[1] Y. Kurokawa, S. Tomita, S. Miyajima, A. Yamada, M. Konagai, Proc. 24th EU PVSEC, Hamburg, Germany, p. 398–403 (2009).

[2] P. Löper , D. Stüwe , M. Künle , M. Bivour , C. Reichel , R. Neubauer , M. Schnabel , M. Hermle , O. Eibl , S. Janz , M. Zacharias , and S. W. Glunz, Adv. Mater. **24**, p. 3124 (2012).

[3] I. Perez-Wurfl, L.Ma,D.Lin,X.Hao,M.A.Green,G.Conibeer, Solar Energy Mater. & Solar Cells **100**, p. 65 (2012).

[4] C.Y. Liu, U. R. Kortshagen, Nanoscale Res Lett. **5**, p. 1253 (2010).

[5] S. Yamada, Y. Kurokawa, S. Miyajima, A. Yamada, M. Konagai, 35th IEEE Photovoltaic Specialists Conference (PVSC), p. 766 (2010).

[6] F. Meillaud, A. Shah, C. Droz, E. Vallat-Sauvain, and C. Miazza, Solar Ener. Mat. and Solar Cells **90** (18-19), p. 2952 (2006).

[7] J. M. Perez, J. Villalobos, P. McNeill, J. Prasad, R. Cheek, J. Kelber, J. P. Estrera, P. D. Stevens, and R. Glosser, App. Phys. Lett. **61**, p. 563 (1992).

[8] G. Mariotto, F. Ziglio, and F.L. Freire Jr., Jour. of Non-Cryst. Solids **192 & 193**, p. 253 (1995).

[9] R. R. Kunz, P. M. Nitishin, H. R. Clark, M. Rothschild, and B. Ahern, Appl. Phys. Lett. **67**, p. 1766 (1995).

[10] S.Yu. Turishchev, V.A. Terekhov, V.M. Kashkarov, E.P. Domashevskaya, S.L. Molodtsov, D.V. Vyalykh, Jour. of Electron Spectro. and Related Phenomena **156–158**, p. 445 (2007).

[11] J. M. Buriak, Chemical Reviews **102** (5), p. 1271 (2002).

Appendix A

FTIR peaks reference table

Peak position (cm^{-1})	Attribution
As prepared material	
611-617	Si-Si stretch
624	SiH bend in Si$_3$-SiH
626	SiH wag
661	SiH wagging
662	Si-H$_2$ roll
905-910	SiH$_2$ scissor
1105	Si-O-Si asymmetric stretch (from bulk)
2087	SiH stretch
2110	SiH$_2$ stretch
2136 – 2138	Si-H$_3$ stretch
After organic modification	
1031-1160	SiO stretch in O-SiO and C-SiO
1463 - 1470	CH$_3$ asymmetric deformation, methylene bend
1640	C=C
1716 - 1720	C=O
2856	CH$_x$ stretch
2918 - 2921	CH$_2$ asymmetric stretch
2927	CH stretch in CH$_2$
2958-2960	CH$_3$ asymmetric stretch

Appendix B

Typical PN wafer formation process description

Base wafer:

Ø4 inches, one side mirror

N type (Sb doped)

Crystal alignment: (100)

Resistivity: 0.01- 0.02 Ω.cm ($1x10^{18}$ – $4x10^{18}$ cm-^{3})

Thickness: 525 ±25 μm

Top side treatment:

On top mirror side: P type layer (Boron) by Ion implantation (Single implantation).

Implantation parameters 1:

Energy: 30 keV

Dose: $2x10^{15}$ ions/cm^2

Post-implantation anneal:

1000^oC / 45 min

Implantation parameters 2:

Energy: 30 keV

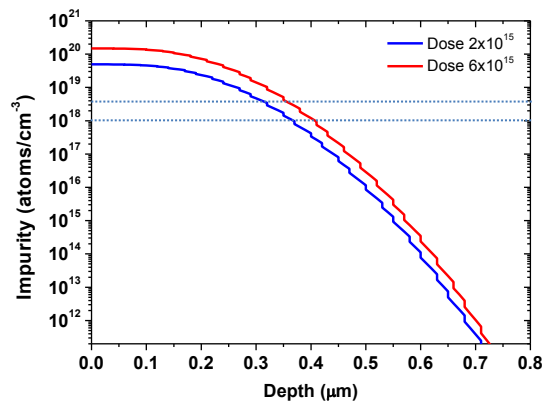Dose: $6x10^{15}$ ions/cm^2

Post-implantation anneal:

1000^oC / 45 min

Fig. 1: *Simulated implantations and subsequent annealing step for $2x10^{15}$ and $6x10^{15}$ions/cm^2 dose.*
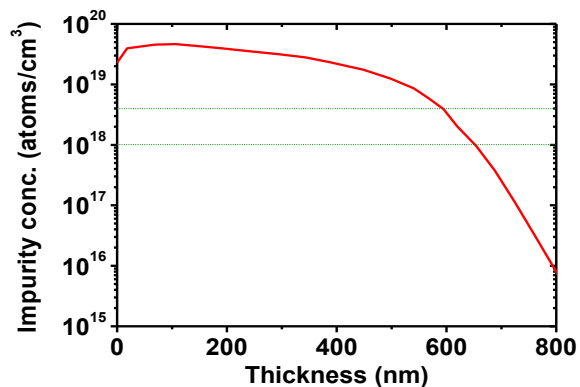

Fig. 2: *Impurity profile obtained by SIMS measurement on wafer implanted with a dose of $2x10^{15}$ ions/cm^2.*

169

Appendix C

Typical in-house nano-porous silicon fabrication recipes and corresponding physical characteristics

Substrate	HF conc. %	Current density mA/cm^2	Porosity %	Formation rate μm/min
P	35	50	57	2.8
P	27.5	20	62	1.1
P	27.5	50	68	2.4
P	27.5	75	72	3.35
P	15	10	80	0.3
P+	17.5	80	70	3.16
P+	15	80	80	2.73
P+	10	50	90	1.66
N (illum.)	15	5	80	0.2
N+	10	5	80	0.215
N+	27.5	100	NA (Low)	5.7
PN (illum.)	27.5	50	NA	3.6
PN (illum.)	27.5	25	NA	2

P type resistivity 4 – 8 Ω.cm.

P+ type resistivity ~ 0.01Ω.cm.

All anodizations were conducted under dark condition unless indicated

Appendix D

Separation parameters in function of the material type:

Sample type	Solution content	Current density	Duration
p	HF:Ethanol 1:1	≥ 250 mA/cm^2	3 to 5s
p+	HF:Ethanol 1:1	≥ 250 mA/cm^2	5s
n	HF:Ethanol 1:1	≥ 250 mA/cm^2	10s
n+	HF:Ethanol 1:1	≥ 250 mA/cm^2	10s
n+p-	HF:Ethanol 1:1	300 to 400 mA/cm^2	5s
p+n+	HF:Ethanol 1:1	Special pattern, see section below	See section below

Separation of p+n+ layers.

Pattern used to separate the p+n+ layer.
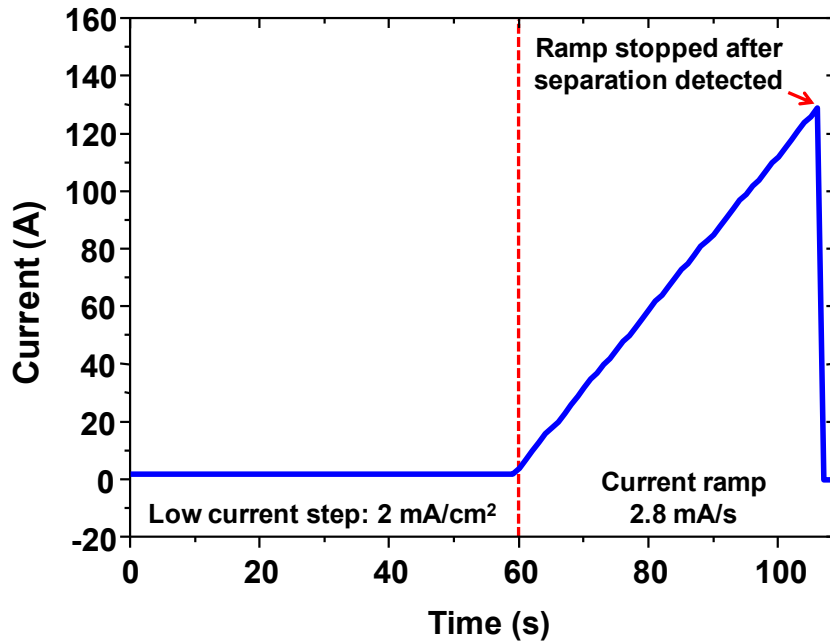
Appendix E

Summary of results obtained on np type material

Example 1, n+p+ type (doping level and junction depth similar to the the p+n+ substrate presented in this study)

Anodization condition:

HF(55%) : Ethanol(99.5%) 1:1 - 15 mA/cm^2 - 15 min - Under dark condition

Thickness: 22.7 microns

Aperture area of the device: 0.3423 cm^2

Contacting structure: Au-psi-Al

PV characterization results:

Voc: -0.268

Jsc: 1.91687x10^{-5} A/cm^2

Observations:

n+p+ devices shows a very low rectification with a reverse PV effect compare to the expected polarity of the device based on the original junction structure. The reversal of the PV characteristics might indicate that the p type layer becomes n after porosification, a phenomenon observed in several of our devices which appears to be dependent on the formation conditions. The reversal has been observed in n+p- devices as well.
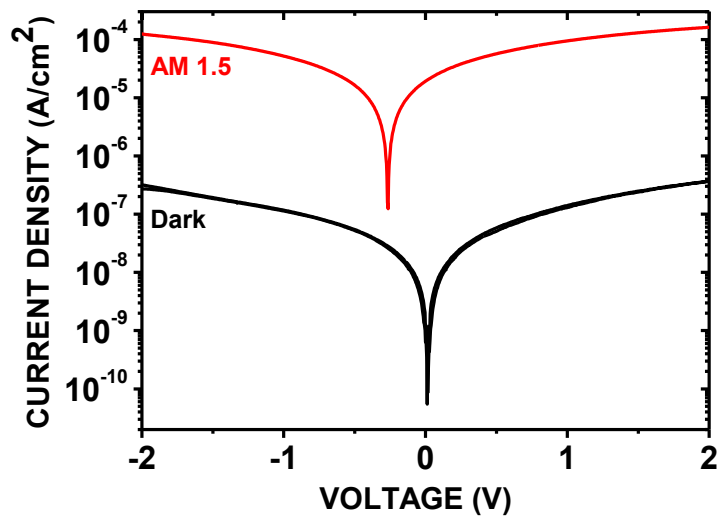

Fig. 1: *PV effect detected in n+p+ layers with a reversed photovoltaic characteristic, showing the strong modification of the material and majority carrier nature occurring after porosification.*
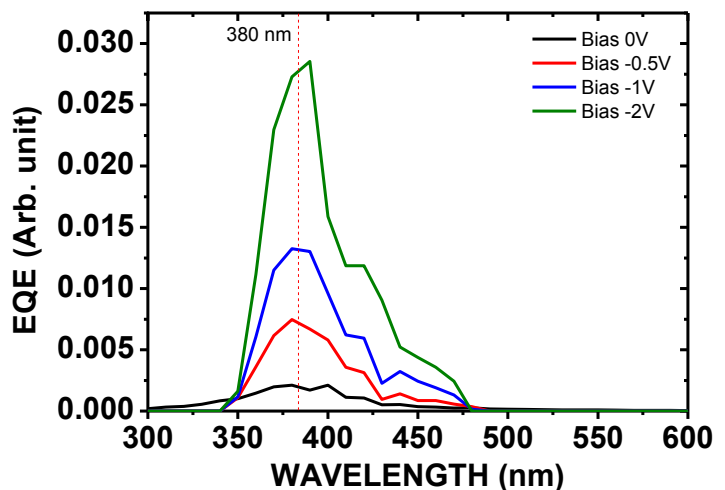

Fig. 2: *Corresponding spectral response of p+n+ free-standing membranes at different bias voltage. The response is distinctly different than the response observed in n+p+ layers.*

Example 2, n+p- type (p concentration ~1x10^{16}, n type concentration 5x10^{19}, junction depth 1.3 µm)

Anodization condition:

HF(55%) : Ethanol(99.5%) 1:1 - 15 mA/cm^2 - 20 min – Illumination from a tungsten during the first 1 min.

Aperture area of the device: 0.1073 cm^2

Contacting structure: Au-PSi-Al

PV characterization results:

Voc: 0.62 V

Jsc: 7.02092x10^{-6} A/cm^2

Observations:

In the case of n+p- type membranes, several trends were observed in the devices characteristics. Similarly to the example 1 in this appendix, a reversed PV effect was observed for samples anodized at relatively high current density (J $\geq$ 25 mA/cm2). For lower current formation and with help of front illumination during the formation, more typical PV characteristics with relatively high V$_{oc}$ could be detected in the n+p- configuration as well as seen in **Fig. 3**. The use of the n+p- structure has the advantage of being easier to anodized due to the forward polarization of the junction during the electrochemical processing but its practical used is limited by the strong porosity of the lower p type layer wich renders the material highly resistive and mechanically fragile compare to its pn type counterpart.
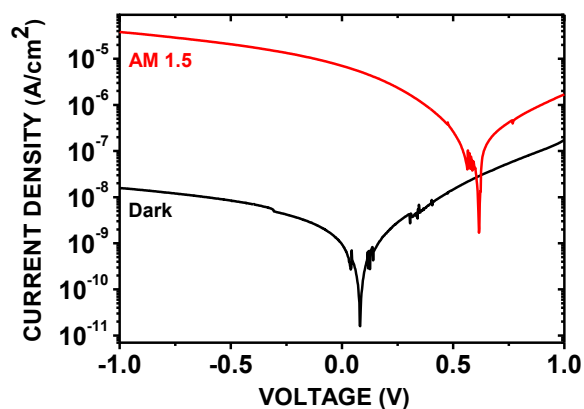

Fig. 3: *PV effect detected in n+p- layers with a relatively high V$_{oc}$ of 0.62 V. The photocurrent was limted compare to p+n+ layer due to the strong resistivity of the p- type material.*
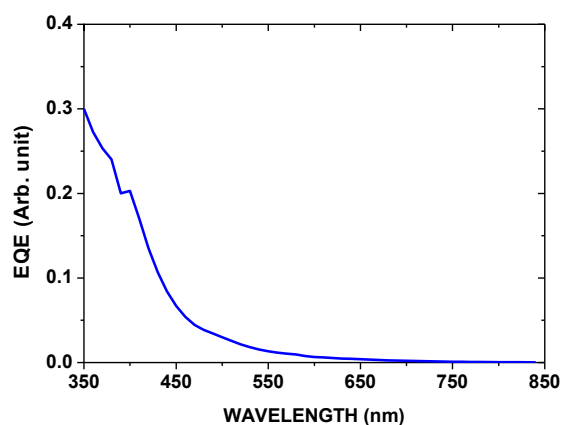

Fig. 4: *Corresponding IPCE spectra of a free-standing n+p- layer.*

研究業績

関連論文

1. **R. Mentek**, D. Hippo, B. Gelloz, and N. Koshida, Photovoltaic effect with high open circuit voltage observed in electrochemically prepared nanocrystalline silicon membranes, Materials Science and Engineering B, under review.

2. **R. Mentek**, B. Gelloz, and N. Koshida , *Photovoltaic Property of Wide-Gap Nanocrystalline Silicon Layers*, **Japanese Journal of Applied Physics 51** 02BP05 (2012).

3. **R. Mentek**, B. Gelloz, and N. Koshida , *Fabrication and Optical Characterization of Self-Standing Wide-Gap Nanocrystalline Silicon Layers*, **Japanese Journal of Applied Physics 49** 04DG22 (2010).

国際会議発表

1. **R. Mentek**, B. Gelloz, D. Hippo and N. Koshida, *Large open-circuit-voltage photovoltaic effect in nanocrystalline silicon layers*, International Conference on Solid State Devices and Materials, p. 1178 (Fukuoka, 2013).

2. **R. Mentek**, B. Gelloz, D. Hippo and N. Koshida, *High Open-Circuit Voltage Observed in Nanocrystalline Silicon Membrane Cells*, Photovoltaic Technical Conference: Thin film and Advanced Solutions, Aix-en-Provence, S1P2 Thin Film Silicon (2013).

3. **R. Mentek**, D. Hippo and N. Koshida, *Photovoltaic Properties of Nanosilicon Membrane Cells*, 5th International Symposium on Innovative Solar Cells (2013).

4. **R. Mentek**, B. Gelloz, D. Hippo and N. Koshida, *Photovoltaic Characterization Of Wide-Gap Nanocrystalline Silicon membranes cells*, International Conference on Solid State Devices and Materials, p. 1003 (Kyoto, 2012).

5. N. Koshida, T. Ohta, **R. Mentek** and B. Gelloz, *(Invited) Photonic and Related Functional Applications of Quantum-sized Nanosilicon*, Fifth International Conference on Optical, Optoelectronic and Photonic Materials and Applications, p.55 (Nara, 2012).

6. **R. Mentek**, B. Gelloz, D. Hippo and N. Koshida, *Photovoltaic characterization of wide-gap nanocrystalline silicon layers*, Photovoltaic Technical Conference: Thin film and Advanced Solutions, Aix-en-Provence, D1-2/04 (2012).

7. N. Koshida, **R. Mentek** and D. Hippo, *Photoelectric Functions of Nanosilicon as a Wide-Gap Material*, 4th International Symposium on Innovative Solar Cells (Tokyo University, 2012).

8. **R. Mentek**, B. Gelloz, and N. Koshida, *Photovoltaic Characterization Of Wide-Gap Nanocrystalline Silicon Layers*, International Conference on Solid State Devices and Materials p. 1357 (2011).

9. **R. Mentek**, B. Gelloz, and N. Koshida, *Photovoltaic Characterization Of Wide-Gap Nanocrystalline Silicon Layers*, Photovoltaic Technical Conference: Thin film and Advanced Solutions, Aix-en-Provence, Session 1 (2011).

10. **R. Mentek**, B. Gelloz, M. Kawabata and N. Koshida, *Photoelectric properties of nanocrystalline silicon as a wide-gap top-cell material*, 3rd International Symposium on Innovative Solar Cells (2010).

11. **R. Mentek**, B. Gelloz, M. Kawabata and N. Koshida, *Optical and Photoelectrical Characterizations of Wide-gap Nanocrystalline Silicon Layers*, International Conference on Solid State Devices and Materials p. 911 (2010).

12. N. Koshida, B. Gelloz, **R. Mentek**, H. Yoshimura and Y. Hirano, *Properties of Quantum-sized Nanosilicon as a Functional Photonic Material*, Material Research Society 2010 Spring meeting, invited paper **T8.3.**

13. **R. Mentek**, B. Gelloz, H. Yoshimura and N. Koshida, *Fabrication and Optical Characterization of Self-standing Wide-gap Nanocrystalline Silicon Layers*, 2nd

International Symposium on Innovative Solar Cells, p. 231 (2009).

14. **R. Mentek**, B. Gelloz, N. Koshida, *Fabrication and Optical Characterization of Self-standing Wide-gap Nanocrystalline Silicon Layers*, International Conference on Solid State Devices and Materials p. 218 (2009).

15. **R. Mentek**, H. Yoshimura, B. Gelloz, J. Shirakashi, N. Koshida, *Fabrication of self-standing wide-gap nanocrystalline silicon layers*, International Symposium on Innovative Solar Cells, p. 144 (2009).

国内学会発表

1. **R. Mentek** et al, *Large open-circuit-photovoltage effect in nanocrystalline silicon membrane cells*, Jap. Soc. Appl. Phys. 74th Fall Meeting, (Kyoto, 2013) 16-085.

2. **R. Mentek** et al, *Photovoltaic Properties of Wide-gap Nanocrystalline Silicon Membrane Cells,* Jap. Soc. Appl. Phys. 60th Spring Meeting, (Kanagawa, 2013) 16-050.

3. **R. Mentek** et al, *Photovoltaic Property of Free-Standing Nanocrystalline Silicon Layers,* Jap. Soc. Appl. Phys. 73rd Fall Meeting, (Matsuyama, 2012) 16-086.

4. **R. Mentek** et al, *Photovoltaic Characterization of Wide-gap Nanocrystalline Silicon Layers,* Jap. Soc. Appl. Phys. 59th Spring Meeting, (Tokyo, 2012) 16-095.

5. **R. Mentek** et al, *Photovoltaic Properties of Wide-gap Nanocrystalline Silicon Layers*, Jap. Soc. Appl. Phys. 72nd Fall Meeting, (Yamagata, 2011) 16-049.

6. **R. Mentek** et al, *Photovoltaic Properties of Wide-gap Nanocrystalline Silicon Layers*, Jap. Soc. Appl. Phys. 58th Spring Meeting, (Kanagawa, 2011).

7. **R. Mentek** et al, *Fabrication and Opto-electrical Characterization of Self-standing Wide-gap Nanocrystalline Silicon Layers*, Jap. Soc. Appl. Phys. 71th Fall Meeting, 14-283 (Nagasaki, 2010).

8. **R. Mentek** et al, *Non-contact Silicon Ingot Slicing by Electrochemical Anodization (III)*, Jap. Soc. Appl. Phys. 57th Spring Meeting, 14-156 (Tsukuba, 2010).

9. **R. Mentek** et al, *Non-contact Silicon Ingot Slicing by Electrochemical Anodization (II)*, Jap. Soc. Appl. Phys. 70th Autumn Meeting, p. 1319 (Toyama, 2009).

10. **R. Mentek** et al, *Non-contact Silicon Ingot Slicing by Electrochemical Anodization*, Jap. Soc. Appl. Phys. 56th Spring Meeting, p. 1500 (Tsukuba, 2009).

11. **R. Mentek** et al, *Non-contact Silicon Ingot Cut by Electrochemical Anodization*, Jap. Soc. Appl. Phys. 69th Autumn Meeting p. 1290 (Nagoya, 2008).

12. 蕨迫光紀、兼堀恵一、山田宏治、嶋田壽一、**Romain Mentek**、増永昌弘２、津端修一、Bernard Gelloz、越田信義、陽極酸化によるシリコンインゴットのスライス、第 5 回学振 175 委員会「次世代の太陽光発電システム」シンポジウム（2008）.

その他

1. Bernard Gelloz, **Romain Mentek**, and Nobuyoshi Koshida, *Interrelated Ultraviolet and Long-lived Blue luminescence bands of Oxidized Nanocrystalline Porous Silicon*, International Conference on Solid State Devices and Materials, p. 218 (Fukuoka, 2013).

2. R. Suda, M. Ito, M. Yagi, A. Kojima, **R. Mentek**, N. Mori, J. Shirakashi, and N. Koshida, *Ballistic Electro-Deposition of Thin Si, Ge, and SiGe Films*, International Conference on Solid State Devices and Materials, p. 254 (Fukuoka, 2013).

3. B. Gelloz, **R. Mentek**, N. Koshida, *Blue and UV Luminescence Properties of Oxidized Nanosilicon and Pure Porous Glass*, Jap. Soc. Appl. Phys. 74th Fall Meeting, (Kyoto, 2013) 14-144.

4. M. Ito, R. Suda, M. Yagi, A. Kojima, **R. Mentek**, J. Shirakashi, and N. Koshida, *Liquid-phase deposition of thin Si, Ge, and SiGe films based on ballistic electron injection*, Jap. Soc. Appl. Phys. 74th Fall Meeting, (Kyoto, 2013) 13-086.

5. N. Koshida, N. Ikegami, A. Kojima, **R. Mentek** and B.Gelloz, *(Invited) Ballistic Electron Effects in Nanosilicon and Their Applications*, ECS 223rd Meeting, The

Electrochemical Society, E3-0796 (2013).

6. B. Gelloz, **R. Mentek** and N. Koshida, *(Invited) Ultraviolet and Long-Lived Blue Luminescence of Oxidized Porous Silicon*, ECS 223rd Meeting, The Electrochemical Society, E3-0798 (2013).

7. B. Gelloz, **R. Mentek** and N. Koshida, *Interlinked Ultraviolet and Blue Emissions in Oxidized Nano-silicon,* Jap. Soc. Appl. Phys. 60th Spring Meeting, (Kanagawa, 2013) 14-163.

8. B. Gelloz, **R. Mentek** and N. Koshida, *Relaxation Processes and Functions of Blue Phosphorescent Porous Silicon*, PRiME 2012, The Electrochemical Society, 2378 (2012).

9. T. Ohta, **R. Mentek**, B. Gelloz, N. Mori and N. Koshida, *Liquid-Phase Deposition of Thin Si and Ge Films Based on Ballistic Electro-reduction*, PRiME 2012, The Electrochemical Society, 3189 (2012).

10. N. Koshida, T. Ohta, **R. Mentek** and B. Gelloz, *(Invited) Photonic and Related Functional Applications of Quantum-sized Nanosilicon*, Fifth International Conference on Optical, Optoelectronic and Photonic Materials and Applications, p.55 (Nara, 2012).

11. N. Koshida, **R. Mentek** and D. Hippo, *Photoelectric Functions of Nanosilicon as a Wide-Gap Material*, 4th International Symposium on Innovative Solar Cells (Tokyo University, 2012).

12. B. Gelloz, **R. Mentek** and N. Koshida, *Optical properties of phosphorescent nano-silicon electrochemically doped with terbium*, **Phys. Status Solidi C 9**, No. 12, p. 2318–2321 (2012).

13. N. Koshida, T. Ohta, Y. Hirano, **R. Mentek** and Bernard Gelloz, *Functional Device Applications of Nanosilicon*, Key Engineering Materials, Volume 470, p. 20 (2011).

14. B. Gelloz, **R. Mentek**, T. Djenizian, F. Dumur, L. Jin and N. Koshida, *Electropolymerization of Poly(para-phenylene)vinylene Films onto and Inside Porous Si layers of different types and morphologies*, **J. Electrochem. Soc.**,

Volume 157, Issue 12, D648-D655 (2010).

15. N. Koshida, B. Gelloz, **R. Mentek**, H. Yoshimura and Y. Hirano, *Properties of Quantum-sized Nanosilicon as a Functional Photonic Material*, Material Research Society 2010 Spring meeting, invited paper **T8.3.**

16. B. Gelloz, **R. Mentek**, T. Djenizian, F. Dumur, L. Jin and N. Koshida, (Invited) *Electropolymerized Poly(para-phenylene)vinylene Films onto and Inside Porous Si*, ECS Transactions Volume 28, p. 91-103 (2010).

17. B. Gelloz, **R. Mentek**, and N. Koshida , *Specific Blue Light Emission from Nanocrystalline Porous Si Treated by High-Pressure Water Vapor Annealing*, **Japanese Journal of Applied Physics** **48** 04C1191 (2009).

18. B. Gelloz, **R. Mentek**, and N. Koshida, *Specific Blue Light Emission from Nanocrystalline Porous Si Treated by High-Pressure Water Vapor Annealing,* International Conference on Solid State Devices and Materials p. (2008).

19. B. Gelloz, **R. Mentek**, K. Nishikawa, and N. Koshida. "Controlled Blue Photoluminescence of Nanocrystalline Porous Silicon Treated by High-Pressure Wator Vapor Annealling". Materials Research Society Symposium **MM4.20** (2008)

20. B. Gelloz, M. Masunaga, T. Shirasawa, **R. Mentek**, T. Ohta, and N. Koshida, *Enhanced Controllability of Periodic Silicon Nanostructures by Magnetic Field Anodization*, ECS Transactions Vol. **16**, pp 195-200 (2008).

21. B. Gelloz, T. Shibata, **R. Mentek**, and N. Koshida, *Pronounced Photonic Effects of High-Pressure Water Vapor Annealing on Nanocrystalline Porous Silicon,* Materials Research Society Symposium Proceeding Group IV Semiconductor Nanostructures, **958**, 0958-L08-02 (2007).

Acknowledgement

I would like to express my sincere gratitude to Professor Nobuyoshi Koshida for providing the opportunity to stay and work in his laboratory for almost 7 years now, and for introducing me to various financial support program (Jiritsu, Human Resource Development Program for Scientific Powerhouse etc…) and work opportunities through his venture company Quantum 14. Many thanks to my academic supervisor Professor Suda and examination jury member Professor Deng, Professor Sameshima, Professor Shirakashi and Professor Ueno for their helpful comments and suggestions toward improving my thesis work.

I would like to express my gratitude to:

- The Quantum 14 executive staff, Dr. Toshikazu Shimada, Dr. Terunori Warabisako and Hiroshi Tomita for managing the joint development of the electrochemical slicing technology
- All the members directly involved with the experimental work on the electrochemical slicing: Dr. Keiichi Kanehori (Quantum 14), Kouji Yamada (Quantum 14), Masamitsu Mori (Quantum 14), Masahiro Masunaga (TUAT), Shuichi Tsubata (TUAT), Takamasa Yamakawa (TUAT).
- Dr. Hitoshi Sai (AIST), Dr. Tetsuya Kaneko (AIST) for their collaboration and help with a-Si and ITO deposition at the AIST Tsukuba facility.
- Dr. Bernard Gelloz for his introduction to the Koshida laboratory, to porous silicon material and for our continuous collaboration on studying the luminescent properties of porous silicon.
- The Koshida laboratory members, Dr. Toshiyuki Oota, Dr. Hideo Yoshimura, Tomonori Sakaguchi, Kouta Nishikawa, Mari Kawabata, Takaaki Kimura, Akira Kojima and Daihei Hippo. A special thanks to Dr. Naokatsu Ikegami for teaching me absolutely unusable yojijukugo!
- Pr. Junichi Shirakashi and all the members of his laboratory.

And finally I would like to thank Dr. Etienne Gheeraert and Brice Duhamel from the Polytech Grenoble international relation office for allowing my original 1 year stay in TUAT STEP exchange program. I also thank all the staff members of TUAT exchange student center and especially Pr. Tatsuo Noma for his formal introduction to my current laboratory.